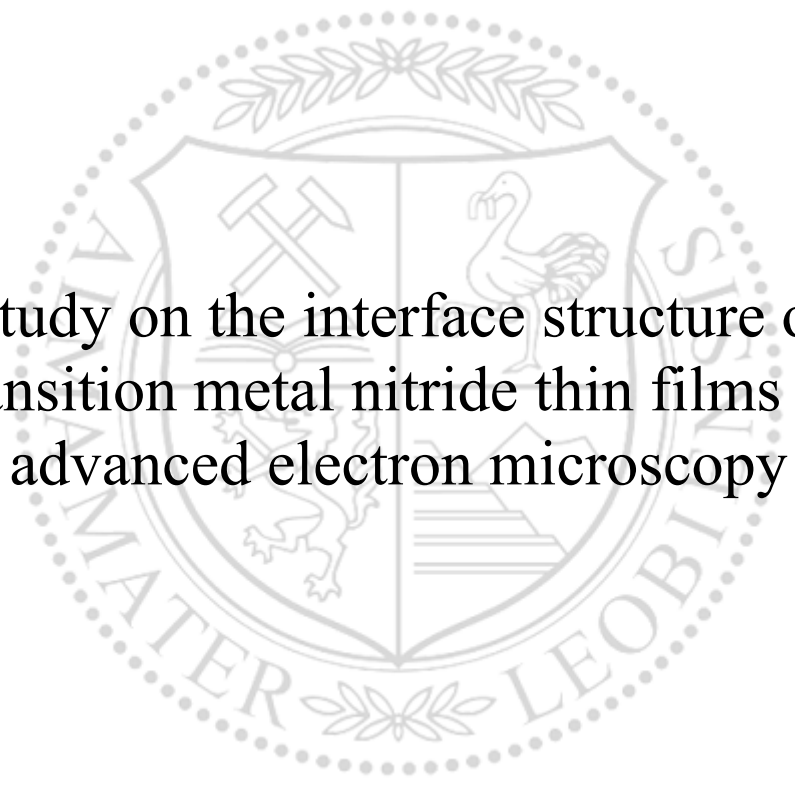Chair of Materials Physics

Doctoral Thesis

Study on the interface structure of transition metal nitride thin films by advanced electron microscopy

Zhuo Chen

March 2021

AFFIDAVIT

I declare on oath that I wrote this thesis independently, did not use other than the specified sources and aids, and did not otherwise use any unauthorized aids.

I declare that I have read, understood, and complied with the guidelines of the senate of the Montanuniversität Leoben for "Good Scientific Practice".

Furthermore, I declare that the electronic and printed version of the submitted thesis are identical, both, formally and with regard to content.

Date 02.03.2021

zhuo chen

_____

Signature Author
Zhuo Chen

MONTANUNIVERSITÄT LEOBEN
www.unileoben.ac.at

Zhuo Chen
Josef-Heissl-Straße 26
8700 Leoben

To the Dean of graduate Studies of the Montanuniversitaet Leoben

Declaration of Approval for the Digital Publication of Scientific Theses

I am aware that the thesis entitled "Study on the interface structure of transition metal nitride thin films by advanced electron microscopy" will be subject to a plagiarism assessment and may be stored by Montanuniversität Leoben for an unlimited period of time.

I agree that the University Library of Montanuniversität Leoben may publish the thesis open access in the World Wide Web. For embargoed theses this will be done after the embargo expires.

Note: in case you refuse the open access publication in the World Wide Web, the thesis will only be published in printed form (after a possible embargo has expired) in the University Library (dissertations also in the Austrian National Library).

I hereby agree with the open access publication of my thesis on the World Wide Web:

⊠ Yes

O No

Date 02.03.2021

zhuo chen

Signature Author

Acknowledgements

First, I want to sincerely appreciate my supervisor **PD. Dr. Zaoli Zhang** for his support and help. Your professional knowledge has greatly helped my experiments. Moreover, thank you for your continuous revision and guidance on the publication of the manuscript. Without your guidance, these works would not have been possible. I am honored that you can be my teacher.

I am very grateful to **PD. Dr. David Holec**, **Dr. Matthias Bartosik,** and **Prof. Paul H. Mayrhofer** for many scientific discussions. Thank **David** for providing theoretical simulations, which greatly help understand my experimental results, and **Matthias** and **Paul** for depositing various interesting coatings. Furthermore, I would also like to thank **Prof. Jürgen Eckert**, my mentor, for his support.

I would like to express the appreciation to **Lukas Löfler**, **Dr. Ganesh Kumar Nayak** for their DFT and MD simulations, **Dr. Oliver Renk** for discussion on the plastic deformation mechanism.

I gratefully acknowledge my colleagues **Ulrich Haselmann**, **Qinqin Shao,** and **Dr. Yonghui Zheng** for the great support in image simulation and TEM experiments. I would also like to thank the technicians: **Herwig Felber**, **Gabriele Felber,** and **Jan Michalička (**at Ceitec Nano, Brno）for their help in TEM sample preparation and TEM operation training. In addition, I would like to thank all of my colleagues and friends at Erich Schmid Institute of Materials Science.

Finally, I want to thank my parents. Over the years, they have provided excellent help and encouragement to my life and research abroad.

Abstract

Multilayer coatings have excellent hardness and toughness, which largely depends on their microscopic interface structure. Therefore, characterizing the interface of materials on the atomic scale is very important for a comprehensive understanding of the mechanical properties of multilayer coatings. This thesis is to study the interface characteristics of transition metal nitrides (TMNs) multilayer hard coatings and their interface-related phenomena by a spherical aberration-corrected transmission electron microscopy.

The first part of this thesis studies the interface effect on the metastable phase stability. HRTEM studies reveal that the different growth orientation exhibits a dissimilar capability to stabilize the metastable phase. Contrary to the <111> orientation, in both <110> and <100> orientations, several unusually highly mismatched cubic-CrN/wurtzite-AlN interface structures form as soon as wurtzite-AlN is present. DFT studies suggest that the larger critical thickness of the AlN layers in <100> and <110> orientation is allowed by the lower surface energy and higher cubic/wurtzite interfacial energy. These findings enrich the metastable-phase stabilization mechanism in multilayer and further offer a pathway for the design of high-quality superlattice coating.

The second part of this thesis studies the phenomenon of interface intermixing driven by plastic deformation. Using the atomic-resolution electron microscopy and spectroscopy, together with theoretical calculations (MD and DFT simulation), a nanoindentation-induced large-scale alloying (forming a solid solution) at the TiN/AlN superlattice interfaces is first revealed. The alloying substantially reduces the interface density and leads to a sharp drop in the dislocation density, consequently reducing the achievable strength. These findings rationalize the mechanism responsible for the currently not well-understood inverse Hall-Petch effect in superlattice coatings with a relatively small bilayer period.

In the final part, the TMN CrN twinning at the heterophase interface and the deformation mechanism of the twin interface have been studied in detail. A high density of rock-salt CrN twins with $\Sigma3\{112\}$ incoherent twin boundaries (ITB) was found in the $\{111\}\|\{0002\}$ textured film. It has been proved that the high density of twins is related to the existence of the wurtzite $\{0002\}$ interface terrace. Based on the HRTEM observations and atomic-model analyses, supplemented with theoretical calculations, several nucleation modes of twins with $\Sigma3 \{112\}$ ITB and $\Sigma3 \{111\}$ CTB (coherent twin boundary) are proposed. Simultaneously, the migration behavior of CrN CTB is further studied in this thesis via *in-situ* atomic-resolution TEM. It is found that CTB migration is associated with a boundary structure alternating from an N-

terminated to Cr-terminated, involving Cr and N atom respective motion, i.e., asynchronous CTB migration. Local strain analysis and DFT simulations further reveal the dynamic and thermodynamic mechanism of such asynchronous migration. These findings uncover an atomic-scale dynamic process of defect nucleation and CTB migration in a binary system, which provides new insight into the atomic-scale interface deformation mechanism in TMNs.

Kurzfassung

Mehrschichtbeschichtungen weisen eine ausgezeichnete Härte und Zähigkeit auf, was weitgehend von ihrer mikroskopischen Grenzflächenstruktur abhängt. Daher ist die Charakterisierung der Grenzfläche von Materialien auf atomarer Ebene für ein umfassendes Verständnis der mechanischen Eigenschaften von Mehrlagenbeschichtungen sehr wichtig. In dieser Arbeit werden die Grenzflächeneigenschaften von mehrlagigen Hartstoffbeschichtungen aus Übergangsmetallnitriden (TMNs) und ihre grenzflächenbezogenen Phänomene mit Hilfe von sphärischer aberrationskorrigierter Transmissionselektronenmikroskopie untersucht.

Der erste Teil dieser Arbeit untersucht den Grenzflächeneffekt auf die Stabilität der metastabilen Phase. HRTEM-Studien zeigen, dass die unterschiedliche Wachstumsorientierung eine unterschiedliche Fähigkeit zur Stabilisierung der metastabilen Phase aufweist. Im Gegensatz zur <111> -Orientierung bilden sich sowohl in <110> - als auch in <100> - Orientierung mehrere ungewöhnlich stark nicht fehlangepasste kubische CrN / Wurtzit-AlN-Grenzflächenstrukturen, sobald Wurtzit-AlN vorhanden ist. DFT-Studien legen nahe, dass die größere kritische Dicke der AlN-Schichten in <100> - und <110> -Orientierung durch die niedrigere Oberflächenenergie und die höhere Grenzflächenenergie zwischen kubischer Kristallstruktur und Wurtzit ermöglicht wird. Diese Ergebnisse bereichern den Stabilisierungsmechanismus der metastabilen Phase in Mehrlagenschichten und bieten darüber hinaus einen Weg für das Design von hochwertigen Übergitterbeschichtungen.

Im zweiten Teil dieser Arbeit wird das Phänomen der Grenzflächenvermischung aufgrund plastischer Verformung untersucht. Unter Verwendung der Elektronenmikroskopie und Spektroskopie mit atomarer Auflösung sowie theoretischen Berechnungen (MD- und DFT-Simulation) wird zunächst eine durch Nanoindentation induzierte großflächige Legierung (Bildung einer festen Lösung) an den TiN/AlN-Übergittergrenzflächen nachgewiesen. Das Legieren verringert die Grenzflächendichte erheblich und führt zu einem starken Abfall der Versetzungsdichte, wodurch die erreichbare Festigkeit verringert wird. Diese Ergebnisse rationalisieren den Mechanismus, der für den derzeit nicht gut verstandenen inversen Hall-Petch-Effekt in Übergitterbeschichtungen mit einer relativ kleinen Doppelschichtperiode verantwortlich ist.

Im letzten Teil wurden die TMN-CrN-Zwillinge an der Heterophasengrenzfläche und der Verformungsmechanismus der Zwillingsgrenzfläche eingehend untersucht. Eine hohe Dichte von Steinsalz-CrN-Zwillingen mit $\Sigma 3\{112\}$ inkohärenten Zwillingsgrenzen (ITB) wurde in dem $\{111\}\|\{0002\}$ texturierten Film gefunden. Es wurde nachgewiesen, dass die hohe

Zwillingsdichte mit der Existenz der Wurtzit-{0002}-Schnittstellenterrasse zusammenhängt. Basierend auf den HRTEM-Beobachtungen und Atommodellanalysen, ergänzt durch theoretische Berechnungen, werden verschiedene Keimbildungsmodi von Zwillingen mit Σ3 {112} ITB und Σ3 {111} CTB (kohärente Zwillingsgrenze) vorgeschlagen. Gleichzeitig in dieser Arbeit wird das Migrationsverhalten von CrN CTB mittels In-situ-TEM mit atomarer Auflösung weiter untersucht. Dabei wird herausgefunden, dass die CTB-Migration mit einer Grenzstruktur verbunden ist, die von einer N-terminierten zu einer Cr-terminierten wechselt und dabei eine entsprechende Bewegung des Cr- und N-Atoms beinhaltet, d.h. eine asynchrone CTB-Migration. Lokale Dehnungsanalysen und DFT-Simulationen zeigen ferner den dynamischen und thermodynamischen Mechanismus einer solchen asynchronen Migration. Diese Ergebnisse decken einen dynamischen Prozess der Defektkeimbildung und CTB-Migration auf atomarer Ebene in einem binären System auf, der neue Einblicke in den Deformationsmechanismus der Grenzfläche auf atomarer Ebene in TMNs bietet.

Acronyms and Abbreviations

TMNs	Transition metal nitrides
rs-CrN	Rocksalt chromium nitride
w-AlN	Wurtzite aluminum nitride
SL	Superlattice
CVD	Chemical vapor deposition
PVD	Physical vapor deposition
XRD	X-ray diffraction
TEM	Transmission electron microscopy
HRTEM	High-resolution transmission electron microscopy
Cs	Spherical aberration coefficient
HAADF	High-angle annular dark-field
STEM	Scanning transmission electron microscopy
BF	Bright-field
DF	Dark-field
SAED	Selected-area electron diffraction
FFT	Fast Fourier transform
EDXS	Energy dispersive X-ray spectroscopy
EELS	Electron energy loss spectroscopy
SFEs	Stacking fault energies
CTB	Coherent twin boundary
ITB	Incoherent twin boundary
TD	Twin defect
CLS	Confined layer slip
IBS	Interface barrier strength
DFT	Density functional theory
MD	Molecular dynamics
VASP	Vienna Ab initio Simulation Package

Contents

1 Introduction

For a long time, thin-film technology has been applied to computer storage devices, electronic semiconductor devices, batteries, optical coatings, and protective coatings. Among these films, ceramic films, e.g., metal oxide, carbide, and nitride ceramics, have a wider range of applications. Since the ceramic materials' relatively high hardness, such films can be used to protect the substrate from corrosion oxidation and wear. Experimental studies [1-8] have shown that transition metal nitrides (TMNs) are extremely hard materials. When they are applied as multilayers, their hardness exceeds 40 GPa, which is several times the hardness of the monolithic (single-layer) nitride coating [1]. Thus, nitride multilayer coatings are promising for a variety of practical applications.

Since the mid-1980s, the deposition method and the growth mechanism of super-hard CVD or PVD multilayer film have been reported [1, 2, 7, 9-11]. For the early multilayer, it was just a simple arrangement of two materials with different compositions alternately, while the thickness of a single layer is significant (10-100 nm). However, people were soon recognized that a significant reduction of the thickness of the individual layers (down to a few nanometers) and applied superlattice structure could greatly enhance thin film mechanical properties. The performance improvement can be attributed to the interface effect in nanoscale multilayer. However, the relationship between interface structure and macroscopic mechanical properties at the atomic scale has not yet been fully understood.

Previous research [12-16] on CrN/AlN multilayer coatings has shown that the hardness can be significantly enhanced when the AlN layer's thickness is less than 4.0 nm. Lowering the individual layer thickness can increase the number of interfaces and stabilize the phase structure. For a thinner AlN, XRD and TEM characterization shows that the multilayer has a rock-salt (*rs*)/rock-salt (*rs*) superlattice structure [12-15]. Unfortunately, a thicker AlN layer (beyond the critical thickness) will lead to a phase transformation from the rock-salt to the wurtzite (*w*) phase in CrN/AlN multilayer, which has a relatively low hardness (23–25 GPa), poor adhesion, and low wear resistance. So far, the influence of the AlN layer thickness on the multilayer has been known. However, how the crystallographic orientation affects the stability of AlN is still unclear. Therefore, **PUBLICATION I** is devoted to a study on the crystallographic orientation and interface structure effects on metastable phase (*rs*-AlN) stability.

The classic Hall-Petch strengthening relationship indicates that the smaller grain size has higher mechanical properties. In multilayer thin films, a similar effect can be achieved by lowering the individual layer thicknesses; the increasing number of interfaces enhances the

hardness. According to this, numerous efforts have been devoted to designing novel multilayers with a small bilayer thickness in order to acquire superior mechanical properties for potential applications. Although the coherent interface's (superlattice coating) multilayer with a bilayer-period thickness of just a few nanometers showed the best combination of hardness, toughness, and elastic modulus [12, 17, 18], the interface may broaden significantly due to the intermixing, which affects the multilayer performance accordingly. Currently, the deformation-induced interfacial intermixing in multilayer coatings is entirely unknown and overlooked. Through detailed electron microscopy study and theoretical calculations, **PUBLICATION II** investigates the nanoindentation-caused alloying (or intermixing) in the TiN/AlN superlattice. The paper further demonstrates that such mixing changes the dislocation behavior, which thus provides a new understanding of nano-scale multilayers' strength mechanisms.

Superlattice coatings have good strength and hardness. However, the disadvantage of TMNs superlattice coatings is poor ductility and plasticity, which often limit their usage in numerous applications. The studies on nanocrystalline metal material already point out that twin boundaries are beneficial to improve their strength, ductility, and plasticity [19-21]. Motivated by this idea, we speculate that it may also be the case for TMNs, i.e., twinning might further enhance the mechanical properties of TMNs. However, in reality, it is not easy to generate numerous twins in transition-metal nitride films due to its high stacking fault energies (SFEs) [22-24]. Coming up with an effective route to introduce more twins into TMNs is of significance. Thus, **PUBLICATION III** is devoted to investigating the heterophase interface-facilitated twin nucleation mechanism, demonstrating a new method to synthesize high-density growth twins in TMNs.

Since it was very difficult to have high-density twins in TMNs, the deformation mechanism related to twinning behavior in TMNs is less explored and poorly understood. TMNs' crystal structures do not possess simple geometric arrangements, which determine their more complicated deformation mechanism than pure metals. For complex material deformation, Kronberg proposed a synchronous slip and twinning deformation mechanism in 1957, whereby two shears operate in opposite directions on adjacent atomic planes [25]. This mechanism has been shown to work in the Laves phase and α-Alumina [26, 27]. However, due to the difficulty of *in-situ* characterization of such complex materials, there has been no experimental evidence to support this deformation mechanism. To explore the atomic-scale deformation mechanism in TMNs, **PUBLICATION IV** reports a study on *in-situ* atomic-scale observation of twin boundary defect nucleation/CTB (coherent twin boundary) migration. It reveals a new

2

asynchronous shearing deformation mechanism in CrN. Thus, this new finding vastly improves our understanding of an atomic-scale deformation mechanism in complex materials.

2 Background and Motivation

2.1 Transition metal nitrides hard coatings

TMNs are mainly composed of metal elements of groups IV to VI, which belong to the interstitial alloys or compounds. TMNs thin films can be synthesized by PVD or CVD deposition technology, which mainly includes TiN, CrN, AlN, WN, TaN, VN, HfN, NbN, and ZrN. For some TMNs, the crystal structure generally has a cubic or hexagonal structure. Different crystal structures lead to differences in mechanical properties. For example, previous DFT calculations [28, 29] indicate that the AlN cubic phase shows better intrinsic mechanical properties than the hexagonal phase. Furthermore, the difference in hardness, modulus, and toughness between TMNs can also be attributed to its complex and different bonding structure. Generally speaking, bonds in TMNs consist of a mixture of covalent, metal, and ionic bonds. More covalent bonds will significantly increase its strength, and more metal bonds will help improve ductility (as seen in Fig. 2.1).
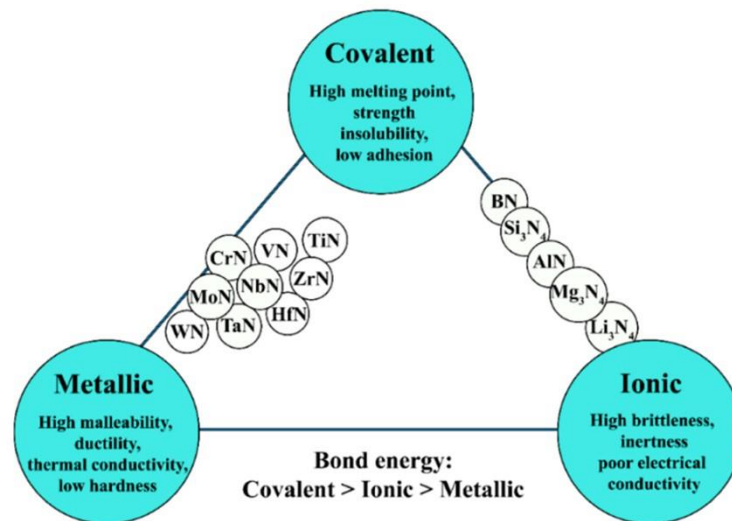

Figure 2.1 Classification of transition metal hard coatings chemical bonds and properties. The figure is taken from Ref. [30, 31].

Although, people realize that the monolithic (single layer) TMNs coatings can effectively protect cutting tools. However, with the improvement of the industry's requirements for material hardness and toughness, the single-layer coating has limitations. Current research is focused on three ways to improve the properties of TMNs coatings. (i) Developing of alloying

3

hard coatings like $Ti_{1-x}Al_xN$, $Cr_{1-x}Al_xN$, $Ti_{1-x}Cr_xN$ $Zr_{1-x}Al_xN$, and $Ti_{1-x}W_xN$ [32-37]. (ii) developing coatings with nanocomposite structure such as TiSiN [38], TiAlSiN [39], TiAlCrSiN [40]. (iii) Developing of multilayer coatings such as CrN/AlN, TiN/AlN, CrN/TiN, TiN/WN, and CrN/NbN[14, 41-46].

For preparing these complex or multilayer coatings, current methods include not only traditional chemical vapor deposition (CVD) but also developed various methods, such as plasma-assisted physical vapor deposition (PVD), plasma-assisted chemical vapor deposition (PACVD), and laser-assisted methods like pulsed laser deposition (PLD) [47-49]. These methods have greatly improved TMNs materials' design, which allows us to precisely control the microstructure of the material to prepare the material with the best performance.

Complex hard coatings not only have the advantages of high-temperature properties and oxidation resistance but also have the potential to increase the fracture toughness by modifying the electronic (high valence electron concentration) effects and bonding characteristics [33, 36, 37, 50]. And, Veprek *et al* suggested that the phase segregation in strongly immiscible complex TiSiN coating will form sharp and strong interfaces, which provide the nanocomposite material with high strength [38]. For multilayer coatings, they usually exhibit better strength, hardness, elastic modulus, and toughness than counterpart monolithic layer because of the effect of the interface. The multilayer interface can effectively hinder the movement of dislocations across the interface and inhibit crack propagation. Among these multilayer coating systems, the hardness of *rs*-TMN/*rs*-TMN with an epitaxial superlattice structure is much higher than other systems [12,17, 18]. However, the atomic-scale mechanism of interface effects related to mechanical properties is practically unknown, and so far, this piece of information is rare. Therefore, understanding the interface structure and its impacts at the atomic scale will greatly expand our knowledge and get insight into the structure-property relation of TMNs and further help future hard coating design.

2.2 Interfaces and grain boundaries

2.2.1 Interphase interfaces

The interface between phases may have a different crystal structure, crystallographic orientation, composition, or lattice parameter. According to their atomic structure, three different types of interphase interfaces can be distinguished, including the coherent, semi-coherent, and incoherent interface (see Figure 2.2). The coherent interface can be defined as two crystal phases with a similar crystallographic orientation, lattice parameters, and crystal structure. For coherent interfaces, the difference in lattice parameters (mismatch) between the two phases is generally less than 5%. For semi-coherent or incoherent interfaces, two crystal phases may have a larger lattice mismatch (larger than 5%) or different crystal structures. Since the more significant lattice mismatch, the semi-coherent or incoherent interface is accommodated by a periodic array of misfit dislocations. Furthermore, due to the effects of more broken bonds, interfacial dislocations, and more inhomogeneous chemistry composition, semi-coherent or incoherent interfaces have higher energy than coherent interfaces.
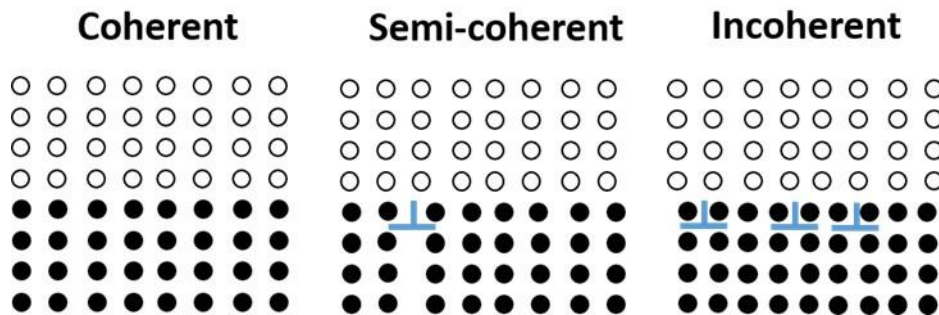

Figure 2.2 Schematic representation of coherent, semi-coherent and incoherent interface.

TMNs have similar lattice constants and crystal structure. The multilayer materials composed of two nitride hard materials are mainly with *fcc/fcc* coherent interface or *fcc/hcp* semi-coherent interface, e.g., *rs*-CrN/*rs*-AlN and *rs*-CrN/*w*-AlN. Superlattice TMNs with *fcc/fcc* coherent interface usually has better elastic modulus and hardness [1, 11, 12, 18, 42, 45, 51-53]. This can be explained by the widely accepted concept of dislocation motion blocking at the layer interfaces due to coherency strain causing periodical strain–stress field and differences in the shear moduli of the individual layer materials. Therefore, the mechanism of the mechanical properties of the coherent interface has been more extensively studied.

2.2.2 Twin boundaries

Single-phase polycrystalline materials are composed of many grains with different crystallographic orientations, and their interfaces can be defined as grain boundaries. The grain boundary requires 5 degrees of freedom, including the different rotation axis, rotation angle and boundary plane. Thus, according to their geometric orientation relationship, grain boundaries can be categorized into tilt boundaries, twist boundaries and mixed types. For tilt grain boundaries, they are included in low-angle grain boundaries (misorientation angle <15°) and large-angle grain boundaries (misorientation angle > 15°).

Among these large-angle grain boundaries, there is a special grain boundary structure, i.e., twin boundary. In *fcc* materials, twin boundary contains two possible structures: $\Sigma3\{111\}$ coherent twin boundary (CTB) and $\Sigma3\{112\}$ incoherent twin boundary (ITB) (as seen in Figure 2.3). For *fcc* metals, high density twins with $\Sigma3\{111\}$ CTB can significantly enhance their strength [19, 20], ductility [21], electrical conductivity [54] and thermal stability [55, 56]. The main mechanism of twin strengthening is that the coherent twin boundary effectively prevents the movement of dislocations, serving as a stable interface for strengthening the materials. In *fcc* metals, there are three possible dislocation-TB interaction modes: slip transfer mode (hard mode I), confined-layer slip mode (hard mode II), and twinning partial slip mode (soft mode) [57, 58].
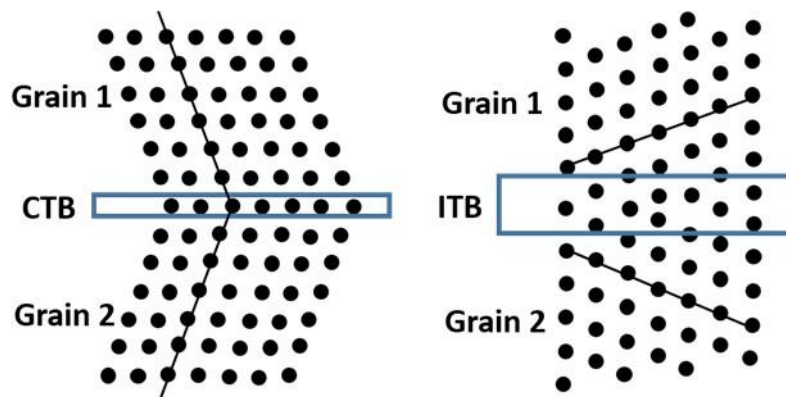

Figure 2.3 Schematic representation of $\Sigma3$ {1 1 1} coherent twin boundary and $\Sigma3$ {1 1 2} incoherent twin boundary.

$\Sigma3\{112\}$ incoherent twin boundaries (ITBs) have been found to play crucial roles in plastic deformation and de-twinning process in nano-twins metallic materials [56, 59, 60]. ITB is a dislocation walls composed of a series of high-density partial dislocations [56]. So, 1/6a [112] type partial dislocations may dissociate from the ITB. The de-twinning process is accomplished via the collective glide of multiple twinning dislocations that form an ITB. Previous research

shows that ITB in nano twins can effectively resist the accumulation of dislocations and cause significant work hardening and the ITB step migration to further adapt to the plasticity under high stress [60].

For hard materials, previous reports show that nano-twins in c-BN [61] and diamond [62] can significantly increase the hardness, i.e. over 100 GPa and 200 GPa by introducing a nano-twins structure in c-BN and diamond. Twinning in SiC nano-wires can also improve elastic strengthening [63]. The coherent twin boundaries can serve as barriers for dislocation motion or be regarded as grain boundaries, refining the grain size. For metal materials, lower SFEs cause their twinning behavior to occur in the deformation or annealing process. However, there are very few reports on twinning in TMNs coatings. This is because of the high SFEs of transition metal nitrides. Previous simulations indicated that the SFE for rock-salt VN,TiN, ZrN ,HfN and CrN is about 0.85 J/m^2 [22],1.10 J/m^2 [64], 1.01 J/m^2 [24],1.03 J/m^2 [24] and 1.11 J/m^2 [65], respectively. Compared with fcc metals, i.e., Al (0.160 J/m^2), Cu (0.045 J/m^2) Ag (0.022 J/m^2) and Au (0.04 J/m^2), the SFEs of rock-salt TMNs materials are significantly high. The much high SFEs result in deformation or annealing induced twinning in transition-metal nitrides difficult. In addition, the DFT calculation results show that the stacking fault structure of TMN (i.e., TiN) is much more complicated than that of fcc metals, which have two stable stacking faults, i.e., a/6⟨112⟩ displacement and a/3⟨112⟩displacement (Figure 2.4, position 3 and 4). Therefore, due to the complicated structure, the twining behavior is rarely explored in experiments. Exploring the twin growth mechanism and twin boundary effect of high SFEs TMNs will have great theoretical and practical applications in the future.
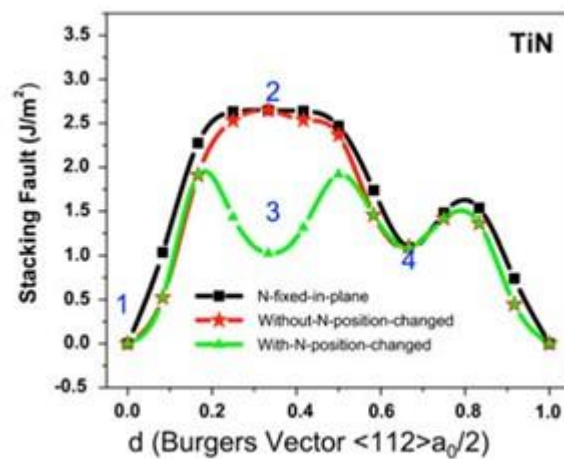

Figure 2.4 The TiN GSF energies as a function of shear displacement along ⟨112⟩ in {1 1 1} plane [64].

2.3 Coherent interface stabilizing metastable phases

Aluminum nitride (AlN) has two metastable phases with rock-salt structure (B1), zinc-blende structure (B3) and one stable structure wurtzite structure (B4) (as seen in Figure 2.5). The wurtzite (*w*) AlN with a hexagonal crystal structure and the space group is *P6₃mc*. For rock-salt (*rs*) structure AlN, two individual atoms, i.e., Al and N, form an *fcc* sublattice, where the space group is *Fm$\bar{3}$m*. Under high pressure, wurtzite AlN can be transformed into rock-salt structure [66]. Previous studies have shown that the phase transition of AlN can have two possible paths (hexagonal and tetragonal paths), where the hexagonal path has the lower energy barrier for the phase transition [67].
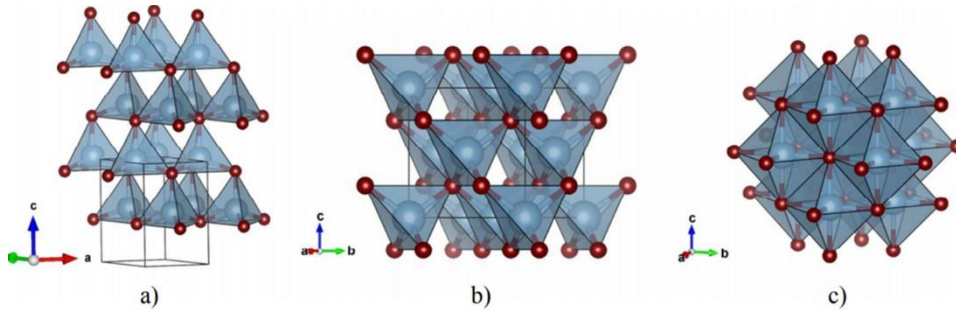

Figure 2.5 Crystal lattice structures of AlN. a) wurtzite, b) NaCl and c) ZnS type. The figure is taken from Ref.[68].

In addition to the high-pressure synthesis of metastable phase (*rs*-AlN), the *rs*-AlN can also be stabilized by the other *rs*-TMNs template [12-16], e.g., TiN, CrN or NbN. Epitaxial stabilization of the *rs*-AlN phase can be achieved by a thinner AlN layer thickness (as seen in Figure 2.6 and Figure 2.7) or an increase in the intermediate layer thickness (needs to be at least as thick as the targeted AlN layer thickness) [51]. Chawla *et al.* combined the finite element modeling and density functional theory (DFT) methods to explain the effect of coherency state on *rs*-AlN stability, i.e., smaller lattice constant difference helps to stabilize *rs*-AlN[28]. Thermodynamically, the stabilization of the *rs*-AlN phase can be explained by considering the overall energetics (including strain energy and interfacial energy) contributions competition mechanism [69].
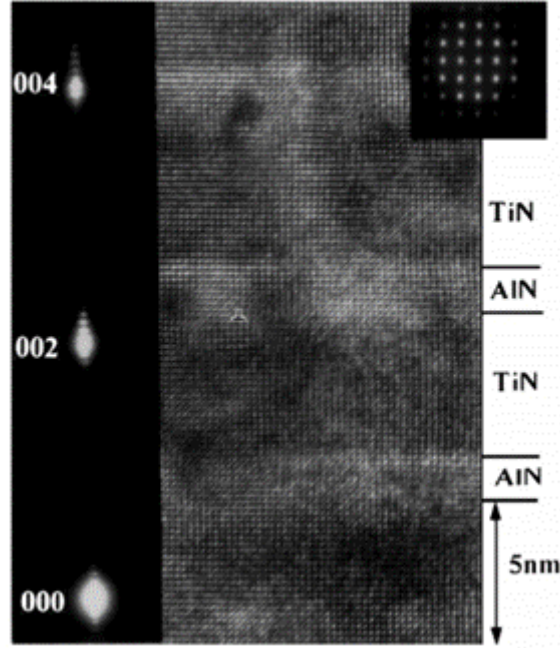
Figure 2.6 HRTEM image of *rs*-AlN/*rs*-TiN superlattice with the layer thickness of AlN 1.7 nm and TiN 5.1 nm, respectively [69].

The total energy model can be used to justify the observed critical thicknesses and eventually also to predict them. The total energy, E_T, per unit (surface/interface/section) area can be expressed as:

$$E_T^{c,w} = t \cdot (E_{Strain}^{c,w} + E_B^{c,w}) + \gamma_I^{c,w} + \gamma_S^{c,w}. \tag{2.1}$$

$E_{Strain}^{c,w}$ is the strain energy density related to the lattice mismatch, $\gamma_I^{c,w}$ is the interface energy (including the effect of broken bonds due to an imperfect crystallographic match, interface dislocations and inhomogeneous chemistry), and $\gamma_S^{c,w}$ is the surface energy (penalty due to broken bonds at the free surface). $E_B^{c,w}$ is the bulk (chemical) energy density (per unit volume). For smaller layer thickness (AlN below 3.0 nm), the strain energy is only a small contribution to the total energy. At this time, the interface energy will be the main contribution of the total energy. When the *rs*-AlN structure is formed with a smaller layer thickness, the coherent interface will provide less interface energy to stabilize its metastable structure. In contrast, the formation of the *w*-AlN phase will significantly increase its interfacial energy, and the strain energy will be relaxed. This will greatly increase the wurtzite phase stability in the thicker AlN layer.
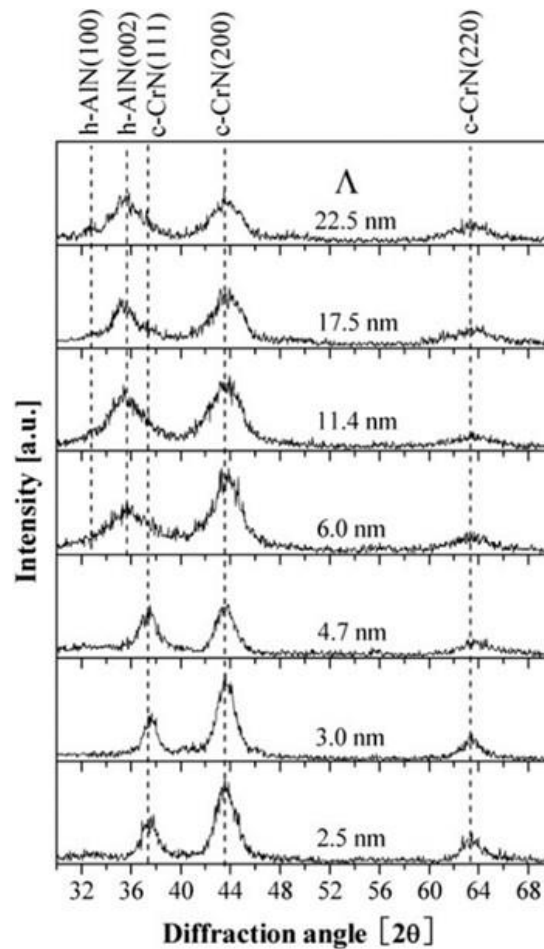
Figure 2.7 XRD patterns show the phase structure from AlN, CrN single-layer and AlN/CrN multilayered coatings Ref. [44].

2.4 Interface effect on mechanical strength

So far, according to the bilayer thickness, different strengthening mechanisms are applied to describe the hardness/strength in metal or ceramic multilayer coatings, i.e., (i) the Hall-Petch-like strengthening relationship based on dislocations piling up at the interface [70, 71], which is applicable at the sub-micrometer to micron length scales (Fig. 2.8); (ii) the confined layer slip (CLS) mechanism [72-74], usually applies to coatings with a period of 10-100 nm; (iii) the interface barrier strength (IBS) mechanism [52, 75, 76], which considers a single dislocation cutting cross the interface and is suitable for nanoscale thin multilayer coatings (layer thickness <10 nm).
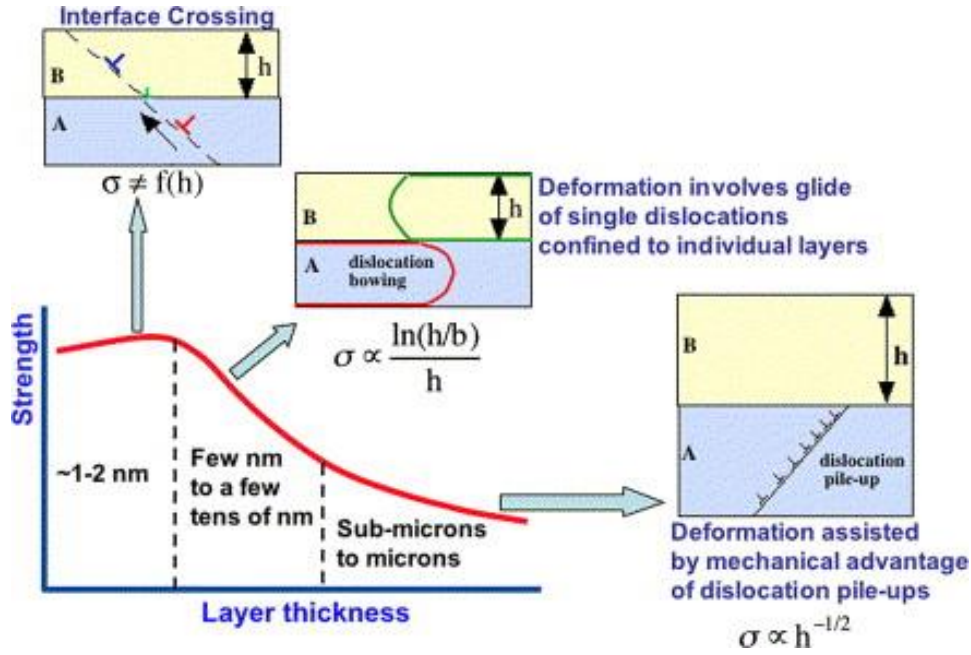
Figure 2.8 Schematic illustration of the dislocation mechanisms of multilayer strength operative at different length scale [73].

For *rs*-TMN/*rs*-TMN superlattice, most research has focused on nano-scale bilayer coatings since they usually have the best hardness, elastic modulus or toughness. Superlattice having very thin layer thickness exhibits a high density of interfaces, which can hinder dislocation motion across boundaries. The nano-scale superlattice increases in hardness can be described by Chu and Barnett's model [52]. When an interface exists, a dislocation at a distance *x* from the interface is repelled by a shear stress, i.e., dislocation critical migration stress on glide planes at angle θ with the interface normal, given by the following formula:

$$\tau = \frac{\alpha \Delta G b \, cos\theta}{2x} \tag{2.2}$$

Where *b* is the magnitude of the dislocation Burgers vector, *a* is $\frac{1}{4}\pi$ for screw dislocations, and $\frac{1}{4}\pi(1-v)$ for edge dislocations, and v is the Poisson's ratio. ΔG is the shear modulus difference between two layers. Thus, due to the different shear modulus between the two layers, the shear stresses required for dislocations to glide across layers will increasing, which greatly enhances the yield stress. Besides the modulus difference, the outstanding mechanical properties of the epitaxial superlattice coating can also be attributed to the coherent strain and the interface charge density. The previous DFT simulation shows that the disparate character of cleavage properties within different orientation interfaces of the superlattice—providing indications regarding crack initiation processes—is linked to the changes in bond lengths [77]. The electronic structure of TMNs interface was studied by Řeháka and Holec [78]. They show

11

that the cleavage properties are strongly related to the interplanar distances and charge density. The higher the accumulated charge density, the smaller the interplanar distance and the higher is the cleavage strength.

For nanoscale superlattice coatings, the mechanical strength usually increases as the bilayer period thickness decreases. However, the experimental results show that too small bilayer-period will decrease the mechanical strength of the multilayer coating. As seen in Figure 2.9, the peak hardness of SL TMNs can be found in the bilayer thickness of 3-8 nm. However, for a smaller bilayer-period (lower than 3~4 nm), the hardness of multilayer will decrease. Currently, there are two viewpoints related to interface effects to explain such inverse Hall-Petch phenomenon. (i) Component interdiffusion/intermixing occurs at the interface during the film synthesis or annealing [42, 46, 79-81]; thereby reducing the stress field's amplitude and the difference in shear modulus. (ii) The interface barrier to slip transmission decreases as the dislocation core dimension approaches the layer thickness [73, 82].
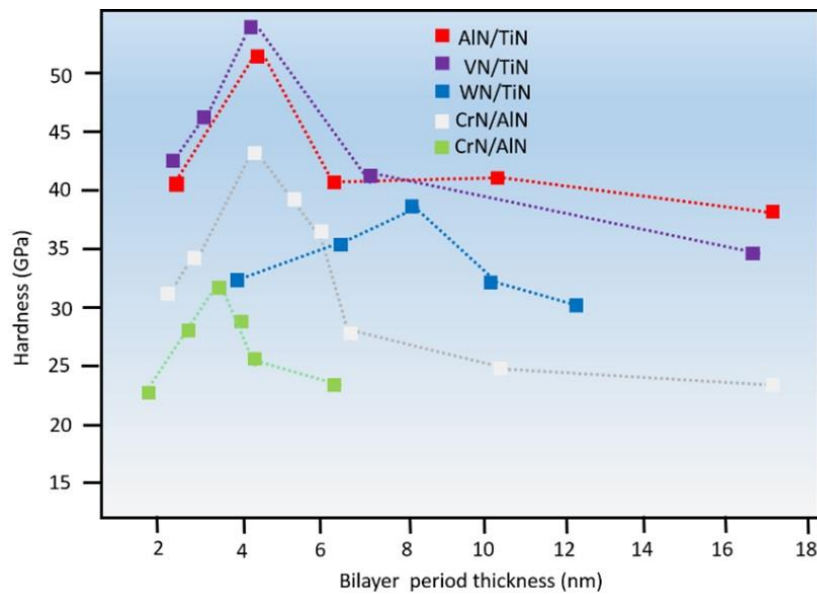

Figure 2.9 A summary of hardness versus the bilayer period for various rock-salt/rock-salt nitride superlattices [1, 17, 45, 51, 53].

2.5 A brief introduction to HRTEM

2.5.1 HRTEM imaging mechanism

The earliest optical microscope appeared in Europe in the 17th century, where the imaging principle was proposed by E. Abbe in 1873. For an optical microscope, its resolution is shown in the following equation:

$$d = \frac{0.61\lambda}{n\sin\alpha} \tag{2.3}$$

where λ is the wavelength of visible light, α is the half angle of the pencil of light that enters the objective, and n is the index of refraction of the media surrounding the radiating points. For optical microscopes, the wavelength of visible light (~380-700 nm) greatly limits its resolution. Since the electron has a much smaller wavelength (2.5 pm at 200 KeV), a very high-resolution transmission electron microscopy (TEM) was developed. In 1932, Knoll and Ruska proposed the idea of the electron as the light source of a microscope and successfully developed the world's first TEM, for which Ruska won the Nobel Prize in 1986. High-resolution TEM (HRTEM) technology originated in the 1950s, but the imaging mechanism was unclear. In the early 1970s, Cowley and Moodie proposed using the multi-slice propagation dynamics of electron diffraction to explain the amplitude and phase theory of electron waves [83], which provides a theoretical basis for HRTEM imaging.

The contrast in TEM images can arise due to the differences in the phase of the electron waves scattered through a thin sample, i.e., the HRTEM image is the interference image formed by the phase difference between all transmission beams and diffraction beams. Thus, a high-resolution transmission electron microscopy is phase-contrast imaging. For HRTEM, the resolution is mainly affected by electron wavelength, spherical aberration, and chromatic aberration. The resolution *d*, as shown in the following equation:

$$d = \frac{0.61\lambda}{\alpha} + C_S^{1/4} \cdot \lambda^{3/4} + C_c(\frac{\Delta E}{E}) + \cdots \tag{2.4}$$

Since the electron beam's wavelength depends on the accelerating voltage, i.e., $\lambda = \frac{1.226}{\sqrt[2]{U}}$, higher acceleration voltage will also obtain higher resolution. Therefore, before the 2000s, the main way to improve TEM resolution was to increase its acceleration voltage. JEOL has produced ultra-high-voltage electron microscope with an acceleration voltage of 1250 KeV, and its point resolution can reach approximately 1 Å. Although the resolution has been significantly improved, this high-voltage microscope is too expensive, large in size, and strong radiation damage. So, a high-voltage electron microscope has not been widely used.

In 1949, German theoretical physicist Otto Scherzer proposed that when there is a spherical aberration (C_S), the highest resolution can be achieved by appropriately increasing the underfocus value, i.e., Scherzer underfocus. Under this condition, the point resolution of TEM depends on the spherical aberration coefficient (Cs) (as seen in Figure 2.10) and electron wavelength (λ). For 100 keV TEM, the wavelength of electrons has ~ 0.037 Å, while the actual resolution is only 0.8 nm. The limited resolution can be attributed to the intrinsic imperfections of electron lenses in TEM, i.e., spherical aberration. Neither optical lenses nor electromagnetic lenses can be absolutely perfect. For a convex lens, the converging ability of the edge of the lens is stronger than that of the center of the lens, which causes all the light (electrons) to be unable to converge to a focal point. In the optical lens group, the combination of convex and concave lens can effectively reduce spherical aberration, but the electromagnetic lens cannot be used as a concave lens. Thus, spherical aberration is difficult to correct in TEM.
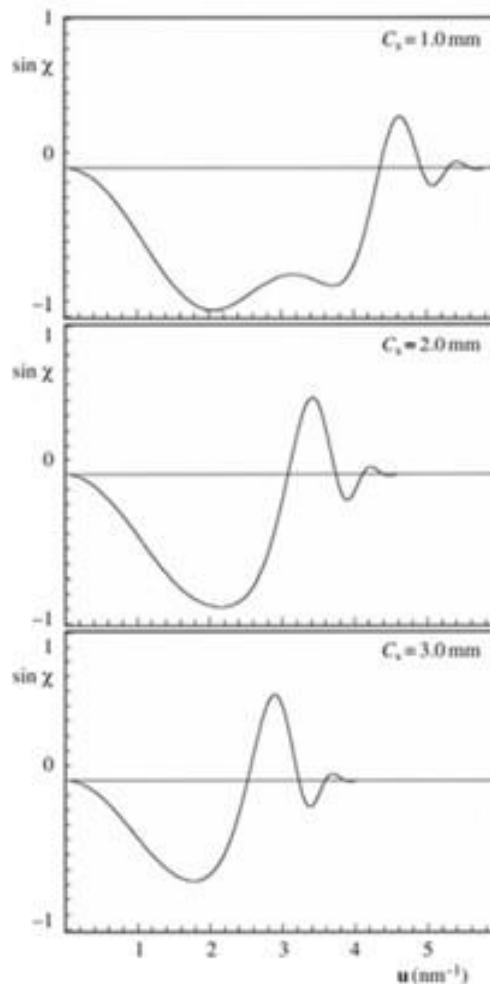

Figure 2.10 Point resolution under different spherical aberration coefficients. The smaller Cs values can achieve a higher spatial resolution. (Accelerating voltage = 200 kV, defocus = –60 nm). The figure is taken from Ref [84].

2.5.2 Application of spherical aberration corrector

In the 1990s, with the advancement of electron optics theory and computer technology, it became possible to develop TEM with spherical aberration correctors. Harald Rose, Maximilian Haider, and Knut Urban started the research and development of spherical aberration correction optical components in 1991, and successfully developed the world's first TEM spherical aberration corrector in 1998. The prototype spherical aberration corrector is mounted on the Philips CM200, and its point resolution has been increased from 0.24 nm to 0.13 nm, officially bringing the transmission electron microscope industry into a new era of atomic resolution. Due to the invention of the spherical aberration corrector, this allows us to tune the spherical aberration (C_S) to negative values and results in a novel negative C_S imaging technique. Jia et al. [85] proposed that negative spherical aberration imaging can remarkably improve the light elements' contrast (such as oxygen, carbon, and nitrogen atoms) in high-resolution images without losing atomic resolution.

In this thesis, a 200 keV field emission TEM (JEOL 2100F) equipped with an image-side C_S-corrector (CEOS) was used in the HRTEM study, demonstrating a resolution of 1.2 Å at 200 keV. This image-side C_S-corrected high-resolution TEM has excellent advantages for the atomic-level characterization of material boundaries/interfaces. The first is to reduce the image delocalization when imaging the boundaries/interfaces/defects in materials. In the atomic image of the periodic structure, delocalization is not apparent. Once the aperiodic interface or surface is imaged, delocalization will occur significantly. However, reducing the spherical aberration will substantially improve the delocalization effect, which is much beneficial for the characterization of defect structure. Secondly, in a TEM with aberration correction of the objective lens, a small beam tilt does not cause other image faults like astigmatism or coma, which allows us to characterize boundaries/interfaces structure of polycrystalline materials with higher resolution.

3 Summary of publication results

3.1 Orientation-dependent metastable phase stability

   PUBLICATION I characterized a gradient AlN/CrN multilayer coating. Due to the change in the layer thickness of the AlN, its phase structure will have B1 (*fcc*) or B4 (*hcp*) structure. The microstructure of gradient multilayer was studied in detail using conventional TEM and C_S-corrected TEM. As seen in Figs. 3.1 (a) and (b), the $\{111\}_{c\text{-CrN}}\|\{111\}_{c\text{-AlN}}$ and $\{111\}_{c\text{-CrN}}\|\{0001\}_{w\text{-AlN}}$ textures can be observed from 1st to 4th block (one block including 10 gradient thickness layers AlN and 10 constant thickness CrN). In (111)/(0001) texture region, the critical thickness for stabilizing cubic AlN is about 1.0 nm to 2.0 nm (as seen in Figs 3.1. (c)).
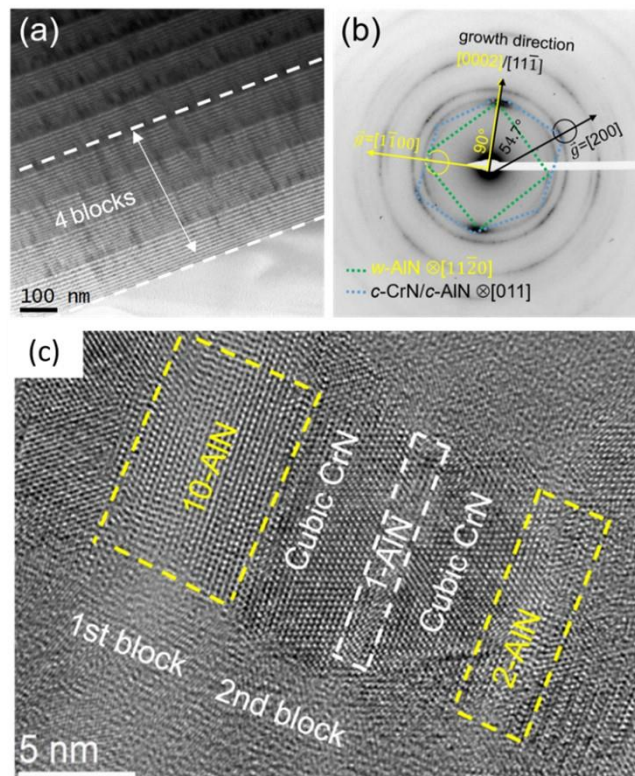

Figure 3.1 (a) TEM cross-sectional bright-field image and (b) corresponding diffraction pattern. (c) HRTEM image of a columnar grain (last layer in the 1st block and first two layers in the 2nd block).

   However, in the region far from the substrate (with random growth orientation), the critical thickness of cubic AlN ranges is increased (as seen Figs. 3.2 (a)-(c)). According to our statistical result (Figs. 3.2 (d)), grains with the <111> growth-orientation show a similar critical layer thickness with (111)/(0001) texture region, while at the <100> and <110> growth-orientations

this critical thickness is larger. We also observe that only <111> growth-orientation shows low-mismatch wurtzite/rock-salt interfaces and other orientations with a high-mismatch mode.
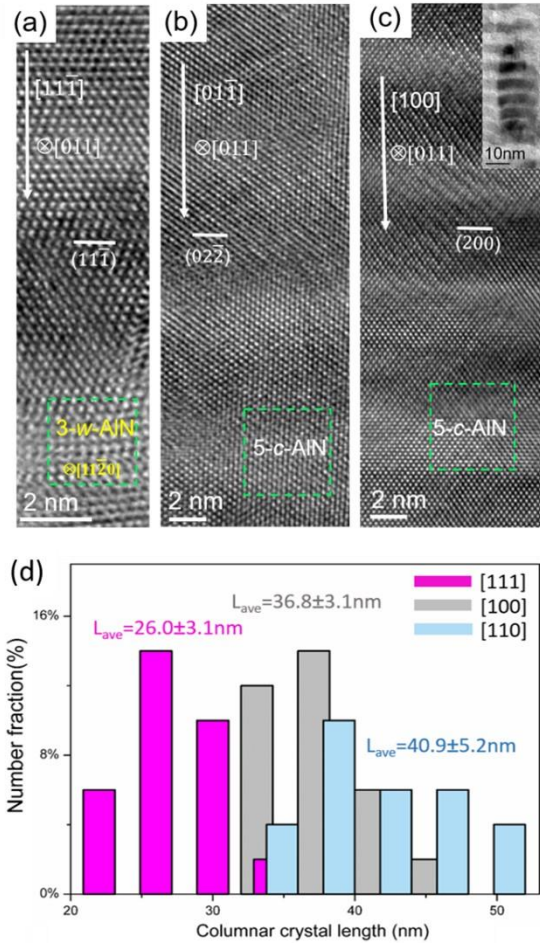

Figure 3.2 HRTEM images of one portion of several columnar grains, (a) [11$\bar{1}$], (b) [01$\bar{1}$] and (c) [100] growth-orientation. (d) Histogram distributions of columnar grain lengths in different orientations acquired by HRTEM images.

Since the interface structure of wurtzite/rock-salt on <100> and <110> mode with a high-mismatch mode, i.e., higher interface energy, it provides a better energy advantage for cubic phase stability. Furthermore, combined with DFT calculation, I qualitatively compare the strain energy, surface energy and interface energy at a different orientation, which finally confirmed <111> growth-orientation have a smaller critical layer thickness.

3.2 Superlattice interface intermixing and its effect

It is generally believed that the intermixing phenomenon in multilayer coatings is due to the thermal diffusion of the film deposition or annealing process. However, deformation-induced multilayer intermixing is entirely unknown. Combined with advanced TEM characterization and simulations, I confirmed the nanoindentation-induced intermixing in *rs*-TiN/*rs*-AlN multilayer. The STEM-HAADF image, elemental mapping and HRTEM show significant

17

layered features in the as-deposited *rs*-TiN/*rs*-AlN multilayer (Figure 3.3 (a)-(c)). However, after nanoindentation, TEM characterization indicates the intermixing behavior of multilayers. Both atomic-scale elemental mapping (Figure 3.3 (e)) and HRTEM (Figure 3.3 (f)) reflect the superlattice intermixing, and homogenous lattice forms, accompanied by the layer features vanishing.
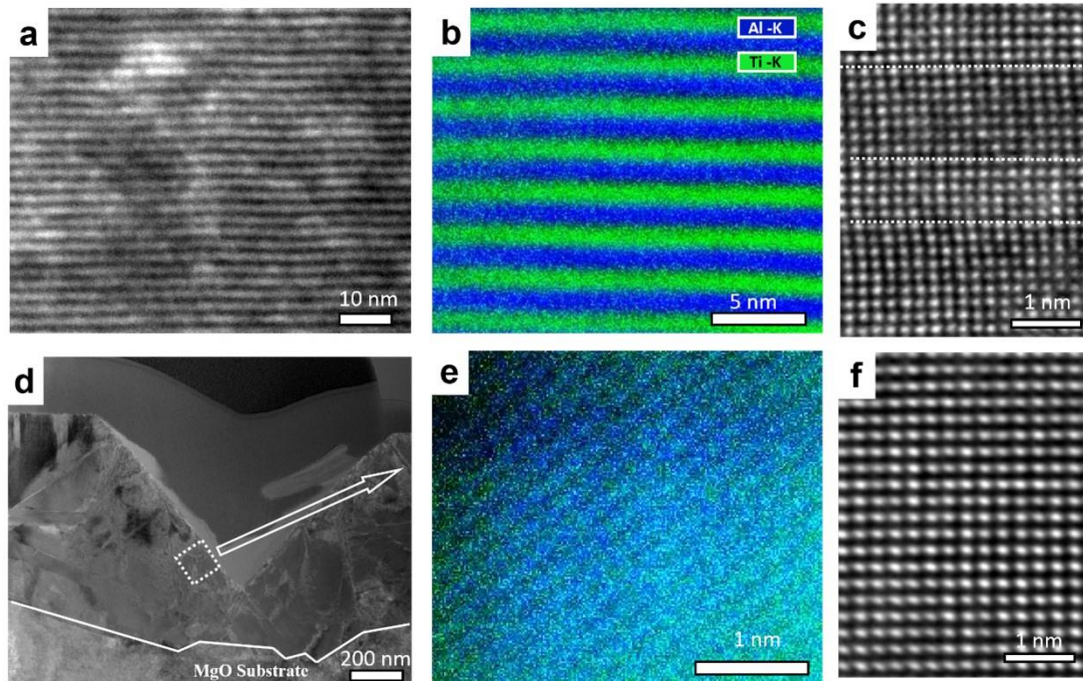

Figure 3.3 (a) Cross-sectional HAADF image of as-deposited SL. (b) EDXS mapping (Ti and Al K-peak signal) of as-deposited *rs*-TiN/*rs*-AlN multilayer. (c) HRTEM shows atomic-scale image of as-deposited *rs*-TiN/*rs*-AlN multilayer on [100] projection (d) Cross-sectional overall STEM bright-field (STEM-BF) image of indented multilayer. (e) Atomic-resolution EDXS mapping at the surface region of impression. (d) A cross-sectional HRTEM image of the indented SL at the surface region.

Based on HRTEM observation (Figs. 3.4 (a)-(c)), I also found that the formation of solid solution will greatly reduce the dislocation density. Quantitative statistical analysis (Figs. 3.4 (d)) reveals that the dislocation density in the deformed SL is high (7.2-$13.4 \times 10^{13}/cm^2$) while at the surface solid solution region it is relatively low (1.0-$2.8 \times 10^{13}/cm^2$), close to the value of the as-deposited SL (0.9-$1.9 \times 10^{13}/cm^2$). The reduction of the dislocation density in solid solution region can be attributed to the fact that the modulus difference between the two layers becomes smaller at the beginning of alloying, and the shear stress required for sliding across dislocations can be significantly reduced. Hence, the mobility of the dislocations after solid solution formation is improved and this greatly reduces dislocation density. Based on the above results, I propose that the SL intermixing affects dislocation behavior (increase dislocation

18

migration ability and reduce dislocation density), and eventually worsensthe hardness/strength, which also explains that the hardness decrease of multilayer with a very samll bilayer thickness.
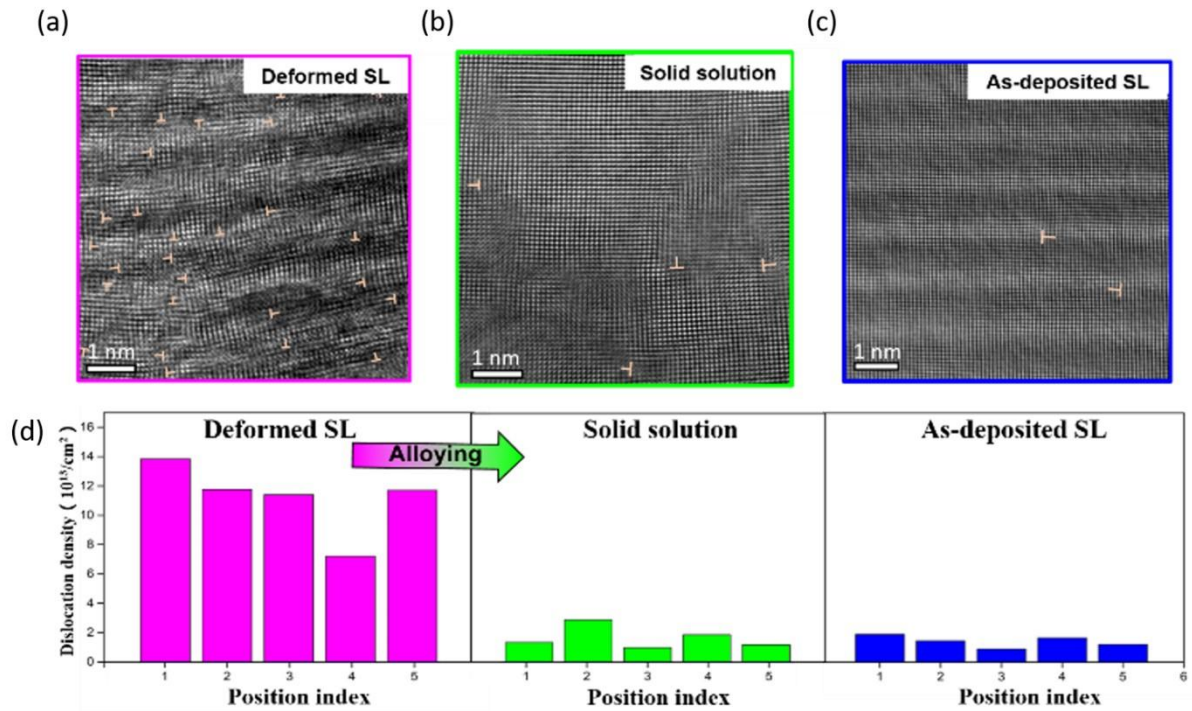

Figure 3.4 (a)-(c) Typical HRTEM images recorded from the deformed SL, the surface solid solution area, and the as-deposited SL, respectively. (d) Dislocation density statistics from the respective regions.

3.3 Hetero-phase interfaces induced growth-twins

In a gradient CrN/AlN multilayer, several possible types of interfaces exist, including *rs*-CrN/*rs*-AlN coherent interface and *rs*-CrN{111}/*w*-AlN{0002} semi-coherent interface. SAED (selected-area electron diffraction) patterns and HRTEM (Figs. 3.5) show that a high density of rock-salt twins with $\Sigma 3\{112\}$ ITBs was found in {111}/{0002} textured film area, i.e. semi-coherent interface induced *rs*-CrN growth twins. Through the quantitative measurement of HRTEM, I found that the twinning behavior on the *w*-AlN interface is related to interface steps (Figs. 3.6). Specifically, twins are frequently formed in a single-atomic-layer terrace, however, hardly in a double atomic-layer terrace.
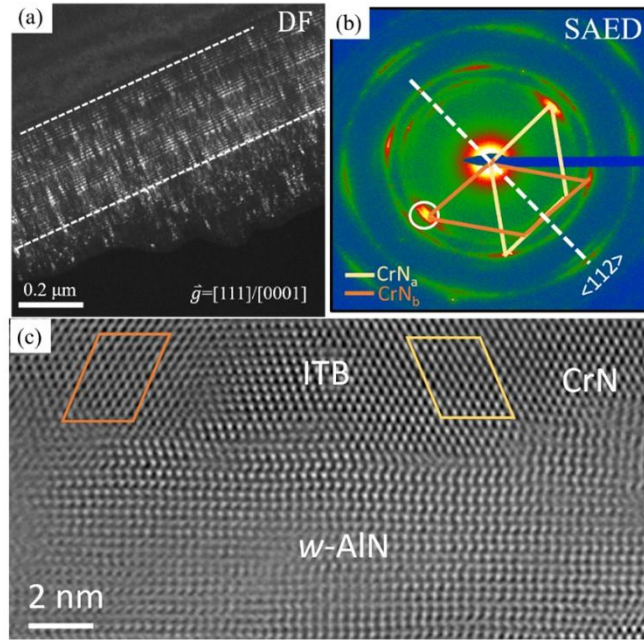
Figure 3.5 (a) TEM cross-sectional dark-field images from the 1st to 6th block area (dark-field images taken from the (0002)/(111) reflection). (b) is a corresponding selected area electron diffraction pattern. (c) HRTEM i

Combining DFT calculation and atomic model analysis, I propose that the growth of twins caused by this step structure can be attributed to the mirror symmetry relationship of fcc/hcp interface in texture areas. For matrix mode (without twins) on the single-layer *w*-AlN-{0002} terrace, the orientation of the *rs*-CrN is consistent. However, due to the interface stacking sequence variants, the interface structure of the upper and lower positions of the terrace is different. For example, the stacking sequence of the *rs*-CrN is AβBγCα (along the <111> direction) and the stacking sequence of the *w*-AlN is AβBα (along the <0001> direction). However, the interface structure with α$_{(rs\text{-}CrN)}$/A$_{(w\text{-}AlN)}$ and γ$_{(rs\text{-}CrN)}$/A$_{(w\text{-}AlN)}$ stacking sequence is different, and the interface energy is also different (confirmed by our DFT calculation). For twin mode on a single-layer *w*-AlN terrace, due to the mirror-symmetric interface, there is no change in the interface structure at the upper and lower positions of the terrace (as seen in Figs. 3.7). Therefore, the nucleation in the twin mode will be energy favorable (due to the completely consistent *fcc/hcp* interface structure). The formation of twins with ITBs can be interpreted by the *rs*-CrN/*w*-AlN interface structure (with a mirror-symmetry)-induced thermodynamically stable nucleation. Furthermore, we also see that the growth-twins with Σ3{111} coherent twin boundaries (CTB) appear in the non-textured film area further away from the substrate. Based on the HRTEM observations and atomic model analyses, supplemented with theoretical calculations, I proposed a CTB twin mode dominated by the larger columnar grains' growth

misorientation angle. Several nucleation modes of twins with Σ3{112} ITB and Σ3{111} CTB are proposed (detailed in **PUBLICATION III**).
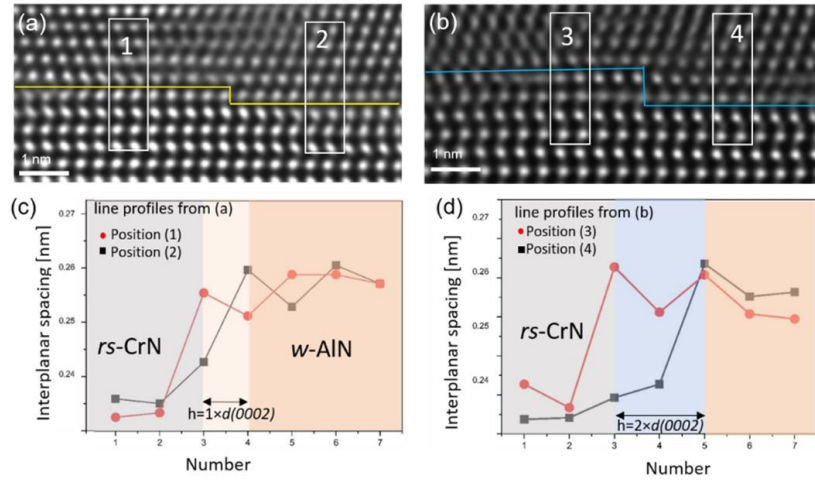

Figure 3.6 (a) HRTEM images of a single atomic-layer terrace in the *rs*-CrN/*w*-AlN interface. The twins with ITBs can be found in the CrN layers. (b) HRTEM images of a double atomic-layer terrace in the *rs*-CrN/*w*-AlN interface. (c) Two intensity line profiles obtained by integrating over the framed regions in (a). (d) Two intensity line profiles obtained by integrating over the framed regions in (b).
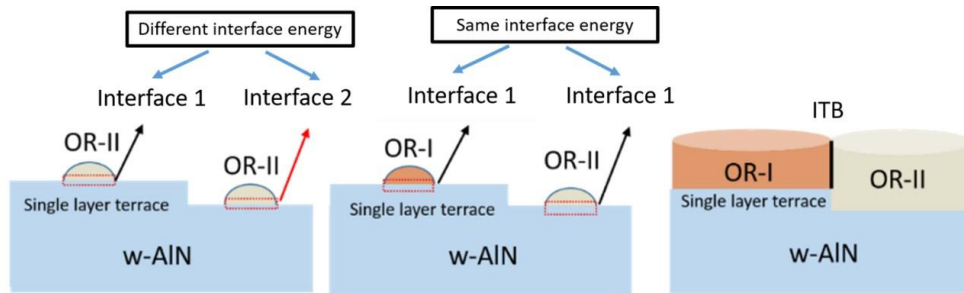

Figure 3.7 Schematic illustration of the nucleation process on a single-layer terrace *w*-AlN.

3.4 In-situ observation of coherent twin boundary migration in CrN

For *fcc* metals, the mirror-symmetry plane for Σ3{111} CTB is the metal atom {111} plane. However, the binary rock-salt structure of TMNs has a double *fcc* structure, i.e., transition metal and nitrogen atoms sit on two inter-penetrating *fcc* lattice. Thus, for the rock-salt TMNs, two CTB structures exist in a Σ3{111} CTB, i.e., TM (TM=Transition Metal)-{111} or N-{111} as a mirror-symmetry plane of CTB (Figs. 3.8 (a)). Using *in-situ* atomic-resolution electron microscopy, I demonstrate two different twin boundary defect (TD) nucleation and CTB migration modes in rock-salt CrN. The first is that TD nucleation and CTB migration start from the CTB/ITB junction, where for such a migration mode, the boundary structure is unvaried (Figs. 3.8 (b) and (c)). The second is TD nucleation and CTB migration begins from the

CTB/surface junction, where the CTB boundary structure exhibits alternating, i.e., part of the N-terminated CTB has transformed into the Cr-terminated CTB (Figs. 3.8 (d) and (e)). In Figs. 3.9, the initial CTB has the N-terminated boundary structure. After about 300 ms, a transient state appears with a boundary structure in between N-terminated and Cr-terminated CTB. The Cr atoms adjacent to the CTB have migrated by a vector of $1/6a[112]$. However, N atoms are still unaltered. After an additional 300 ms, a final state of the CTB migration with a Cr-terminated structure has been reached. Thus, based on the experimental observation, CTB migration and TD motion's dynamic process is asynchronous.
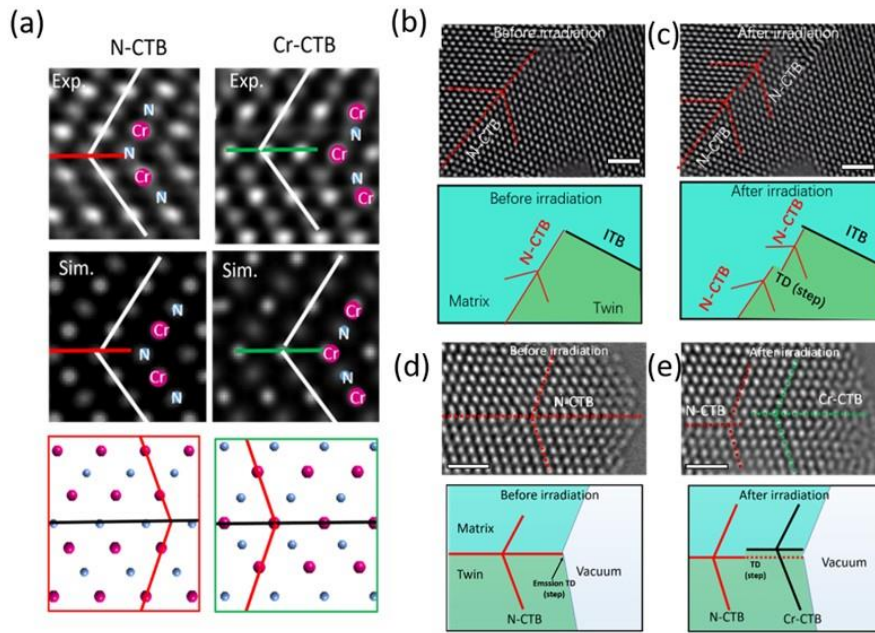
Figure 3.8 (a), HRTEM experimental ('Exp.') and simulation ('Sim.') images of N-terminated and Cr-terminated CTB from a thin area. (b) and (c), Series of HRTEM and schematic images show the twin defect nucleation and CTB migration from the CTB/ITB junction. (d) and (e), Series of HRTEM and schematic images of twin defect nucleation and CTB migration from the CTB/surface junction. The CTB marked with a red line has an N-terminated structure ('N-CTB'), and the green line indicates that the CTB has a Cr-terminated structure ('Cr-CTB').

Figure 3.9 (a)-(c) HRTEM images of the initial state, transitional state, and final stage of CTB migration from N-terminated to Cr-terminated, respectively.

Such an asynchronous migration process is also proved by calculated energy barriers of different migration mode using DFT. Asynchronous mode (first migrat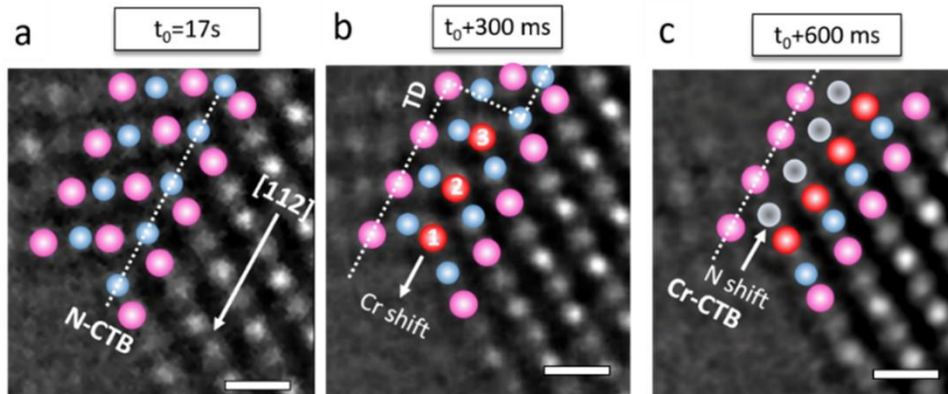ion is the Cr atom, followed by N) exhibits the lowest energy barrier to migration, i.e., the "resistance" during the initial CTB migration process is much smaller than in the other modes. Thus, this is really what we experimentally observed.
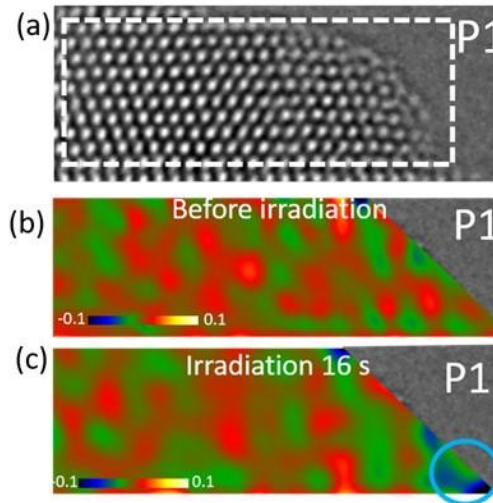

Figure 3.10 (a) Snapshots of Movie S2 (t=16 s, 1 second before the CTB migration). White frames (labeled as p1 and p2 position) are used for GPA measurement. (b) and (c) GPA results of different irradiation time (before irradiation and t=16 s).

Furthermore, through GPA anlaysis, we confirm that high-current density electron beam irradiation can effectively cause stress/strain concentration at the surface/CTB junction, which is the main driving force for CTB migration and TD motion. The shear strain mapping (ε_{xy}) with different irradiation times is shown in Figs. 3.10. For the upper part of the CTB (p1 position), the surface region exists a maximum ~ 1% shear strain (ε_{xy}) before the beam irradiation. It reaches ~ 4% shear strain after irradiation for t=16 s (just 1s before the TD motion and CTB migration). It displays a considerable strain concentration at the surface region, and the shear strain is rapidly attenuated towards the interior. Therefore, under beam irradiation, a substantial increase of shear strain at the surface provides a driving force to trigger the CTB migration and TD movement.

4 Conclusions

In this thesis, a systematic HRTEM-based study has been carried out to explore the atomic-scale interface structure and its effects. The following main conclusions can be drawn from this work:

(i) By observing the atomically-resolved images of *c*-CrN/*c*-AlN superlattices, an orientation-dependent critical layer thickness of metastable cubic AlN is revealed. In the <111> texture area, the critical thickness for stabilizing cubic AlN is about 1.0 nm to 2.0 nm. However, in the random growth region, the critical thickness of cubic AlN ranges from 2.0 nm to 4.1 nm. According to our HRTEM observations and statistical analysis, the *c*-AlN/*c*-CrN grains with the <111> growth-orientation show a smaller critical layer thickness for c-AlN, while at the <100> and <110> growth-orientations this critical thickness is larger.

(ii) Atomic-resolution structure and chemical composition analysis reveal that nanoindentation can trigger local alloying (or intermixing) in the nitride superlattice, which is validated by MD simulations. During the superlattice's deformation, since the coherent state of the interfaces is broken, the energy stored at the interface acts as the main driving force for alloying. Furthermore, the interface intermixing changes the dislocation behavior and subsequently affects the mechanical properties.

(iii) TEM observation of the gradient multilayer shows that a high density of rock-salt twins with Σ3{112} ITBs were found in {111}‖{0002} textured film areas. The atomic-resolved images of *rs*-CrN{111}‖*w*-AlN{0002} interfaces reveal that a single-atomic-layer terrace is closely associated with the formation of such growth-induced twin formations. The mirror-symmetric *w*-AlN/*rs*-CrN interfaces (for a twin on the single-atomic-layer terrace) hardly cause any change in the interface structure and energy variations. However, due to the interface structure and energy variations, growth-twins are more difficult to nucleate on the double atomic-layer terrace, which is also present. In the non-textured film area (far away from the substrate area), rock-salt twins with Σ3{111} CTB are occasionally found. Due to the interface orientation variation, two twin nucleation modes with different misorientation angles of growth direction for Σ3{111} CTB were found.

(iv)   *In-situ* observation of twin boundary migration shows two different CTB migration and TD nucleation mode. Twin boundary defect emission at the CTB/ITB junction has a 1/6a[112] Burgers vector. Moreover, the CTB migration from the CTB/ITB junction does not involve boundary structure alternating. However, when the CTB migration begins from the CTB/surface junction, the CTB migration involves a boundary structure alternating from the N-terminated to Cr-terminated. Moreover, both TEM observations and DFT calculations confirm that the Cr- terminated CTB has high energy and thus metastable. *In-situ* HRTEM observation reveals that Cr and N atom respective motion in this way is asynchronous. This is ascribed to the shear-strain-induced CTB structure distortion and the different migration energy barriers.

Bibliography

[1] U. Helmersson, S. Todorova, S.A. Barnett, J.E. Sundgren, L.C. Markert, J.E. Greene, Growth of single-crystal TiN/VN strained-layer superlattices with extremely high mechanical hardness, Journal of Applied Physics 62(2) (1987) 481-484.

[2] J.E. Sundgren, J. Birch, G. Håkansson, L. Hultman, U. Helmersson, Growth, structural characterization and properties of hard and wear-protective layered materials, Thin Solid Films 193-194 (1990) 818-831.

[3] L. Hultman, M. Shinn, P.B. Mirkarimi, S.A. Barnett, Characterization of misfit dislocations in epitaxial (001)-oriented TiN, NbN, VN, and (Ti,Nb) N film heterostructures by transmission electron microscopy, Journal of Crystal Growth 135(1) (1994) 309-317.

[4] P.C. Yashar, W.D. Sproul, Nanometer scale multilayered hard coatings, Vacuum 55(3) (1999) 179-190.

[5] M. Kobayashi, Y. Doi, TiN and TiC coating on cemented carbides by ion plating, Thin Solid Films 54(1) (1978) 67-74.

[6] W.D. Nix, Mechanical properties of thin films, Metallurgical Transactions A 20(11) (1989) 2217.

[7] H. Holleck, H. Schulz, Preparation and behaviour of wear-resistant TiC/TiB2, TiN/TiB2 and TiC/TiN coatings with high amounts of phase boundaries, Surface and Coatings Technology 36(3) (1988) 707-714.

[8] J.E. Sundgren, Structure and properties of TiN coatings, Thin Solid Films 128(1) (1985) 21-44.

[9] W. Schintlmeister, W. Wallgram, J. Kanz, Properties, applications and manufacture of wear-resistant hard material coatings for tools, Thin Solid Films 107(2) (1983) 117-127.

[10] H. Holleck, M. Lahres, P. Woll, Multilayer coatings—influence of fabrication parameters on constitution and properties, Surface and Coatings Technology 41(2) (1990) 179-190.

[11] P.B. Mirkarimi, L. Hultman, S.A. Barnett, Enhanced hardness in lattice-matched single-crystal TiN/V0.6Nb0.4N superlattices, Applied Physics Letters 57(25) (1990) 2654-2656.

[12] J. Lin, J.J. Moore, B. Mishra, M. Pinkas, W.D. Sproul, Nano-structured CrN/AlN multilayer coatings synthesized by pulsed closed field unbalanced magnetron sputtering, Surface and Coatings Technology 204(6) (2009) 936-940.

[13] I.W. Kim, Q. Li, L.D. Marks, S.A. Barnett, Critical thickness for transformation of epitaxially stabilized cubic AlN in superlattices, Applied Physics Letters 78(7) (2001) 892-894.

[14] J. Lin, J.J. Moore, B. Mishra, M. Pinkas, X. Zhang, W.D. Sproul, CrN/AlN superlattice coatings synthesized by pulsed closed field unbalanced magnetron sputtering with different CrN layer thicknesses, Thin Solid Films 517(20) (2009) 5798-5804.

[15] D. Chen, X.L. Ma, Y.M. Wang, Thickness-dependent structural transformation in the AlN film, Acta Materialia 53(19) (2005) 5223-5227.

[16] J. Lin, N. Zhang, Z. Wu, W.D. Sproul, M. Kaufman, M. Lei, J.J. Moore, Thick CrN/AlN superlattice coatings deposited by the hybrid modulated pulsed power and pulsed dc magnetron sputtering, Surface and Coatings Technology 228(Supplement 1) (2013) S601-S606.

[17] M. Setoyama, A. Nakayama, M. Tanaka, N. Kitagawa, T. Nomura, Formation of cubic-AlN in TiN/AlN superlattice, Surface and Coatings Technology 86-87 (1996) 225-230.

[18] R. Hahn, M. Bartosik, R. Soler, C. Kirchlechner, G. Dehm, P.H. Mayrhofer, Superlattice effect for enhanced fracture toughness of hard coatings, Scripta Materialia 124 (2016) 67-70.

[19] L. Lu, X. Chen, X. Huang, K. Lu, Revealing the Maximum Strength in Nanotwinned Copper, Science 323(5914) (2009) 607-610.

[20] K. Lu, L. Lu, S. Suresh, Strengthening Materials by Engineering Coherent Internal Boundaries at the Nanoscale, Science 324(5925) (2009) 349-352.

[21] M. Dao, L. Lu, Y.F. Shen, S. Suresh, Strength, strain-rate sensitivity and ductility of copper with nanoscale twins, Acta Materialia 54(20) (2006) 5421-5432.

[22] T. Fu, X. Peng, Y. Zhao, T. Li, Q. Li, Z. Wang, Molecular dynamics simulation of deformation twin in rocksalt vanadium nitride, Journal of Alloys and Compounds 675 (2016) 128-133.

[23] S.K. Yadav, X.Y. Liu, J. Wang, R. Ramprasad, A. Misra, R.G. Hoagland, First-principles density functional theory study of generalized stacking faults in TiN and MgO, Philosophical Magazine 94(5) (2014) 464-475.

[24] H. Yu, M. Bahadori, G.B. Thompson, C.R. Weinberger, Understanding dislocation slip in stoichiometric rocksalt transition metal carbides and nitrides, Journal of Materials Science 52(11) (2017) 6235-6248.

[25] M.L. Kronberg, Plastic deformation of single crystals of sapphire: Basal slip and twinning, Acta Metallurgica 5(9) (1957) 507-524.

[26] M.F. Chisholm, S. Kumar, P. Hazzledine, Dislocations in Complex Materials, Science 307(5710) (2005) 701-703.

[27] N. Shibata, M.F. Chisholm, A. Nakamura, S.J. Pennycook, T. Yamamoto, Y. Ikuhara, Nonstoichiometric Dislocation Cores in α-Alumina, Science 316(5821) (2007) 82-85.

[28] C. Vipin, H. David, H.M. Paul, Stabilization criteria for cubic AlN in TiN/AlN and CrN/AlN bi-layer systems, Journal of Physics D: Applied Physics 46(4) (2013) 045305.

[29] A.J. Wang, S.L. Shang, Y. Du, Y. Kong, L.J. Zhang, L. Chen, D.D. Zhao, Z.K. Liu, Structural and elastic properties of cubic and hexagonal TiN and AlN from first-principles calculations, Computational Materials Science 48(3) (2010) 705-709.

[30] A.S. Pogrebnjak, K.; Bondar, O, Nanocomposite Multilayer Binary Nitride Coatings Based on Transition and Refractory Metals: Structure and Properties, Coatings 9(155) (2019).

[31] H. Holleck, V. Schier, Multilayer PVD coatings for wear protection, Surface and Coatings Technology 76-77 (1995) 328-336.

[32] M. Bartosik, C. Rumeau, R. Hahn, Z.L. Zhang, P.H. Mayrhofer, Fracture toughness and structural evolution in the TiAlN system upon annealing, Sci Rep 7(1) (2017) 16476.

[33] D.G. Sangiovanni, V. Chirita, L. Hultman, Toughness enhancement in TiAlN-based quarternary alloys, Thin Solid Films 520(11) (2012) 4080-4088.

[34] Z. Shi, H. Wei, H. Zhang, T. Jin, X. Sun, Q. Zheng, Nanotwinned Ti(O,C) induced by oriented attachment in a hot-pressed Nb–Ti–Al alloy, Acta Materialia 105 (2016) 114-120.

[35] L. Zhou, D. Holec, P.H. Mayrhofer, Erratum: "First-principles study of elastic properties of cubic Cr1−xAlxN alloys" [J. Appl. Phys. 113, 043511 (2013)], Journal of Applied Physics 113(7) (2013) 079901.

[36] D.G. Sangiovanni, L. Hultman, V. Chirita, I. Petrov, J.E. Greene, Effects of phase stability, lattice ordering, and electron density on plastic deformation in cubic TiWN pseudobinary transition-metal nitride alloys, Acta Materialia 103 (2016) 823-835.

[37] D.G. Sangiovanni, L. Hultman, V. Chirita, Supertoughening in B1 transition metal nitride alloys by increased valence electron concentration, Acta Materialia 59(5) (2011) 2121-2134.

[38] S. Veprěk, S. Reiprich, A concept for the design of novel superhard coatings, Thin Solid Films 268(1) (1995) 64-71.

[39] D. Yu, C. Wang, X. Cheng, F. Zhang, Microstructure and properties of TiAlSiN coatings prepared by hybrid PVD technology, Thin Solid Films 517(17) (2009) 4950-4955.

[40] Y.-Y. Chang, C.-P. Chang, D.-Y. Wang, S.-M. Yang, W. Wu, High temperature oxidation resistance of CrAlSiN coatings synthesized by a cathodic arc deposition process, Journal of Alloys and Compounds 461(1) (2008) 336-341.

[41] P. Yashar, S.A. Barnett, J. Rechner, W.D. Sproul, Structure and mechanical properties of polycrystalline CrN/TiN superlattices, Journal of Vacuum Science & Technology A 16(5) (1998) 2913-2918.

[42] H.C. Barshilia, A. Jain, K.S. Rajam, Structure, hardness and thermal stability of nanolayered TiN/CrN multilayer coatings, Vacuum 72(3) (2003) 241-248.

[43] G.S. Kim, S.Y. Lee, J.H. Hahn, S.Y. Lee, Synthesis of CrN/AlN superlattice coatings using closed-field unbalanced magnetron sputtering process, Surface and Coatings Technology 171(1) (2003) 91-95.

[44] J.-K. Park, Y.-J. Baik, The crystalline structure, hardness and thermal stability of AlN/CrN superlattice coating prepared by D.C. magnetron sputtering, Surface and Coatings Technology 200(5) (2005) 1519-1523.

[45] J. Buchinger, N. Koutná, Z. Chen, Z. Zhang, P.H. Mayrhofer, D. Holec, M. Bartosik, Toughness enhancement in TiN/WN superlattice thin films, Acta Materialia 172 (2019) 18-29.

[46] L. Hultman, C. Engström, M. Odén, Mechanical and thermal stability of TiN/NbN superlattice thin films, Surface and Coatings Technology 133-134 (2000) 227-233.

[47] W. Schintlmeister, O. Pacher, Preparation and properties of hard-material layers for metal machining and jewelry, Journal of Vacuum Science and Technology 12(4) (1975) 743-748.

[48] W.D. Sproul, Physical vapor deposition tool coatings, Surface and Coatings Technology 81(1) (1996) 1-7.

[49] C. Mitterer, F. Holler, D. Reitberger, E. Badisch, M. Stoiber, C. Lugmair, R. Nöbauer, T. Müller, R. Kullmer, Industrial applications of PACVD hard coatings, Surface and Coatings Technology 163-164 (2003) 716-722.

[50] M. Mikula, D. Plašienka, D.G. Sangiovanni, M. Sahul, T. Roch, M. Truchlý, M. Gregor, L.u. Čaplovič, A. Plecenik, P. Kúš, Toughness enhancement in highly NbN-alloyed Ti-Al-N hard coatings, Acta Materialia 121 (2016) 59-67.

[51] M. Schlögl, B. Mayer, J. Paulitsch, P.H. Mayrhofer, Influence of CrN and AlN layer thicknesses on structure and mechanical properties of CrN/AlN superlattices, Thin Solid Films 545(Supplement C) (2013) 375-379.

[52] X. Chu, S.A. Barnett, Model of superlattice yield stress and hardness enhancements, Journal of Applied Physics 77(9) (1995) 4403-4411.

[53] V. Pankov, M. Evstigneev, R.H. Prince, Room-temperature fabrication of hard AlN/TiN superlattice coatings by pulsed laser deposition, Journal of Vacuum Science & Technology A 20(2) (2002) 430-436.

[54] L. Lu, Y. Shen, X. Chen, L. Qian, K. Lu, Ultrahigh Strength and High Electrical Conductivity in Copper, Science 304(5669) (2004) 422-426.

[55] J.A. Brown, N.M. Ghoniem, Structure and motion of junctions between coherent and incoherent twin boundaries in copper, Acta Materialia 57(15) (2009) 4454-4462.

[56] J. Wang, N. Li, O. Anderoglu, X. Zhang, A. Misra, J.Y. Huang, J.P. Hirth, Detwinning mechanisms for growth twins in face-centered cubic metals, Acta Materialia 58(6) (2010) 2262-2270.

[57] Y.T. Zhu, X.L. Wu, X.Z. Liao, J. Narayan, L.J. Kecskés, S.N. Mathaudhu, Dislocation–twin interactions in nanocrystalline fcc metals, Acta Materialia 59(2) (2011) 812-821.

[58] K. Lu, Stabilizing nanostructures in metals using grain and twin boundary architectures, Nature Reviews Materials 1(5) (2016) 16019.

[59] J. Wang, A. Misra, J.P. Hirth, Shear response of $\Sigma 3\{112\}$ twin boundaries in face-centered-cubic metals, Physical Review B 83(6) (2011).

[60] D. Bufford, Y. Liu, J. Wang, H. Wang, X. Zhang, In situ nanoindentation study on plasticity and work hardening in aluminium with incoherent twin boundaries, Nature communications 5 (2014) 4864.

[61] Y. Tian, B. Xu, D. Yu, Y. Ma, Y. Wang, Y. Jiang, W. Hu, C. Tang, Y. Gao, K. Luo, Z. Zhao, L.M. Wang, B. Wen, J. He, Z. Liu, Ultrahard nanotwinned cubic boron nitride, Nature 493(7432) (2013) 385-8.

[62] Q. Huang, D. Yu, B. Xu, W. Hu, Y. Ma, Y. Wang, Z. Zhao, B. Wen, J. He, Z. Liu, Y. Tian, Nanotwinned diamond with unprecedented hardness and stability, Nature 510 (2014) 250.

[63] Z.J. Lin, L. Wang, J. Zhang, X.-Y. Guo, W. Yang, H.-K. Mao, Y. Zhao, Nanoscale twinning-induced elastic strengthening in silicon carbide nanowires, Scripta Materialia 63(10) (2010) 981-984.

[64] S.K. Yadav, X.Y. Liu, J. Wang, R. Ramprasad, A. Misra, R.G. Hoagland, First-principles density functional theory study of generalized stacking faults in TiN and MgO, Philosophical Magazine 94(5) (2013) 464-475.

[65] Y. Zhang, Z.-R. Liu, D.-W. Yuan, Q. Shao, J.-H. Chen, C.-L. Wu, Z.-L. Zhang, Elastic Properties and Stacking Fault Energies of Borides, Carbides and Nitrides from First-Principles Calculations, Acta Metallurgica Sinica (English Letters) (2019).

[66] Vollst, Auml, H. Dt, E. Ito, M. Akaishi, S.-i. Akimoto, O. Fukunaga, High Pressure Synthesis of Rocksalt Type of AlN, Proceedings of the Japan Academy, Series B 66(1) (1990) 7-9.

[67] R.F. Zhang, S. Veprek, Deformation paths and atomistic mechanism of B4→B1 phase transformation in aluminium nitride, Acta Materialia 57(7) (2009) 2259-2265.

[68] J. Zagorac, D. Zagorac, M. Rosić, J.C. Schön, B. Matović, Structure prediction of aluminum nitride combining data mining and quantum mechanics, CrystEngComm 19(35) (2017) 5259-5268.

[69] A. Madan, I.W. Kim, S.C. Cheng, P. Yashar, V.P. Dravid, S.A. Barnett, Stabilization of Cubic AlN in Epitaxial AlN/TiN Superlattices, Physical Review Letters 78(9) (1997) 1743-1746.

[70] P.M. Anderson, C. Li, Hall-Petch relations for multilayered materials, Nanostructured Materials 5(3) (1995) 349-362.

[71] A. Misra, H. Krug, Deformation Behavior of Nanostructured Metallic Multilayers, Advanced Engineering Materials 3(4) (2001) 217-222.

[72] M.A. Phillips, B.M. Clemens, W.D. Nix, A model for dislocation behavior during deformation of Al/Al3Sc (fcc/L12) metallic multilayers, Acta Materialia 51(11) (2003) 3157-3170.

[73] A. Misra, J.P. Hirth, R.G. Hoagland, Length-scale-dependent deformation mechanisms in incoherent metallic multilayered composites, Acta Materialia 53(18) (2005) 4817-4824.

[74] J.D. Embury, J.P. Hirth, On dislocation storage and the mechanical response of fine scale microstructures, Acta Metallurgica et Materialia 42(6) (1994) 2051-2056.

[75] J.S. Koehler, Attempt to Design a Strong Solid, Physical Review B 2(2) (1970) 547-551.

[76] S.I. Rao, P.M. Hazzledine, Atomistic simulations of dislocation–interface interactions in the Cu-Ni multilayer system, Philosophical Magazine A 80(9) (2000) 2011-2040.

[77] N. Koutná, P. Řehák, Z. Chen, M. Bartosik, M. Fallmann, M. Černý, Z. Zhang, M. Friák, M. Šob, P.H. Mayrhofer, D. Holec, Correlating structural and mechanical properties of AlN/TiN superlattice films, Scripta Materialia 165 (2019) 159-163.

[78] P. Řehák, M. Černý, D. Holec, Interface-induced electronic structure toughening of nitride superlattices, Surface and Coatings Technology 325 (2017) 410-416.

[79] H.C. Barshilia, K.S. Rajam, Raman spectroscopy studies on the thermal stability of TiN, CrN, TiAlN coatings and nanolayered TiN/CrN, TiAlN/CrN multilayer coatings, Journal of Materials Research 19(11) (2004) 3196-3205.

[80] P.H. Mayrhofer, C. Mitterer, L. Hultman, H. Clemens, Microstructural design of hard coatings, Progress in Materials Science 51(8) (2006) 1032-1114.

[81] H.-J. Lee, K.-W. Kwon, C. Ryu, R. Sinclair, Thermal stability of a Cu/Ta multilayer: an intriguing interfacial reaction, Acta Materialia 47(15) (1999) 3965-3975.

[82] R.G. Hoagland, R.J. Kurtz, C.H. Henager, Slip resistance of interfaces and the strength of metallic multilayer composites, Scripta Materialia 50(6) (2004) 775-779.

[83] J.M. Cowley, A.F. Moodie, The scattering of electrons by atoms and crystals. I. A new theoretical approach, Acta Crystallographica 10(10) (1957) 609-619.

[84] D.B.W.C.B. Carter, Transmission Electron Microscopy: A Textbook for Materials Science, 2016.

[85] C.L. Jia, M. Lentzen, K. Urban, Atomic-Resolution Imaging of Oxygen in Perovskite Ceramics, Science 299(5608) (2003) 870-873.

5 Papers

5.1 Publications included into this thesis

PUBLICATION I

Z. Chen, D. Holec, M. Bartosik, P.H. Mayrhofer, Z. Zhang, Crystallographic orientation dependent maximum layer thickness of cubic AlN in CrN/AlN multilayers, *Acta Materialia* 168 (2019) 190-202. DOI: 10.1016/j.actamat.2019.02.004

PUBLICATION II

 Z. Chen, Y. Zheng, L. Löfler, M. Bartosik, G. Nayak, O. Renk, D. Holec, Z. Zhang, Surprising superlattice intermixing triggered by nanoindentation and its effect (*Acta Materialia* submission manuscript under revision).

PUBLICATION III

Z. Chen, Q. Shao, M. Bartosik, P.H. Mayrhofer, H. Chen, Z. Zhang, Growth-twins in CrN/AlN multilayers induced by hetero-phase interfaces, *Acta Materialia* 185 (2020) 157-170. DOI: 10.1016/j.actamat.2019.11.063

PUBLICATION IV

Z. Chen, Y.Zheng, L.Löfler, M.Bartosik, H.Sheng, C. Gammer, D. Holec, Z. Zhang, Real-time atomic-resolution observation of coherent twin boundary migration in CrN (*Acta Materialia*, in print) DOI: 10.1016/j.actamat.2021.116732

5.2 Publications not included into this thesis

[1] N. Koutná, P. Řehák, Z. Chen, M. Bartosik, M. Fallmann, M. Černý, Z.L. Zhang, M. Friák, M. Šob, P.H. Mayrhofer, D. Holec, Correlating structural and mechanical properties of AlN/TiN superlattice films, *Scripta Materialia* 165 (2019) 159-163. DOI: 10.1016/j.scriptamat.2019.02.021

[2] J. Buchinger, N. Koutná, Z. Chen, Z. L. Zhang, P.H. Mayrhofer, D. Holec, M. Bartosik, Toughness enhancement in TiN/WN superlattice thin films, *Acta Materialia* 172 (2019) 18-29. DOI: 10.1016/j.actamat.2019.04.028

[3] J. Buchinger, A. Wagner, Z. Chen, Z.L. Zhang, D. Holec, P.H. Mayrhofer, M. Bartosik, Fracture toughness trends of modulus-matched TiN/(Cr,Al)N thin film superlattices, *Acta Materialia* 202 (2021) 376-386. DOI: 10.1016/j.actamat.2020.10.068

[4] J. Buchinger, L. Löfler, J. Ast, A. Wagner, Z. Chen, J. Michler, Z.L. Zhang, P.H. Mayrhofer, D. Holec, M. Bartosik, Fracture properties of thin film TiN at elevated temperatures, *Materials & Design* **194** (2020) 108885. DOI: 10.1016/j.matdes.2020.108885

[5] Z. L. Zhang, Z. Chen, D. Holec, C.H. Liebscher, N. Koutná, M. Bartosik, Y. Zheng, G. Dehm, P.H. Mayrhofer, Mapping the mechanical properties in nitride coatings at the nanometer scale, *Acta Materialia* 194 (2020) 343-353. DOI: 10.1016/j.actamat.2020.04.024

[6] F.X. Li, P. Chen, Z. Chen, P.D. Hao, J.H. Yi, K. G.Prashanth, J. Eckert, Face centered cubic titanium in high pressure torsion processed carbon nanotubes reinforced titanium composites, *Journal of Alloys and Compounds* 806 (2019) 939-945.DOI: 10.1016/j.jallcom.2019.07.277

[7] M. Fallmann, Z. Chen, Z.L. Zhang, P.H. Mayrhofer, M. Bartosik, Mechanical properties and epitaxial growth of TiN/AlN superlattices, *Surface and Coatings Technology* 375 (2019) 1-7.DOI: 10.1016/j.surfcoat.2019.07.003

[8] F.X. Li, P.D. Hao, J.H. Yi, Z. Chen, K.G. Prashanth, T. Maity, J. Eckert, Microstructure and strength of nano-/ultrafine-grained carbon nanotube-reinforced titanium composites processed by high-pressure torsion, *Materials Science and Engineering*: **A** 722 (2018) 122-128.DOI: 10.1016/j.msea.2018.03.007

[9] Yonghui Zheng, Zhuo Chen, Hao Lu, Yan Cheng, Xin Chen, Yunbin He and Zaoli Zhang The formation of TiO_2/VO_2 multilayer structure via directional cationic diffusion, *submitted* to *Nanoscale (under review).*

Publication I

Crystallographic orientation dependent maximum layer thickness of cubic AlN in CrN/AlN multilayers

Zhuo Chen[1], David Holec[2], Matthias Bartosik[3], Paul H. Mayrhofer[3], Zaoli Zhang[1]*

[1]Erich Schmid Institute of Materials Science, Austrian Academy of Sciences, A-8700 Leoben, Austria

[2]Department of Materials Science, Montanuniversität Leoben, A-8700 Leoben, Austria

[3] Institute of Materials Science and Technology, TU Wien, A-1060 Vienna, Austria

* Corresponding author: zaoli.zhang@oeaw.ac.at

Abstract

Metastable rock-salt (face centered cubic, c-) AlN can be grown in CrN/AlN multilayers when the AlN layer is thin enough. Exceeding a certain critical thickness, the thermodynamically stable wurtzite (w) structure grows. In this work, a bilayer-period-gradient (21 repeated blocks, each consisting of 10 bilayers with AlN layer-thicknesses ranging from 1.0 nm to 10.0 nm), ~2.0-µm-thick, reactively magnetron sputtered multilayer was characterized in detail with a spherical aberration-corrected transmission electron microscope (TEM). The studies are complemented by DFT (density functional theory) calculations.

The high resolution TEM (HRTEM) studies reveal that the <111> growth-orientation is not as effective as the <110> and <100> growth-orientations in stabilizing the metastable c-AlN. The critical thickness for the c-AlN layers (before the thermodynamically stable w-AlN forms) is around ~2.0 nm for the <111> growth-orientation but reaches as high as 4.1 nm for both <110> and <100> growth-orientations. Contrary to the <111> orientation, in both <110> and <100> orientations several unusually highly mismatched c-CrN/w-AlN interface structures form as soon as w-AlN is present. DFT studies suggest that the larger critical thickness of the AlN layers in <100> and <110> orientation is allowed by the lower surface energy and higher

cubic/wurtzite interfacial energy. The combination of HRTEM and DFT studies allows answering open questions on the impact of crystallographic orientations and interface structures, and also provides a better understanding on the growth mechanisms of c-AlN, necessary for the outstanding mechanical properties of AlN-containing multilayers.

Keywords: AlN/CrN multilayer; texture; interfacial energy; high resolution transmission electron microscopy; phase stability;

1. Introduction

Multilayer nitride thin films are perspective material systems for wear and tribological applications due to their extreme hardness and wear resistance [1, 2]. The microstructure of nanocrystalline materials is crucial for determining their outstanding mechanical and other physical properties. For example, the interface structure affects the thermal stability, the texture influences the anisotropy of the mechanical properties, the phase composition affects the mechanical properties of the film and oxidation resistance [3-6].

Aluminum nitride (AlN) crystallizes in several modifications, a stable wurtzite structure B4 (hereafter labeled '*w*') with a hexagonal symmetry, and two metastable phases with cubic symmetry: B1 (hereafter labeled '*c*' or *cubic*; rock-salt structure, NaCl prototype) and B3 (zinc-blende structure, ZnS prototype). Previous studies [1, 7-10] on multilayer nitride coatings have shown that the AlN phase exhibits wurtzite-type structure when the AlN layer thickness is larger than 4.0 nm in CrN/AlN system, which can also lead to a low hardness (23–25 GPa), poor adhesion and low wear resistance of the coatings. However, thinner AlN layers lead to an epitaxial stabilization of the rock-salt AlN phase in CrN/AlN multilayers thus enabling for its excellent mechanical properties. The stabilization of the c-AlN phase can be explained by considering the overall energetics including strain energy and interfacial energy contributions [11]. For the TiN/AlN multilayer films with smaller layer thickness (AlN below 3.0 nm), the strain energy is only a small contribution to the total energy. The rock-salt c-AlN structure is formed at small layer thicknesses (despite its higher energy of formation than the *w*-AlN) since it possesses lower interfacial energies than the *c*-TiN/*w*-AlN structure [7, 12]. The stability of the metastable AlN phase also depends on the interlayer (stable cubic nitride) thickness. Schlögl *et al.* proposed that the CrN layer thickness needs to be at least as thick as the targeted c-AlN layer thickness, in order to provide sufficient strength for a full stabilization of the AlN layers

in their metastable cubic structure by coherency strains [5]. Nevertheless, an upper limit for the c-AlN thickness exists due to thermodynamic reasons. The X-ray nano-diffraction experiments revealed that the coherent growth between c-CrN and c-AlN (stabilized by the CrN template) layers is achieved only when the AlN layer thickness is below ~4.0 nm [3]. Above ~4.0 nm, the nucleation of the thermodynamically stable wurtzite AlN is favored, leading to a coherency breakdown [3]. Chawla *et al.* combined the finite element modeling and density functional theory (DFT) methods to explain how the coherency state of the substrate–layer interface affect the *c*-AlN stability, i.e. a small lattice constant of the stable cubic interlayer helps to stabilize *c*-AlN, whereas a large lattice constant promotes *w*-AlN stability [13]. Despite the above mentioned achievements, relationships between the *c*-AlN phase stability and the crystallographic growth-orientation as well as the interface structure has hardly been addressed to date.

To identify the role of these individual mechanisms, a bilayer-period-gradient CrN/AlN multilayer film has been synthesized. The entire coating is composed of 21 blocks, within each block, the AlN layer thickness increases from 1.0 nm to 10.0 nm while keeping the interlayer CrN thickness constant at 4.0 nm. This gradient CrN/AlN thin film is used to study the effect of the layer thickness on the AlN phase change and to track the growth morphology variation. Dark-field transmission electron microscopy (TEM) provides a large scale representation of the texture evolution and the phase composition of our gradient multilayer thin film. The Cs-corrected high-resolution TEM enables genuine atomic level observations, and thus was used to study phase composition, interface atomic structure and strains. Using these techniques, we are able unambiguously show that the maximum thickness for the epitaxially stabilised metastable cubic AlN is strongly dependent on the crystallographic orientation, and is the highest for the <100> and <110> orientations. The results are corroborated by detailed first principles calculations on surface and interface energies and bulk-related total (free) and strain energies.

2. Experimental details

2.1. Material fabrication

The CrN/AlN multilayer film with a total thickness of ~2 μm is composed of 21 repeating blocks consisting of 10 bilayers composed of 4 nm thin CrN layers and AlN layers having different thicknesses. The thickness of the AlN layer was ~1 nm for the first bilayer and around

10 nm for the last one (within a block), with a stepwise increase of 1 nm from one bilayer to the following. Hereafter in the text, labels of 1-AlN to 10-AlN refer to AlN layers with corresponding nominal thicknesses (1.0 nm-10.0 nm) in a certain block (cf. Fig. 1). The film was synthesized in an AJA International Orion 5 reactive magnetron sputter system by DC powering one 2" Cr and one 3" Al target (both 99.6% purity, Plansee Composite Materials GmbH, Austria) at 500 °C substrate temperature in an Ar/N_2 gas mixture (flow ratio of 5 sccm Ar/5 sccm N_2) at a total pressure of 0.4 Pa. The chosen power densities of ~12.3 (Cr target) and ~11.0 W/cm^2 (Al target) resulted in the deposition rates of ~10 and ~24 nm/min for CrN and AlN, respectively. The nanolayer structure was realized using computer controlled shutters, which were mounted in front of the permanently running targets. To achieve a dense coating morphology, a bias voltage of -50 V was applied to the growing film during the deposition process (floating potential was ~ -20 V). The substrate holder rotated with a constant rotation speed of ~1 Hz throughout the whole process.

Prior to the deposition, the polished Si (100) substrate (10 x 10 x 0.5 mm^3) were ultrasonically pre-cleaned in acetone and ethanol for 5 min each, thermally cleaned at 500 °C for 20 min inside the evacuated deposition chamber (base pressure at room temperature was ~5×10^{-4} Pa), and Ar-ion etched for 10 min at the same temperature in an Ar atmosphere at a pressure of 6 Pa by applying a constant bias voltage of -750 V to the substrate.

2.2. Material characterization

Cross-sectional transmission electron microscopy (TEM) specimens were prepared using a standard TEM sample preparation approach including cutting, grinding and dimpling. Ar ion milling was carried out at a voltage of 4.0 kV with an angle of 6°, followed by a final low voltage ion-milling of 2.5 kV with an angle of 2° as a final step.

The morphology of the film was examined by bright/dark-field imaging and selected-area electron diffraction (SAED) using a Philips CM12 transmission electron microscope working at an accelerating voltage of 120 kV. (The overall film structure was characterized by X-ray diffraction using a Panalytical XPert Pro MPD θ-θ diffractometer in Bragg Brentano configuration with Cu Kα radiation ($\lambda \approx 1.54$ Å). A 200 kV field emission TEM/STEM (JEOL2100F) equipped with an image-side C_S corrector was used in this study, which demonstrates a resolution of 1.2 Å at 200 kV. The image size of all TEM micrographs recorded on a CCD camera was kept at 2004 × 1335 pixel. The exposure time for the HRTEM images was set to 1.0 s. The aberration coefficients were set to be sufficiently small for obtaining the HRTEM images under slightly over-focus conditions (close to Scherzer defocus). The strain

field in CrN/AlN multilayer was calculated on the C_S-corrected high-resolution TEM images by the geometric phase analysis (GPA) method. According to the GPA algorithm, the displacement field can be obtained by selecting two non-collinear Bragg vectors in the power spectrum generated from a high-resolution TEM image. Strain map was calculated with respect to this reference lattice defined by $\overrightarrow{\boldsymbol{g_1}}$ = [220] AlN/CrN and $\overrightarrow{\boldsymbol{g_2}}$ = [2$\overline{2}$0] AlN/CrN.

To obtain the overall length distribution of columnar grains we used Digital Micrograph software. Since the HRTEM image clearly reveals the growth-orientation and atomic structures, it facilitates the determination of the grain orientation relationships. The length distribution of columnar grains with different growth-orientations from the 5th to 15th block was statistically analyzed using HRTEM images recorded at 300-600Kx (all images taken along Si substrate [011] direction). The length of cubic columnar grains in CrN/AlN multilayers was measured by drawing a profile from the first layer of c-CrN in each block to the top of the columnar grains. About 20 columnar grains in cubic/cubic <111> growth direction, 17 columnar grains in cubic/cubic <100> growth direction and 15 columnar grains in cubic/cubic <110> growth direction were used for determining the distribution of columnar grain lengths.

2.3. DFT calculations

First principles calculations were performed using the Vienna Ab initio Simulation package (VASP) [14, 15] employing projector augmented pseudopotentials [16] and the exchange-correlation potential within the Perdew-Burke-Ernzerhof-parameterized generalized gradient approximation (GGA-PBE) [17]. The plane wave energy cut-off was set to 500 eV. The reciprocal space was sampled with equivalent of ~1600 k-points per single-atom cell using the Monkhorst-Pack mesh, and the number of k-points was decreased correspondingly depending on the actual cell-size. CrN was considered in a ferromagnetic state. This has been shown to be energetically as well as elastically a reasonable approximation for the paramagnetic state [18]. Such approximation is necessary in the present case due to the large computational demands resulting from supercells needed for the surface and interface energy calculations, and presents a compromise between the true 0K ground state (anti-ferromagnetic arrangement) and room temperature paramagnetic state. The supercells used for calculating interface energies contained equal numbers of Al and Cr atoms (in addition to N atoms), and the bilayer period induced by periodic boundary conditions was between 50 and 60 Å, depending on a particular interface orientation. The orientation relationships considered here were c-CrN(111)[1$\overline{1}$0]/w-AlN(0001)[11$\overline{2}$0], c-CrN(111)[1$\overline{1}$0]/c-AlN(111)[1$\overline{1}$0], c-CrN(110) [1$\overline{1}$0]/w-AlN(1$\overline{1}$00)[11$\overline{2}$0]

and c-CrN(110) [1$\bar{1}$0]/c-AlN(110) [1$\bar{1}$0]. The calculation of the w-AlN(1$\bar{1}$01) surface energy followed the same procedure as described in Ref. [19].
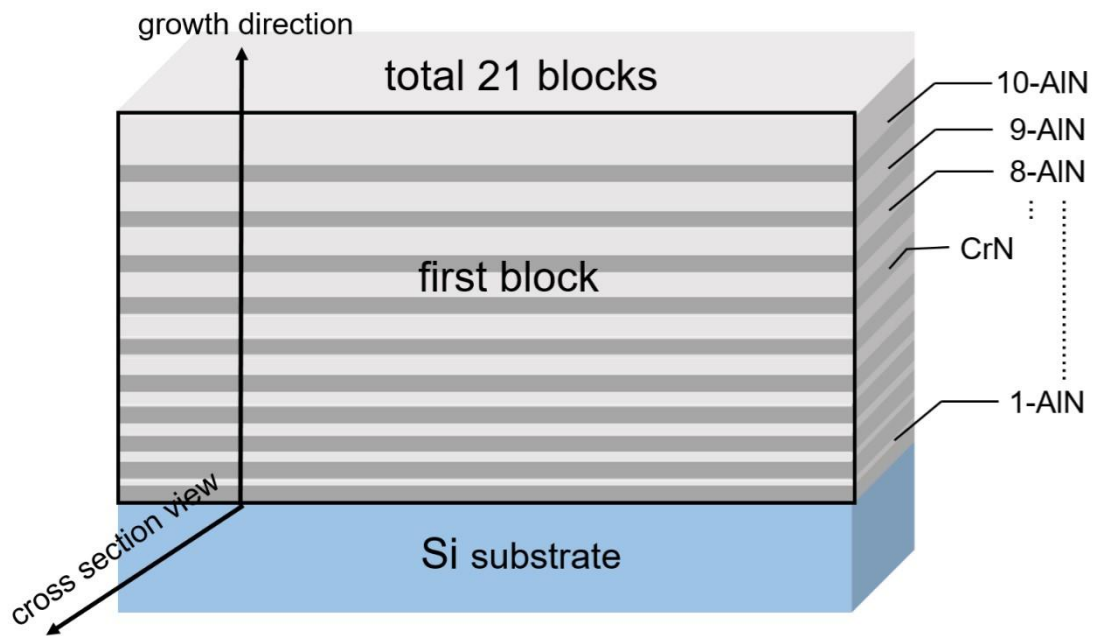

Fig. 1. A schematic view of the bilayer-gradient CrN/AlN multilayer on Si (100) substrate. Presented is the first block (out of 21 repeated ones in total).

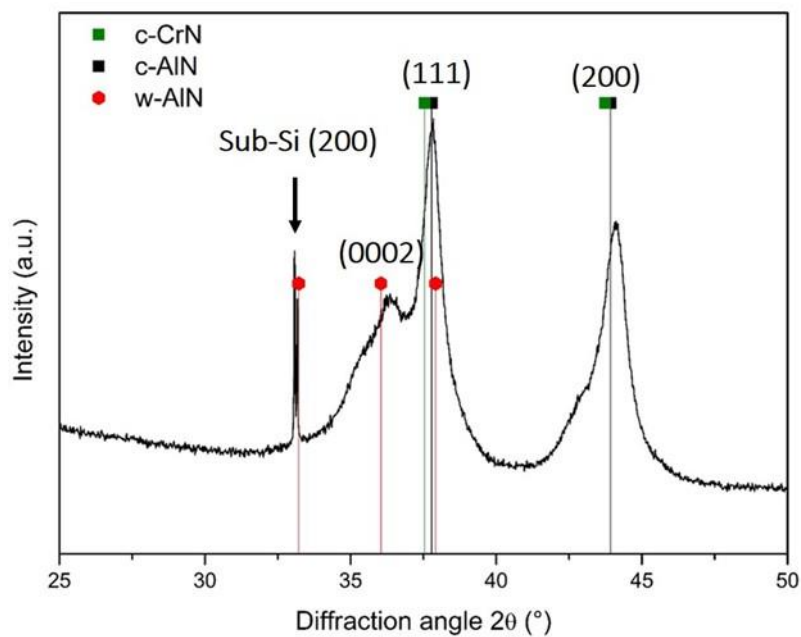## 3. Experimental results

3.1. Microstructure evolution

Fig. 2. X-ray diffraction pattern of the bilayer-gradient CrN/AlN multilayer on a Si (100) substrate.

The overall phase structure was characterized using X-ray diffraction. Fig. 2 reveals the structures of AlN and CrN phases: c-CrN/c-AlN (B1) are represented by their characteristic fingerprints consisting of (111) and (200) peaks while w-AlN (B4) is revealed by its (0002) peak. The morphology of the multilayered film is further investigated by analyzing a cross-sectional TEM sample. The bright-field images (Fig. 3) clearly reveal the blocks with a bilayer-gradient structure, in which bright and dark contrasted layers, corresponding to AlN and CrN, can be recognized, respectively. The inserted line profile in Fig. 3a shows the gradient structure (AlN layer thickness ranging from 1.0 nm to 10.0 nm) and the block is about 95.1 nm thick.

A close examination of the overall morphology reveals that the layers in the 1st to 4th block are uniform (contain very flat interfaces) and gradually develop the wavy-like morphology further away from the substrate (from the 4th block on). This indicates that the surface roughness increases with increasing film thickness. The film grows with columnar nanocrystals along the growth direction. These columnar grains can be classified into two groups. For the initial phase of the film deposition (1st till 4th block) in Fig. 3a, several slender columnar grains can be observed (type-A grains, indicated by a white frame). The width of type-A columnar grains ranges from 10 to 20 nm, whereas the maximum grain length can reach up to 200 nm. The total thickness of one block is ~95 nm (using nominal thicknesses one obtains 10 times 4 nm-thin-CrN layers plus $(1 + 2 + 3 + 4 + 5 + 6 + 7 + 8 + 9 + 10$ nm) AlN layers = 95 nm), cf. also with the inset in Fig. 3a. Hence, type-A columnar grains can extend over several blocks. Additionally, the film contains also another type of columnar grains (type-B, yellow frame) after a certain thickness, i.e. far away from substrate (from the 5th block on, see Fig. 3b). These grains are shorter than type-A ones, are constrained to within one block, and appear as 'rice-shaped'. Type-B columnar grains grow from the first CrN layer in each block and are terminated by an AlN layer in the same block, which limits their length. After it is terminated within one block, and before another block starts, type-B columnar grains grow again. The type-B columnar grains with a length of 20-50 nm have widths from 10 to 20 nm. As will be revealed in the following HRTEM images, the crystallographic orientation is different within these two types of columnar grains, causing a distinct stability of the cubic AlN phase.

To sum up, the TEM bright-field result shows that the morphology of the columnar grains is significantly different in different film locations. The slender type-A columnar grains are

located in the substrate-near film area, while the much shorter type-B columnar grains form far away from the substrate.
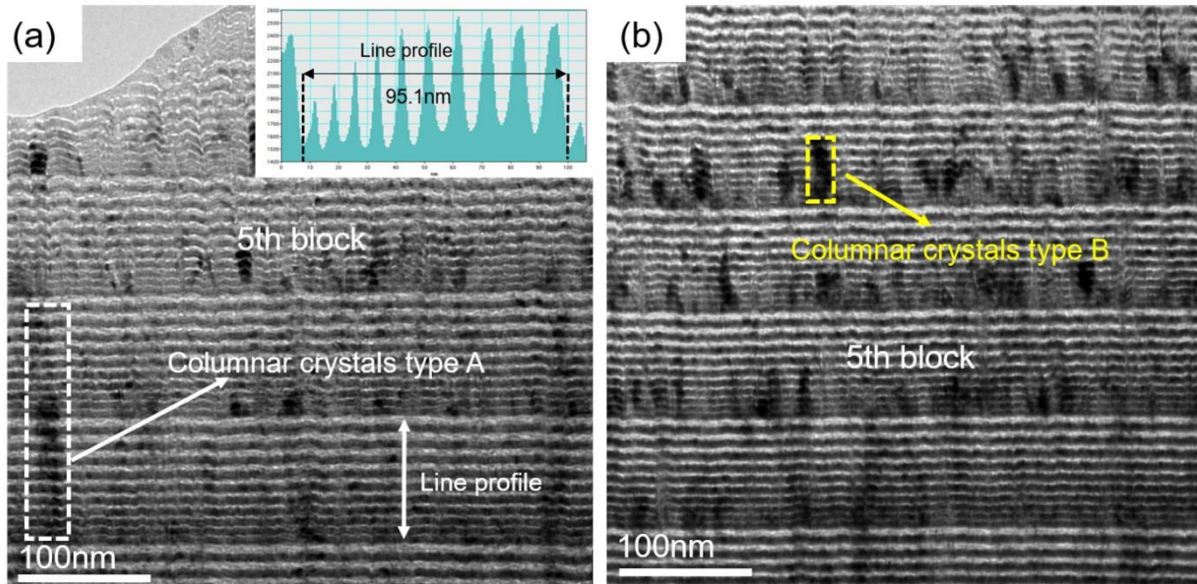

Fig.3. Cross-sectional TEM bright-field images taken (a) from the 3rd to 6th block and (b) from the 4th to 8th block. Inserted (contrast) line profile indicates the thickness of the 3rd block. White and yellow frames mark the type-A and type-B columnar grains (see text for explanation).
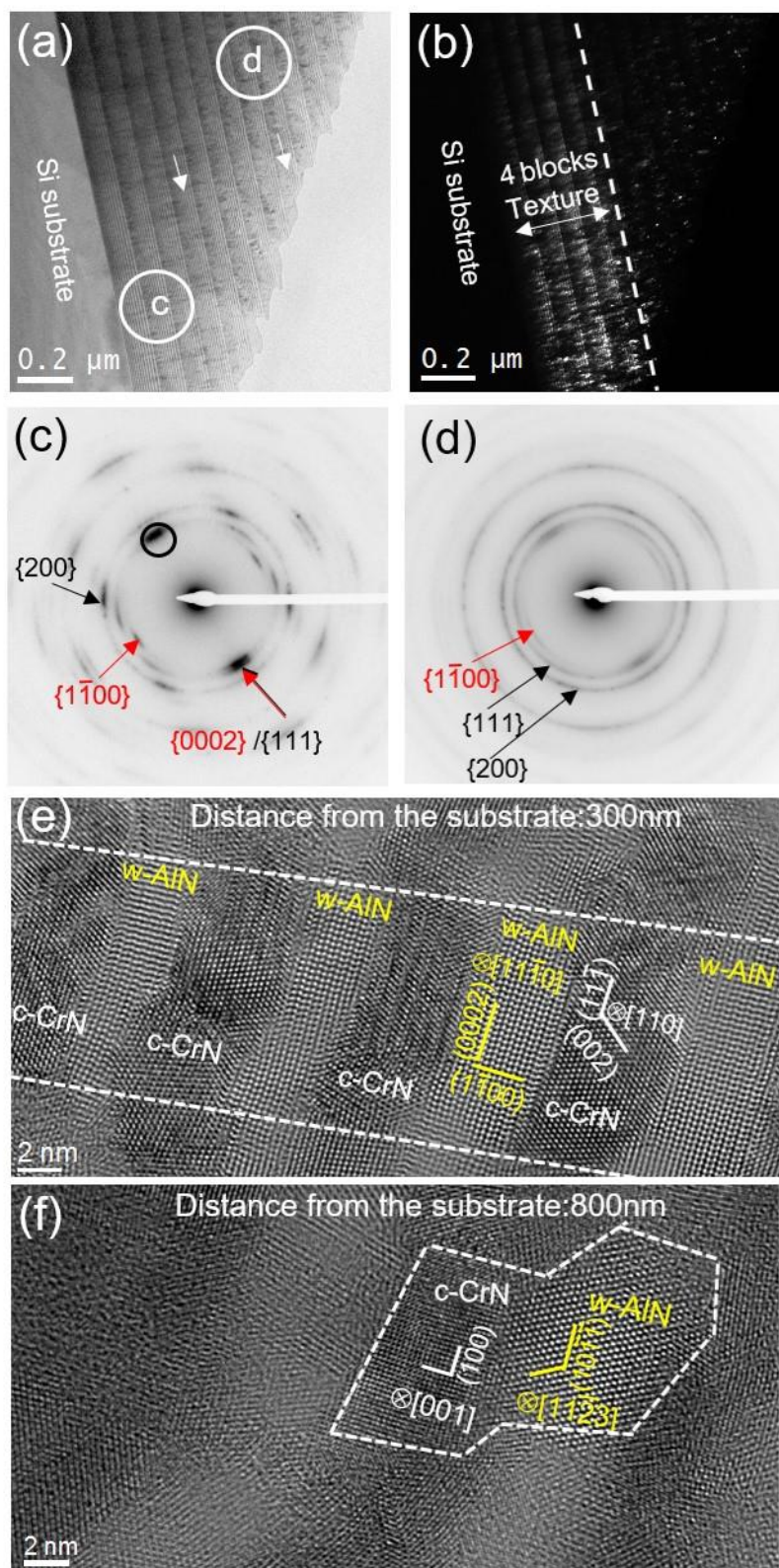
3.2. Crystallographic orientation evolution

Fig.4. (a) and (b) TEM cross-sectional bright-field and dark-field images (objective aperture position shown in Fig.4c). (c) and (d) are the SAED patterns from positions marked in Fig.4a. (e) HRTEM image of *c*-CrN/*w*-AlN (type-A columnar grain from 3-AlN to 6-AlN) grain in the 4th block. (f) HRTEM image of *c*-CrN/*w*-AlN grain (9-AlN) in the 9th block. The dotted lines

indicate the well oriented region. Positions of Fig.4e and Fig.4f can be found in Fig.4a (white arrow).

In order to investigate the preferred grain orientation, the gradient multilayer is characterized by the cross-sectional bright/dark-field images and selected area electron diffraction (SAED). The SAED pattern of the CrN/AlN multilayer taken from the area near the substrate (labeled in Fig. 4a) corresponds to a mixture of reflections from c-CrN/c-AlN and w-AlN (Fig.4c). These reflections can be indexed as wurtzite $\{0002\}$ and $\{1\bar{1}00\}$, and cubic $\{111\}$ and $\{200\}$. The discrete nature and high symmetry of strong diffraction dots in Fig. 4c indicate the presence of a strong texture with a preferred growth orientation of c-CrN $<111>$ $\|$ w-AlN $<0001>$ direction. This can be observed from the 1st to 4th block (0-380 nm away from the substrate, cf. the dark-field image Fig. 4b). HRTEM recorded from one typical slender columnar grain (type-A) extending from 3-AlN to 6-AlN is shown in Fig. 4e, where the brighter layers in the columnar grain are w-AlN (viewed along the $[11\bar{2}0]$ direction) while the darker layers are cubic CrN (viewed along the $[110]$ direction). The $(0002)_{w\text{-AlN}}$ planes in w-3-AlN to w-6-AlN are parallel to c-CrN $(11\bar{1})$ planes, and perpendicular to the film growth direction. Hence, the textured SAED (Fig. 4c) is consistent with HRTEM observation (Fig. 4e). The typical orientation relationship and growth directions of c-CrN and w-AlN grains in the strongly textured region can be found, i.e. $\{111\}<110>_{c\text{-CrN}}\|\{0001\}<11\bar{2}0>_{w\text{-AlN}}$.

However, the texture gradually disappears above the 4th block (over 380 nm away from the substrate), as demonstrated by the appearance of corresponding polycrystalline diffraction rings (Fig. 4d). Comparison of SAED patterns (Fig. 4c and Fig. 4d) suggests that grains grow randomly over a large distance without any preferred orientation, and there may exist other crystallographic orientations (not along the $<111>\|<0001>$ growth direction) far away from the substrate area. Actually, intensive HRTEM observations indeed confirm the presence of other crystallographic growth orientations in this region, i.e. Fig. 4f, showing a growth orientation of $<100>_{c\text{-CrN}}\|<10\bar{1}\bar{1}>_{w\text{-AlN}}$ observed from the w-AlN /c-CrN interface in the 9th block (note that $(100)_{c\text{-CrN}}\|(10\bar{1}\bar{1})_{w\text{-AlN}}$ is indicated in the image).

To summarize, the microstructure and growth orientation varies depending on the film area. We found a strong texture from the 1st to 4th block and their grains exhibit a slender column structure (type-A). By HRTEM and SAED, we show that the slender type-A column grains are mainly the w-AlN/c-CrN multiphase structure in thicker AlN part and their crystallographic

growth orientations are the $<0001>_{w\text{-AlN}} // <111>_{c\text{-CrN}}$ directions in the strongly textured area. However, significant microstructure and growth orientation variations are found far away from the substrate area (block 5-21).

3.3 Critical thickness of c-AlN layers

3.3.1 Lower critical thickness of c-AlN layers in <111> growth-orientation in strongly textured areas
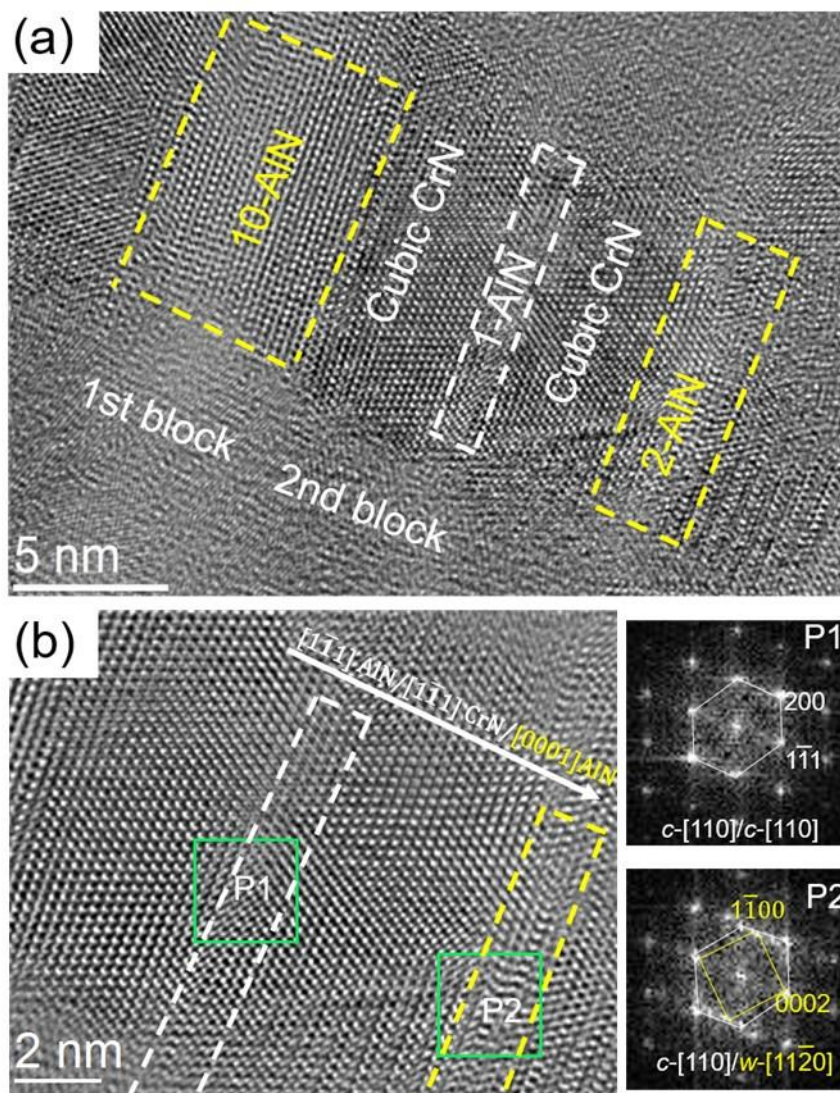

Figure 5 (a) HRTEM image of type-A columnar grain (last layer in the 1st block and first two layers in the 2nd block). (b) Enlarged filtered image of the 1-AlN and 2-AlN layers. FFT images corresponding to the 1-AlN (P1 position) interface and 2-AlN (P2 position) interface region.

The yellow framed areas are *w*-AlN while white ones are *c*-AlN. The growth direction is denoted by arrows.

In Sec. 3.1 and 3.2, we show that the type-A columnar grains present near the substrate area are mainly composed of *c*-CrN/*w*-AlN. Note that our HRTEM image (Fig.4e) only shows the phase structure for the thicker AlN layers. For the thinner AlN layer in the type-A columnar grains, it is more likely to form a cubic phase structure. In order to investigate the critical thickness of the *c*-AlN layers in the strongly textured areas (1st-4th block), we focus our HRTEM observations on the thinner AlN layer. Figure 5a shows an atomic resolution image of the type-A columnar grain at the location from 10-AlN (the 1st block) to 2-AlN (2nd block). There exists a weak bright contrast in the thinner AlN layers, i.e. 1-AlN and 2-AlN, in the HRTEM image. However, they can be easily distinguished in the bright-field image, i.e. Fig. 3a. Along the growth direction, the measured interplanar spacing is 0.249 nm of the 10-AlN layer corresponding to $\{0002\}_{w\text{-AlN}}$ planes (JCPDS 25-1133 $d_{\{0002\}w\text{-AlN}}$=0.249 nm). According to the FFT analysis (at P1 position), no other phases are found in the 1-AlN layer of the second block.

Along the growth direction, the measured interplanar spacing of 1-AlN is 0.231 nm, corresponding to $\{111\}_{c\text{-AlN}}$ planes (JCPDS 46-1200 $d_{\{111\}c\text{-AlN}}$=0.233 nm). This indicates that the expected thin cubic AlN is formed and the cubic CrN/AlN layer have the <111> growth direction (with a [110] view direction). The interplanar spacing of the 2-AlN layer is measured as 0.250 nm (Fig. 5b), which fits well to the *w*-AlN {0002} planes. Combined with the FFT result at the P2 position showing extra reflections, it can be concluded that the 2-AlN layer already shows the presence of a wurtzite structure with a [11$\bar{2}$0] zone axis. The measured thickness of the 2-AlN layer is about 1.9 nm. Consequently, the critical thickness for the *c*-AlN stability is surprisingly low as compared with the previous reports, in which AlN layers retained their metastable cubic structure up to a layer thickness of ~3.0 nm [1, 5].
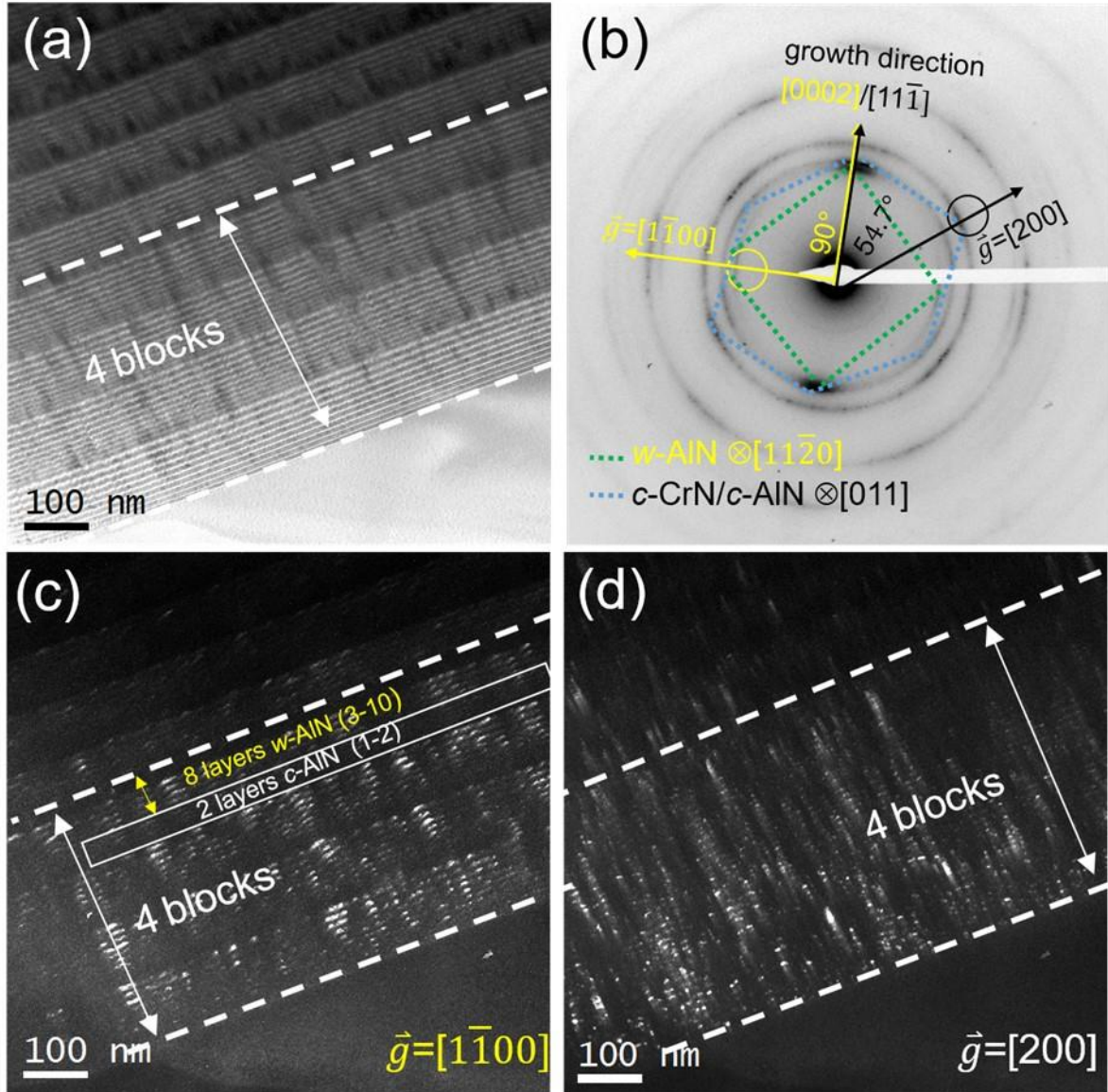
44

Fig.6. (a) TEM cross-sectional bright-field image and (b) corresponding diffraction pattern near the substrate area. In order to obtain dark field images of grains in the growth-direction (cubic <111> and wurtzite <0001>), the aperture is located at positions marked by yellow and black circles in the SAED pattern. (c) and (d) are dark-field images from the same area taken under the wurtzite $\vec{g}$=[1$\bar{1}$00] and cubic $\vec{g}$=[200] reflections. The white framed area is a cubic region of the CrN/AlN layers (from 1-AlN to 2-AlN).

In order to investigate the overall critical thickness for obtaining *c*-AlN layers in the strongly textured region, we carried out a comprehensive microscopy study on the microstructure of the metastable phase. Figures 6a and 6b show a cross-sectional bright-field image and a corresponding diffraction pattern acquired from 1st till 4th block (close to the

substrate). The diffraction pattern contains, in addition to the rings, many spotty reflections, which can be indexed as w-AlN (along [11$\bar{2}$0]) and c-AlN/c-CrN (along [011]), as shown in Fig. 6b. Fig. 6c shows the dark-field image of w-AlN (using $\vec{g}$=[1$\bar{1}$00]), and grains with the <0001> growth direction. Using the smallest objective aperture to separate the cubic and wurtzite reflections in the diffraction pattern, the bright regions in Fig. 6c display only the textured grains of w-AlN (between these bright layers are cubic CrN). Here, eight bright layers of w-AlN (from 3-AlN to 10-AlN, as indicated) can be distinguished in each period, and there are 10 to 15 nm-thick dark zones (from 1-AlN to 2-AlN) present from the 1st till the 4th block, denoting the absence of wurtzite phases, which are actually cubic area (as indicated). Such cubic zones can be confirmed in the dark-field image when using cubic $\vec{g}$=[200], where the dark layers never fulfill the cubic diffraction condition, i.e. are wurtzite, while the layers with white spots locally diffract for the cubic diffraction vector, and hence are identified as cubic (Fig. 6d). We note that the contrast in cubic layers depends on the local interface in-plane orientation. Analogously, the dark regions (from 1-AlN to 2-AlN) in Fig. 6c – recorded under the hexagonal diffraction condition – have the cubic structure, which is the grain with c-AlN/c-CrN. Hence, the cubic AlN phase only exists in the 1-AlN or 2-AlN layer (note that 2-AlN is a mixture area since some parts of the layer also show the wurtzite bright layer in Fig. 6c). The above observations are consistent with our HRTEM results on the critical thickness of metastable cubic-AlN layer, presented in Fig. 5b. Furthermore, combining the results from Fig.4e and Fig. 6a, the type-A columnar grain structure can be completely determined to be c-AlN/c-CrN in thinner AlN layers and w-AlN/c-CrN in thicker AlN layers. Thus, we can conclude that the majority of c-AlN grains grow along the <111> direction but with a low epitaxial phase stabilization (the critical thickness for c-AlN layers is about 2.0 nm) near the substrate area (1-4 block).

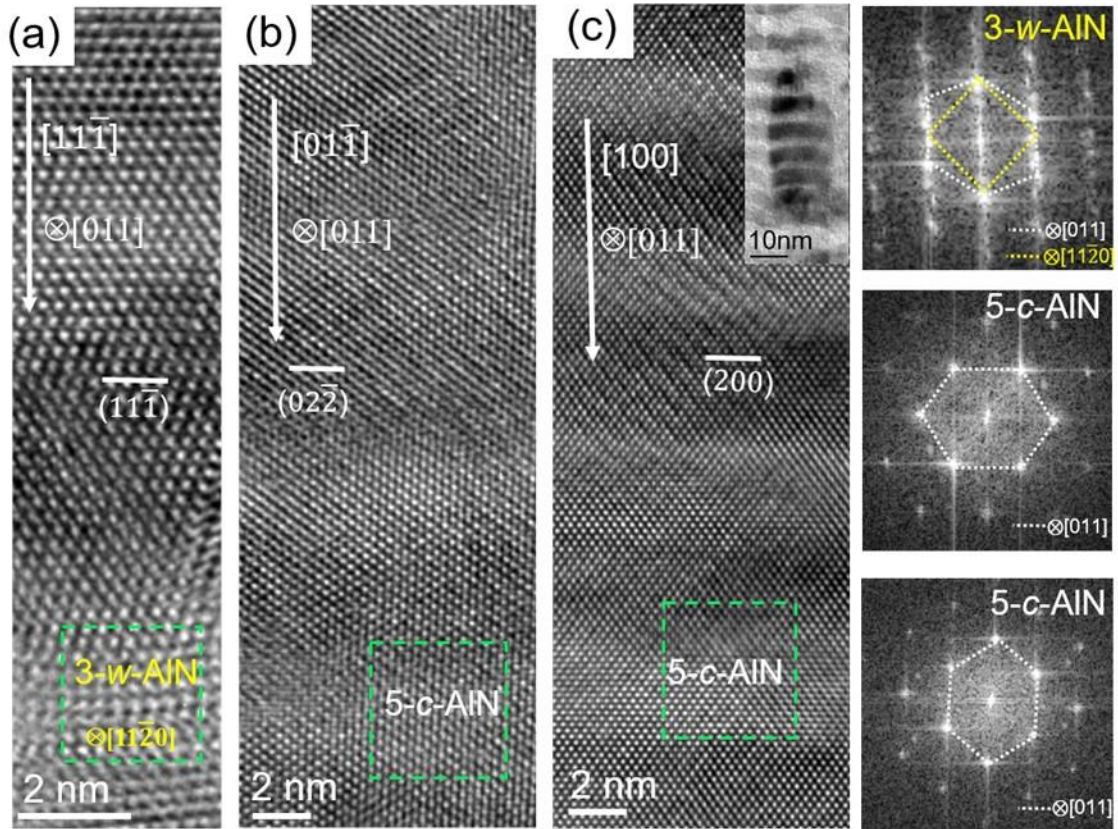## 3.3.2 Larger critical thickness of c-AlN layers in <110> and <100> growth-orientation

Fig.7. HRTEM images of one portion of several columnar grains (type-B), (a) [11$\bar{1}$], (b) [01$\bar{1}$] and (c) [100] growth-orientation, distributed in the 9th, 10th, and 13th block, respectively. A low magnification image of type-B columnar grain is inserted in (c). The growth directions are denoted by arrows. FFT images displayed on the right-hand side correspond to the 3-AlN/CrN ([11$\bar{1}$] growth-orientation), 5-AlN/CrN ([01$\bar{1}$] growth-orientation), and 5-AlN/CrN ([100] growth-orientation) interface area, respectively (taken from the respective green marked areas). Note that yellow and white polygons in the FFT images indicate the wurtzite and cubic phases, respectively.

In Sec. 3.2, we showed that the *c*-AlN with <111> growth-orientation is present in the strongly textured region close to the substrate. However, for the areas far away from the substrate, thicker *c*-AlN layers can be found with different growth orientation. This already indicates that the critical thickness for the *c*-AlN layers is orientation-dependent.

According to our extensive HRTEM observations, type-B columnar grains (corresponding to the yellow marked region in Fig. 3b) have the cubic/cubic superlattice structure with various growth-orientations. However, the dominant growth-orientations of the type-B columnar grains are [11$\bar{1}$], [01$\bar{1}$] and [100]. Representative HRTEM images taken along [11$\bar{1}$], [01$\bar{1}$] and [100]

47

growth directions are shown in Figs. 7a-c (primary electron beam directions are [011] directions), respectively. For the bottom AlN layer in Fig. 7a, the FFT shows extra reflections which suggest the wurtzite AlN structure (as highlighted in the FFT image by a yellow polygon). The measured critical thickness before wurtzite AlN phases form is about 2.6 nm. Furthermore, the c-AlN maximum layer thickness in Fig.7a is also consistent with the experimental result in the <111> textured region, i.e. the critical thickness for c-AlN layers is about 2.0 nm in blocks 1-4. The measured critical thickness before the wurtzite AlN phase form is about 2.6 nm.

Contrarily, the $[01\bar{1}]$ and [100] growth-orientations yield the FFT without extra reflections, i.e. containing only the *c*-AlN reflections still in the 5-AlN/CrN interface areas. Hence, the *c*-AlN can be found even in the 5-AlN layer with a measured thickness of 4.0 nm (Fig. 7b) and 4.1 nm (Fig. 7c), respectively. The layer thickness of *c*-AlN in both $[01\bar{1}]$ and [100] growth-orientation is also larger than the previously reported critical thicknesses of 3.3 nm and 3.0 nm for *c*-AlN [1, 5]. To summarize, c-AlN layers with the <100> and <110> growth orientation shows a higher phase stability far away from the substrate area while those with the <111> growth orientation maintains the low phase stability.

3.3.3 Statistics of the orientation-dependent critical thickness for c-AlN layers
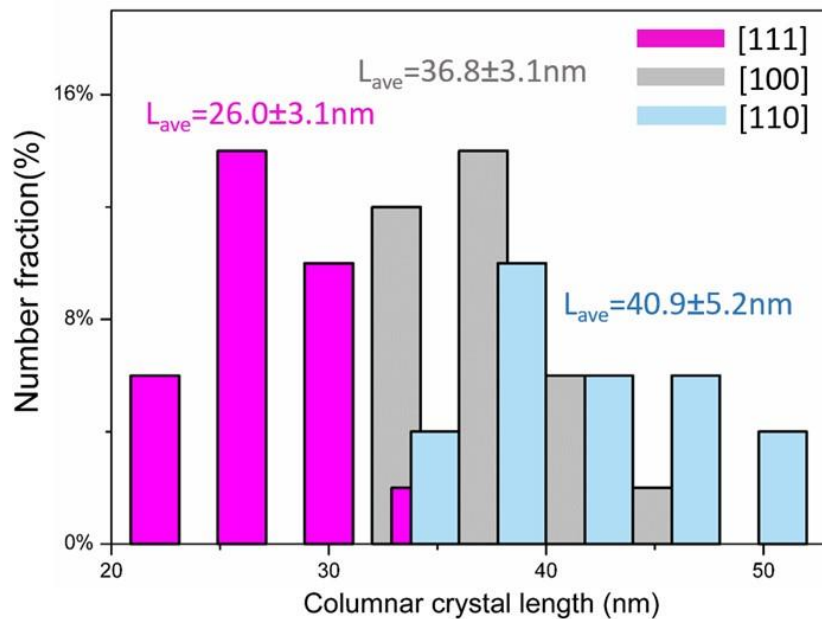
Fig. 8. Histogram distributions of type-B columnar grain lengths in different orientations acquired by HRTEM images in the 5th till 15th block (all images taken along the Si substrate [011] direction).

In this section, we discuss a statistical analysis of HRTEM measurements to further prove that the critical thickness for c-AlN layers is orientation-dependent. The comparison of the individual c-AlN critical thicknesses (Figs. 7a-c) suggests that these are orientation-dependent. The cubic-AlN layer in both [01$\bar{1}$] and [100] growth-orientation (Fig. 7b, Fig. 7c) can be stabilized up to ~4.0 nm, while in [11$\bar{1}$] growth-orientation (Fig. 7a) the critical thickness is only ~2.0 nm. A consistent result is obtained also for the type-A grains: AlN grains in Fig. 6c also exhibit a lower critical thickness (cubic AlN exists only in 1-AlN and 2-AlN layer) in <111> growth-orientation of textured areas (1st till 4th block).

According to HRTEM observations, the type-B columnar grains have the cubic-CrN/cubic-AlN superlattice structure. In our gradient structure, the cubic/cubic columnar grain length is actually related to the c-AlN critical layer thickness (type-B columnar grain length = $(n-1)t_{c\text{-}CrN}+t_{1\text{-}c\text{-}AlN} + t_{2\text{-}c\text{-}AlN} +..... + t_{n\text{-}c\text{-}AlN}$ where n is the number of the thickest AlN layer, which is still cubic-structured). Hence, the thicker c-AlN layers are always present in the much longer columnar grains as shown in Figs. 7b and 7c. In Fig.7c, we determined the maximum cubic AlN layer thickness to be about 4.1 nm in the 5-AlN layer and the type-B cubic/cubic columnar grain lengths (its low magnification image can be found in Fig.7c right-hand side) to be about 34 nm. However, in Fig.7a, the maximum cubic AlN layer thickness is found to be about 2.6 nm in the 3-AlN layer and the type-B columnar grain lengths is about 23 nm. Consequently, the length of the cubic/cubic columnar grains (type-B) is actually an indirect measure for the critical thickness of the c-AlN layers. The specific orientation of columnar grains, i.e. in the <111>, <100> and <110>, can be clearly resolved via HRTEM images. The distribution of columnar grain lengths along these specific orientations is plotted in Fig.8, clearly exhibiting an orientation dependence. The length of columnar grains with <111> growth-orientation ranges from 20.0 to 30.0 nm, whereas both <100> and <011> oriented grains range from 34.0 to 51.0 nm. The average length in <100> and <110> is 36.8±3.1 nm and 40.9±5.2 nm, respectively, larger than that of the <111> growth-orientation being 26.0±3.1 nm. Furthermore, the average overall columnar crystal length of the three different growth directions is consistent with HRTEM observations (as shown in Figs. 7) of c-AlN critical layer thicknesses, i.e. the lowest critical thickness for stabilizing AlN in the cubic structure can be found in <111> growth direction. Hence, the average length in three different growth directions implies that there are

many more c-AlN layers in type-B columnar grains and much larger critical cubic-AlN thicknesses in <100> and <110> directions than in the <111> growth direction. The data furthermore suggest that the largest critical thickness for c-AlN layers is present for the <110> growth-orientation.

3.4 Cubic/Cubic and Cubic/Wurtzite interface structures
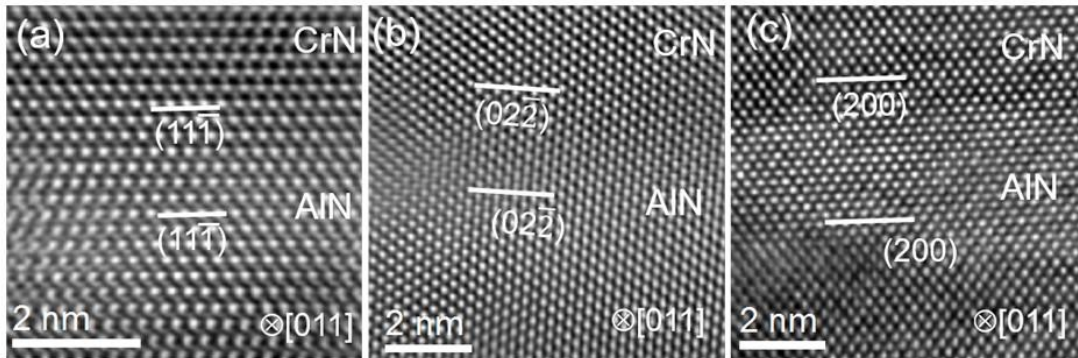

Fig. 9. HRTEM filtered images of interfaces in type-B columnar grains with (a) $(11\bar{1})$, (b) $(02\bar{2})$ and (c) (200) orientations. These are enlarged sections of the images presented in Figs. 7a-c from the c-CrN/c-AlN interface area.

Since c-CrN has a very similar lattice constant (4.14 Å JCPDS 11-0065) as c-AlN (4.04 Å JCPDS 46-1200), the c-AlN has always a good lattice matching relationship with c-CrN. Therefore, the typical coherent interface structures, such as $\{111\}_{CrN}||\{111\}_{AlN}$, $\{110\}_{CrN}||\{110\}_{AlN}$ and $\{100\}_{CrN}||\{100\}_{AlN}$ (Figs. 9a-c), often appear in the c-AlN/c-CrN superlattice grains.

The c-CrN/w-AlN interface, however, exhibits an evolution of interface structures in different regions, i.e. low-mismatch interfaces in the textured regions and high mismatch interfaces far from the substrate. Fig. 10b shows the semi-coherent interfaces of the $(1\bar{1}1)[110]_{c\text{-}CrN}||(0002)[11\bar{2}0]_{w\text{-}AlN}$ in the 1st block, which possesses a relatively low mismatch structure (e.g., in Fig. 10b 11 $(\bar{1}11)$ c-CrN planes match with 10 $(1\bar{1}00)$ w-AlN planes). These can be easily found at the region close to the substrate (Fig. 10a, lower part). However, a variety of different w-AlN/c-CrN interface structures can be found at the location far from the substrate (from the 5th block on). For example, Fig. 10c shows a new type of c-CrN/w-AlN interface structure (at the 8-AlN layer) with an orientation relationship of $(1\bar{1}00)_{w\text{-}AlN}||(2\bar{2}0)_{c\text{-}CrN}$ and $(0002)_{w\text{-}AlN}||(002)_{c\text{-}CrN}$. In Fig. 10d, the w-AlN grain grows along the [0001] direction, and the

50

upper cubic-CrN grows along the CrN [001] direction and the tilt angle between (0002) and (002) planes is around 3°. In Fig. 10e, the *w*-AlN (10$\overline{1}\overline{1}$) plane is parallel with the cubic CrN (002) (viewed along [11$\overline{2}$3]$_{w\text{-AlN}}$ and [110]$_{c\text{-CrN}}$). The misorientation angle between the (10$\overline{1}\overline{1}$)$_{w\text{-AlN}}$ and (200)$_{c\text{-CrN}}$ planes is around 2°. The *w*-AlN/*c*-CrN interface structure can generally be classified into a low-mismatched interface mode and high-mismatched interface mode. The low-mismatched interface mode with the higher distance of two misfit dislocations, e.g., 11 ($\overline{1}$11) planes match with 10 (1$\overline{1}$00) planes in Fig.10b. The high-mismatched interface mode have the lower distance of two misfit dislocations, e.g., 6 (002) planes match with 5 (0002) planes in Fig. 10c, 8 (1$\overline{1}$1) planes match with 7 (1$\overline{1}$00) planes in Fig. 10d, or 4 (020) planes match with 3 (1$\overline{1}$00) planes in Fig. 10e.

To sum up, the c-AlN deposited on cubic CrN layer will form the typical coherent interface structures. However, the w-AlN layer deposited on cubic CrN layer may form the different interface structure (low-mismatched *c*-CrN/*w*-AlN interface and high-mismatched *c*-CrN/*w*-AlN interface). Considering the interface structure changes will significantly affect the interface energy of w-AlN and the existence of competitive growth between the two phases of AlN. Change of the interface structure may also be the influencing factor of the phase stability change in the position far away from the substrate area (as shown in Sec. 3.3). We will explain in detail the effects of the interface structure in the discussion section 4.2.1.
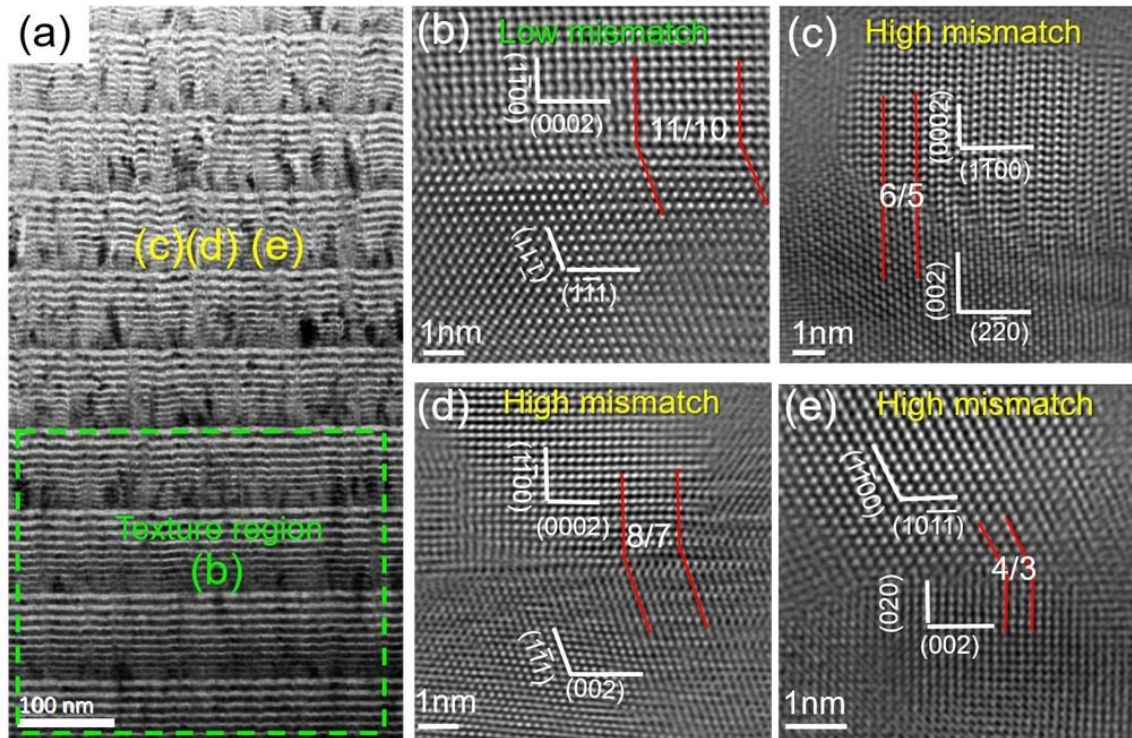
Fig. 10 (a) Low-magnification bright-field image, where the locations for figures (b)-(e) are labeled. HRTEM image of the *w*-AlN/*c*-CrN interface from (b) 2nd block. (c), 10th block, (d) 7th block and (e) 9th block, showing the relation between the *w*-AlN and *c*-CrN with different interface orientations. The grain growth direction is from *c*-CrN to *w*-AlN (in the image bottom to top). Red lines show the lattice mismatch at *w/c* interfaces.

4. Discussion

4.1 Preferred growth-orientation in multilayers

In this section, we mainly discuss the *w*-AlN and *c*-AlN growth-orientation in multilayers. Previous studies reported on some typical textures in TMNs (transition metal nitride) multilayer films, such as the cubic <111> growth-direction [10, 20, 21] and the wurtzite <0001> growth direction [6, 22-26]. But the texture formation mechanism of multilayer films has hardly been addressed to date. According to our dark-field results (Fig. 3c and Fig. 6d), a strong texture is observed near the substrate area. However, the texture gradually randomizes with increasing thickness, starting from the 5th block on.

The preferred growth orientation (texture) in monolithically grown thin films can often be explained by surface energy and strain energy minimization [27-31], next to kinetically driven effects [32]. For example in c-TiN thin films, the strain energy minimization dominates the texture evolution for thicker films, while the surface energy minimization dominates the texture evolution for thinner films [29]. The strain energy in multilayers will mainly depend on the interface structure and thus the induced coherency (or mismatched) strains. The $\{111\}<110>_{c\text{-}CrN}$ ‖$\{0001\}<11\bar{2}0>_{w\text{-}AlN}$ interface is semi-coherent, which very easily fully relaxes [33]. Moreover, the maximum layer thickness of c-AlN only exists in the 1-AlN and 2-AlN layers (in the substrate near regions, which are highly textured), having thicknesses below 2 nm. Hence, the strain energy is not the main factor that affects the w-AlN and c-AlN growth-orientation in the strongly textured areas (close to the substrate).

As discussed before, also some highly mismatched interfaces can be found far away from the substrate regions (as shown in Fig. 10b-e). The low mismatch $\{111\}‖\{0001\}$ interface has a lower density of broken bonds (related to the chemical energy) due to perfect crystallographic match of the cubic and wurtzite close packed planes, and a lower lattice mismatch (related to the [misfit] dislocation energy). Hence, the semi-coherent $\{111\}‖\{0001\}$ interface is expected to possess a lower interfacial energy as compared to those highly mismatched w-AlN/c-CrN interfaces (observed in the area above the 5th block). Such low mismatch $\{111\}‖\{0001\}$ interfaces dominate the w-AlN/c-CrN growth-orientation near the substrate area. This leads to the cubic AlN also maintaining the <111> growth-orientation.

The grain orientation changes from c-AlN (111) and w-AlN (0001) to other growth-orientations will greatly minimize surface energies. Holec *et al.* [34] presented first-principles calculations on the surface energies of cubic (rock-salt, B1) and wurtzite (B4) AlN allotropes, which are summarized in **Table 1**. The w-AlN or c-AlN in <0001> or <111> orientations exhibit the largest surface energies. Hence, the changes of growth-orientation will greatly minimize the surface energy, i.e. 220 meV/Å2 energy difference from $<0001>_{w\text{-}AlN}$ to $<1\bar{1}00>_{w\text{-}AlN}$ growth-orientation (energy subtraction), and 327 meV/Å2 energy difference from $<111>_{c\text{-}AlN}$ to $<100>_{c\text{-}AlN}$ growth-orientation. Furthermore, the interfaces in the textured area near the substrate are flat and smooth, thus further improving the match of the w-AlN (0001) and CrN (111) planes. The incoming particle flux (from the target) is nearly perpendicular to the substrate surface, hence perpendicular to the growth plane. However, surface roughening with the wavy-like morphology, which may originate from diffusion, relaxation and intermixing effects, develops (cf. Fig. 3) further away from the substrate (above the 4th block). Part of the

incident particle flux is no longer perpendicular to the CrN (111) plane. This increases the probability of *w*-AlN growth on other *c*-CrN lattice planes. Although this will increase the *w*-AlN/*c*-CrN interface energy (as compared with the low mismatch {111}/{0001} interface), the AlN surface energy will be greatly reduced. This may explain the presence of some highly mismatched interface structures in the area far away from the substrate (as shown in Fig. 10c-e).

	cubic AlN		wurtzite AlN
(111)[a]	410 meV/Å2	(0001)[a]	365 meV/Å2
(110)[a]	194 meV/Å2	(1$\bar{1}$00)[a]	145 meV/Å2
(100)[a]	83 meV/Å2	(11$\bar{2}$0)[a]	243 meV/Å2
		(10$\overline{11}$)[b]	287 meV/Å2

Table 1. Energies of different surfaces in cubic and wurtzite AlN

[a] Reference [36]

[b] Present work

4.2 Metastable *c*-AlN
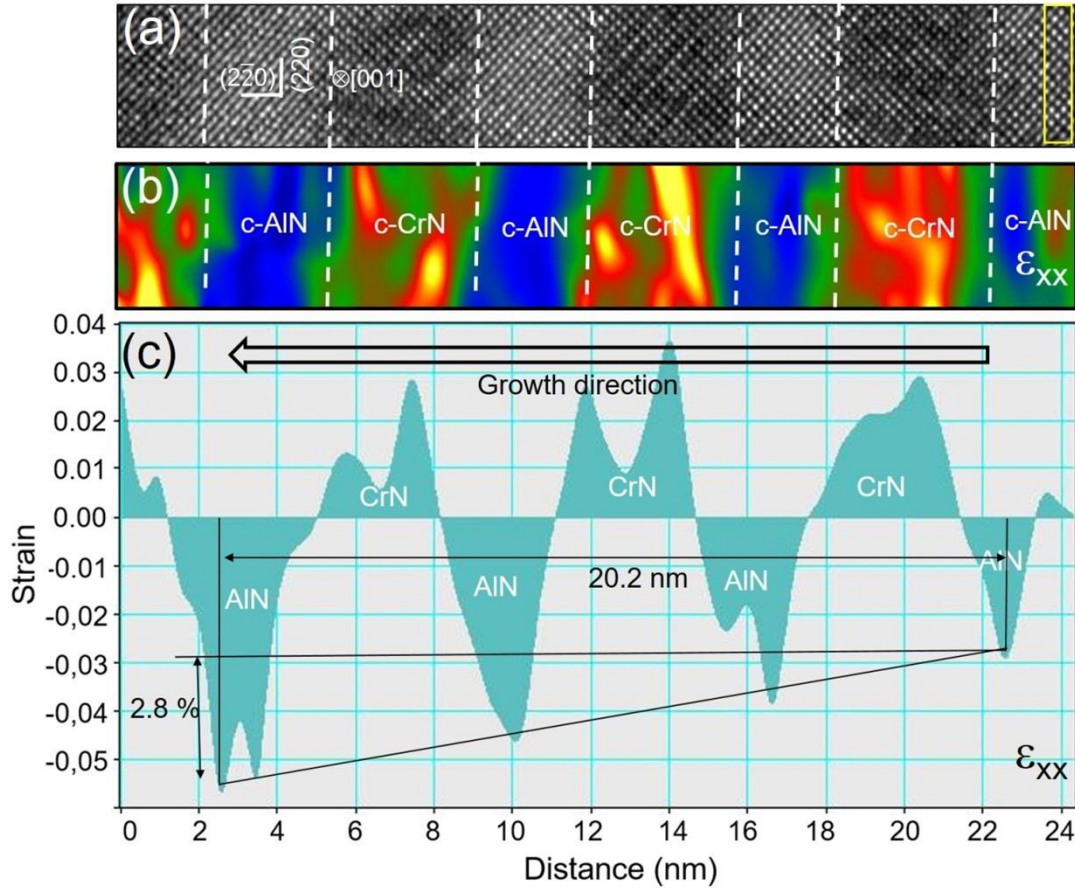
4.2.1 Effect of the AlN layer thickness

Fig.11. (a) HRTEM image of cubic/cubic type-B columnar grain in the area far away from the substrate (10th block), with the growth-direction along the [1$\overline{1}$0] direction from right to left and viewed along the [001] direction. AlN is cubic structured from the 2nd till the 5th layer. (b) corresponding in-plane strain (ε_{xx}) map. The yellow marked box in (a) is used for the reference. (c) profile of in-plane strain (entire colored maps region) along the growth-direction.

Cubic AlN (B1 structure) is a metastable phase and as such has internal bulk energy higher as compared to the thermodynamically stable wurtzite AlN. However, as a result of epitaxial stabilization, c-AlN can be present in CrN/AlN multilayers, which result from a different contribution of the coherent strain energy, surface energy and interfacial energy between AlN and c-CrN for cubic and wurtzite AlN polymorphs.

Strain energy is one of the major contributions to the overall energetics, significantly determining the phase constitution in AlN stabilized multilayer epitaxial systems [7, 11, 35-37]. The distribution of the relative strain in the bilayer period systems was previously reported [38-40], indicating homogeneous strains along the growth direction. However, the strain distribution in our bilayer-gradient CrN/AlN multilayer remains unknown. Figure 11a shows the HRTEM image of cubic/cubic columnar grain with <110> growth-direction, where the

brighter areas are 2-AlN to 5-AlN layers in the 10th block. Figure 11b is a corresponding ε_{xx} strain map. The compressive strains within the AlN layers ($\varepsilon_{xx}<0$) and the tensile strains within the CrN layers ($\varepsilon_{xx}>0$) are revealed. A strain profile acquired by integrating ε_{xx} in Fig. 11b along the vertical y axis is shown in Fig. 11c. Apparently, strains are not uniformly distributed. We found that the first layer CrN has 2%-2.8% tensile strain (ε_{xx}) as compared with the reference area (2-c-AlN layer), which is close to the calculated 2.4% tensile misfit strain ($\varepsilon = \frac{a_{CrN} - a_{AlN}}{a_{CrN}} =$ 2.4%, a_{CrN} =4.14 Å (JCPDS 11-0065) and a_{AlN}=4.04 Å(JCPDS 46-1200)). More importantly, increasing the AlN layer thickness from 2-AlN to 5-AlN layer increases the local strain by 2.8%. Furthermore, we also notice that the tensile strain in CrN layer decreases along the growth direction, although the thickness of the c-CrN layers remains constant. Note that no misfit dislocations were found in HRTEM image (Fig.11a), which means c-CrN/c-AlN interfaces are fully in a coherent state. For 4-AlN layer, the out-of-plane compressive strain increase will increase the in-plane tensile strain (due to the Poisson's tension). Thus, the in-plane tension of the CrN layer will also increase in order to maintain the full coherent state. Finally, the last layer CrN have the higher out-plane contraction and show the tensile strain decreasing as the c-AlN layers become thicker as in Fig. 11c.

Our strain map confirms the existence of strains gradient in the cubic/cubic coherent interface structure. In the w-AlN/c-TiN semi-coherent {0001}||{111} interface, the misfit strain is fully relaxed by dislocation glide in cubic {111}<110> slip systems and/or in the w-AlN {0001}<11$\bar{2}$0> slip system [33]. The close relation between TiN and CrN suggests that similar behaviors may be valid in the w-AlN/c-CrN semi-coherent {0001}||{111} and other highly-mismatched w-AlN/c-CrN interfaces. Hence, the layer thickness-related coherency strain in the c-AlN/c-CrN is much higher than within the w-AlN/c-CrN superlattice system. Consequently, the phase transformation from cubic AlN to wurtzite AlN reduces the coherency strain and strain energy [3, 7, 11, 13].

4.2.2 Mechanism of the orientation-dependent critical thickness for c-AlN layers

In this section, we present a simple total energy model, which can be used to justify the observed critical thicknesses and eventually also to predict them. The total energy, E_T, per unit (surface/interface/section) area can be expressed as:

$$E_T^{c,w} = t \cdot (E_{Strain}^{c,w} + E_B^{c,w}) + \gamma_I^{c,w} + \gamma_S^{c,w}. \tag{1}$$

$E_{Strain}^{c,w}$ is the (coherency) strain energy density (per unit volume) related to the lattice mismatch, $\gamma_I^{c,w}$ is the per unit area interface energy (including the effect of broken bonds due to an imperfect crystallographic match, interface dislocations and inhomogeneous chemistry), and $\gamma_S^{c,w}$ is the per unit area surface energy (penalty due to broken bonds at the free surface). c and w superscripts refer to the cubic and wurtzite modification of AlN. $E_B^{c,w}$ is the bulk (chemical) energy density (per unit volume), $E_B^c > E_B^w$ reflecting the metastability of the cubic phase with respect to the stable wurtzite phase. t is the AlN layer thickness. The critical thickness (maximum thickness of c-AlN to have lower total energies than w-AlN) is defined by $E_T^c = E_T^w$:

$$t = \frac{\gamma_I^w - \gamma_I^c + \gamma_S^w - \gamma_S^c}{E_{Strain}^c - E_{Strain}^w + E_B^c - E_B^w}. \tag{2}$$

Note that the strain energy, interface energy and surface energy are orientation-dependent. For the w-AlN interface energy, γ_I^w, it is lower for the low mismatch {111}/{0001} interface than for the high mismatch c/w interfaces (as discussed in section 4.1). However, the c/c coherent interface energy is much smaller (no broken bonds, no interface dislocations) than the c/w semi-coherent interface energy.

For strain energy, the previous reports show that the obviously elastic modulus anisotropy were only found in cubic (rocksalt) AlN [41, 42]. However, the wurtzite AlN is isotropic [41]. Thus, we mainly consider the strain energy anisotropy of cubic (rocksalt) AlN. The strain energy (E_{Strain}) density corresponding to the two-dimensional bi-axial strain state (ε) for cubic materials can be expressed as [43]:

$$E_{Strain} = \frac{1}{2}(\sigma_{11} + \sigma_{22})\varepsilon = M\varepsilon^2$$

σ_{11} and σ_{22} are biaxial stress. ε is the biaxial strain. M is the biaxial modulus of the material. Hence, the strain energy is orientation-dependent, which is due to the biaxial modulus. For grains in the [111] growth orientation the biaxial elastic modulus $M_{[111]}$ is given by [44]

$$(3)$$

$$M_{[111]} = \frac{6C_{44}(C_{11} + 2C_{12})}{C_{11} + 2C_{12} + 4C_{44}} \tag{4}$$

For grains in the [001] growth orientation the biaxial elastic modulus is given by [44]

$$M_{[001]} = C_{11} + C_{12} - \frac{2C_{12}^2}{C_{11}} \tag{5}$$

For grains in the [01$\bar{1}$] growth orientation the biaxial elastic modulus is given by [44]

$$M_{[01\bar{1}]} = \frac{(2C_{11} + 6C_{12} + 4C_{44})}{4} - \frac{(2C_{11} + 2C_{12} - 4C_{44})}{4} \frac{(2C_{11} + 3C_{12} - 4C_{44})}{(C_{11} + C_{12} + 2C_{44})} \tag{6}$$

For B1-AlN, Holec et al. [42] showed that the elastic constants: C_{11}=418 GPa, C_{12}=169 GPa and C_{44}= 308 GPa, respectively. Then, $M_{[111]}$=705 GPa, $M_{[001]}$ =450 GPa and $M_{[01\bar{1}]}$ =772 GPa can be obtained accordingly. Thus, the strain energy density for the three orientations follows $E_{strain}^{001} < E_{strain}^{111} < E_{strain}^{011}$. This further demonstrates that c-AlN with <100> growth orientation has much lower strain energy which in turn increases the cubic phase stability.

Some simulations and experiments demonstrated the impact of surface energy on structural stability, which is thus a decisive parameter for the film microstructure and makes a non-negligible contribution to the overall energetic balance, Eq. ((v), [13, 45-49]. Because of the coherent interface structure of c-AlN/c-CrN, the growth-orientation of c-AlN and CrN are always the same. Hence, from the *c*-CrN/*w*-AlN orientation observation, we can estimate the difference in surface energies of *c*-AlN and *w*-AlN. According to our observation of *c*-CrN/*c*-AlN and *c*-CrN/*w*-AlN growth-orientations, the energy-controlled competitive nucleation and growth process between the cubic AlN and wurtzite AlN on the *c*-CrN surface may exist, see also **Table 1**.

The simulation results show that the surface energy of the top facet favors the wurtzite phase in <111>||<0001> growth orientation, i.e. $\gamma_S^c - \gamma_S^w$=45 meV/Å2(see **Table 1**). For the other *c*-CrN/*w*-AlN orientation case, i.e., the <110>||<1$\bar{1}$00> growth-orientation in Fig. 10c, the situation is almost the same, i.e. $\gamma_S^c - \gamma_S^w$=49 meV/Å2 (see **Table 1**). But for the cubic <100> growth-orientation as shown in Figs. 10d and 10e, the surface energies of the top facet favor the cubic phase formation. The cubic <100> orientation case exhibits the much lower surface energy of $\gamma_{S(100)}^c$=83 meV/Å2 compared with their wurtzite counterparts, i.e. $\gamma_{S(0001)}^w$=365 meV/Å2 or $\gamma_{S(10\bar{1}1)}^w$=287 meV/Å2 (see **Table 1**). For the cubic AlN layer the <100> growth-orientation has much lower surface energy than the <110> and <111>, which have benefit to minimize the total energies. Furthermore, the lower surface energies of cubic AlN decrease the nucleation energies and promote the crystal growth. In contrast, wurtzite AlN (1$\bar{1}$01) and (0001) growth-plane have much higher surface energies, which increase the *w*-AlN nucleation barrier and retard *w*-AlN crystal growth.

Based on these considerations, the orientation-dependent critical layer thickness for c-AlN can be qualitatively explained by the anisotropy of interface energy, strain energy and surface

energy. These three energies determine the total energies for combinations with c-AlN or w-AlN layers of different orientations. The higher total energy of w-AlN combinations retards the w-AlN crystal growth. In contrast, the lower total energy of c-AlN combinations promotes the c-AlN crystal growth, allowing for larger critical layer thicknesses of c-AlN before the thermodynamically stable w-AlN wins.

4.2.3 Larger critical thickness for c-AlN layers in <110> direction than in <111> direction

In Sec. 4.2.2, we discussed the origins of orientation-dependent critical thicknesses of the c-AlN layers due to the interface energy, strain energy and surface energy anisotropy. According to our statistic results, the critical thickness of the c-AlN layers is larger in <110> direction than in the <111> direction (as shown in Fig.8). Due to the similar surface energy differences in <110>∥<1$\overline{1}$00> and <111>∥<0001> direction ($\gamma_S^c - \gamma_S^w$ =45 meV/Å2 in <111>∥<0001> direction and $\gamma_S^c - \gamma_S^w$ =49 meV/Å2 in <110>∥<1$\overline{1}$00>), their contribution to the total energy is minimal. However, c-AlN strain energy in <110> direction is higher than <111> direction. Hence, the AlN total energies in the <111> and <110> growth-orientations will mainly depend on their interface energy and the strain energy, which requires simulation to compare the c-AlN stability in <111> and <110> growth-orientations.

Based on our extensive HRTEM observations, the *c*-CrN <111> growth-orientation has a specific interface structure with wurtzite AlN, which is a typical *c*{111}<110>∥*w*{0001} <11$\overline{2}$0> semi-coherent interface. However, for the *c*-CrN <110> and <100> growth-orientation, other types of *c*-CrN/*w*-AlN interface structures with higher lattice mismatch are also present. Some unusual interfaces, such as {110}<110>$_{c\text{--CrN}}$∥{1 $\overline{1}$ 00}<11 $\overline{2}$ 0>$_{w\text{-AlN}}$,{100}<100>$_{c\text{—CrN}}$ ∥{10$\overline{1}$ $\overline{1}$}<11$\overline{2}$3>$_{w\text{-AlN}}$ and {100}<100> $_{c\text{--CrN}}$ ∥{10$\overline{1}$ $\overline{1}$}<11$\overline{2}$3>$_{w\text{-AlN}}$, are also observed far away from the substrate area (see Figs. 10c-e). Some of the above interface orientation relationships have been already reported in other systems, i.e. AlN/TiN {0001}∥{100} [50], AlN/VN {110}∥{1$\overline{1}$00} [51], and TiN/ZrAlN {110}∥{1$\overline{1}$00} [46]. The simulated results of the reported interface energy values of other nitride systems, *c*-TiN/*w*-AlN and *c*-ZrN/*w*-AlN [46], show that the *c*-{110}∥*w*-{1$\overline{1}$00} interface energy is much higher than that of the *c*-{111}∥ *w*-{0001} interface.

With DFT (for details, see supplementary material) we evaluated the evolution of total energies (including the strain and interface energies) of w-AlN and c-AlN with two different orientations as a function of their layer thickness. For these calculations, no misfit dislocations were considered. Figures 12a and 12b are the interface orientations during the growth, while Figs. 12c and 12d show the calculated total energy differences of cubic-wurtzite AlN ΔE_T, i.e. $\Delta E_T = E_T^c - E_T^w$, with two different orientations. In Eq. (2), the critical thickness (maximum thickness of c-AlN to be stable) is defined by c-CrN and w-AlN total energy. Hence, the dashed line position $(\Delta E_T = 0)$ is the simulation value of the c-AlN critical layer thickness. Figure 12d shows that the critical thickness of the metastable c-AlN layer is larger in the <110> growth-orientation with respect to the <111> orientation. This is in agreement with our HRTEM observations (please note that our DFT results should rather be interpreted qualitatively than quantitatively) of thicker c-AlN layers in this direction, $t_{111} < t_{110}$. The combination of HRTEM and DFT completely reveals the effect of crystallographic orientation on the critical layer thickness of c-AlN.
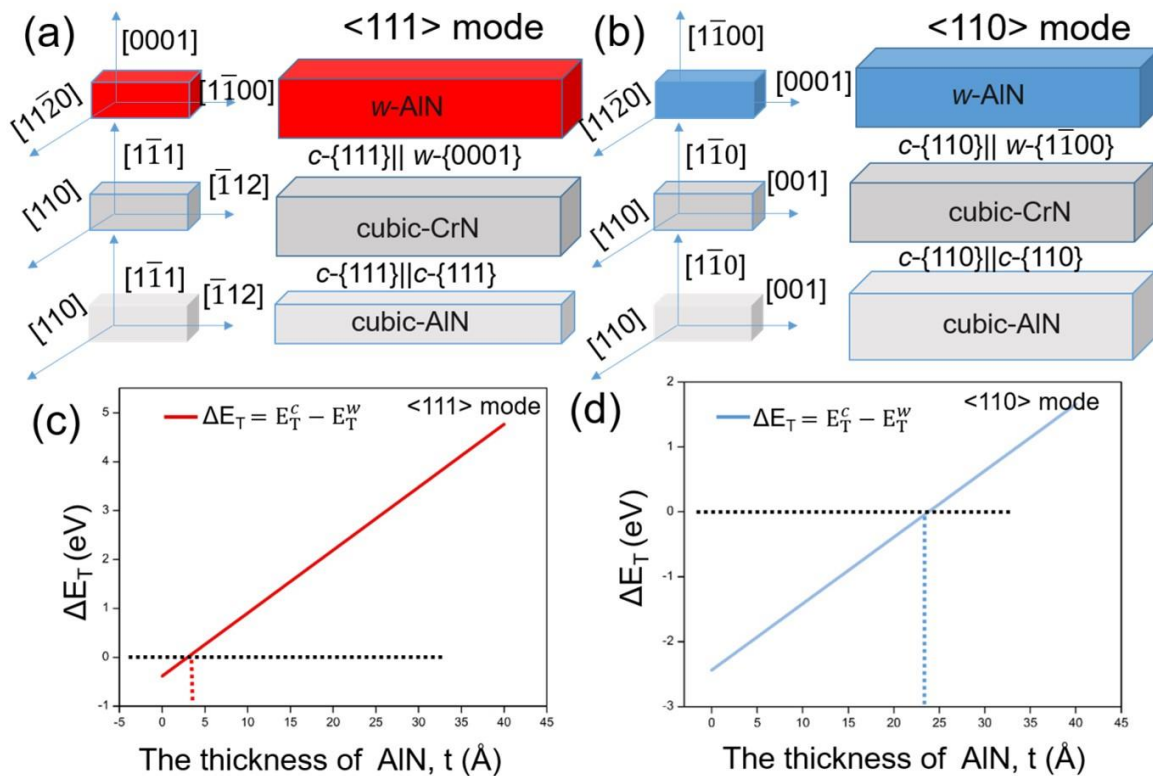

Fig.12. Schematic of orientation relationships in cubic/wurtzite and cubic/cubic interface structure in the (a) <111>, and (b) <110> growth modes. Calculated total energy difference as a function of the AlN layer thickness in (c) <111> (the red line), and (d) <110> modes (the blue

line). The dashed line position corresponds to the critical phase transition layer thickness. The total energy is evaluated per unit interface pattern, which 1 atom in the <111> mode and 2 atoms in the <110> mode.

5. Conclusions

The cross-sectional microstructure of a multilayer with different AlN layer thicknesses was studied in detail using conventional TEM and C_S-corrected TEM. From the SAED patterns and dark-field image investigations, the $\{111\}_{c\text{-CrN}}||\{111\}_{c\text{-AlN}}$ and $\{111\}_{c\text{-CrN}}||\{0001\}_{w\text{-AlN}}$ textures can be observed from the first to the fourth repeated block (each of the 21 blocks consists of 10 bilayers composed of 4-nm-thin CrN combined with either 1, 2, 3, 4, 5, 6, 7, 8, 9, and 10 nm thin AlN layers).

By observing the atomically-resolved images of c-CrN/c-AlN superlattices, the critical layer thickness of cubic AlN in different thin film positions is revealed. Near the substrate area (the first to the fourth block), the critical thickness for stabilizing cubic AlN is about 1.0 nm to 2.0 nm. However, in the region far from the substrate, the critical thickness of cubic AlN ranges from 2.0 nm to 4.1 nm. The c-CrN/w-AlN interface structure with a high mismatch can be found in these areas far away from the substrate. According to our HRTEM observations and statistical analysis, the c-AlN/c-CrN grains with the <111> growth-orientation show a smaller critical layer thickness for c-AlN, while at the <100> and <110> growth-orientations this critical thickness is larger. The origin for this is a combined effect of the growth plane surface energy, strain energy anisotropy and the change of c-CrN/w-AlN interface structures. Our results clearly show that in addition to surface and strain energy also the different possible interface structure geometries need to be considered.

Acknowledgements

References

[1] J. Lin, J.J. Moore, B. Mishra, M. Pinkas, W.D. Sproul, Nano-structured CrN/AlN multilayer coatings synthesized by pulsed closed field unbalanced magnetron sputtering, Surface and Coatings Technology 204(6) (2009) 936-940.

[2] P.H. Mayrhofer, C. Mitterer, L. Hultman, H. Clemens, Microstructural design of hard coatings, Progress in Materials Science 51(8) (2006) 1032-1114.

[3] M. Bartosik, J. Keckes, P.O.Å. Persson, H. Riedl, P.H. Mayrhofer, Interface controlled microstructure evolution in nanolayered thin films, Scripta Materialia 123(Supplement C) (2016) 13-16.

[4] J.-K. Park, Y.-J. Baik, The crystalline structure, hardness and thermal stability of AlN/CrN superlattice coating prepared by D.C. magnetron sputtering, Surface and Coatings Technology 200(5) (2005) 1519-1523.

[5] M. Schlögl, B. Mayer, J. Paulitsch, P.H. Mayrhofer, Influence of CrN and AlN layer thicknesses on structure and mechanical properties of CrN/AlN superlattices, Thin Solid Films 545(Supplement C) (2013) 375-379.

[6] Y.Y. Wang, M.S. Wong, W.J. Chia, J. Rechner, W.D. Sproul, Synthesis and characterization of highly textured polycrystalline AlN/TiN superlattice coatings, Journal of Vacuum Science & Technology A: Vacuum, Surfaces, and Films 16(6) (1998) 3341-3347.

[7] I.W. Kim, Q. Li, L.D. Marks, S.A. Barnett, Critical thickness for transformation of epitaxially stabilized cubic AlN in superlattices, Applied Physics Letters 78(7) (2001) 892-894.

[8] J. Lin, J.J. Moore, B. Mishra, M. Pinkas, X. Zhang, W.D. Sproul, CrN/AlN superlattice coatings synthesized by pulsed closed field unbalanced magnetron sputtering with different CrN layer thicknesses, Thin Solid Films 517(20) (2009) 5798-5804.

[9] D. Chen, X.L. Ma, Y.M. Wang, Thickness-dependent structural transformation in the AlN film, Acta Materialia 53(19) (2005) 5223-5227.

[10] J. Lin, N. Zhang, Z. Wu, W.D. Sproul, M. Kaufman, M. Lei, J.J. Moore, Thick CrN/AlN superlattice coatings deposited by the hybrid modulated pulsed power and pulsed dc magnetron sputtering, Surface and Coatings Technology 228(Supplement 1) (2013) S601-S606.

[11] A. Madan, I.W. Kim, S.C. Cheng, P. Yashar, V.P. Dravid, S.A. Barnett, Stabilization of Cubic AlN in Epitaxial AlN/TiN Superlattices, Physical Review Letters 78(9) (1997) 1743-1746.

[12] J.P. Schaffer, The Science and Design of Engineering Materials Irwin, Chicago, 1995.

[13] V. Chawla, D. Holec, P.H. Mayrhofer, Stabilization criteria for cubic AlN in TiN/AlN and CrN/AlN bi-layer systems, Journal of Physics D: Applied Physics 46(4) (2013) 045305.

[14] G. Kresse, J. Furthmüller, Efficiency of ab-initio total energy calculations for metals and semiconductors using a plane-wave basis set, Computational Materials Science 6(1) (1996) 15-50.

[15] G. Kresse, J. Furthmüller, Efficient iterative schemes for ab initio total-energy calculations using a plane-wave basis set, Physical Review B 54(16) (1996) 11169-11186.

[16] G. Kresse, D. Joubert, From ultrasoft pseudopotentials to the projector augmented-wave method, Physical Review B 59(3) (1999) 1758-1775.

[17] J.P. Perdew, K. Burke, M. Ernzerhof, Generalized Gradient Approximation Made Simple, Physical Review Letters 77(18) (1996) 3865-3868.

[18] L. Zhou, F. Körmann, D. Holec, M. Bartosik, B. Grabowski, J. Neugebauer, P.H. Mayrhofer, Structural stability and thermodynamics of CrN magnetic phases from ab initio calculations and experiment, Physical Review B 90(18) (2014) 184102.

[19] D. Holec, P.H. Mayrhofer, Surface energies of AlN allotropes from first principles, Scr Mater 67(9) (2012) 760-762.

[20] M.-S. Wong, G.-Y. Hsiao, S.-Y. Yang, Preparation and characterization of AlN/ZrN and AlN/TiN nanolaminate coatings, Surface and Coatings Technology 133-134(Supplement C) (2000) 160-165.

[21] P. Yashar, S.A. Barnett, J. Rechner, W.D. Sproul, Structure and mechanical properties of polycrystalline CrN/TiN superlattices, Journal of Vacuum Science & Technology A: Vacuum, Surfaces, and Films 16(5) (1998) 2913-2918.

[22] F. Mei, N. Shao, L. Wei, Y. Dong, G. Li, Coherent epitaxial growth and superhardness effects of c-TiN/h-TiB2 nanomultilayers, Applied Physics Letters 87(1) (2005) 011906.

[23] M. Wen, H. Huang, K. Zhang, Q. Meng, X. Li, L. Kong, C. Hu, W. Zheng, The AlN layer thickness dependent coherent epitaxial growth, stress and hardness in NbN/AlN nanostructured multilayer films, Surface and Coatings Technology 235(Supplement C) (2013) 367-375.

[24] J. Xu, L. Yu, S. Dong, I. Kojima, Structure transition of BN layers and its influences on the mechanical properties of AlN/BN nanomultilayers, Thin Solid Films 516(23) (2008) 8640-8645.

[25] A. Karimi, G. Allidi, R. Sanjines, Relative orientation of the constituents on the degree of crystallographic coherence in AlN/TiN superlattices, Surface and Coatings Technology 201(7) (2006) 4062-4067.

[26] J.E. Sundgren, Structure and properties of TiN coatings, Thin Solid Films 128(1) (1985) 21-44.

[27] J.I. Jeong, J.H. Hong, J.S. Kang, H.J. Shin, Y.P. Lee, Analysis of TiC and TiN films prepared by an arc-induced ion plating, Journal of Vacuum Science & Technology A: Vacuum, Surfaces, and Films 9(5) (1991) 2618-2622.

[28] M. Kobayashi, Y. Doi, TiN and TiC coating on cemented carbides by ion plating, Thin Solid Films 54(1) (1978) 67-74.

[29] J.P. Zhao, X. Wang, Z.Y. Chen, S.Q. Yang, T.S. Shi, X.H. Liu, Overall energy model for preferred growth of TiN films during filtered arc deposition, Journal of Physics D: Applied Physics 30(1) (1997) 5.

[30] U.C. Oh, J.H. Je, Effects of strain energy on the preferred orientation of TiN thin films, Journal of Applied Physics 74(3) (1993) 1692-1696.

[31] D. Gall, S. Kodambaka, M.A. Wall, I. Petrov, J.E. Greene, Pathways of atomistic processes on TiN(001) and (111) surfaces during film growth: an ab initio study, Journal of Applied Physics 93(11) (2003) 9086-9094.

[32] I. Petrov, P.B. Barna, L. Hultman, J.E. Greene, Microstructural evolution during film growth, Journal of Vacuum Science & Technology A 21(5) (2003) S117-S128.

[33] A. Moatti, J. Narayan, High-quality TiN/AlN thin film heterostructures on c-sapphire, Acta Materialia 145 (2018) 134-141.

[34] D. Holec, P.H. Mayrhofer, Surface energies of AlN allotropes from first principles, Scripta Materialia 67(9) (2012) 760-762.

[35] I. Petrov, E. Mojab, R.C. Powell, J.E. Greene, L. Hultman, J.E. Sundgren, Synthesis of metastable epitaxial zinc-blende-structure AlN by solid-state reaction, Applied Physics Letters 60(20) (1992) 2491-2493.

[36] I.W. Kim, A. Madan, M.W. Guruz, V.P. Dravid, S.A. Barnett, Stabilization of zinc-blende cubic AlN in AlN/W superlattices, Journal of Vacuum Science & Technology A: Vacuum, Surfaces, and Films 19(5) (2001) 2069-2073.

[37] N. Li, S.K. Yadav, J. Wang, X.-Y. Liu, A. Misra, Growth and Stress-induced Transformation of Zinc blende AlN Layers in Al-AlN-TiN Multilayers, Scientific Reports 5 (2015) 18554.

[38] G.P. Dimitrakopulos, P. Komninou, T. Kehagias, S.L. Sahonta, J. Kioseoglou, N. Vouroutzis, I. Hausler, W. Neumann, E. Iliopoulos, A. Georgakilas, T. Karakostas, Strain relaxation in AlN/GaN heterostructures grown by molecular beam epitaxy, physica status solidi (a) 205(11) (2008) 2569-2572.

[39] P. Bayle, T. Deutsch, B. Gilles, F. Lançon, A. Marty, J. Thibault, Quantitative analysis of the deformation and chemical profiles of strained multilayers, Ultramicroscopy 56(1) (1994) 94-107.

[40] X. Gu, Z. Zhang, M. Bartosik, P.H. Mayrhofer, H. Duan, Dislocation densities and alternating strain fields in CrN/AlN nanolayers, Thin Solid Films 638(Supplement C) (2017) 189-200.

[41] A.J. Wang, S.L. Shang, Y. Du, Y. Kong, L.J. Zhang, L. Chen, D.D. Zhao, Z.K. Liu, Structural and elastic properties of cubic and hexagonal TiN and AlN from first-principles calculations, Computational Materials Science 48(3) (2010) 705-709.

[42] D. Holec, M. Friák, J. Neugebauer, P.H. Mayrhofer, Trends in the elastic response of binary early transition metal nitrides, Physical Review B 85(6) (2012) 064101.

[43] J.A. Floro, C.V. Thompson, R. Carel, P.D. Bristowe, Competition between strain and interface energy during epitaxial grain growth in Ag films on Ni(001), Journal of Materials Research 9(9) (2011) 2411-2424.

[44] W.D. Nix, Mechanical properties of thin films, Metallurgical Transactions A 20(11) (1989) 2217.

[45] F. Reichel, L.P.H. Jeurgens, G. Richter, P.A. van Aken, E.J. Mittemeijer, The origin of high-mismatch orientation relationships for ultra-thin oxide overgrowths, Acta Materialia 55(17) (2007) 6027-6037.

[46] K. Yalamanchili, F. Wang, H. Aboulfadl, J. Barrirero, L. Rogström, E. Jiménez-Pique, F. Mücklich, F. Tasnadi, M. Odén, N. Ghafoor, Growth and thermal stability of TiN/ZrAlN: Effect of internal interfaces, Acta Materialia 121(Supplement C) (2016) 396-406.

[47] P.H. Mayrhofer, F.D. Fischer, H.J. Böhm, C. Mitterer, J.M. Schneider, Energetic balance and kinetics for the decomposition of supersaturated Ti1−xAlxN, Acta Materialia 55(4) (2007) 1441-1446.

[48] J.M. McHale, A. Auroux, A.J. Perrotta, A. Navrotsky, Surface Energies and Thermodynamic Phase Stability in Nanocrystalline Aluminas, Science 277(5327) (1997) 788-791.

[49] V. Chawla, D. Holec, P.H. Mayrhofer, The effect of interlayer composition and thickness on the stabilization of cubic AlN in AlN/Ti–Al–N superlattices, Thin Solid Films 565 (2014) 94-100.

[50] X.L. Ma, N. Shibata, Y. Ikuhara, Interface Characterization of AlN/TiN/MgO(001) Prepared by Molecular Beam Epitaxy, Journal of Materials Research 14(4) (2011) 1597-1603.

[51] Q. Li, I.W. Kim, S.A. Barnett, L.D. Marks, Structures of AlN/VN Superlattices with Different AlN Layer Thicknesses, Journal of Materials Research 17(5) (2011) 1224-1231.

Publication II

Surprising large-scale superlattice intermixing triggered by nanoindentation and its effect

Zhuo Chen[1], Yonghui Zheng[1], Lukas Löfler[2], Matthias Bartosik[3], Ganesh Kumar Nayak[2], Oliver Renk[1], David Holec[2], Paul H. Mayrhofer[3], Zaoli Zhang[1]*

1 Erich Schmid Institute of Materials Science, Austrian Academy of Sciences, A-8700 Leoben, Austria

2 Department of Materials Science, Montanuniversität Leoben, A-8700 Leoben, Austria

3 Institute of Materials Science and Technology, TU Wien, A-1060 Vienna, Austria

* Corresponding author: zaoli.zhang@oeaw.ac.at

Abstract

Mechanical properties of nanoscale multilayer coatings are to a large extent governed by the number of interfaces and their characteristics. While for a reduced layer thickness increasing strength and toughness values have been reported, properties degrade for layer thicknesses of just several nanometers. Here we report on an entirely overlooked phenomenon occurring during indentation of nanolayers, presumably explaining the degradation of properties. Nanoindentation, commonly used to determine properties of hard coatings, is found to disrupt and intermix the multilayer structure due to the deformation imposed. Detailed electron microscopy studies and atomistic simulations provide evidence for surprising large-scale intermixing in an epitaxial transition metal nitride superlattice thin film induced by nanoindentation. The formation of a solid solution reduces the interfacial density and leads to a sharp drop in the dislocation density, consequently lowering the achievable strength. Our results also resolve a long-standing issue about the strength softening in multilayer when the layer thickness falls in several nanometer regions.

1. Introduction

It is well-established that the intrinsic length scales of materials determines their performance

[1]. For instance, the classic Hall-Petch strengthening relationship[2, 3] predict "the smaller, the stronger" and accordingly increased strength for an increase of the boundary or interface density. In multilayer thin films, a similar effect can be achieved by lowering the individual layer thicknesses; the increasing number of interfaces enhances the hardness. According to this, numerous efforts have been devoted to design novel multilayers with a small bilayer thickness in order to acquire superior mechanical properties for potential applications. In general, multilayer structures with a bilayer-period thickness of just a few nanometers showed the best combination of hardness, toughness, and elastic modulus [4-11]. For instance, the results of Kim and Lin *et al*. indicate that TMN (transition metal nitride) CrN/AlN superlattice coatings with several nanometer bilayer periods exhibit a 1.6 times higher hardness value compared to their single-layered counterpart coatings[12, 13]. Among the multilayer coatings, the combination of *rs*-TMN (rock-salt transition metal nitride)/*rs*-TMN with an epitaxial superlattice structure shows excellent mechanical properties[7, 13, 14]. The outstanding mechanical properties of the epitaxial superlattice coating are attributed to different effects, including interface coherency strains and the modulus difference [4, 7, 15, 16].

However, the beneficial effect of reduced bilayer thicknesses on mechanical properties is not observed for any layer spacing. It has been reported that, similar to nanocrystalline metals [17-22], the hardness and toughness of the multilayer coating decrease again when the bilayer-period thickness is reduced below a certain critical value, being on the order of a few nanometer[4-11, 13]. For TMNs multilayer, the current understanding for this degradation of properties is that component intermixing already occurs during the thin film deposition and annealing process[5, 23-26]. Thereby the interface density, coherent stress fields and differences in shear modulus diminish, explaining the reduced strength levels measured. This explanation actually suggests that the thin film synthesis process limits the maximum achievable mechanical properties.

However, large-scale component intermixing can be frequently observed also by severe plastic deformation [27-30]. One may thus ask whether the deformation of the multilayer coating during nanoindentation, usually used to evaluate the mechanical properties of multilayers (i.e., hardness and elastic modulus, etc.), may also trigger component intermixing and decrease of the mechanical properties. If so, the measurement itself would affect the property to be measured, which may make the experimentally determined mechanical strength far lower than the intrinsic theoretical properties. Nevertheless, this important issue remains uncertain and has never been addressed before. Since the bilayer thickness of multilayer films below the peak

66

strength is only a few nanometers, detecting potential small-scale structural and composition variations is quite challenging. Clarifying this issue is however mandatory to develop an even stronger multilayer structure. Modern advanced transmission electron microscopy (TEM), cross-sectional focused ion beam (FIB) cutting, and large-scale atomistic simulations allow probing the atomistic origin of material properties and provide the possibility to address such fundamental questions.

In this work, cross-sectional TEM specimens were prepared from the region beneath the indented superlattice (with a bilayer period thickness of 2.5 nm) thin film using FIB milling. Cs-corrected high-resolution TEM was applied to characterize the possible structural and chemical composition changes from the nanoscale to the atomic scale. Combining TEM experimental observations at multiple-scales, we find large-scale compound intermixing in an *rs*-TiN/*rs*-AlN SL beneath the indenter tip, while the SL remains intact in the unaffected region. This indicates that the intermixing process is triggered by the deformation imposed by the indenter. Given the comparably low strain, e.g., in comparison with severe plastic deformation (SPD)[27-29], the observed phenomenon is rather unexpected in this context. Together with atomistic simulations, this intermixing mechanism is validated and explored in detail. Based on these findings, the strength reduction for the smallest bilayer-period thicknesses can be rationalized from the loss of interface fraction and dislocation density caused by the large-scale intermixing. Linking the atomistic insights of our study with the macroscopic mechanical properties of the coating and understanding the intermixing process could contribute to designing even stronger coatings in the future.

2. Methods

2.1 Material fabrication

The TiN/AlN superlattice thin film (~ 1.5 μm total film thickness, TiN ~1.7 nm, AlN ~0.8 nm) was synthesized using an AJA International Orion 5 lab-scale deposition system equipped with a computer-controlled shutter system. The reactive magnetron sputtering process was carried out at 700 °C (substrate temperature) in an Ar/N_2 mixed gas atmosphere with a total pressure of 0.4 Pa and an Ar/N_2 flow ratio of 7 sccm / 3 sccm. To avoid intermixing of the two layer materials via excessive ion bombardment, we applied a rather low bias potential of –40 V (floating potential ~ –20 V) to the MgO (100) substrate, just enough to obtain a dense coating

morphology. The three-inch Ti and two-inch Al target were DC-powered setting constant target currents of 1.0 and 0.5 A, respectively. Further details can be found in Ref [31].

2.2 Material characterization

The nanoindent was performed with an Ultra Micro Indentation System (UMIS, Fischer-Cripps Laboratories) equipped with a cube corner diamond tip using a maximum load of 150 mN. The cross-sectional TEM specimens were prepared using a FEI Quanta 200 3D DBFIB.

A 300 kV field emission TEM (JEOL ARM300F) equipped with double C_S-corrector was used in this study. The high-angle annular dark-field (HAADF) images in the STEM mode use the probe convergence semi-angle of ∼24 mrad. The STEM−HAADF images were taken by an annular dark-field image detector with the inner semi-angle larger than 64 mrad. Two windowless EDXS detectors, each of which has an active area of 100 mm^2, are equipped on a JEM Grand ARM300F microscope, which are very close to the specimen with a high solid angle (1.7 sr).

A 200 kV field emission TEM (JEOL2100F) equipped with an image-side C_S-corrector was used in the HRTEM study, which demonstrates a resolution of 1.2 Å at 200 kV. The aberration coefficients were set to be sufficient small under which the HRTEM images were taken under slightly over-focus conditions (close to the Scherzer defocus). The quantitative determination of the interplanar spacing was carefully carried out by fitting intensity line profiles using a Gaussian function taken from the <100> direction.

The point spectra shown in Fig.3 were recorded under TEM mode with a camera length of 25 cm with a dispersion of 0.2 eV per channel. The spectra were processed in Digital Micrograph (DM version 3.42). Firstly, the background was subtracted using the power-law model. For comparison, the spectra were then aligned to the N-K edge's onset to examine the variations of N-K and T-L edges, such as the chemical shift and shape change.

STEM-EELS spectrum images were acquired using a dispersion of 0.2 eV per channel, a collection semi-angle of 10 mrad, and a convergence semi-angle of 2.5 mrad. The images were aligned to the Ti-L$_3$ peak and processed in DM. Due to a slight energy width difference of Ti-L$_2$ and Ti-L$_3$ between the solid solution Ti$_{1-x}$Al$_x$N and layered TiN/AlN (as seen in Fig.3a). In the end, an energy difference map (Ti-L$_2$-Ti-L$_3$) is obtained using the energy of the Ti-L$_2$ subtracting that of the Ti-L$_3$, which can be used to distinguish the solid solution and layered region (shown in Fig. 3b).

In Fig. 9e, the x-axis (position index) represents different HRTEM images (recorded in 600kx-800kx) in adjacent location with 5 atomic-scale images in each region (as-deposited, deformed SL and solid solution). The dislocation density was obtained according to the following formula, $\rho = N/A$, where ρ is the dislocation density, N is the number of dislocations, A is the area.

2.3 Molecular dynamic simulations

The MD simulations were performed using LAMMPS[32] and an AlTiN MEAM potential[33]. The simulation box was created with Atomsk[34] with initial dimensions of 17.85 nm for the x, y and z axis and contains 592704 atoms. The layer thickness is according to the synthesized films and stacked along the z axis. Before the indentation the energy of the cell was minimized until a difference of 10^{-5} eV was reached. As timestep 0.1 fs was chosen. The indenter was modeled by the LAMMPS fix indent and has spherical shape with a radius of 3.5 nm. This LAMMPS fix creates a virtual object exerting forces on atoms which decay with distance from the indenter center. From its starting position above the surface of the cell, the indenter was moved at a constant rate of 0.28 Å/ps in negative z direction. Every 500 time steps the positions of the cells were stored along.

To track the state of intermixing in different regions during the indentation, the number of the atoms of the two metal species was counted for fixed volumes distributed in the simulation box. At each timestep the relation between Al and Ti was calculated allowing monitoring the transition from binaries to an intermixing within the volume. The occurring dislocations were tracked using the DAX function of OVITO[35]. To be able to apply the function of *rs*-nitrides the function run just on the N sub lattice.

2.4 DFT calculation

We used density functional theory (DFT), implemented in the Vienna Ab initio Simulation Package(VASP) to estimate the barriers for diffusion governing the intermixing process[36, 37]. GGA-PBE[37] was employed for the electron-electron exchange and correlation potential. The potentials used for the element Ti treat semi-core states Ti ($[Ne]3s^2 3p^6 3d^2 4s^2$) as valence. Ion-electron interactions were described using the projector augmented wave method[38] with a plane-wave energy cutoff of 500 eV. Supercells with 64 and 216 lattice sites yielded energies differing less than 1meV/at., hence a supercell of 64 atoms (a 2 x 2 x 2 supercell of conventional rock-salt structure) was used as a defect-free TiN and AlN. For these cubic supercells, a Monkhorst-Pack k-point mesh [39] of 10 x 10 x 10 was used for Brillouin zone sampling with a Methfessel-Paxton [40] smearing of 0.2 eV.

The energy difference between an initial and a transition states of a jump needs to be determined to calculate its jump frequency. Each initial state was completely relaxed with respect to internal coordinates, volume, and shape. We quantitatively determined the transition state with the saddle point along the minimum energy diffusion path by a nudged elastic band (NEB) [41] method as implemented in VASP. The jumps between the initial and final states in both interstitial and vacancy-mediated cases are symmetric, hence we optimize the number of images by assuming the transition state in between. Hence, we tested five images versus three images versus single image NEB calculations for both interstitial and vacancy-mediated TiN barriers. Finding a good agreement (varying number of images lead to barrier height variations within 0.01eV) for the remaining systems we performed a single image NEB calculation.

3. Results

3.1 Large-scale superlattice intermixing during nanoindentation
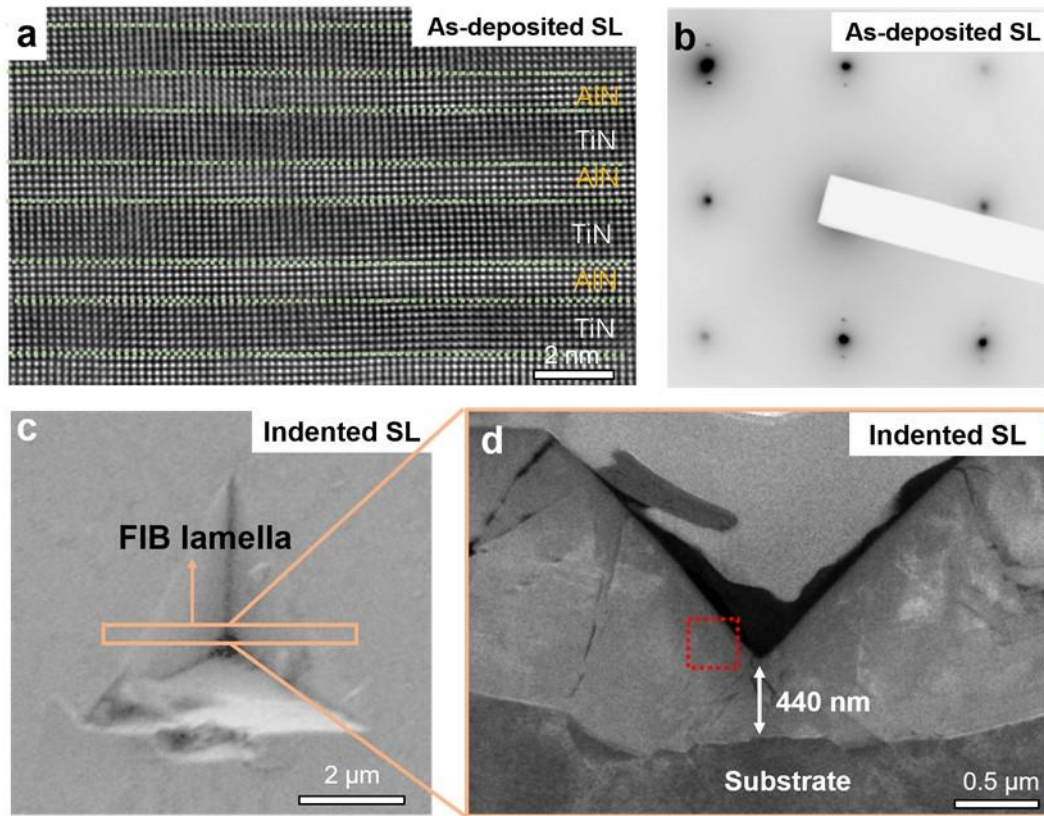
Figure 1 a, Typical HRTEM image of the as-deposited *rs*-TiN/*rs*-AlN SL. **b,** Selected-area electron diffraction pattern of as-deposited SL. **c,** SEM top view of the indented SL. **d,** Cross-sectional low magnification STEM HAADF image of the indented SL, with some cracks visible.

The coating used here is an *rs*-TiN/*rs*-AlN superlattice deposited on a MgO (100) substrate, where the AlN layer thickness is ~0.8 nm, and that of the TiN layer is ~ 1.7 nm. The overall morphology of the as-deposited SL can be seen in the Supplementary Fig. 1. The HRTEM image (Fig. 1a) clearly reveals that in the SL structure, the layer with the bright contrast is AlN, while the layer with the dark contrast is TiN. Moreover, the as-deposited TiN/AlN SL (Fig. 1a) exhibits a well-defined epitaxial SL structure with a thin AlN layer stabilized in the rock-salt structure and a certain orientation relationship $((100)_{TiN}/(100)_{AlN})$. Selected-area electron diffraction (SAED, Fig. 1b) with the superlattice spots also confirms that the periodic SL has a fully epitaxial growth of the cubic structures, indicating the excellent quality of the thin film. Fig.1c shows a top view of the indent and the position of the FIB prepared cross-sectional TEM lamella. A low magnification image (STEM-HAADF, Fig. 1d) illustrates the overall

71

morphology of the indented cross-section. From the residual impression (i.e., V-shaped) of the indent, the indent depth was measured to be about 800 nm.
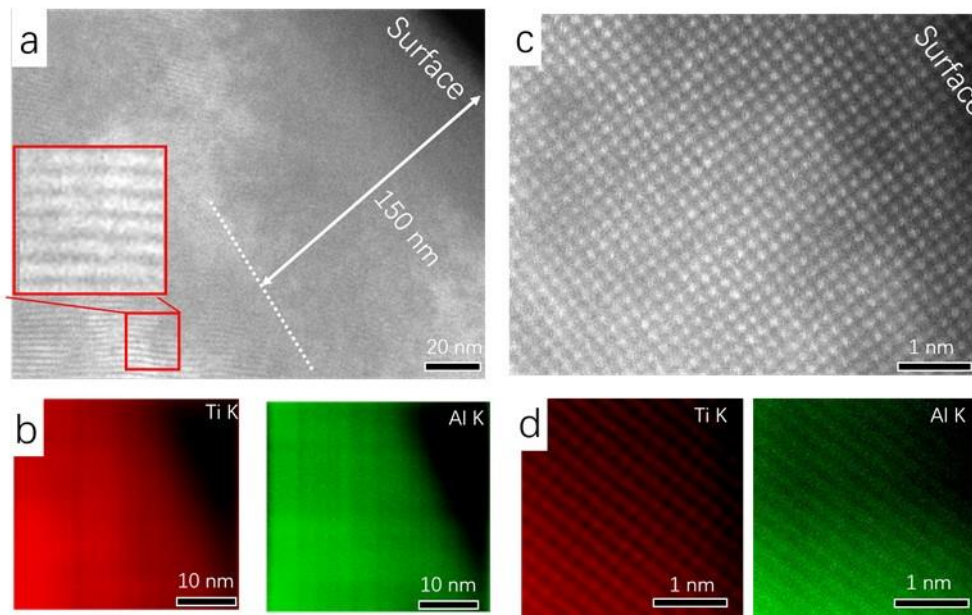

Figure 2 a, Cross-sectional HAADF image of the indented SL. **b,** Overall EDXS mappings (Ti and Al K-peak signal) taken near the contact with the indenter, as indicated by the red frame in Fig.1d. **c, d,** Atomic-resolution HAADF and elemental mapping (EDXS) near the contact region with the indenter.

When focusing on very small scales of a few nanometers, an unexpected intermixing phenomenon can be detected. The high-angle annular dark-field (HAADF) image in Fig. 2a shows the morphology of the indented coating near the surface of the residual impression (see the red frame in Fig. 1d). At positions further away from the surface (~ 250 – 300 nm), the TiN/AlN SL structure is still visible, as can be seen in the inserted image in Fig. 2a. However, when moving closer to the surface of the residual impression, starting at ~150 nm away from the surface, the deposited layered morphology of the SL cannot be detected anymore. Instead, a homogeneous single-phase area has formed around the residual impression. The energy-dispersive X-ray spectroscopy (EDXS) elemental mapping over a large area (shown in Fig. 2b) also clearly points towards a rather homogeneous chemical composition towards the surface imprint region, without any periodic chemical features of Ti or Al appearing. This strongly indicates that the deformation imposed by nanoindentation induces large-scale intermixing of the SL multilayer structure.

Furthermore, local atomic-resolution STEM-HAADF/EDXS observations unambiguously corroborate that multilayer intermixing (element intermixing) has taken place during the indentation process. Fig. 2c shows the atomic structure image (STEM-HAADF) along the cubic [100] projection close to the surface of the residual impression, exhibiting a homogeneous distribution of image contrast, while the layered features remain absent (a HAADF image with a larger field of view is shown in Supplementary Fig. S2). Further, atomic-scale elemental mapping displayed in Fig. 2d exactly reflects that superlattice intermixing has occurred at the area close to the indenter tip. Careful inspection of the mapping reveals that Al and Ti atoms reside at identical atom column positions, which finally confirms the formation of a cubic $Ti_{1-x}Al_xN$ solid solution from the superlattice structure. Quantitative evaluation of the EDXS mapping reaches an atomic *ratio between Ti and Al of 2:1 in the* solid solution *region (the EDXS quantitative result is* obtained from Fig. 2b and 2d), which is consistent with the atomic ratio in the *as-deposited SL*, i.e., 1.7 nm (8 atomic layers of TiN)/0.8 nm (4 atomic layers of AlN). Therefore, *we conclude indentation induces the formation of a homogeneous* single-phase $Ti_{0.66}Al_{0.33}N$ solid solution around the contact surface region. Moreover, the lattice constants vary accordingly.
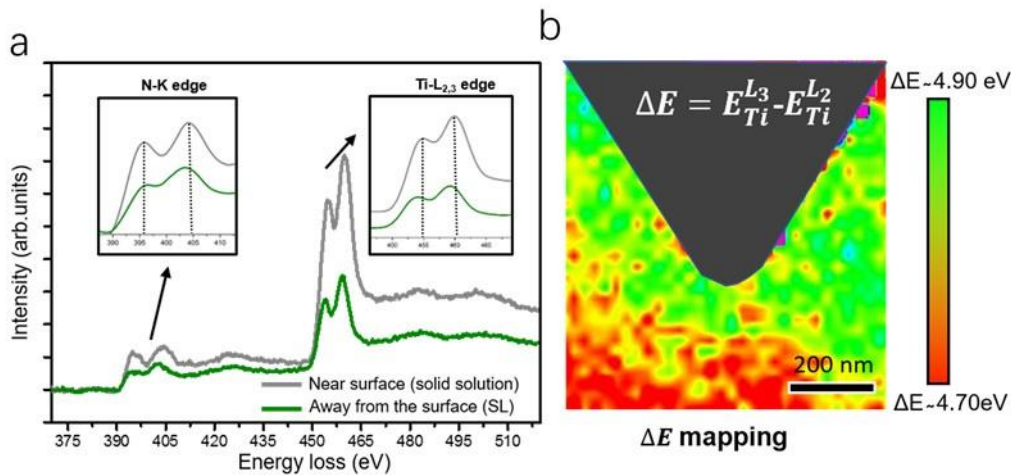

Figure 3 a, EELS taken from near the surface region (solid solution) and region away from the surface (deformed superlattice). Enlarged N-K and Ti-L edges are inserted. **b,** Mapping of the energy difference (ΔE) between Ti-L_2 and Ti-L_3. ΔE on the surface green area is approximately 4.9 eV and far away from the surface red area is approximately 4.7 eV.

In addition, the *intermixing* phenomenon also changes the electronic structure. Theoretical calculations revealed the influence of TMN alloying on electron density and chemical bonds [4,

42-44]. Fig. 3a experimentally shows core-level EELS spectra recorded from the solid solution (the surface region) and the deformed superlattice regions (away from the surface region). The close comparison reveals that for the solid solution region, (i) the N-K (second peak) and Ti-L edges slightly shift to a higher energy position; (ii) the intensity of the first peak of the N-K edge is also relatively increased; (iii) the gap between L_2 and L_3 *pea*ks slightly changes. The gap changes *in* Ti-$L_{2,3}$ edge allows further mapping of the solid solution region around the indenter. Fig.3b displays the map of the energy difference $\Delta E = E_{L2}^{Ti} - E_{L3}^{Ti}$, which actually demonstrates the distribution of the solid solutio*n* region near the surface. Despite the small energy difference, it is still possible to visualize its distribution. As can be seen, the created solid solution zone is mainly located around the contact region of the indenter. This analysis is consistent with the HAADF observation in Fig. 2a.

3.2 Molecular dynamic simulations
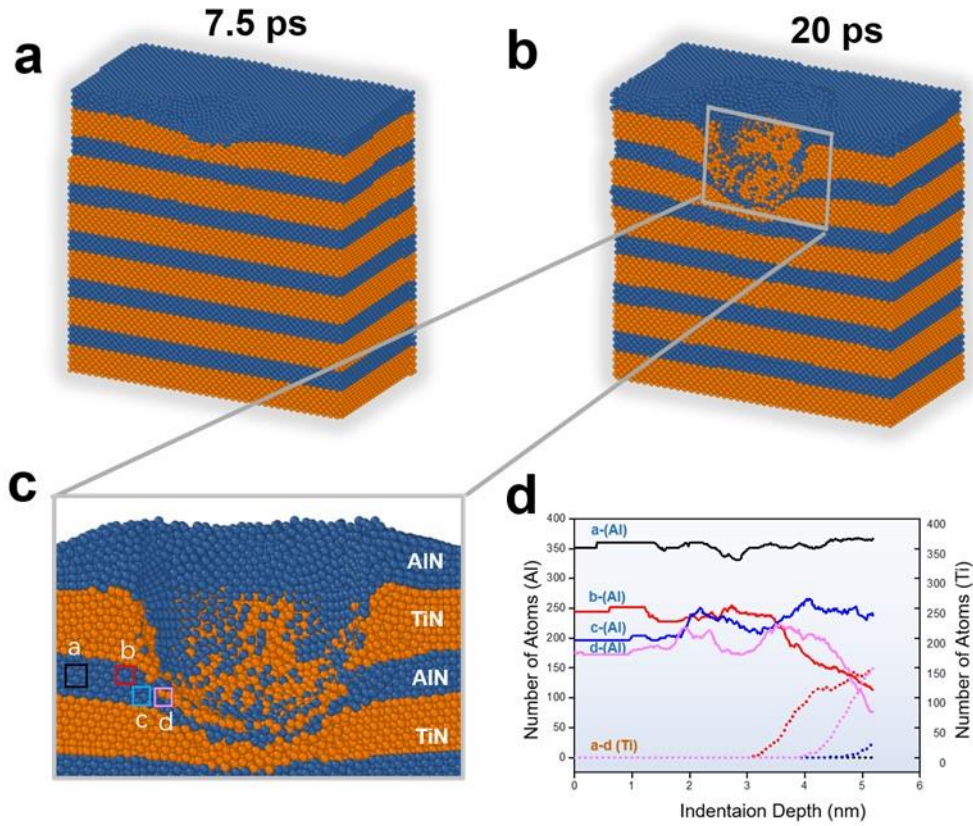
Figure 4 a b, Cross-sectional view of the TiN/AlN superlattice near the indenter obtained from MD simulation (after 7.5 and 20 ps respectively). **c,** Snapshot of region next to the nanoindenter tip (after 20 ps), where positions *a,b,c,d* are used for quantitative measurements (with a volume of 2Å×2Å). The colored rectangles represent the positions where the atom distribution is calculated (positions *a-d*). **d,** Quantitative measurements indicating how the number of Al/Ti atoms changes with indentation depth. Solid lines represent the number change of Al atoms while dashed lines denote the number change of Ti atoms.

The nanoindentation induced superlattice intermixing is further substantiated by extensive molecular dynamic (MD) simulations. Although the maximum indentation depth simulated by MD is only ~5.0 nm, the simulation still sheds light at the initial stages of the microstructural changes of the superlattice during the contact. In Fig. 4a, for shallow indentation depths, the MD simulation only shows the deformation of the contact layer without any noticeable intermixing behavior. When the indentation depth continues to increase (Fig. 4b), the elemental intermixing in the first two bilayers becomes obvious. The quantitative measurement results (as

seen in 4d) indicate how the number of Al/Ti atoms in the evaluation boxes evolves with indentation depth. Similar to the experiments, the MD simulations reveal that the intermixing behavior largely depends on the distance from the indent. According to the atomic ratio variations of the four analyzed volumes during nanoindentation (Fig.4d, profiles), the obvious intermixing behavior requires at least an indentation depth of more than 3 nm, reflected in the increasing Ti and decreasing Al atom numbers. For position *b* (near the interface) or position *d* (near the indenter), the intermixing is more obvious than in the analyzed volume *c* (away from the interface) or *a* (away from the indenter), but gradually diminishes when moving further away towards the unaffected volume. Therefore, our MD results demonstrate that intermixing can occur in the affected volumes around the indenter tip, which agrees well with the experimental observations.

3.3 Superlattice intermixing mechanism
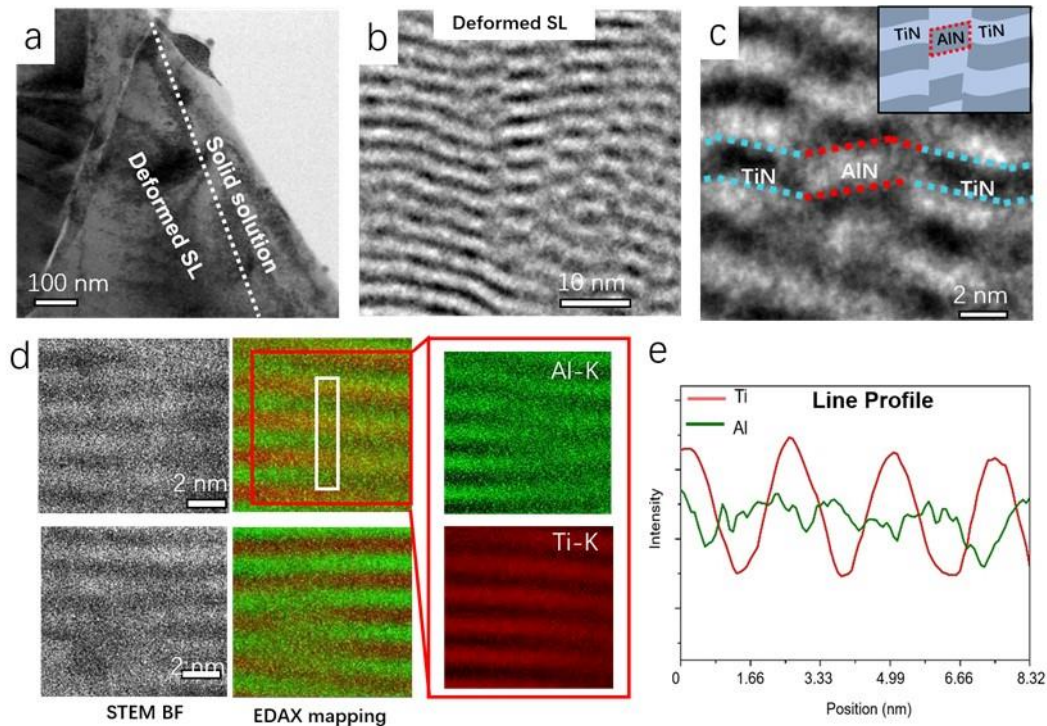
Figure 5 a, TEM-BF micrograph presenting a cross-sectional overview of the imprint surface region. **b,** TEM-BF shows the deformed SL away from the imprint surface position. **c,** Enlarged BF image of the deformed SL. **d,** STEM-BF and EDXS maps at the deformed SL, with local Ti-K/Al-K maps shown on the right-hand side. **e,** The line profile is taken from the white rectangle in **d**.

After demonstrating that intermixing occurs, the question is, how it happens during nanoindentation? Previous researches indicate that intermixing of nitride layers could occur at elevated temperatures[31, 32, 33, 34, 35]. However, these thermally-driven diffusion phenomena only appear near the interface and no large-scale solid solution formation has been reported yet. Contrary, the observed intermixing is similar to bulk mechanical alloying observed due to severe plastic strains applied, e.g., during ball milling, drawing, rolling, and torsion [24, 25, 26, 36, 37, 38, 39]. These processes were found to allow for a complete dissolution of the minority phase within the matrix, and the solubility can exceed the equilibrium value, i.e., forming a supersaturated solid solution even in an immiscible system [24, 25, 26 40]. However, the equivalent strains applied in the SPD process are huge compared to those realized by the cube corner indenter (i.e., ~ 20%).

Nevertheless, the observations clearly indicate that the formation of $Ti_{1-x}Al_xN$ solid solution is related to the imposed plastic deformation. A perfect solid solution is only obtained closely around the residual impression of the indenter, while moving towards the unaffected volume, the amount of the solid solution gradually reduces (supplementary Figs. S3). In this transition region a deformed TiN/AlN SL structure appears (as roughly indicated in Fig. 5a, deformed SL). The deformed SL exhibits a significant wavy-like structure (see Fig. 5b) compared to the as-deposited coating. This waviness or fragmentation of the perfect as-deposited layers could be initiated by imposed deformation during nanoindentation, as the required dislocation motion can easily create steps along the interface. Given the extremely small thickness of the multilayer structure, these steps might be of similar height (i.e., a Burgers vector amounts up to 30 % of the layer thickness), thus easily disrupts or fragments the SL. As shown in Fig. 5d, a small piece of AlN is "broken" from the AlN layer and displaced "into" the TiN layer region. Such a tiny piece can be easily dissolved by the Gibbs-Thomson effect, similar to the process of dissolving nanoscale clusters into the matrix during SPD[27, 45, 46]. Thus, accompanied by the SL deformation, the intermixing of species is largely enhanced.

To further understand the intermixing process, we utilize EDXS to map elemental distribution in the deformed SL region, and DFT calculation to evaluate the migration barrier. In some positions of the deformed SL, the distinct SL structure is disrupted. The EDXS mapping (Fig. 5d) indicates that a pronounced intermixing has already occurred there, but likely with different mixing capabilities for the different species. This is clearly demonstrated in the EDXS line profiles (Fig. 5e), where Al atoms migrate across the layers but Ti atoms do not, further proved by our atomic-scale EDXS mapping in supplementary Figs. S4. Such profiles are obviously

different from those taken from the undeformed SL (supplementary Fig. S5), where no noticeable chemical intermixing is observed.
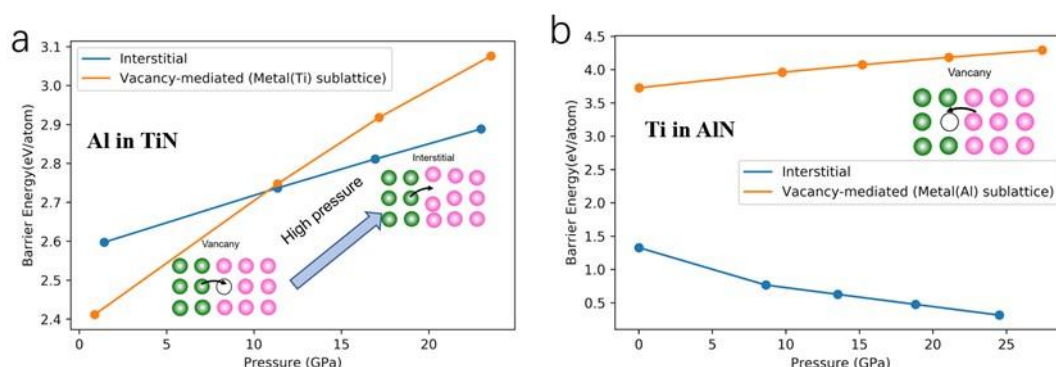

Figure 6 a and b DFT calculations of the migration energy barrier for aluminum (Al) in titanium nitride (TiN) and titanium (Ti) in aluminum nitride (AlN), respectively. The blue and yellow solid lines show the pressure dependence of the energy barrier for interstitial- and vacancy-mediated mechanisms, respectively.

The EDXS result (Fig. 5d) suggests that the Al atom migration distance is larger than that of Ti. This observation is supported by the calculated migration energy barriers for Al in TiN and Ti in AlN. DFT results of the energy barrier variation with pressure in the case of Al in TiN, for two migration mechanisms, namely interstitial- and vacancy-mediated mechanisms are shown in Fig.6a. Regarding Al migration in TiN (are shown in Fig.6b), the vacancy-mediated migration is more prominent in the low-pressure condition, however, with an increase of the pressure (after ~ 14 GPa), the interstitial-mediated mechanism comes into play. Considering also the formation energy of vacancies and interstitials in TiN (see left panel of Fig. S6), vacancies are the favored defect. For Ti migration in AlN, the energy barrier exhibits a very low value (~1 eV) for the interstitial mechanism. However, the energies to form a point defect in AlN are very high: 12.89 eV and 7.64 eV for the Ti interstitial and Al vacancy, respectively (Fig. S6, right panel). Consequently, defects are expected to be very scarce and presumably make Ti migration in AlN very difficult. Al migration in TiN (vacancy mediated) is thus expected to be facilitated compared to Ti migration through AlN.

However, from a kinetic perspective, diffusion coefficients at room temperature are negligible and the diffusion distance is significantly smaller than the layer thickness (as seen in supplementary discussion). Hence, the intermixing process is most likely caused by the applied deformation driving atomic displacements during the nanoindentation process. The imposed

deformation may as well activate Ti atoms (with higher energy barriers) to also migrate into the AlN matrix and eventually to form a uniform single-phase $Ti_{1-x}Al_xN$ solid solution (as seen Figs. 2a-d).

4. Discussion

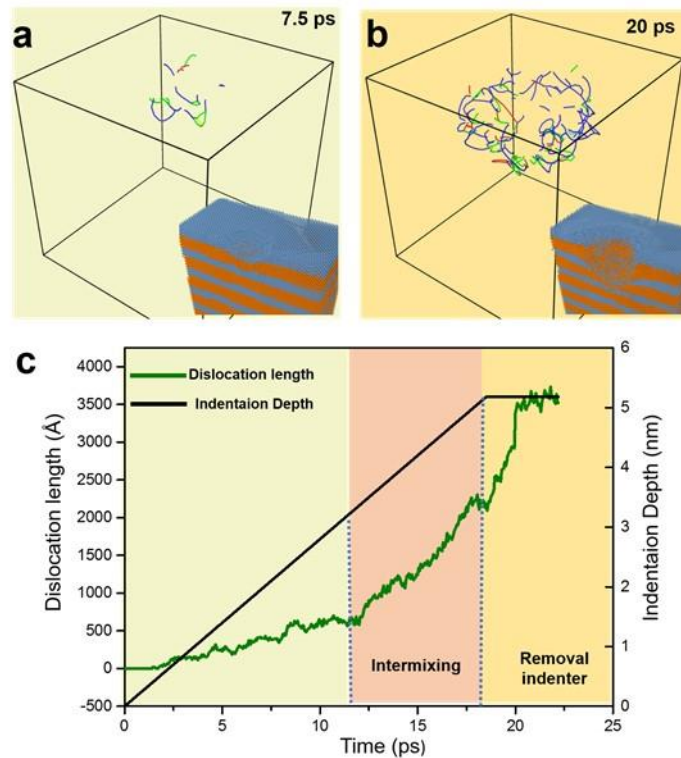## 4.1 Interface deformation-driven intermixing

Figure 7 a b, MD simulation showing that the number of dislocations varies with the depth of the indenter (after 7.5 and 20 ps, respectively). Note the dislocation network under the indenter with the green, red and blue curved lines representing the dislocations. **c,** The development of the dislocation length (green line) during the indentation sequence in the MD simulation. Dislocations appear prior to any intermixing, and the intermixing occurs after 11 ps (from the result in Fig. 4d). The black line represents the indentation depth during the calculations.

When excluding enthalpy, the pressure increases the "intrinsic resistance" to atomic mixing (as DFT calculations show, Supplementary Fig. S7). However, the enthalpy contribution of the interfaces during plastic deformation can act as a driving force for the solid solution formation and might be large enough to overcome the positive mixing enthalpy of solid solution [28], in particular in the case of a small bilayer period with a high density of interfaces. Our MD

simulation shows no apparent intermixing behavior in the early contact of the indenter, and this stage presents a lower dislocation density (as seen in Fig. 4a and Fig. 7a). When the dislocation density is further increased (as the indentation depth increases, and so the strain in case of the spherical indenter), interface intermixing occurs (as seen in Fig. 4b and Fig. 7b). The relationship between dislocation density and intermixing behavior is clearly shown in Fig. 7c. Thus, the MD result suggests that the interface intermixing phenomenon is strongly related to the SL plastic deformation, in agreement with the experimental results. To rationalize the driving forces for the intermixing phenomenon we simply consider the total energy change of the system in the following.

The total energy of rs-TiN/rs-AlN, E_T^{SL}, per unit (surface/interface/section) area in one bilayer period can be expressed as:

$$E_T^{SL} = t_1 \cdot E_s^{AlN} + t_2 \cdot E_s^{TiN} + t_1 \cdot E_b^{AlN} + t_2 \cdot E_b^{TiN} + E_I^{TiN/AlN} \qquad (1)$$

E_s is the strain energy density (per unit volume), E_b is the bulk (chemical) energy density (per unit volume) and $E_I^{TiN/AlN}$ is the interface energy. t_1 and t_2 are the layer thicknesses of TiN and AlN, respectively (t_1=0.8nm and t_2=1.7nm). Since the formed solid solution contains no interfaces, the total energy of cubic Ti$_{1-x}$Al$_x$N, E_T^{TiAlN}, per unit (surface/interface/section) area in certain thickness (2.5 nm) can be expressed as:

$$E_T^{TiAlN} = (t_1 + t_2) \cdot (E_s^{TiAlN} + E_b^{TiAlN}) \qquad (2)$$

When $E_T^{TiAlN} < E_T^{SL}$, the lower total energy of the solid solution favors the intermixing process of the superlattice. However, for a given stress state, the elastic strain energy difference between the superlattice and the solid solution is negligible (see **Appendix 1**). Therefore, reduction or relaxation of the elastic strain energy cannot be considered to be the main driving force for intermixing. If so, plasticity would not be a prerequisite for intermixing, what is neither observed in the experiment, nor in the MD simulations.
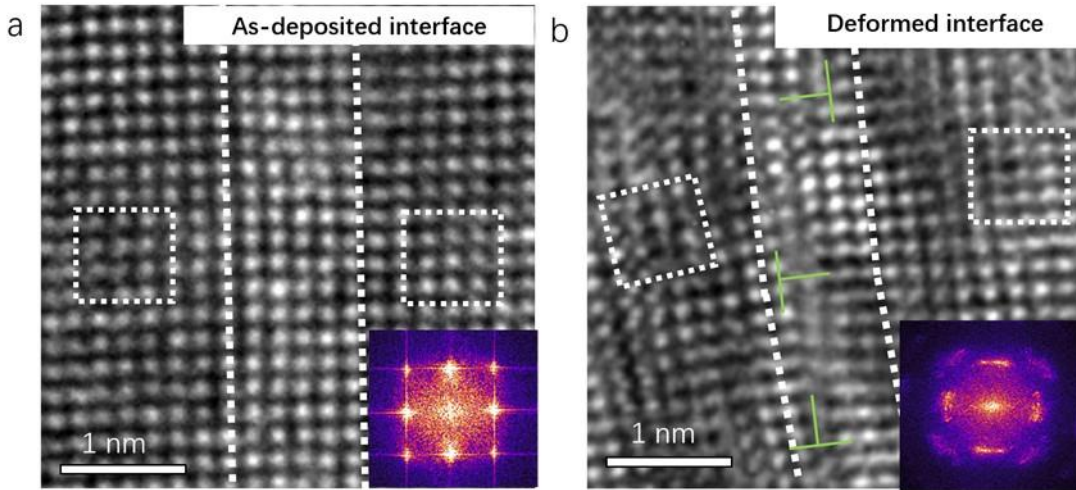
Figure 8 a, HRTEM image showing the interface structure of the as-deposited SL. **b,** HRTEM image showing the interface structure of the deformed SL (after indentation). Inserted images of **a** and **b** show fast Fourier transform (FFT) results of HRTEM images of the as-deposited and the deformed SL. The white boxes labeled in **a** and **b** show the orientation difference on both sides of the interface.

However, plastic deformation will greatly increase the interface energy of the SL. The TEM observations demonstrate that deformation of the SL induces an evolution from a coherent interface (Fig. 8a) to an incoherent-like interface (Fig. 8b), associated with many misfit dislocations (as seen in the following section) and considerable lattice distortions. Accumulation of these misfit dislocations may further explain the wavy appearance of the deformed superlattice. These distortions are also visible in the FFT, resulting in a broadening of the reflection spots (Fig. 8b). Such an imperfect crystallographic match at the interface significantly increases the interface energy. For instance, the *rs*-TMN/*rs*-TMN coherent interface energy is usually less than <20 meV/Å^2, while the semi-coherent *w*-AlN/TiN(001) interface energy is already ≈ 180 meV/Å^2 [47-49]. Thus, the plastic deformation imposed by the indenter causes a sharp increase of the interfacial energy, which can act as a main driving force for superlattice intermixing. Especially for small bilayer periods, a single-phase structure can become quite beneficial as deduced from the simple total energy balance. According to Equation 1, reducing the thickness of TiN and AlN increases the fraction of the interface energy to the total energy of the SL, while from these energetic considerations intermixing should become increasingly difficult for thicker bilayer periods.

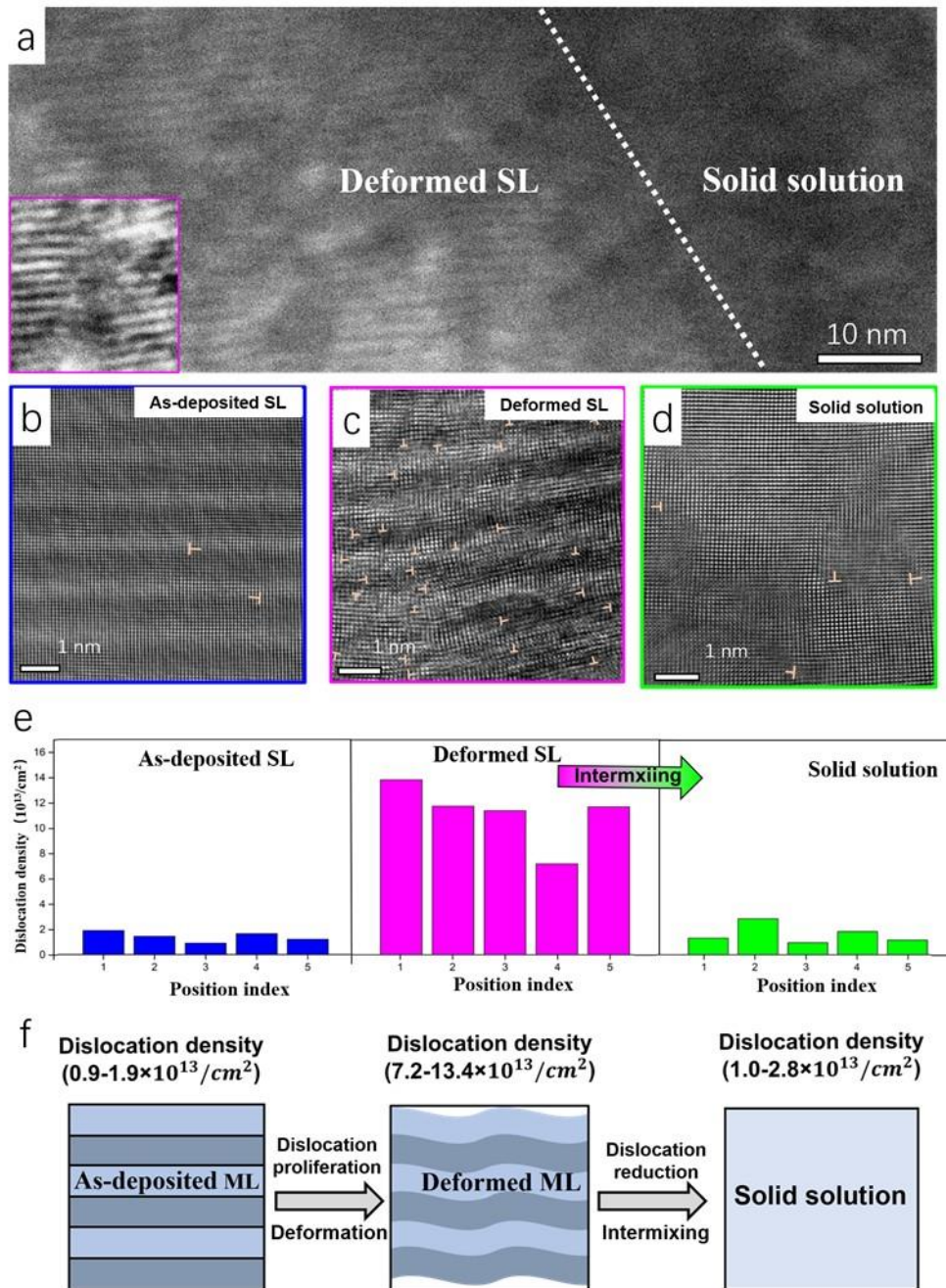## 4.2 Effect of intermixing on dislocation behavior and strength

81

Figure 9 a, HAADF image showing the distribution of solid solution and deformed multilayer regions. A locally enlarged HAADF image taken from the deformed multilayer is inserted, clearly showing its different morphology. **b, c, d,** Typical HRTEM images recorded from the as-deposited SL, deformed SL and the solid solution area. **e,** Dislocation density statistics from the respective regions. **f,** Schematic illustrations of the layered structure evolution and dislocation density change from the as-deposited SL, to the deformed multilayer and to the solid solution region.

So far, three strengthening mechanisms are applied to describe the variations in hardness or strength of multilayer coatings, i.e., the Hall-Petch-like strengthening relationship based on

dislocations piling up at the interface [50, 51], the confined layer slip (CLS) mechanism[52-54] and the interface barrier strength (IBS) mechanism[10, 15, 55]. Most of these models explain the hardness/strength according to the relationship between dislocations and interfaces and the respective changes if the layer volumes become confined, but none of them considers the effect of intermixing on the dislocation behavior during deformation.

For nanoscale *rs*-TMN/*rs*-TMN superlattice coatings, the mechanical strength usually increases as the bilayer period thickness decreases [4-6, 8, 11, 13]. This is rationalized by the interface barrier strength (IBS) mechanism, i.e., hindering dislocations crossing the interface and dislocation pile ups. For a smaller bilayer-period (less than 3~4 nm) the hardness of the multilayer coating decreases. Currently this softening is attributed to the composition mixing during the deposition process. However, our high-spatial-resolution elemental analysis clearly shows that even for the superlattice with a thickness of only 1.7 nm/0.8 nm, no apparent interface chemical intermixing and diffusion occur (as confirmed by the elemental profiles recorded from the undeformed SL region, supplementary Fig. S5). Therefore, this phenomenon is not necessarily coupled to strong interface chemical intermixing and interdiffusion during deposition.

Based on our intensive study, the strength reduction of nano-scale multilayers can be reasonably explained by deformation triggered large-scale intermixing. After indentation, three distinct regions are identified, i.e., a solid solution region around the residual imprint, the deformed SL, and further away the unaffected as-deposited SL (Fig.9a). The dislocation distribution between them differs significantly, as seen in Figs. 9b-d. The dislocation density (Fig.9e) in the deformed SL is quite high (7.2-$13.4 \times 10^{13}/cm^2$), while in the solid solution region, it is relatively low (1.0-$2.8 \times 10^{13}/cm^2$), close to the value of the as-deposited SL (0.9-$1.9 \times 10^{13}/cm^2$).
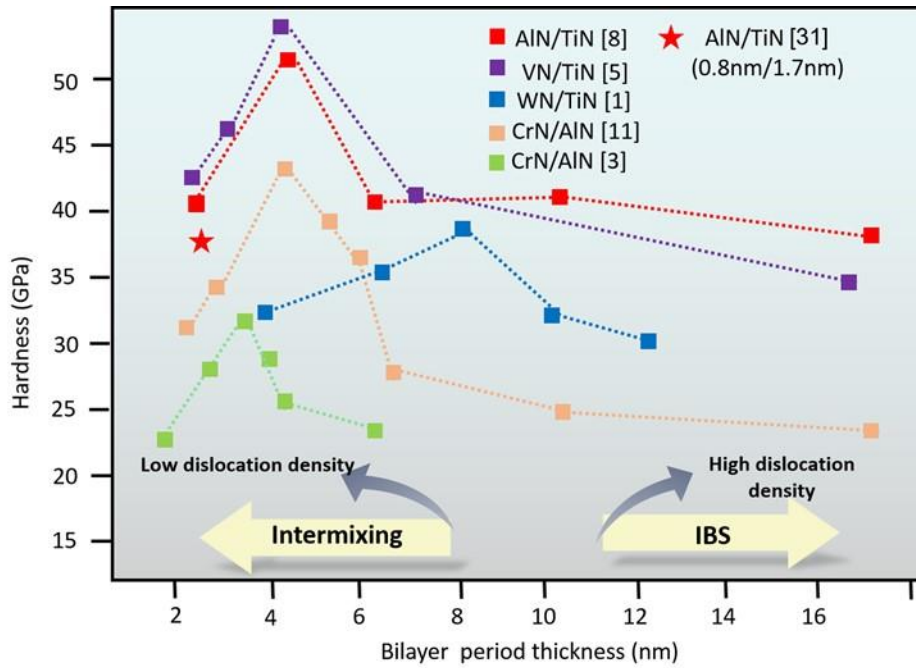
Figure 10, A summary of hardness values plotted against the bilayer period thickness for various rock-salt/rock-salt nitride superlattices, including the present TiN/AlN (2.5 nm bilayer thickness of AlN + TiN).

As discussed above, a lower dislocation density is found close to the surface of the imprint in the solid solution region. We propose that the dislocation density at the imprint surface underwent a variation from a high value to a low value, as the structure transformed from the SL to the solid solution (as seen in schematic Fig.9f). For the SL, the interface is the source for nucleation and emission of many dislocations. And, the SL interface itself poses the dominant resistance to slip transfer across the interface[56]. However, the formation of the solid solution will reduce the dislocations' nucleation ability (ascribing to the disappearing of the interfacial structure) on the one hand. The creation of the uniform single-phase solid solution will also increase the migration ability of dislocations on the other hand (as analyzed in **Appendix 2**). This clarifies the dislocation behavior during interface intermixing, i.e., the dislocation migration ability increases while the dislocation density reduces because of forming a uniform solid solution, what consequently lowers the hardness/strength. Considering that the interface energy acts as the main driving force for intermixing, a smaller bilayer-period SL facilitates alloying through deformation. Importantly, this provides a reasonable explanation for the longstanding issue—the hardness/strength reduction in multilayer coatings when the bilayer period becomes extremely small (as seen in Fig.10).

Furthermore, our work significantly improves the understanding of the structural stability of

complex nitride coating systems, such as ceramic-like $Ti_{1-x}Al_xN$ or $Cr_{1-x}Al_xN$, where the spinodal decomposition phenomenon [57-59] is considered to be the controlling mechanism to obtain superior high-temperature mechanical strength. Under practical working conditions, hard-coating tools withstand high mechanical and thermal loads. However, the current research considers only the temperature effect on structural modifications but hardly the deformation effect, which is definitely generated in service. Our research points out that deformation may trigger the reverse process of spinodal decomposition, i.e., superlattice intermixing. Therefore, it also raises uncertainty about the strength of such complex nitride coatings under the actual load. Deformation-driven intermixing process (weaken the strength) and temperature-induced spinodal decomposition process (enhance the strength) will compete. Therefore, it requires further verification of the structural changes under high mechanical and thermal loads for such complex nitride coatings.

5. Summary

Atomic-resolution structure and chemical composition analysis unambiguously reveal that nanoindentation causes large-scale intermixing in a nitride superlattice coating with small bilayer thicknesses, further validated by MD simulations. Although nanoindentation induces only a limited equivalent strain, the observed formation of the $Ti_{1-x}Al_xN$ solid solution can be clearly related to the plastic deformation of the SL imposed by nanoindentation. A single-phase solid solution is only observed near the indenter tip, while moving further away from the tip, a heavily distorted SL structure followed by a perfect unaffected SL multilayer structure can be observed. It is suggested that the coherent interfaces of the superlattice are progressively destroyed during deformation as misfit dislocations accumulate. This causes a substantial rise of the interfacial energy, which provides the main driving force for multilayer intermixing. The intermixing causes a drop not only in the interface fraction but also in the dislocation densities. Thus, our findings rationalize the mechanism responsible for the currently not well-understood inverse Hall-Petch effect in superlattice hard coatings with the finest bilayer thicknesses [4-11, 13].

Appendix 1

For *rs*-TiN/*rs*-AlN in the stage of elastic deformation, the superlattice interface will maintain a coherent state. Therefore, the change of total energy will depend on the strain energy. The strain energy density E_s corresponding to the two-dimensional bi-axial stress state for cubic

materials can be expressed as:

$$E_s = \frac{1}{2}(\sigma_{11} + \sigma_{22}) \cdot \varepsilon = M\varepsilon^2 = \frac{\sigma^2}{M} \tag{3}$$

For (001) growth plane:

$$M_{(100)} = c_{11} + c_{22} - \frac{2c_{12}^2}{c_{11}} \tag{4}$$

Thus, $M_{[100]}^{TiN}$=670 GPa, $M_{[100]}^{AlN}$=451 GPa and $M_{[100]}^{Ti_{0.66}Al_{0.33}N}$=603 GPa (elastic constant from the Ref.[60]). Here, assuming that SL and solid solution are under the same stress state, then the energy difference is very small. For example, if bi-axial stress of 20 GPa is introduced, the difference in strain energy in one period (2.5 nm) between superlattice and $Ti_{1-x}Al_xN$ is only 4.6 meV/$Å^2$. This means the driving force for the superlattice intermixing process is insufficient if only strain energies are considered.

Appendix 2

When an interface restricts the motion of a dislocation, the dislocation at a distance x from the interface is repelled by shear stress, i.e., dislocation critical migration stress on glide planes at angle θ with the interface normal, given by the following formula[15]:

$$\tau = \frac{\alpha \Delta G b \, cos\theta}{2x} \tag{5}$$

Where b is the magnitude of the dislocation Burgers vector, a is $\frac{1}{4}\pi$ for screw dislocations, and $\frac{1}{4}\pi(1-v)$ for edge dislocations and v is the Poisson's ratio. ΔG is the shear modulus difference between rs-TiN and rs-AlN. When the intermixing initiates, the modulus difference between the two layers becomes smaller and eventually vanishes with formation of the homogenous solid solution. Thus, the shear stress required for the gliding of the dislocation across the interface can be significantly reduced. Further, nitride alloying also alters the 'inherent' dislocation glide ability. The alloying has the potential to lower the resistance to shear and favors dislocation glide by modifying the electronic (high valence electron concentration) effects and bonding characteristics [43, 44]. Therefore, forming a solid solution changes the dislocation migration ability (increasing) and the dislocation density (reducing), which ultimately affects its yield strength[10, 15, 53].

References

[1] E. Arzt, Size effects in materials due to microstructural and dimensional constraints: a comparative review, Acta Materialia 46(16) (1998) 5611-5626.

[2] E.O. Hall, The Deformation and Ageing of Mild Steel: III Discussion of Results, Proceedings of the Physical Society. Section B 64(9) (1951) 747-753.

[3] N.J. Petch, The Cleavage Strength of Polycrystals, Journal of the Iron and Steel Institute 174 (1953) 25-28.

[4] J. Buchinger, N. Koutná, Z. Chen, Z. Zhang, P.H. Mayrhofer, D. Holec, M. Bartosik, Toughness enhancement in TiN/WN superlattice thin films, Acta Materialia 172 (2019) 18-29.

[5] H.C. Barshilia, A. Jain, K.S. Rajam, Structure, hardness and thermal stability of nanolayered TiN/CrN multilayer coatings, Vacuum 72(3) (2003) 241-248.

[6] M. Schlögl, B. Mayer, J. Paulitsch, P.H. Mayrhofer, Influence of CrN and AlN layer thicknesses on structure and mechanical properties of CrN/AlN superlattices, Thin Solid Films 545(Supplement C) (2013) 375-379.

[7] R. Hahn, M. Bartosik, R. Soler, C. Kirchlechner, G. Dehm, P.H. Mayrhofer, Superlattice effect for enhanced fracture toughness of hard coatings, Scripta Materialia 124 (2016) 67-70.

[8] U. Helmersson, S. Todorova, S.A. Barnett, J.E. Sundgren, L.C. Markert, J.E. Greene, Growth of single-crystal TiN/VN strained-layer superlattices with extremely high mechanical hardness, Journal of Applied Physics 62(2) (1987) 481-484.

[9] P.B. Mirkarimi, L. Hultman, S.A. Barnett, Enhanced hardness in lattice-matched single-crystal TiN/V0.6Nb0.4N superlattices, Applied Physics Letters 57(25) (1990) 2654-2656.

[10] X. Chu, S.A. Barnett, Model of superlattice yield stress and hardness enhancements, Journal of Applied Physics 77(9) (1995) 4403-4411.

[11] V. Pankov, M. Evstigneev, R.H. Prince, Room-temperature fabrication of hard AlN/TiN superlattice coatings by pulsed laser deposition, Journal of Vacuum Science & Technology A 20(2) (2002) 430-436.

[12] G.S. Kim, S.Y. Lee, J.H. Hahn, S.Y. Lee, Synthesis of CrN/AlN superlattice coatings using closed-field unbalanced magnetron sputtering process, Surface and Coatings Technology 171(1) (2003) 91-95.

[13] J. Lin, J.J. Moore, B. Mishra, M. Pinkas, W.D. Sproul, Nano-structured CrN/AlN multilayer coatings synthesized by pulsed closed field unbalanced magnetron sputtering, Surface and Coatings Technology 204(6) (2009) 936-940.

[14] M. Setoyama, A. Nakayama, M. Tanaka, N. Kitagawa, T. Nomura, Formation of cubic-A1N in TiN/A1N superlattice, Surface and Coatings Technology 86-87 (1996) 225-230.

[15] J.S. Koehler, Attempt to Design a Strong Solid, Physical Review B 2(2) (1970) 547-551.

[16] N. Koutná, P. Řehák, Z. Chen, M. Bartosik, M. Fallmann, M. Černý, Z. Zhang, M. Friák, M. Šob, P.H. Mayrhofer, D. Holec, Correlating structural and mechanical properties of AlN/TiN superlattice films, Scripta Materialia 165 (2019) 159-163.

[17] A.H. Chokshi, A. Rosen, J. Karch, H. Gleiter, On the validity of the hall-petch relationship in nanocrystalline materials, Scripta Metallurgica 23(10) (1989) 1679-1683.

[18] G.W. Nieman, J.R. Weertman, R.W. Siegel, Microhardness of nanocrystalline palladium and copper produced by inert-gas condensation, Scripta Metallurgica 23(12) (1989) 2013-2018.

[19] K. Lu, W.D. Wei, J.T. Wang, Microhardness and fracture properties of nanocrystalline Ni P alloy, Scripta Metallurgica et Materialia 24(12) (1990) 2319-2323.

[20] V.Y. Gertsman, M. Hoffmann, H. Gleiter, R. Birringer, The study of grain size dependence of yield stress of copper for a wide grain size range, Acta Metallurgica et Materialia 42(10) (1994) 3539-3544.

[21] J. Schiøtz, F.D. Di Tolla, K.W. Jacobsen, Softening of nanocrystalline metals at very small grain sizes, Nature 391(6667) (1998) 561-563.

[22] P.G. Sanders, J.A. Eastman, J.R. Weertman, Elastic and tensile behavior of nanocrystalline copper and palladium, Acta Materialia 45(10) (1997) 4019-4025.

[23] H.C. Barshilia, K.S. Rajam, Raman spectroscopy studies on the thermal stability of TiN, CrN, TiAlN coatings and nanolayered TiN/CrN, TiAlN/CrN multilayer coatings, Journal of Materials Research 19(11) (2004) 3196-3205.

[24] L. Hultman, C. Engström, M. Odén, Mechanical and thermal stability of TiN/NbN superlattice thin films, Surface and Coatings Technology 133-134 (2000) 227-233.

[25] P.H. Mayrhofer, C. Mitterer, L. Hultman, H. Clemens, Microstructural design of hard coatings, Progress in Materials Science 51(8) (2006) 1032-1114.

[26] H.-J. Lee, K.-W. Kwon, C. Ryu, R. Sinclair, Thermal stability of a Cu/Ta multilayer: an intriguing interfacial reaction, Acta Materialia 47(15) (1999) 3965-3975.

[27] X. Sauvage, F. Wetscher, P. Pareige, Mechanical alloying of Cu and Fe induced by severe plastic deformation of a Cu–Fe composite, Acta Materialia 53(7) (2005) 2127-2135.

[28] A. Bachmaier, M. Kerber, D. Setman, R. Pippan, The formation of supersaturated solid solutions in Fe–Cu alloys deformed by high-pressure torsion, Acta Materialia 60(3) (2012) 860-871.

[29] D. Raabe, S. Ohsaki, K. Hono, Mechanical alloying and amorphization in Cu–Nb–Ag in situ composite wires studied by transmission electron microscopy and atom probe tomography, Acta Materialia 57(17) (2009) 5254-5263.

[30] C. Suryanarayana, Mechanical alloying and milling, Progress in Materials Science 46(1) (2001) 1-184.

[31] M. Fallmann, Z. Chen, Z.L. Zhang, P.H. Mayrhofer, M. Bartosik, Mechanical properties and epitaxial growth of TiN/AlN superlattices, Surface and Coatings Technology 375 (2019) 1-7.

[32] S. Plimpton, Fast Parallel Algorithms for Short-Range Molecular Dynamics, Journal of Computational Physics 117(1) (1995) 1-19.

[33] S.D. Almyras GA, Sarakinos K., Semi-Empirical Force-Field Model for the $Ti_{1-x}Al_xN$ ($0 \leq x \leq 1$) System., Materials 12(215) (2019).

[34] P. Hirel, Atomsk: A tool for manipulating and converting atomic data files, Computer Physics Communications 197 (2015) 212-219.

[35] A. Stukowski, Visualization and analysis of atomistic simulation data with OVITO–the Open Visualization Tool, Modelling and Simulation in Materials Science and Engineering 18(1) (2009) 015012.

[36] G. Kresse, J. Furthmüller, Efficiency of ab-initio total energy calculations for metals and semiconductors using a plane-wave basis set, Computational Materials Science 6(1) (1996) 15-50.

[37] G. Kresse, J. Furthmüller, Efficient iterative schemes for ab initio total-energy calculations using a plane-wave basis set, Physical Review B 54(16) (1996) 11169-11186.

[38] P.E. Blöchl, Projector augmented-wave method, Physical Review B 50(24) (1994) 17953-17979.

[39] H.J. Monkhorst, J.D. Pack, Special points for Brillouin-zone integrations, Physical Review B 13(12) (1976) 5188-5192.

[40] M. Methfessel, A.T. Paxton, High-precision sampling for Brillouin-zone integration in metals, Physical Review B 40(6) (1989) 3616-3621.

[41] D. Sheppard, R. Terrell, G. Henkelman, Optimization methods for finding minimum energy paths, The Journal of Chemical Physics 128(13) (2008) 134106.

[42] D. Holec, R. Rachbauer, D. Kiener, P.D. Cherns, P.M.F.J. Costa, C. McAleese, P.H. Mayrhofer, C.J. Humphreys, Towards predictive modeling of near-edge structures in electron energy-loss spectra of AlN-based ternary alloys, Physical Review B 83(16) (2011) 165122.

88

[43] D.G. Sangiovanni, L. Hultman, V. Chirita, I. Petrov, J.E. Greene, Effects of phase stability, lattice ordering, and electron density on plastic deformation in cubic TiWN pseudobinary transition-metal nitride alloys, Acta Materialia 103 (2016) 823-835.

[44] D.G. Sangiovanni, L. Hultman, V. Chirita, Supertoughening in B1 transition metal nitride alloys by increased valence electron concentration, Acta Materialia 59(5) (2011) 2121-2134.

[45] A.R. Yavari, P.J. Desré, T. Benameur, Mechanically driven alloying of immiscible elements, Physical Review Letters 68(14) (1992) 2235-2238.

[46] A. Bachmaier, G.B. Rathmayr, M. Bartosik, D. Apel, Z. Zhang, R. Pippan, New insights on the formation of supersaturated solid solutions in the Cu–Cr system deformed by high-pressure torsion, Acta Materialia 69 (2014) 301-313.

[47] Z. Chen, D. Holec, M. Bartosik, P.H. Mayrhofer, Z. Zhang, Crystallographic orientation dependent maximum layer thickness of cubic AlN in CrN/AlN multilayers, Acta Materialia 168 (2019) 190-202.

[48] A. Madan, I.W. Kim, S.C. Cheng, P. Yashar, V.P. Dravid, S.A. Barnett, Stabilization of Cubic AlN in Epitaxial AlN/TiN Superlattices, Physical Review Letters 78(9) (1997) 1743-1746.

[49] K. Yalamanchili, F. Wang, H. Aboulfadl, J. Barrirero, L. Rogström, E. Jiménez-Pique, F. Mücklich, F. Tasnadi, M. Odén, N. Ghafoor, Growth and thermal stability of TiN/ZrAlN: Effect of internal interfaces, Acta Materialia 121(Supplement C) (2016) 396-406.

[50] P.M. Anderson, C. Li, Hall-Petch relations for multilayered materials, Nanostructured Materials 5(3) (1995) 349-362.

[51] A. Misra, H. Krug, Deformation Behavior of Nanostructured Metallic Multilayers, Advanced Engineering Materials 3(4) (2001) 217-222.

[52] M.A. Phillips, B.M. Clemens, W.D. Nix, A model for dislocation behavior during deformation of Al/Al3Sc (fcc/L12) metallic multilayers, Acta Materialia 51(11) (2003) 3157-3170.

[53] A. Misra, J.P. Hirth, R.G. Hoagland, Length-scale-dependent deformation mechanisms in incoherent metallic multilayered composites, Acta Materialia 53(18) (2005) 4817-4824.

[54] J.D. Embury, J.P. Hirth, On dislocation storage and the mechanical response of fine scale microstructures, Acta Metallurgica et Materialia 42(6) (1994) 2051-2056.

[55] S.I. Rao, P.M. Hazzledine, Atomistic simulations of dislocation–interface interactions in the Cu-Ni multilayer system, Philosophical Magazine A 80(9) (2000) 2011-2040.

[56] R.G. Hoagland, T.E. Mitchell, J.P. Hirth, H. Kung, On the strengthening effects of interfaces in multilayer fee metallic composites, Philosophical Magazine A 82(4) (2002) 643-664.

[57] A. Hörling, L. Hultman, M. Odén, J. Sjölén, L. Karlsson, Mechanical properties and machining performance of Ti1−xAlxN-coated cutting tools, Surface and Coatings Technology 191(2) (2005) 384-392.

[58] P.H. Mayrhofer, F.D. Fischer, H.J. Böhm, C. Mitterer, J.M. Schneider, Energetic balance and kinetics for the decomposition of supersaturated Ti1−xAlxN, Acta Materialia 55(4) (2007) 1441-1446.

[59] A. Hörling, L. Hultman, M. Odén, J. Sjölén, L. Karlsson, Thermal stability of arc evaporated high aluminum-content Ti1−xAlxN thin films, Journal of Vacuum Science & Technology A 20(5) (2002) 1815-1823.

[60] Y. Teng, S. Zhu, F. Zhang, M. Li, F. Wang, W. Wu, Electronic structure, lattice constant, optical and mechanical properties for NaCl-structured Ti–Al–N by density functional theory, Physica B: Condensed Matter 358(1) (2005) 77-85.
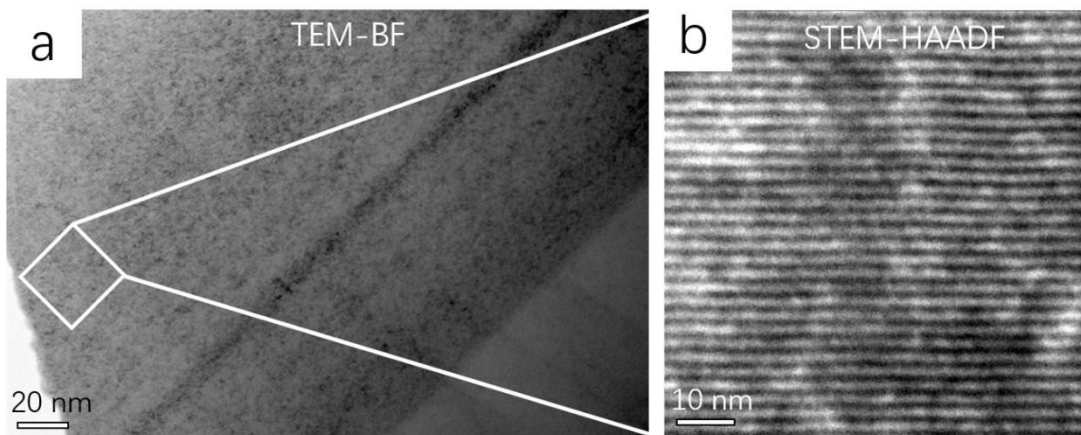
# Acknowledgements

Supplementary Materials

Surprising superlattice intermixing triggered by nanoindentation and its effect
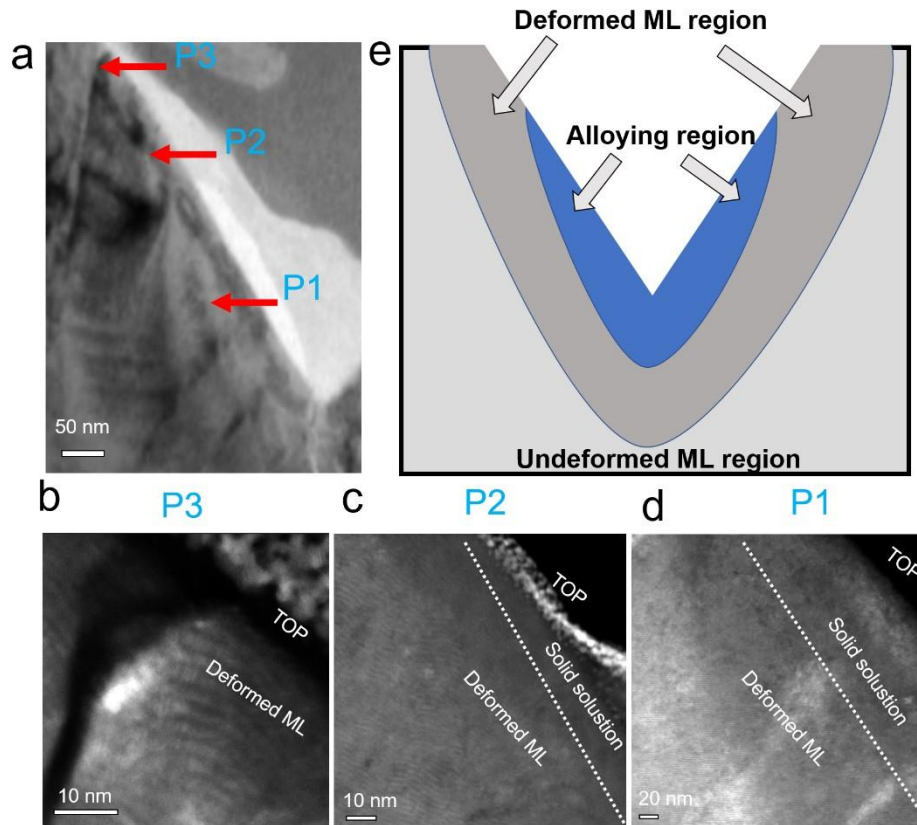
1. Supplementary Figures:

Figures S1-S7:

**Supplementary Figure S1: a,** The bright field image of as-deposited multilayer coating. **b,** HAAD image of as-deposited multilayer, where indicate as-deposited thin film with the periodic alternation of composition
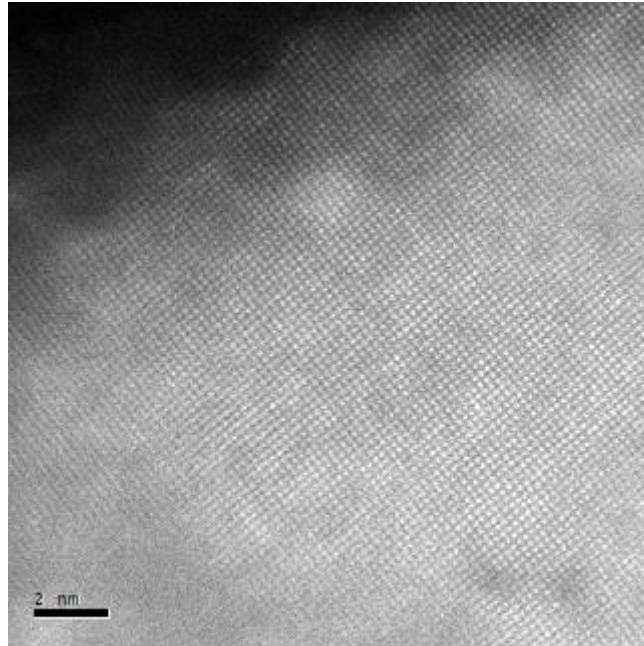
Supplementary Figure S2： Atomic-scale HAAD image of indented multilayer, where image taken near the surface region of impression. HAADF STEM image shows the atomic structure of the cubic [100] projection in the surface region of impression and shows a homogeneous distribution of contrast in a local region, which indicate the surface region is the $Ti_{1-x}Al_xN$ solid solution instead of TiN/AlN SL.

Supplementary Figure S3: a, The bright field image of indented multilayer. **b-d,** HAADF images observation solid solution regions distribution from p3 position to p1 position. In **Fig. S3b,** HAADF shows no solid solution was found in the surface region of impression. As gradually moving close to the tip, the area of the solid solution gradually increase (**Fig. S3c and S3d**). **e,** Schematic image shows the distribution of alloying regions, deformed multilayer regions and undeformed multilayer regions.
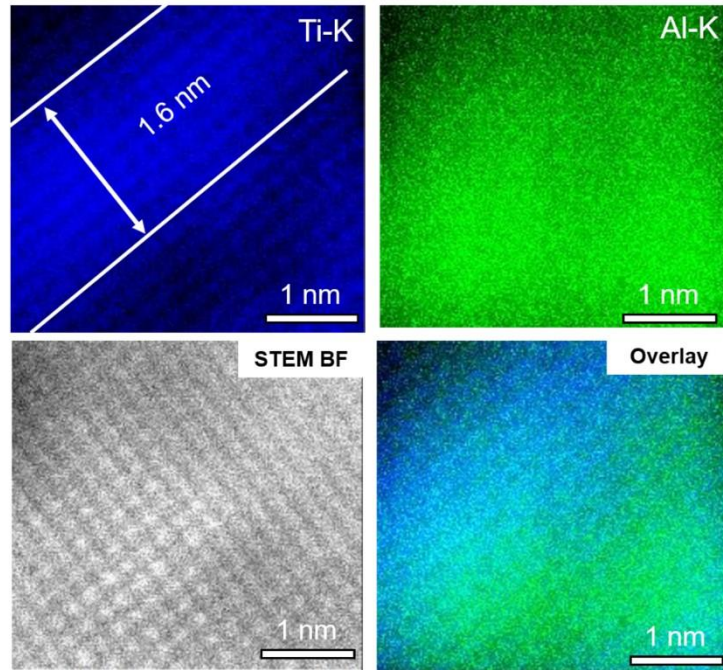
Supplementary Figure S4: Atomic-scale STEM-BF and EDXS mappings (Ti and Al K peak signals) shows the inhomogeneous diffusion in the local region. In Ti-K mapping, the middle of image shows a higher Ti concentration. In same region Al-K mapping, more uniform distribution of Al can be found, where indicate that the diffusion distance of Al is greater than that of Ti.
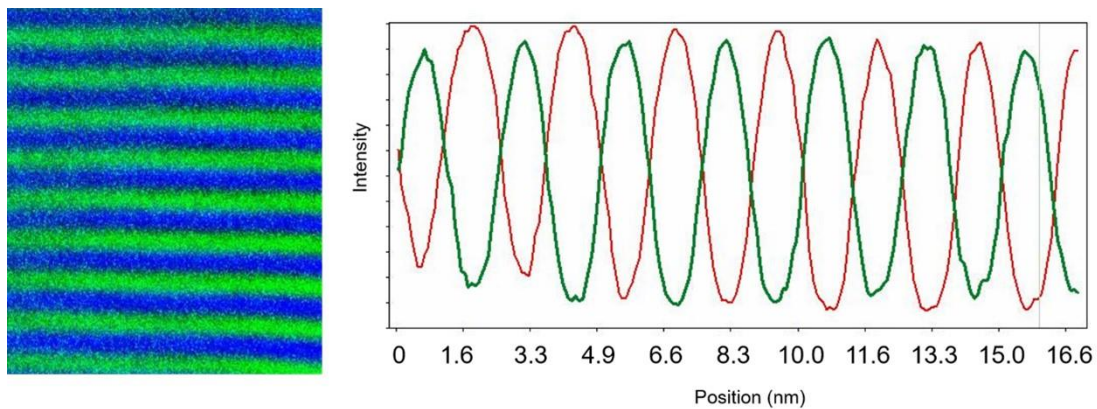
Supplementary Figure S5: EDXS mapping result in undeformed TiN/AlN multilayer region. Meanwhile, the line profile result shows the superlattice without significant interface intermixing phenomenon.
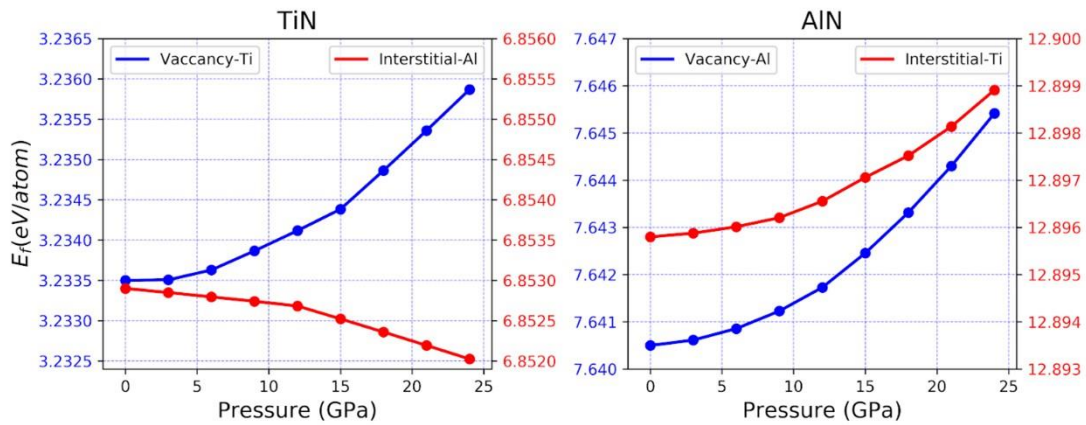
Supplementary Figure S6: DFT calculation of the defect formation energy for aluminum (Al) in titanium nitride (TiN) (interstitial mechanisms and vacancy mechanisms in) and titanium (Ti) in aluminum nitride (AlN) (interstitial mechanisms in and vacancy mechanisms). Compare with the diffusion energy barrier, the pressure has little effect on the defect formation energy of TiN and AlN, where the energy change is only a few meV. In general, the defect formation energy of TiN is lower than that of AlN, which indicate it is more easily to activate Al atoms to diffuse into the TiN matrix through defect-mediated. However, the interstitial mechanism of Ti in AlN diffusion shows very high formation energy ($E_f^{I_{Ti\ in\ AlN}}$ ⌐12.895 eV), which shows the migration mechanisms for the interstitial mechanism (Ti diffusion in AlN) are unreasonable.
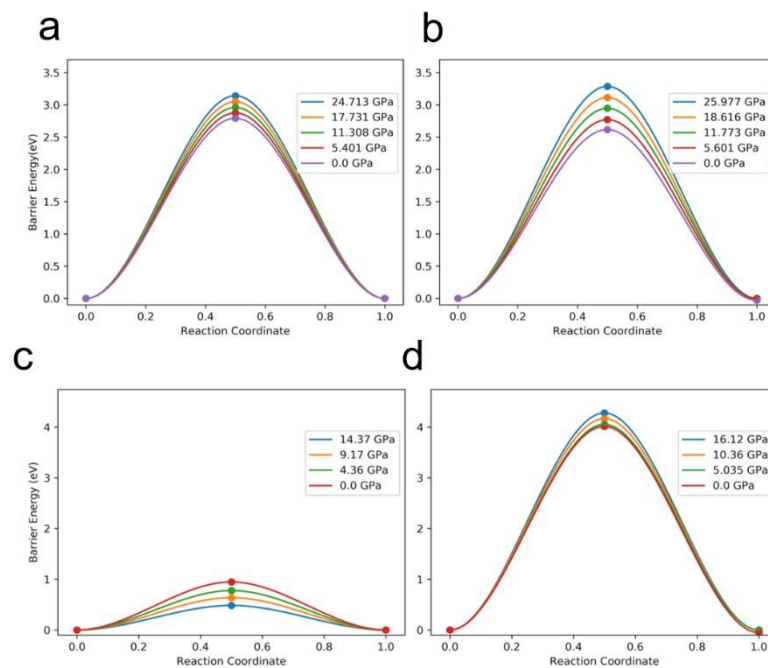
Supplementary Figure S7： DFT calculation of the diffusion energy barrier for aluminum (Al) in titanium nitride (TiN) (interstitial mechanisms in **a** and vacancy mechanisms in **b**) and titanium (Ti) in aluminum nitride (AlN) (interstitial mechanisms in **c** and vacancy mechanisms in **d**), respectively. DFT simulation shows that the pressure of 25 GPa increases the energy barrier of Al diffusion to TiN by 12.5% and 25.4% for the interstitial and vacancy mechanisms, respectively.

2. Supplementary discussion:

Thermal diffusion at room temperature

Our DFT calculation shows that the vacancy defect-mediated diffusion (Al in TiN) have a lowest migration energy and formation energy. Thus, in this section, we mainly discuss the diffusion coefficient and diffusion for vacancy mediated Al in TiN. Vacancy mediated diffusion coefficient is commonly characterized as:

$$D = D_0 e^{-E_f^V/k_B T} e^{-E_m^V/k_B T}$$

D_0 is the diffusion constant, k_B is the Boltzmann constant, T is the temperature, E_f^V and E_m^V are the vacancy formation and migration energies. Currently, the diffusion constant (D_0) of Al in TiN is unknown. Therefore, we use the diffusion constant value was report in previous DFT work of Al in AlN ($\sim 1.2 \cdot 10^{-2}$ cm^2/s [86]). In our case, the E_f^V and E_m^V (at 0 GPa) with 2.4 eV/atom and 3.2 eV/atom, respectively. Thus, the Al in TiN diffusion coefficient in room temperature (298 K) is $\sim 2.8 \cdot 10^{-79}$ nm^2/s. Meanwhile, under the presence of non-equilibrium vacancies, the diffusion coefficient (instantaneous diffusion coefficient, D) for a certain species can be characterized by[87]:

$$D = D^{eq} \frac{C_V^{ex}}{C_V^{eq}}$$

where C_V^{ex} is instantaneous vacancy concentration; C_V^{eq} is equilibrium vacancy concentration. D^{eq} is the diffusion coefficient under equilibrium condition. The change in vacancy concentration due to nanoindentation cannot be estimated at present. Here we refer to the vacancy concentration at room temperature during the HPT (high pressure torsion) process in copper[88] $C_V^{eq} \sim 1.2 \cdot 10^{-19}$ $C_V^{ex} \sim 5.0 \cdot 10^{-3}$ (in fact, the TMN materials may have a lower vacancy concentration in nanoindentation process). Thus, the diffusion coefficient under non-

equilibrium can be estimated as $1.6 \cdot 10^{-62}$ nm^2/s. For Al diffuse in TiN, the required diffusion constant is simply estimated to be $D = L^2/4t$, where L is the distance over which the constituent atoms are gathered (which we estimate to be half of the TiN layer thickness of 0.8 nm), and t is the indentation time (about 10s). This gives $D \sim 1.6 \cdot 10^{-2}$ nm^2/s. Thus, at room temperature, pure thermal drive diffusion coefficient is too small, which is far from reaching the demand for fully intermixing.

References

[1] I.A. Aleksandrov, T.V. Malin, K.S. Zhuravlev, S.V. Trubina, S.B. Erenburg, B. Pecz, Y.V. Lebiadok, Diffusion in GaN/AlN superlattices: DFT and EXAFS study, Applied Surface Science 515 (2020) 146001.

[2] P.M. Fahey, P.B. Griffin, J.D. Plummer, Point defects and dopant diffusion in silicon, Reviews of Modern Physics 61(2) (1989) 289-384.

[3] Z. Zhang, J. Guo, G. Dehm, R. Pippan, In-situ tracking the structural and chemical evolution of nanostructured CuCr alloys, Acta Materialia 138 (2017) 42-51.

Publication III

Growth-twins in CrN/AlN multilayers induced by hetero-phase interfaces

Zhuo Chen[1], Qinqin Shao[1, 2], Matthias Bartosik[3], Paul H. Mayrhofer[3], Hong Chen[4#], Zaoli Zhang[1#]

[1]Erich Schmid Institute of Materials Science, Austrian Academy of Sciences, A-8700 Leoben, Austria

[2] Center for High-Resolution Electron Microscopy, College of Materials Science and Engineering, Hunan University, 410082 Changsha, China

[3] Institute of Materials Science and Technology, TU Wien, A-1060 Vienna, Austria

[4] School of Materials Science and Energy Engineering, Foshan University, 528225 Guangdong, China

Corresponding author: zaoli.zhang@oeaw.ac.at, chenhongcs@126.com;

Abstract

We carry out a detailed transmission electron microscopy study of growth-twins in a high stacking-fault energy transition-metal nitride (TMN) multilayer comprising of 4.2 nm-thin CrN and 1 to ~8 nm-thin AlN layers. A high density of rock-salt TMN twins with $\Sigma3\{112\}$ incoherent twin boundaries (ITB) were found in the $\{111\}\|\{0002\}$ textured film area near the substrate. The extensive high-resolution transmission electron microscopy (HRTEM) observations reveal that rock-salt TMN twins with ITBs are frequently formed in wurtzite $\{0002\}$ interface with a single-atomic-layer terrace ($1\times d_{\{0002\}w\text{-AlN}}$). However, twins with ITBs were hardly observed in the wurtzite $\{0002\}$ interface with a double atomic-layer terrace ($2\times d_{\{0002\}w\text{-AlN}}$). The formation of twins with ITBs can be interpreted by the rs-CrN/w-AlN interface structure (with a mirror-symmetry)-induced thermodynamically stable nucleation. Furthermore, we see that the growth-twins with $\Sigma3$ $\{111\}$ coherent twin boundaries (CTB) appear in the non-textured film area further away from the substrate. Based on the HRTEM observations and atomic model analyses, supplemented with theoretical calculations, several nucleation modes of twins with $\Sigma3$ $\{112\}$ ITB and $\Sigma3$ $\{111\}$ CTB are proposed. These findings offer a new perspective on the formation mechanism of growth-twins in transition-metal nitride materials.

1. Introduction

Twin boundaries with $\Sigma3\{111\}$ and $\Sigma3\{112\}$ are often observed in low stacking-fault energy (SFE) *fcc* (face-centered cubic) materials [1]. Nano-twins with $\Sigma3\{111\}$ coherent twin boundary (CTB) can improve strength [2, 3], ductility [4], electrical conductivity [5] and thermal stability [6, 7]. $\Sigma3\{112\}$ incoherent twin boundaries (ITBs) have been found to play crucial roles in plastic deformation and de-twinning process in nano-twins metallic materials [7-9]. For hard materials, previous reports show that nano-twins in *c*-BN [10] and diamond [11] can significantly increase the hardness, i.e. over 100 GPa and 200 GPa by introducing a nano-twins structure in *c*-BN and diamond. Twinning in SiC nano-wires can also improve elastic strengthening [12]. The coherent twin boundaries can serve as barriers for dislocation motion or be regarded as grain boundaries, refining the grain size. The Hall–Petch relationship reveals generally the smaller the grain sizes the harder the material. Previously reported twinned *c*-BN, diamond and SiC possess excellent elastic properties, therefore, twinning is helpful for improving the hardness. Furthermore, MD simulation shows that two kinds of atoms can serve as the twin boundary (TB) atoms in rock-salt VN. In compressive deformation, the shift of TBs with V atoms to those with N atoms contributes to softening, while the pile-up of dislocations at the TBs contributes to strengthening [13].

However, twinning of transition-metal nitrides (TMN) is difficult. This could be attributed to the high SFEs of transition metal nitrides. Previous MD simulations showed that the SFE for $1/6<112>a$ is 0.85 J/m^2 for rock-salt vanadium nitride (VN) [14]. Density functional theory (DFT) reveals SFEs of rock-salt TiN, ZrN ,HfN and CrN to be about 1.10 J/m^2 [15], 1.01 J/m^2 [16],1.03 J/m^2 [16] and 1.11 J/m^2 [17], respectively. Compared with the intrinsic SFE of pure *fcc* metals, i.e. Al (0.160 J/m^2), Cu (0.045 J/m^2) Ag (0.022 J/m^2) and Au (0.04 J/m^2), the SFEs of rock-salt TMN materials are much higher. The higher SFEs in these TMN materials reflect the complex bonding structure with mixed covalent, ionic and metallic bonding. For high SFEs materials, the generation of stacking-faults and deformation twins by initiating the Shockley twinning partial dislocation needs much larger critical shear stress. Thus, twinning in rock-salt TMN by the slip of partial dislocations is more difficult.

Recently, growth-twins have also been synthesized in high-SFE *fcc* metals, such as Al thin films [18-21]. The twin formation in Al thin film was explained by a mechanism in the nucleation process of the Al crystal on the Si substrate, i.e. some of the nuclei may contain twins and occasionally certain adjacent nuclei may happen to have the twinned orientation [19]. However, the current knowledge of growth-twins in rock-salt TMN multilayer films and its formation mechanism in hetero-phase interfaces, i.e. rock-salt/wurtzite semi-coherent interfaces, is very limited. To identify the role of hetero-phase interfaces, a CrN/AlN multilayer with a steadily increasing thickness of the AlN layers while keeping the CrN layer thicknesses constant, is manufactured. Chromium nitride (CrN) only has one stable structure, being B1 (NaCl prototype, hereafter labeled '*rs*' or *rock-salt*). Aluminum nitride (AlN) has several crystal structures, a stable wurtzite-type structure (hereafter labeled '*w*') with a hexagonal symmetry, and two metastable phases with cubic symmetry: the B1 and B3 (ZnS prototype). According to previous studies, the AlN metastable phase (rock-salt) stability in multilayers depends on the layer thickness [22-24]. Some studies also have shown that the AlN phase exhibits the wurtzite-type structure when the AlN layer thickness is larger than 3-4.0 nm [23-28]. However, thinner AlN layers lead to an epitaxial stabilization of the rock-salt AlN phase in TMN multilayers [22, 24, 26]. The investigated multilayer (with alternating AlN and CrN layers) material of the present study is composed of 21 identical blocks. In each block, the AlN layer thickness is increased from 1.0 nm to 7.8 nm, while the CrN layer is always 4.2 nm thin. The thinner AlN layers crystallize in the metastable rock-salt structure while the thicker ones have the stable wurtzite structure. The 4.0-nm-thin CrN layers possess the rock-salt structure. Therefore, the layered stack can form a large number of *rs*-CrN/*w*-AlN interfaces in one block. This allows exploring the formation mechanism of rock-salt growth-twins at *rs*-CrN/*w*-AlN interfaces.

2. Experimental details

2.1. Material fabrication

The CrN/AlN gradient multilayer film [28] with a total thickness of ~2 μm is composed of 21 repeating blocks consisting of 10 bilayers with an alternative CrN and AlN layer. The thickness of the AlN layer was ~1 nm for the first bilayer and was gradually increased to the 10th layer in one block (the statistical average thickness of AlN deduced from TEM bright field images are: 1.0±0.15 nm, 1.8±0.20 nm, 2.4±0.14 nm, 3.0±0.17 nm, 4.2±0.18 nm, 4.7±0.16 nm, 5.6±0.2 nm, 6.2±0.25 nm, 7.0±0.25 nm and 7.8±0.17 nm) while the CrN layer thickness remained constant (about 4.2±0.2 nm). The film was synthesized in an AJA International Orion 5 reactive magnetron sputter system by DC powering one 2″ Cr and one 3″ Al target (both 99.6% purity,

Plansee Composite Materials GmbH, Austria) at 500 °C substrate temperature in an Ar/N$_2$ gas mixture (flow ratio of 5 sccm Ar/5 sccm N$_2$) at a total pressure of 0.4 Pa. The chosen power densities of ~12.3 (Cr target) and ~11.0 W/cm^2 (Al target) resulted in the deposition rates of ~10 and ~24 nm/min for CrN and AlN, respectively. The nano-layer structure was realized using computer controlled shutters, which were mounted in front of the permanently running targets. To achieve a dense coating morphology, a bias voltage of -50 V was applied to the growing film during the deposition process (floating potential was ~ -20 V). The substrate holder rotated with a constant rotation speed of ~1 Hz throughout the whole process. Prior to the deposition, the polished Al$_2$O$_3$ (1$\overline{1}$02) substrate (10×10 × 0.5 mm^3) were ultrasonically pre-cleaned in acetone and ethanol for 5 min each, thermally cleaned at 500 °C for 20 min inside the evacuated deposition chamber (base pressure at room temperature was ~5×10^{-4} Pa), and Ar-ion etched for 10 min at the same temperature in an Ar atmosphere at a pressure of 6 Pa by applying a constant bias voltage of -750 V to the substrate.

2.2. Material characterization

Cross-sectional TEM specimens were prepared using a standard TEM sample preparation approach including cutting, grinding and dimpling. Ar ion milling was carried out at a voltage of 4.0 kV with an angle of 6°, followed by a final low voltage ion-milling of 2.5 kV with an angle of 2°.

The morphology of the film was examined by bright/dark-field imaging and selected-area electron diffraction (SAED) using a Philips CM12 transmission electron microscope working at an accelerating voltage of 120 kV. A 200 kV field emission TEM/STEM (JEOL2100F) equipped with an image-side C_S-corrector was used in this study, which demonstrates a resolution of 1.2 Å at 200 kV. The aberration coefficients were set to be sufficient small under which the HRTEM images were taken under slightly over-focus conditions (close to Scherzer defocus).

The width distribution of rock-salt twins (with ITBs) from the 1th to 4th block was statistically analyzed using HRTEM images recorded at 400-800K magnification. About 45 HRTEM images and 90 twins (with ITBs) were used for determining the distribution of grain width. The quantitative determination of the interface terrace was carefully carried out by fitting intensity line profiles using a Gaussian function taken from the *rs*-CrN {111} to the *w*-AlN {0002} layer. Following the approach described in Refs [29, 30], the interface terrace can be located and its size quantitatively determined when using the interplanar spacings to distinguish between CrN

and AlN, respectively. The {111} and {0002} plane spacings were carefully determined and plotted as a function of the distance over about 1.7 nm across the interface (7 interplanar spacings).

The angle between the growth and the out-of-plane direction [1$\bar{1}$02] of the Al$_2$O$_3$ substrate, defined as the misorientation angle of the growth direction, was determined from HRTEM images taken at 300-600K magnification from the 1st block to the 21st block. About 50 CrN grains in the 1st to 4th block and 140 CrN grains in the 5th to 21st block were counted to determine the distribution of the misorientation angles of the growth directions.

2.3. DFT calculation

First principles calculations were performed using the Vienna Ab initio Simulation package (VASP) [31, 32] employing projector augmented pseudopotentials [33] and the exchange-correlation potential within the Perdew-Burke-Ernzerhof-parameterized generalized gradient approximation (GGA-PBE) [34]. The plane wave energy cut-off was set to 350 eV. The reciprocal space was sampled with an equivalent of ~1600 k-points per single-atom cell using the Monkhorst-Pack mesh, and the number of k-points was decreased correspondingly depending on the actual cell-size. Using DFT, we evaluated the interface formation energy of two non-identical rs-{111}||w-{0002} interfaces (from model (iv) and ($\bar{\bar{ii}}$)). To calculate the interface energy of rs-CrN/w-AlN, the following equation is used, i.e. $E_I^{CrN} = (E_t\text{-}E_{bulk}^{CrN} - E_{bulk}^{AlN})/2{*}A$, where E_t denotes the total energy of the rs-CrN/w-AlN superlattice, E_{bulk}^{CrN} is the total energy of the corresponding bulk rs-CrN and w-AlN, and A is the surface area.

3. Results

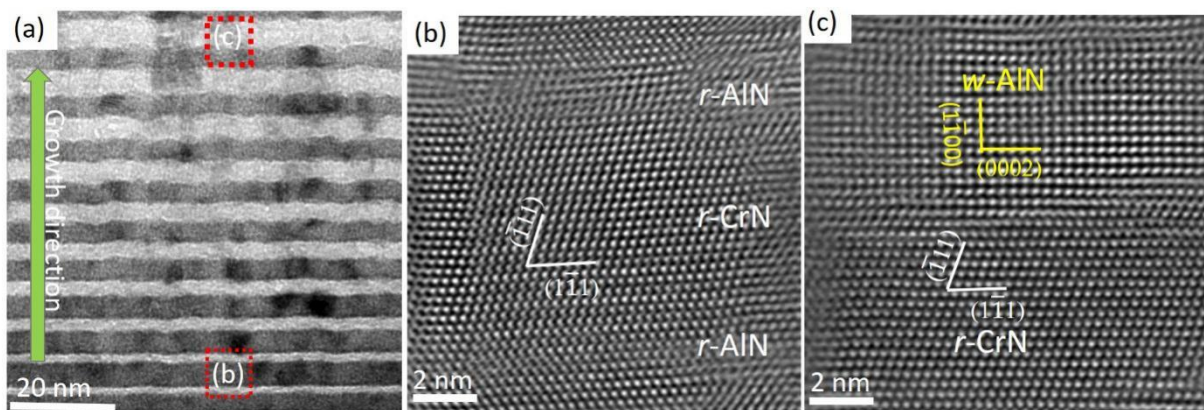## 3.1 Hetero-phase interface in the CrN/AlN multilayer

Fig. 1. (a) Cross-sectional TEM bright-field image taken from the 3rd block. The growth direction is marked with a green arrow. The locations for HRTEM images Fig. 1(b) and Fig. 1(c) are labeled with red frames. (b) and (c) are typical HRTEM images of *rs*-CrN/*rs*-AlN interfaces and *rs*-CrN/*w*-AlN interfaces recorded from the labeled areas in (a).

Since the AlN phase stability is thickness-dependent, two different phases can be readily detected in the current multilayer, i.e. metastable rock-salt AlN and stable wurtzite AlN [28]. The bright-field image (Fig. 1(a)) clearly reveals the increasing thicknesses of the AlN layers (along the growth direction) in one block. The layers with bright contrast are AlN, while the layers with dark contrast are CrN. In the thinner AlN layers (about 1-2 nm thickness), HRTEM (Fig. 1(b)) indicates that AlN exhibits the metastable rock-salt structure. The coherent $\{111\}[1\bar{1}0]_{rs\text{-}AlN}\|\{111\}[1\bar{1}0]_{rs\text{-}CrN}$ interface structure can be found. In the thicker AlN layer (about 7.3 nm), HRTEM (Fig. 1(c)) indicates that AlN possesses the thermodynamically stable wurtzite structure. The *rs*-CrN/*w*-AlN interface is semi-coherent, $\{111\}[1\bar{1}0]\|\{0002\}[11\bar{2}0]$. Our previous studies on the stability of rock-salt AlN already showed that the maximum layer thickness of rock-salt AlN is about 2-4 nm [28]. Thus, for thicker AlN layers, AlN should crystallize in the wurtzite structure and there should be many wurtzite/rock-salt interfaces accordingly.

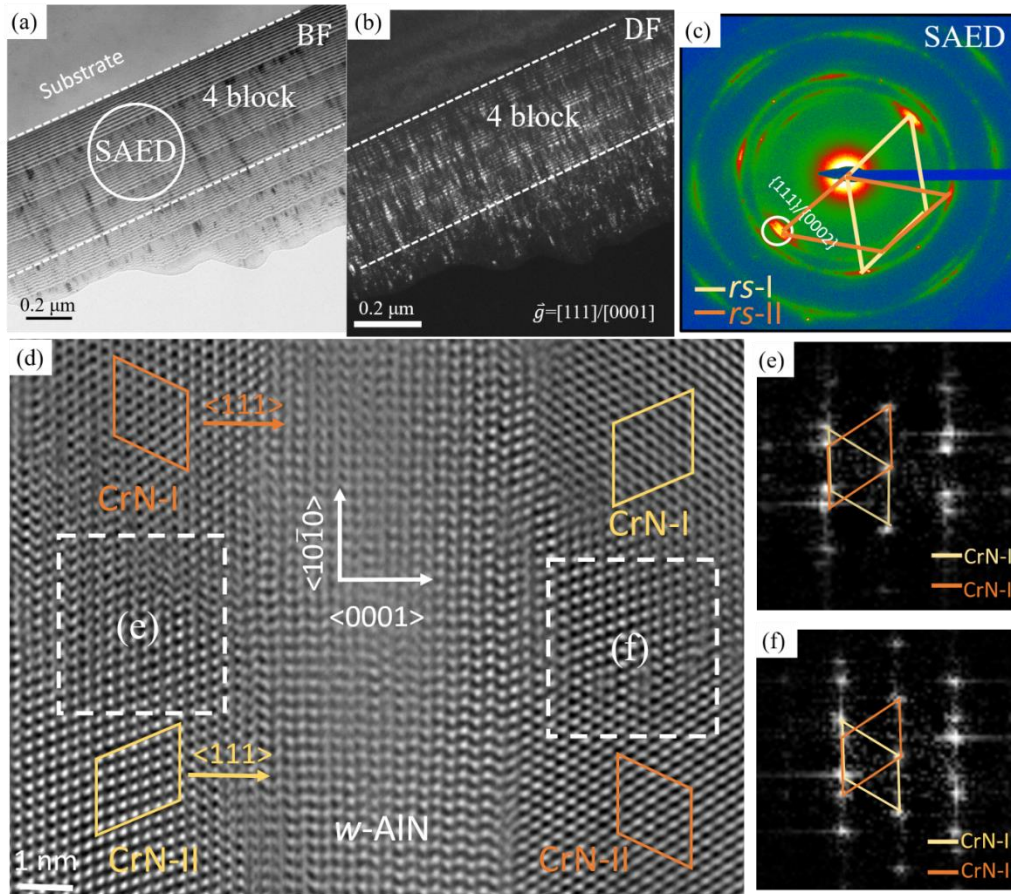## 3.2 Twins (with ITBs) in the textured film area near the substrate (block 1-4)

Fig. 2. (a) and (b) TEM cross-sectional bright-field and dark-field images from the 1st to 6th block area (dark-field images taken from the (0002)/(111) reflection). (c) is a corresponding selected area electron diffraction pattern (aperture position as shown in Fig. 2(a)). (d) HRTEM image of the *rs*-CrN/*w*-AlN multilayer structure in the second block. (e) and (f) are corresponding positions for Fast Fourier Transform (FFT) images.

In order to investigate the morphology and growth orientation of the multilayer, the TEM cross-sectional sample was characterized from bright/dark-field images (BF/DF) and selected-area electron diffraction (SAED). The SAED pattern of the CrN/AlN multilayer taken from a film area near the substrate (labeled in Fig. 2(a)) indicates a textured growth of $\{111\}_{rs}\|\{0002\}_w$ (as confirmed by a high symmetry of strong diffraction dots in Fig. 2(c)). It means that the strong growth direction reflection is the $\{111\}_{rs}\|\{0002\}_w$ reflection. Fig. 2 (b) is a DF image (using the $\{111\}\|\{0002\}$ reflection, i.e. white circle position in Fig.2(c)) reflection, showing the pronounced texture in the area near the substrate (from 1st to 4th block, far away from the substrate 380nm). However, the texture gradually disappears over the 4th block, as proven by polycrystalline diffraction rings shown in Fig. S1 (supplementary material).

103

A close examination of the SAED pattern (Figure 2(c)) reveals that the rock-salt phase grains mainly have two sets of orientations, i.e. as shown in Fig. 2(c) rs-I and rs-II, which also indicates a mirror-symmetric relationship between two sets of rock-salt orientations, i.e. the rock-salt twin relation. Fig. 2(d) shows an atomic resolution image of rs-CrN/w-AlN interfaces in the 2nd block (viewing along [110]/[11$\bar{2}$0]), where the intermediate layer is w-AlN. The orientation relationship of rs-CrN and w-AlN layer in Fig. 2(d) is in agreement with SAED, i.e. {111}<110>$_{rs\text{-CrN}}$ ∥{0002}<11$\bar{2}$0>$_{w\text{-AlN}}$. Further examination of two rs-CrN layers, each layer exhibits two twin-related grains (Fig. 2(d) as labeled CrN-I and CrN-II) with ITBs, in which the twin-related orientation is confirmed by FFT images in Figs. 2(e) and (f).

Taken together the results in Section 3.1 and Section 3.2, and extended HRTEM observations, we summarize as follows: in this gradient multilayer, rs-CrN may contain several possible types of interfaces, including the rs-CrN/rs-AlN coherent interface (e.g. Fig. 1(b)), rs-CrN/substrate-Al_2O_3 incoherent interface (e.g. Fig.S2 in the supplementary materials), rs-CrN{111}/w-AlN{0002} semi-coherent interface and rs-CrN/w-AlN incoherent interface (e.g. Fig.S3 of supplementary materials). However, only in the semi-coherent interface of rs-CrN{111}/w-AlN{0002} the rock-salt twins with Σ3{112} ITB can be found.

This means that: 1) growth twins in rs-CrN are present only on thermodynamically stable w-AlN, not on the metastable rs-AlN layer; 2) no rock-salt growth twins in rs-AlN or w-AlN layers are found.
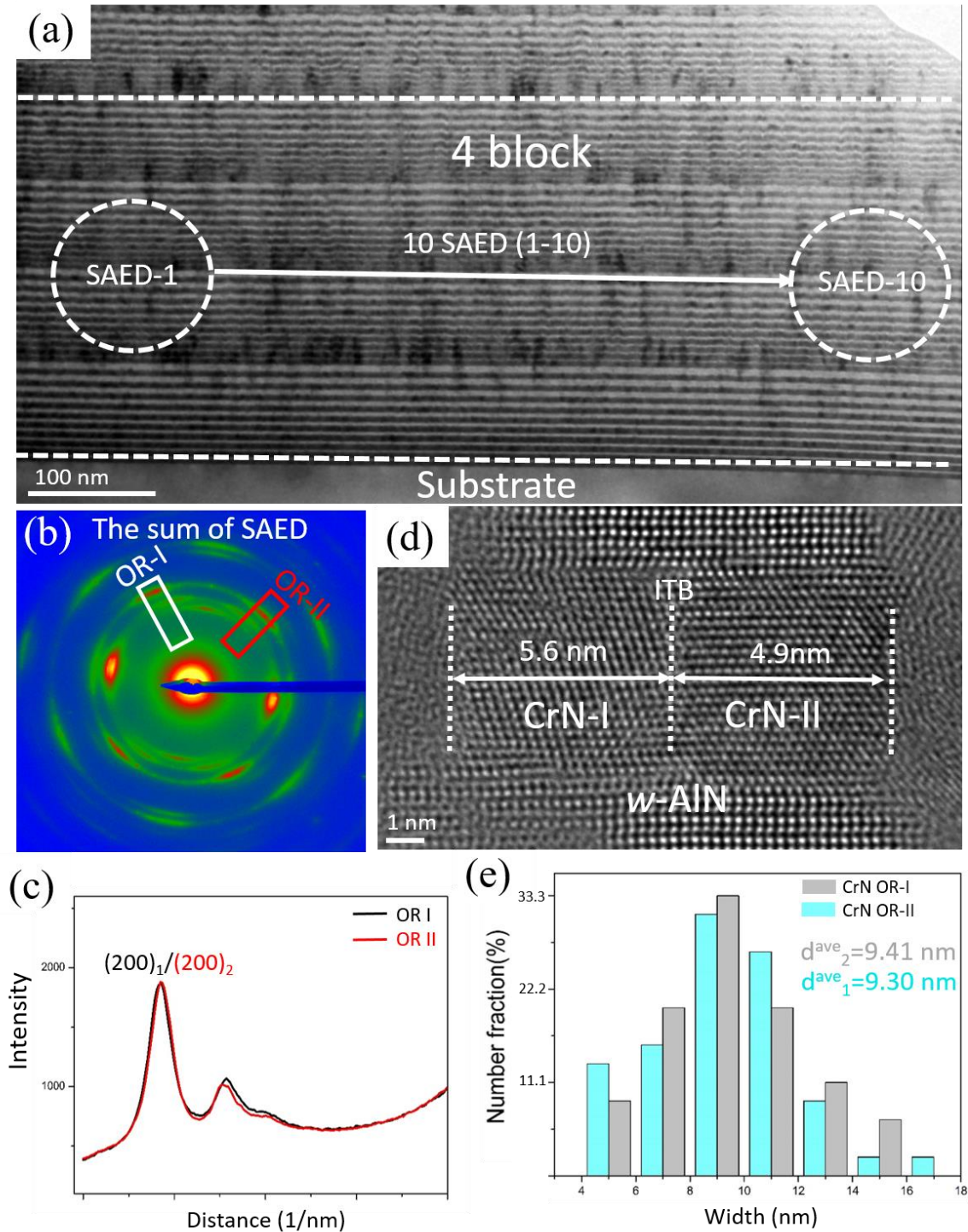
Fig. 3. (a) Cross-sectional TEM bright-field image. The positions of 10 SAED patterns recorded along the arrow are shown in Fig. 3(a). (b) Electron diffraction pattern obtained by summing up the SAED patterns from 10 different positions in the textured film area. Two line profiles are used to show twin-related rock-salt grains. The absolute intensities of the {200} reflections are very similar. (c) Two line profiles result from traces in Fig. 3(b) (from two strong {200} reflections). (d) HRTEM image of CrN twins (with ITBs) with well-defined grain shape taken

105

from the second block. (e) Histogram distributions of CrN twins (with ITBs) width, acquired by HRTEM statistics result from the 1st to 4th block.

In the strongly textured area (near the substrate), interestingly the twin related rock-salt grains (OR-I and OR-II) are similar in size and ratios. Fig. 3(a) depicts a bright-field image taken from the first to the 5th block, and the positions of 10 SAED patterns recorded from left to right between the 2nd and 3rd block (selected area aperture is about 150 nm). The sum of the 10 SAED patterns stems from a larger diffraction area. In Fig. 3(b), the twin orientation of the rock-salt phase becomes obvious. The intensity line profile (as shown in Fig. 3(c)) from traces in Fig. 3(b) shows two strong reflections from rock-salt $(200)_1$ and $(200)_2$ (two twin-related orientations with an angle of 70.52°) having a similar diffraction intensity. Considering that our multilayer is a polycrystalline film, most grain sizes are less than 17 nm. The similar diffraction intensity of $(200)_1$ and $(200)_2$ reflections can to a certain extent indicate that the number of rock-salt grains with twin-related orientations is nearly identical. Thus, a high density of twins with ITBs can be found in the strongly textured film area.

According to our extensive HRTEM observations (about 90 CrN twins), twin-related rock-salt grains are also similar in grain size as demonstrated in Fig. 3(d), in which a HRTEM image of a CrN twin (with an ITB) is shown. The two CrN grains are approximately equal in size. The measured width is about 5.6 nm and 4.9 nm. Fig. 3(e) plots the width distribution of two types of CrN grains with twin-related orientations. The average grain widths of the two twin-related CrN grain types are 9.30 ± 2.60 nm and 9.41 ± 2.50 nm, respectively. As the thickness of all CrN layers is identical, the twin-related CrN grains have similar grain sizes on average.

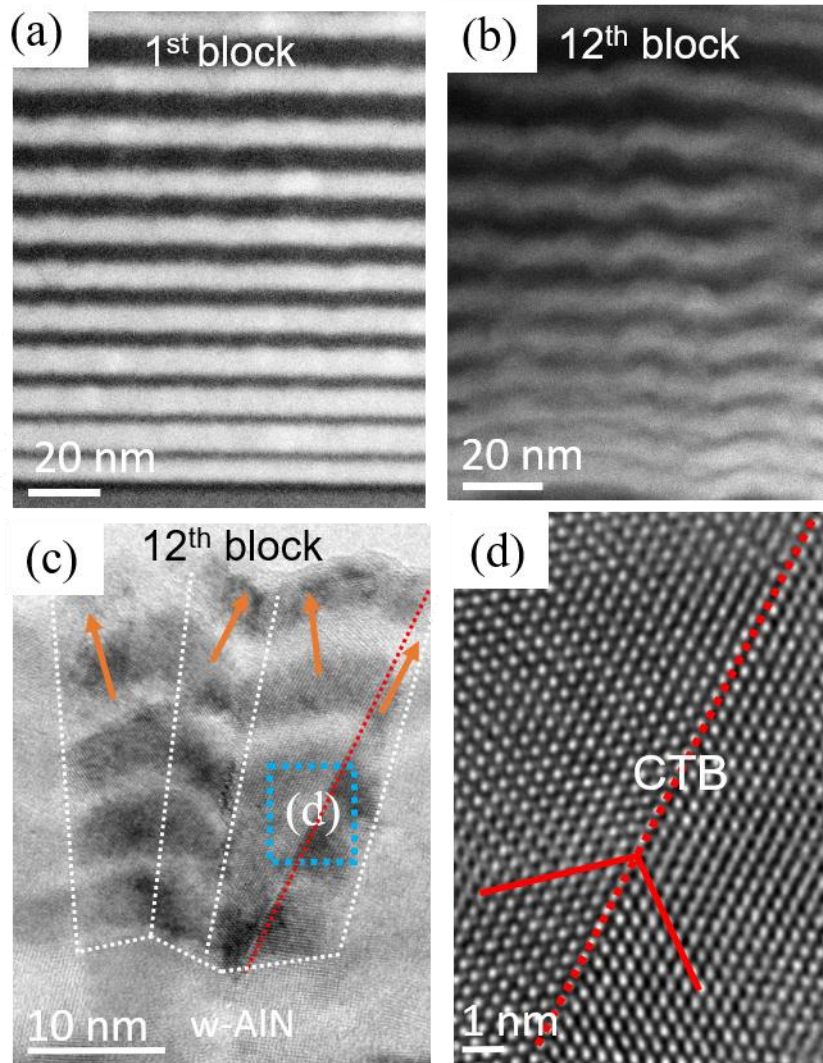## 3.3 Twins (with CTB) in the non-textured film area (block 5-12)

Fig. 4. (a) and (b) Cross-sectional HAADF images taken in the 1st block and 12th block, respectively. (c) A cross-sectional TEM bright-field image recorded at the film area far from the substrate, showing several *rs*-CrN/*rs*-AlN columnar grains growing on a *w*-AlN layer. The growth directions of the columnar grains are labeled (shown in Fig. 4(c)) by orange arrows. White dotted-lines indicate the contour of *rs*-CrN/*rs*-AlN columnar grains. (d) HRTEM image of grain boundary structure of columnar grains from the framed area in (c) showing the $\Sigma3\{111\}$ CTB.

In Sec. 3.2, we showed that a high density of twins with ITBs is present in the strongly textured film region (close to the substrate). For the non-textured area (far away from the substrate), twins with $\Sigma3\{112\}$ ITB are barely detected, instead, some $\Sigma3\{111\}$ CTBs occasionally appear.

107

The HAADF image (Fig. 4(a)) clearly shows that the interfaces in the 1st block are quite smooth. However, with increasing block numbers, the layers possess a wavy-like morphology (Fig. 4(b)). The transition from the smooth to the wavy-like layer morphology can be rationalized by the growth condition change, i.e. particle flux, residual stress [35], substrate temperature [36, 37]. In addition, we also consider if the random or preferred growth orientation may affect the interface roughness. As the growth rate of a grain in a thin film is related to its surface energy [38], the random (non-textured area, far from the substrate) or the preferred growth orientation (textured area, close to the substrate) appear to have different growth rates due to the surface energy anisotropy of CrN and AlN [39, 40]. The resultant wavy-like morphology of films may come from combined effects of all these factors.

Fig. 4(c) illustrates a low magnification image of the *rs*-CrN/*rs*-AlN multilayered columnar grain structure (with the metastable cubic phase in the thinner AlN layers) grown on a *w*-AlN layer in the non-textured area. The HRTEM image in Fig. 4(d) shows the formation of Σ3{111} CTB. We note that the Σ3{111} CTB originates from the sub-layer *w*-AlN, indicating that the rock-salt twin with Σ3{111} CTB is directly grown on the *w*-AlN wavy-like surface. Such wavy-like surface leads to a large misorientation angle of the subsequent growth direction. Thus, it is believed that such higher misorientation angle in growth direction between rock-salt columnar grains (growth directions are labeled in Fig. 4(c)) may play a dominant role in CTB formation. This will be further discussed in Sec. 4.2.

3.4 Formation mode of the twin boundaries
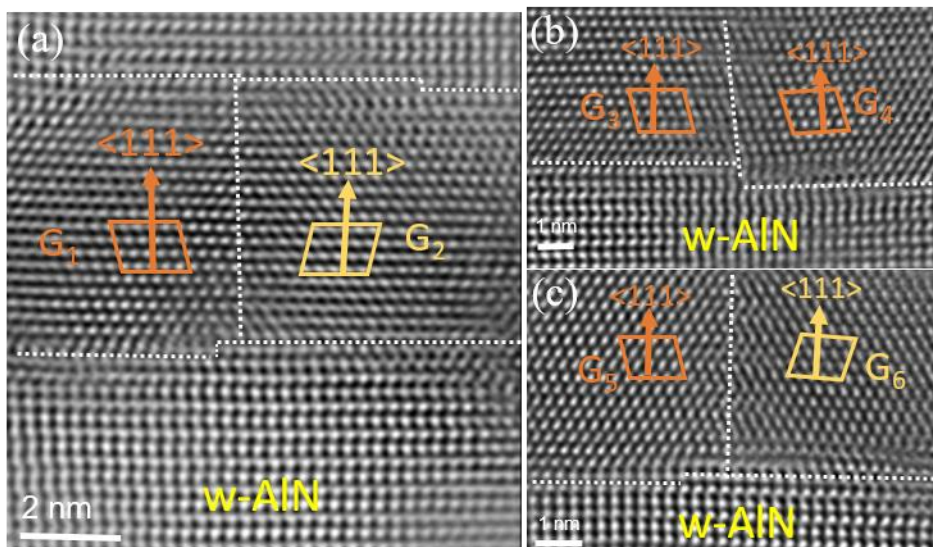
3.4.1 Σ3{112} ITB formation mode

Fig. 5. (a) HRTEM image of a symmetric Σ3{112} ITB-CrN taken in the first block. (b) HRTEM image of *Σ1 GB*-CrN taken in the 4th block. (c) HRTEM image of asymmetric Σ3 GB-CrN taken in the 4th block. Note that twin-related orientations of CrN were labeled by rhombus mark with different colors. 'G$_1$…G$_6$' symbols stand for different grains.

In this section, we will mainly analyze the Σ3{112} ITB formation mode in the textured film region. According to our HRTEM observations, mainly three different grain boundaries (GBs) structures exist between the rock-salt grains, which are: the symmetric tilt Σ3{112} ITB, or the *Σ1 GB,* or the Σ3 asymmetric tilt GB (several degree tilt from the Σ3{112} ITB).

The HRTEM image (Fig. 5(a)) indicates that two CrN grains (G1 and G2 grains) have the same growth direction (as labeled by colored arrows), i.e. between the two {111} growth planes the misorientation of G1 and G2 is 0°. Thus, this is a symmetric tilt Σ3{112} ITB (Fig. 5(a)). Fig. 5(b) shows two CrN grains without twin-related orientation. The misorientation angle between two {111} growth planes are 3.2°±0.1° (i.e. between G3 and G4 grains). Hence, we see a *Σ1 GB* (Fig. 5(b)). Fig. 5(c) shows the asymmetric tilt Σ3 GB (tilted several degrees away from the Σ3{112} ITB) in two twin-related CrN grains. The misorientation between two {111} growth planes is about 3.0°±0.1° (i.e. between G5 and G6). Note that the two sub-layers of the G1 and G2 grains, i.e. the *w*-AlN {0002} growth plane, do not show any misorientation. Correspondingly, the misorientation angles of the two sub-layers for G3/G4 and G5/G6 grains are 3.4°±0.1° and 2.8°±0.1°, respectively. Comparing the misorientation angles of growth planes in the *rs*-CrN grains and sub-layers (*w*-AlN {0002}), similar angles exist between the *rs*-CrN and *w*-AlN growth direction, which suggests that the *rs*-CrN/*w*-AlN interfaces maintain a well-matched relationship (as seen in Figs. 5 (a)-(c)), e.g. the CrN-{111} interface plane is almost parallel to the AlN{0002} interface plane. These results indicate that whether or not a symmetric Σ3{112} ITB forms is related to twin orientation variants and misorientation angles in growth direction.

To summarize, no misorientation of the growth directions can lead to a symmetric tilt Σ3{112} ITB formation, while a small misorientation angle results in an asymmetric tilt Σ3{112} ITB.
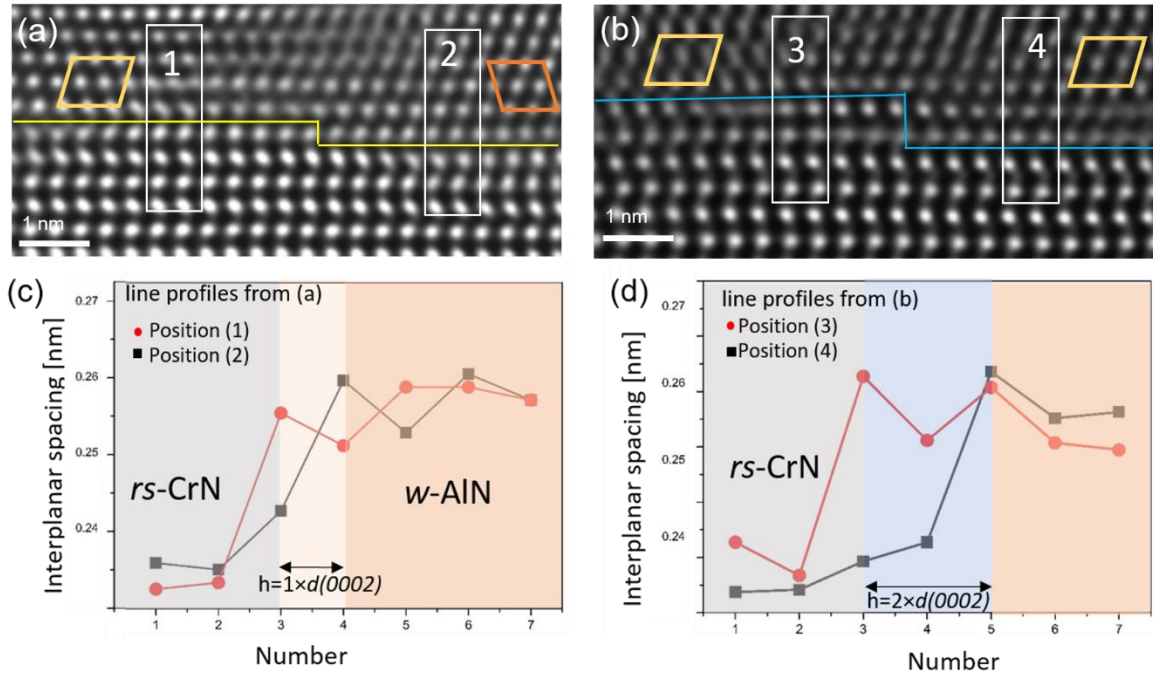
Fig. 6. (a) HRTEM images of a single atomic-layer terrace in the *rs*-CrN/*w*-AlN interface. The twins with ITBs can be found in the CrN layers. (b) HRTEM images of a double atomic-layer terrace in the *rs*-CrN/*w*-AlN interface. In this case, there is no twin detected in the CrN layers. (c) Two intensity line profiles obtained by integrating over the framed regions in (a). (d) Two intensity line profiles obtained by integrating over the framed regions in (b).

For twin orientation variants, Fig. 6 shows two atomic-resolution TEM images of the $\{111\}_{rs\text{-}CrN} \| \{0002\}_{w\text{-}AlN}$ interface terrace, one of which are with a single atomic-layer terrace (Figs. 6(a), $1 \times d_{\{0002\}w\text{-}AlN}$) and the other with a double atomic-layer terrace (Figs. 6(b), $2 \times d_{\{0002\}w\text{-}AlN}$). To see the interface terrace in a more precise way, atomic quantitative line profile analysis was applied. The interplanar spacing in *rs*-CrN $\{111\}$ is 0.2394 nm (JCPDS 11-0065) and in *w*-AlN $\{0002\}$ is 0.2495 nm (JCPDS 25-1133). Two quantitative measurement results are shown in Figs. 6(c) and (d). The larger interplanar spacings (about 0.250-0.265 nm) are from the *w*-AlN side, whereas the smaller spacings (about 0.233-0.250 nm) are from the *rs*-CrN side. At the interface, the spacing variations become out of step, depending on the interface terraces. Thus, via comparing two spacing profiles crossing the interface the single atomic-layer terrace or double atomic-layer terrace in *w*-AlN $\{0002\}$ surface can be easily identified. Interestingly, HRTEM observations (Figs. 6(a)) further reveal that rock-salt twins (with ITB) can be found on a single atomic-layer terrace. However, no rock-salt twins were found on a double atomic-layer terrace (Figs. 6(b)).

110

Together with other extended HRTEM observations, we speculate that the single atomic-layer interface terrace may facilitate the formation of twin orientation variants. The effect of w-AlN {0002} terraces on twin orientation variants will be addressed in Sec.4.1.

3.4.2 Σ3{111} CTB formation mode

In the non-textured area (far from the substrate area, from the 5th block on), twins with Σ3{111} CTB can be occasionally observed. Figs. 7(a) and (b) present rs-CrN/rs-AlN columnar grains (G7-G10) grown on w-AlN layers with Σ3{111} CTBs (as labeled). Compared to the Σ3{112} ITB (shown in Sec. 3.4.1), much larger misorientation angles of the growth directions are found for Σ3{111} CTBs, i.e. the misorientation angles of the growth direction for G7/G8 and G9/G10 are 15.0±0.1° and 39.7±0.1°, respectively. In the textured film area, most of the rs-CrN/w-AlN interfaces have the {111}[110]∥{0002}[11$\overline{2}$0] orientation relationship (as proven by the SAED pattern in Fig. 2(c)). Here, in the non-textured area, however, a variation of the rs-CrN/w-AlN interface structures can be found, i.e. the {002}$_{rs\text{-CrN}}$∥{0002}$_{w\text{-AlN}}$ interface orientation is observed (Fig. 7(a), see CrN G7 and w-AlN). Similar to the above {002}∥{0002} interface, a HRTEM image of the rs-CrN/w-AlN interface with an orientation relationship of {002}[110] $_{rs\text{-CrN}}$ ∥{0002}[11$\overline{2}$0]$_{w\text{-AlN}}$ is shown in Fig.S3 (supplementary material). In G8, G9, and G10 columnar grains, their rs-CrN/w-AlN interfaces have the {111}∥{0002} interface relationship. Hence, in Fig. 7(a), the crystallographic growth orientation for the G7 grain is along the rock-salt <100> direction (yellow label), while for the G8 grain it is along the rock-salt <111> direction. In Fig. 7(b), G9 and G10 have the same crystallographic growth orientation (both along the rock-salt <111> direction).

As the current knowledge on the rock-salt/wurtzite interface structure variation is limited [41-43], the observed {002}∥{0002} interface formation can be simply ascribed to the change of growth conditions in the area far away from the substrate, i.e. substrate temperature, incident particle flux direction, or residual strain change etc. Furthermore, considering that the {100} lattice plane of the rock-salt TMN material usually has the lower surface energy as compared to the {111} lattice plane [44, 45], the {002}∥{0002} interface formation significantly reduces the surface energy and minimizes the total energy. All may explain the presence of some columnar grains exhibiting the <100> crystallographic growth orientation in the wavy-like regions.

To summarize all the results, we found that CTB twins have different formation modes in the non-textured film area. The main differences compared to Σ3{112} ITB formed in the textured area are listed as follows:

(a) The Σ3{112} ITB formation mode occurs when two rock-salt grains have the same <111> growth direction. The Σ3{111} CTB have two possible crystallographic orientation modes: (i) one of the rock-salt grain has the <100> growth direction and the other rock-salt grain the <111> growth direction; and (ii) both rock-salt grains have the <111> growth direction.

(b) The Σ3{112} ITB (symmetric tilt) formation needs two rock-salt grains having 0° misorientation of the growth direction, a small misorientation angle in growth direction results in an asymmetric tilt Σ3{112} ITB formation. However, Σ3{111} CTB formation needs two rock-salt grains having a larger misorientation angle in growth direction.

(c) The density of twins with ITBs is much higher in the textured area while the density of twins with Σ3{111} CTB is much lower in the non-textured area.

(d) The Σ3{112} ITB formation in the textured area is related to the emergence of interface atomic terraces.

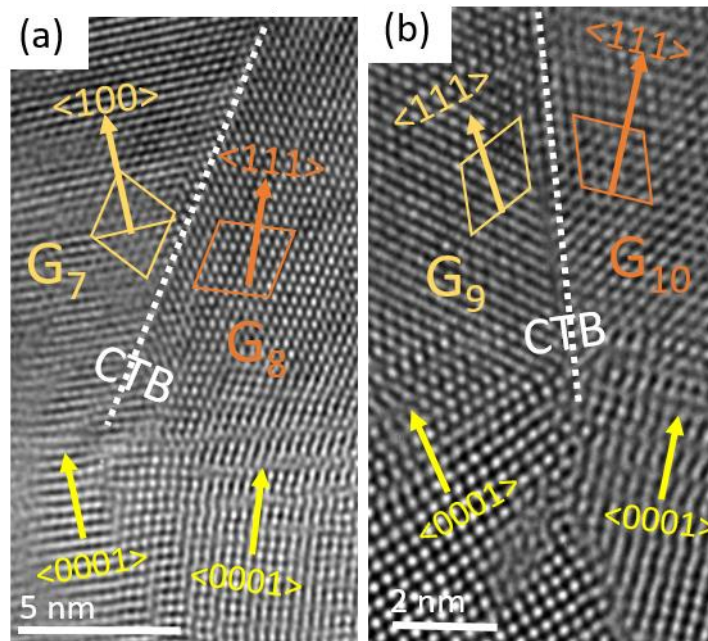Fig. 7. (a) HRTEM image of *rs*-CrN/*rs*-AlN columnar grains with Σ3 {111} CTB growth on a *w*-AlN layer (in the 6th block). The crystallographic growth orientations of columnar grains are <100> (G7) and <111> direction (G8). The misorientation angle of the growth directions

between G7 and G8 is about 15.0±0.1°. (b) HRTEM image of *rs*-CrN/*rs*-AlN columnar grains with Σ3 {111} CTB grown on a *w*-AlN layer (in the 10th block). The crystallographic growth orientations of the columnar grains are the <111> direction (G9 and G10). The misorientation angle of the growth directions between G9 and G10 is about 39.0±0.1°.

4. Discussion

4.1 Twin orientation variants on hetero-phase interfaces

Previous studies demonstrated that the critical shear stress of a partial dislocation is related to the SFE, the grain size, the shear modulus and the burgers vector [46]. Previous reports show that during island growth, an interface traction arises between the island and the substrate[21, 47]. The large enough shear stresses may nucleate full and partial dislocations. Hence, the traction near the island edge may provide sufficient stress to nucleate Shockley partial dislocations, stacking fault and twins at the interface. However, the previous results are based on *fcc* metal Al, whose SFEs is about 160 mJ/m^2. For the high SFE CrN, it is much more difficult to form twins through interface mismatch stress compared to *fcc* metals. Meanwhile, no stacking faults were observed in our extensive HRTEM observations. For rock-salt twins of TMN, it is difficult to nucleate through shear stresses.

Thus, it is reasonable to speculate that the frequently observed rock-salt twins in current TMN multilayer materials are mainly from the nucleation process on the hetero-phase interface. We note that similar growth-twins with ITBs can also be found in *fcc*-metal thin films on a hcp-Al$_2$O$_3$ {0006} substrate, such as Cu [48-50], Pt [51] [52] and Al [48, 53-56] monolithic films. However, twins with ITB formation on the{111}∥{0002} TMN interface is unexplored, which should be associated with the interface atomic structure.

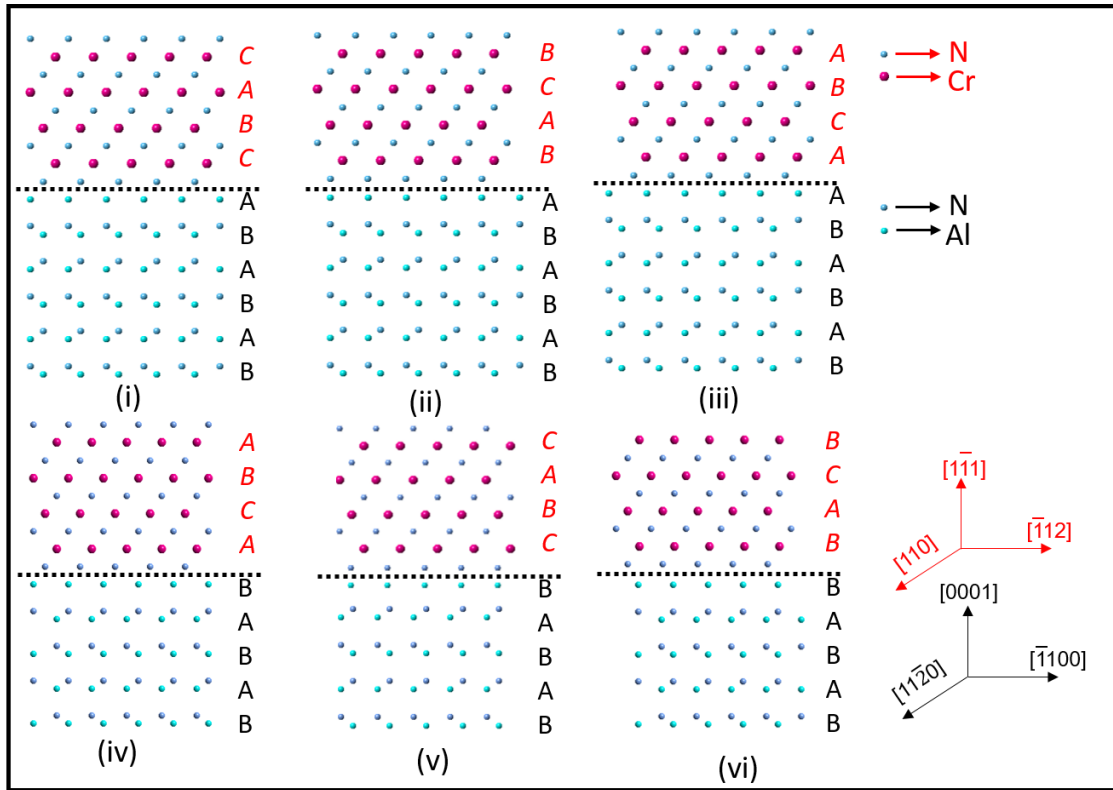## 4.1.1 Interface structure with a single atomic-layer terrace

Fig. 8. Atomic models of six different $\{111\}_{rs\text{-}CrN}||\{0002\}_{w\text{-}AlN}$ interfaces. The projection is along the rs-CrN [110] and w-AlN[11$\overline{2}$0]. The black dotted lines are separating planes.

As known, a relative small difference in the interface energy might be sufficient to produce a strong preference for one of the orientation variants during nucleation. In other words, the same interface energy for two twin-related orientation variants will be the thermodynamically favorable case for twin-island nucleation. In this section, we demonstrate the likely $\{111\}_{rs\text{-}CrN}||\{0002\}_{w\text{-}AlN}$ interface structure and the energy for twins on the w-AlN $\{0002\}$ single atomic-layer terrace (h=1×$d_{\{0002\}w\text{-}AlN}$). The key point is to understand why twin islands can nucleate, and why twins are more energetically favorable than other crystallographic features (dislocations, stacking faults, low-angle GB etc.) on a single atomic-layer terrace.

First, we present several different $\{111\}_{rs\text{-}CrN}||\{0002\}_{w\text{-}AlN}$ interface atomic stacking structures. The stacking sequence of the rs-CrN is AβBγCα (along the <111> direction) and the stacking sequence of the w-AlN is AβBα (along the <0001> direction). They are crystallographically equivalent but not identical. For the $fcc\{111\}||hcp\{0002\}$ interface, 6 different candidate interfaces are presented in Fig. 8 (i)-(vi) (based on lower surface energy Al (0001) plane as the interface [44]), which include $\alpha_{(fcc)}$/A$_{(hcp)}$, $\gamma_{(fcc)}$/A$_{(hcp)}$, $\beta_{(fcc)}$/A$_{(hcp)}$, $\beta_{(fcc)}$/B$_{(hcp)}$, $\alpha_{(fcc)}$/B$_{(hcp)}$ and

$\gamma_{(fcc)}/B_{(hcp)}$ or, if only metal layers are noted (for simplicity), $C_{(fcc)}/A_{(hcp)}$, $B_{(fcc)}/A_{(hcp)}$, $A_{(fcc)}/A_{(hcp)}$, $A_{(fcc)}/B_{(hcp)}$, $C_{(fcc)}/B_{(hcp)}$ and $B_{(fcc)}/B_{(hcp)}$ interfaces [57].

Secondly, we turn to the $\{111\}_{rs\text{-}CrN}\|\{0002\}_{w\text{-}AlN}$ interface stacking structure with a single atomic-layer terrace. The HRTEM image in Fig. 9(c) shows two twin-related CrN grains grown on the w-AlN (0002) plane. Close examination of the interface structure shows that there is one single atomic-layer terrace in the rs-CrN/w-AlN interface. Two enlarged atomic images of the hetero-phase interface (Fig. 9(c), position 1 and 2) show that the interface stacking sequences (when only noting the metal layer positions of rs-CrN and w-AlN) are $ACB(rs\text{-}Cr)/AB(w\text{-}Al)$ and $BCA(rs\text{-}Cr)/BA(w\text{-}Al)$, respectively, which fits with the proposed atomic model (iv) in Fig. 8. Moreover, according to the experimental observations, the constructed interfacial atomic model (Fig. 9(b)) indicates two stacking sequences of the upper and down of the rs-CrN/w-AlN interface, i.e. models ($\overline{\text{iv}}$) and (iv), have a mirror-symmetric relationship. In other words, the model (iv) is projected along $[110]\|[11\overline{2}0]$ while the model ($\overline{\text{iv}}$) is projected along $[\overline{1}10]\|[\overline{1}1\overline{2}0]$, mirrored with model (iv). To conclude, an important result is obtained, namely, that the complete same rs-CrN/w-AlN interface stacking sequence with the identical interface energy is found at the interface position 1 and 2 (corresponding to the upper and lower interface of the single-layer terrace).

Thirdly, we consider the likely nucleation mechanism of CrN twins with mirror-symmetric hetero-interfaces on a single atomic-layer terrace. Experimentally, three possible GBs of CrN in $\{111\}_{rs\text{-}CrN}\|\{0002\}_{w\text{-}AlN}$ textured area were found, i) symmetric tilt $\Sigma3\{112\}$ ITB, i.e. Fig. 5(a); ii) low-angle GB, i.e. Fig. 5(b); iii) asymmetric tilt $\Sigma3\{112\}$ ITB, i.e. Fig. 5(c). Theoretically, the energy of $\Sigma3\{112\}$ ITB (including symmetric and asymmetric tilt) is higher than that of the low-angle GB. From the total energy point of view, ITB growth mode appears thermodynamically unstable. At the initial stage of growth, the crystal nucleus is very small, and therefore, the crystal nucleus does not have an ITB during the nucleation process (as seen schematic image in Fig. 9(d)).

For single layer terrace, there are two possibilities for CrN growth. (a) Matrix formation on single layer w-AlN terrace (as seen the schematic image in Fig. 9(a)). The orientation of the upper and down positions of the terrace are consistent. However, due to the interface stacking sequence variants, the interface structure of upper and lower positions of the terrace are model ($\overline{\text{iv}}$) and ($\overline{\overline{\text{ii}}}$), respectively. (b) Twin formation on single-layer w-AlN terrace (as seen the schematic image in Fig. 9(b)). Due to the mirror-symmetric interface, which is no change in interface structure at upper and lower positions of terrace. The interface structure of upper and

lower positions of the terrace are consistent, i.e. both are model (iv) (as seen HRTEM Fig. 9(c)). Refer to the previous reports [19, 58, 59], we propose to compare the nucleation radius ability of different models. In matrix mode, the total Gibbs free energy for upper and lower position are different because of the creation of different interface structure (different interfaces have different interface energies). The total Gibbs free energy of a disc-shaped 'matrix' nucleus on single-layer terrace upper (interface model iv) and down positions (interface model ii) are given as:

$$\Delta G_{up} = 2\pi rh\gamma - \pi r^2 h \Delta G_v \tag{1}$$

$$\Delta G_{down} = 2\pi rh\gamma - \pi r^2 h \Delta G_v + \pi r^2 \Delta\gamma_i \tag{2}$$

Where the r and h are the respective nucleus radius and height. γ is the surface energy and ΔG_v is the bulk free energy difference between solid and vapor per unit volume driving the nucleation. $\Delta\gamma_i$ is the interfacial energy different between the interface model (iv) and (ii). Although the *rs*-{111}||*w*-{0002} interface structure is quite similar for model (iv) and (ii), the DFT calculated interface formation energies are obviously quite different, i.e. 105 meV/Å^2 for model (iv) and 171 meV/Å^2 for model interface (ii), respectively. Follow the previous derivation [19, 58, 59], the critical nucleation radius for upper and down positions nucleus can be calculated as:

$$r_{up}^{crit} = \frac{\gamma}{\Delta G_v} = \frac{\gamma}{\frac{KT}{\Omega}\ln\left[\frac{J\sqrt{2\pi mKT}}{P_S}\right]} \tag{3}$$

$$r_{down}^{crit} = \frac{\gamma}{\Delta G_v - \frac{\Delta\gamma_i}{h}} = \frac{\gamma}{\frac{KT}{\Omega}\ln\left[\frac{J\sqrt{2\pi mKT}}{P_S}\right] - \frac{\Delta\gamma_i}{h}} \tag{4}$$

k is the Boltzmann constant, Ω is the atomic volume, T is the substrate temperature, J is the deposition flux, m is the atomic mass of the deposited atom and P_S is the vapor pressure above solid. The following values were used in the critical nucleation radius calculation: $\gamma = 2.99$ J/m^2 [40], K = 1.38×10^{23} J/K, T = 773 K, $\Delta\gamma_{i=}$1.05 J/m^2 (DFT calculation results from our work), h=1.19×10^{-10} m, Ps=5×10^{-5} Pa, Ω = 2.87×10^{-29}cm³/atom and J=$\frac{1.34×10^{-19}\text{atom}/m^2}{1.19×10^{-10}m}$× 0.166 ×10^{-9} m/s=1.86×10^{19} atom/m^{2}s. Thus, r_{up}^{crit} is 0.75nm. However, for down positions (interface model ($\overline{ii}$)), the value for $\Delta G_v - \frac{\Delta\gamma_i}{h}$ is negative, which indicate that nucleation driving force is insufficient for our deposition parameters. In other words, matrix mode nucleation cannot overcome the energy barrier caused by interface stacking sequence variants. This is further proving that our HRTEM experiment cannot observe the matrix mode on single-layer terrace.

For twin nucleation on single layer *w*-AlN terrace, maintaining the mirror-symmetric stacking during nucleation will not change its interface energy. The critical nucleation radius for CrN will be same, i.e. $r_{up}^{crit} = r_{down}^{crit}$, which makes upper and down positions have same nucleation

rates. Thus, the probability of nucleation twinning in *w*-AlN single-layer terrace is very high. This is consistent with our observation results of high density twins in texture area (as seen in Figs.3), which indicate the number of two twin relate orientation of *rs*-CrN are same. Furthermore, the critical nucleation radius of the nucleus is less than the *w*-AlN terrace width (as seen Fig.3(d), where the *w*-AlN terrace width shows ~5 nm), which indicate twin model nucleus is possible formation on *w*-AlN terrace.

During island coalescence [60], larger islands may consume smaller islands which is driven by decreasing total surface energy. When CrN twins nucleate at an early stage, two twin-related nuclei with identical critical nucleation radius result in the formation of similarly-sized islands on the *w*-AlN surface. As a consequence, island coalescence no longer takes place. The reason for that is that the mirror-symmetric interface structure with a single atomic-layer terrace allows uniformly coarsening of two twin-related nuclei and eventually forming twins with a similar size. This is consistent with our statistical results of twin width in texture area (as seen in Figs.3). Hence, for a single-layer terrace, twin orientation nucleus with mirror-symmetric *rs*-CrN/*w*-AlN interface structure can nucleate and grow directly on the *w*-{0001} surface, which twin orientation is spontaneously formed and does not require a driving force. The process is more energetically favorable and less expensive. Considering that this twin formation mechanism does not require shear stress, no process from partial dislocations - stacking fault – twins is involved. This twin island growth mode on the *w*-{0001} surface will not be affected by a high SFE. The twin formation mainly depends on the terrace structure of *w*-AlN. To summarize, HRTEM observations combined with atomic model analysis reveal that a single-atomic-layer terrace at the $\{111\}_{rs\text{-CrN}} || \{0002\}_{w\text{-AlN}}$ interface is closely associated with the formation of growth-twins, energetically governing a uniform nucleation of twins.
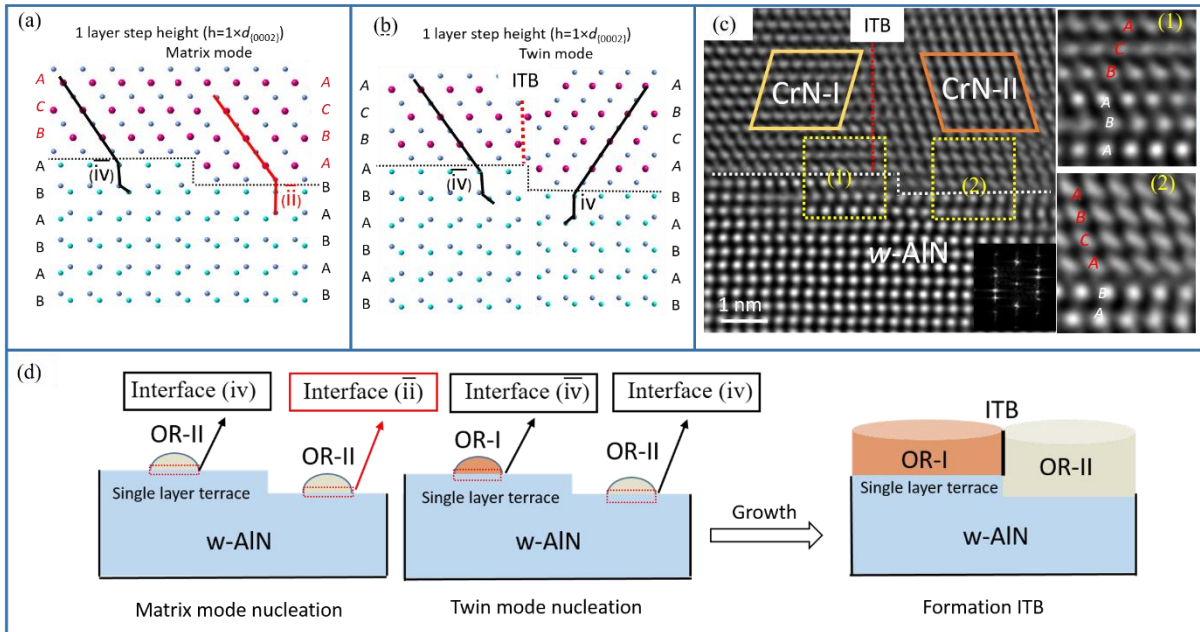
Fig. 9. (a) Schematic of the $\{111\}_{rs\text{-}CrN}\|\{0002\}_{w\text{-}AlN}$ stacking structure of matrix mode CrN growth on single-layer terrace w-AlN. (b) Schematic of the $\{111\}_{rs\text{-}CrN}\|\{0002\}_{w\text{-}AlN}$ stacking structure of twin mode CrN growth on single-layer terrace w-AlN. Two red labels illustrate that the stacking sequence of two rs-CrN/w-AlN interfaces (from upper and lower position in the terrace) exhibits a mirror-symmetric relationship. (c) HRTEM image shows rs-CrN twins with ITBs grown on the w-AlN $\{0002\}$ surface, in which a single atomic-layer terrace (h=1×$d_{\{0002\}w\text{-}AlN}$) of w-AlN can be found. Two enlarged atomic resolution images of the interface stacking structure (yellow frames in Fig. 9 (c)) are inserted on the right-hand side. The $\Sigma 3$ $\{112\}$ ITB is marked with a red dotted-line. (d) Schematics illustrating the nucleation process on single-layer terrace w-AlN.

4.1.2 Interface structure with a double atomic-layer terrace
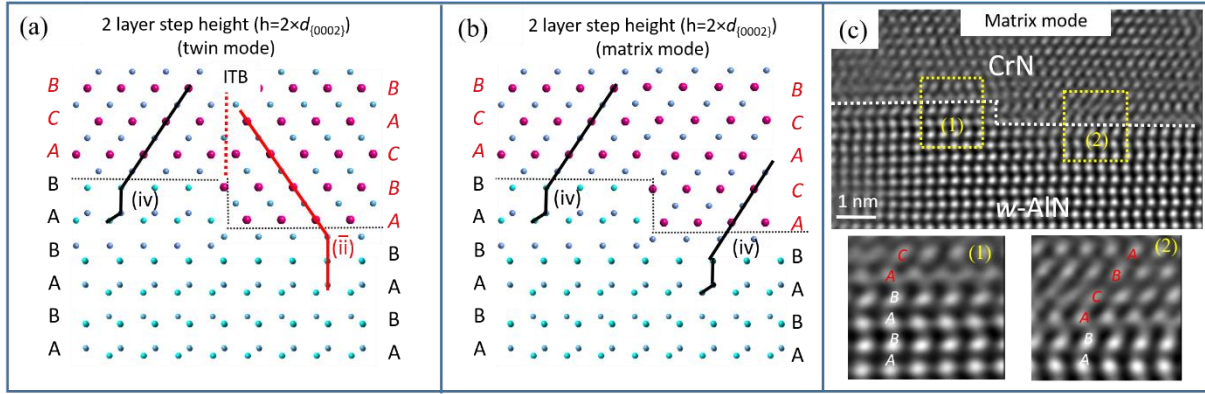
Fig. 10. (a) Schematic model of *rs*-CrN twins (twin mode) on a *w*-AlN {0002} double atomic-layer terrace (h=2×$d_{\{0002\}w\text{-AlN}}$). (b) Schematic model of no twin mode (matrix mode) on a *w*-AlN {0002} double atomic-layer terrace. The interface stacking structure is based on the HRTEM observation in interface position 1 and 2 (yellow frames in Fig. 10 (c)). (c) HRTEM shows the experimental observation of the *rs*-CrN formation on the *w*-AlN {0002} double atomic-layer terrace. No twins (matrix mode) and GBs are observed in the CrN layer. Two local enlarged atomic-resolution images of the interface (indicated in Fig. 10(c) by two frames) are shown at bottom.

Atomic model analysis provides a possibility to construct the hetero-phase interface structure, enabling the analysis of the interface structure and comparison with experimental observations. In the present case, two modes (twin mode and matrix mode) can form on a double atomic-layer terrace (h=2×d$_{\{0002\}w\text{-AlN}}$) as shown in Fig. 10(a) and (b). When a double atomic-layer terrace exists, the *w*-AlN surface always maintains the identical stacking structure, i.e. both parts of the *w*-AlN surface are terminated by layer B (Al-{0002}) in front of and behind the terrace (as shown in Figs. 10(a) and (b)). Thus, for the twin formation mode in Fig.10 (a), the top part of the *rs*-CrN/*w*-AlN interface terrace structure can be described as BCA(*rs*-Cr)/BA(*w*-Al) (model (iv)). The lower part of the *rs*-CrN/*w*-AlN interface terrace structure can be described as CBA(*rs*-Cr)/BA(*w*-Al) (model ($\overline{\overline{\text{ii}}}$), i.e. the mirror-symmetric interface model of model (ii) in Fig. 8). Thus, due to the stacking sequence variation in *rs*-CrN, two non-identical *rs*-CrN{111}/*w*-AlN{0002} interfaces (between the interface model ($\overline{\overline{\text{ii}}}$) and model (iv)) are present in this twin mode. Actually, our HRTEM observations (Figs. 6) confirm that twins were hardly detected on the double-layer terraces. For the matrix mode (as shown in Fig.10 (b)), two parts of the terrace are fully identical, i.e. both interfaces have the same BCA(*rs*-Cr)/BA(*w*-Al)

(model (iv)) interface stacking sequence. In fact, such case is corroborated by HRTEM observations, e.g. Fig. 10(c). Two enlarged interface HRTEM images from Fig. 10(c) clearly show that position 1 and the position 2 have the fully identical interface structure, i.e. both interfaces have model (iv) BCA(rs-Cr)/BA(w-Al) stacking sequence (as shown in Fig. 10(c). Thus, the matrix mode provides completely the same rs-CrN/w-AlN interface structure with identical interface energy on the double atomic-layer terrace.

The higher interface energy for model ($\overline{\text{ii}}$) enlarges the nucleation barrier of twins on the double atomic-layer terrace. Eventually, the lower energy interface structure controls the nucleation process and subsequent growth, consequently, no twins form. Therefore, our analysis points out that the twin formation on the double atomic-layer terrace could be more difficult than on the single atomic-layer terrace, which is essentially ascribed to the change in rs-CrN/w-AlN interface structure and corresponding energy variations.

4.2 Twin nucleation angle on the hetero-phase interface

The previous section 3.2 and 3.3 showed that twins with $\Sigma 3\{112\}$ ITBs are widely distributed in the textured and twins with $\Sigma 3\{111\}$ CTBs are occasionally found in the non-textured film area. Fig.11 (a) schematically illustrates the possible orientation relationship and TB structures. HRTEM observations showed two possible crystallographic growth orientations, i.e. <111> and <100> (see Figs. 7), for the formation of rock-salt twins (including the $\Sigma 3\{112\}$ ITB and $\Sigma 3\{111\}$ CTB formation mode). Based on the experimental observations, the TBs formation occurs along three particular directions (Fig. 11(b)), which are $\overrightarrow{a_1}=[1\overline{1}1]$, $\overrightarrow{a_2}=[\overline{1}11]$ and $\overrightarrow{a_3}=[001]$. Twins with these three particular directions will have different misorientation angles of the growth directions. From the geometric relationship between the grain growth direction (along $\overrightarrow{a_1}=[1\overline{1}1]$, $\overrightarrow{a_2}=[\overline{1}11]$ or $\overrightarrow{a_3}=[001]$, according to experimental observations) and the twin boundaries (including $\Sigma 3\{112\}$ ITB and $\Sigma 3\{111\}$ CTB), 6 specific nucleation angles (scenario 1-6 in Fig. 11(b)) for the formation of TBs of rock-salt grains on a w-AlN layer can be determined.

The twin nucleation angle for $\Sigma 3\{112\}$ ITB (symmetric tilt) as shown in scenario 1, is restricted to the following conditions for the formation of ITBs (symmetric tilt): (i) a specific twin orientation on the single atomic-layer w-AlN terrace (illustrated in Sec.4.1); (ii) 0° misorientation of the growth directions for rock-salt grains (as shown in Sec.3.4.1). Thus, in scenario 1, two rock-salt grains with <111> growth direction ($\overrightarrow{a_1}/\overrightarrow{a_2}$) have 0° misorientation

($\Delta\theta=0°$). The experimental statistical result of the misorientation in the growth directions of the CrN grains in the textured film area is plotted in Fig. 12(a), indicating that most of the CrN grains (about 86%) have an angle difference of -5° to +5° (relative to the substrate out-of-plane direction). According to scenario 1, the $\Sigma3\{112\}$ ITB (symmetric tilt) formation requires two rock-salt grains having 0° misorientation angle in the growth directions. Hence, the small misorientation angles of the CrN grains suggest that there is a much larger probability for the $\Sigma3\{112\}$ ITB formation in the textured film area near the substrate.

Considering the twin nucleation angle for $\Sigma3\{111\}$ CTB mode, as shown in scenario 2-6, the following arguments are considered. The formation of CTB can be explained by the fact that occasionally certain adjacent nuclei may happen to have the twinned orientation [19], which requires rock-salt grains with specific nucleation angle. In scenario 2 and 3, one of the CrN grain has <111> growth orientation and another CrN grain has <100> growth orientation. Two possible nucleation cases favor the CTB formation. Such cases will need $\overrightarrow{a_2}/\overrightarrow{a_3}$ having 15.78° difference ($\Delta\theta=15.78°$) or $\overrightarrow{a_3}/\overrightarrow{a_1}$ having 70.52° difference ($\Delta\theta=70.52°$). In scenario 4 and 5, both CrN grains exhibit <111> growth orientation. The CTB formation requires $\overrightarrow{a_1}/\overrightarrow{a_2}$ having $\Delta\theta=39.96°$ or $\overrightarrow{a_2}/\overrightarrow{a_2}$ having $\Delta\theta=70.52°$. For both grains with <100> growth orientation, only one possible misorientation favors the CTB formation, i.e. $\overrightarrow{a_3}/\overrightarrow{a_3}$ having $\Delta\theta=70.52°$ misorientation angle (as shown in scenario 6). Such nucleation angles are theoretically possible. Some nucleation angles cannot be completely achieved. The CTB formation in scenario 3, 5 and 6 requires too high nucleation angle difference, i.e. $\Delta\theta=70.52°$. Our HRTEM observations (Figs. 7 and Fig. S4 in the supplementary material) only confirm the presence of scenario 2 ($\Delta\theta=15.78°$) and scenario 4 ($\Delta\theta=38.96°$) growth modes.

The distribution of the CrN grain misorientation angles of growth direction from 5th block to 21st block (non-textured area) is plotted in Fig. 12(b), revealing that most of the CrN grains (about 94%) have a difference of -25° to +25° (relative to the [1$\bar{1}$02] direction of the Al$_2$O$_3$ substrate, being parallel to the growth direction of the film). This means that the CrN grains grow with a large misorientation angle in the film area far away from the substrate. Moreover, Fig. 12 (b) also indicates that the possible maximum misorientation angle is about 60°. Hence, scenario 3, 5 and 6 should not be formed in our rs-CrN/w-AlN multilayer.

Overall, these results and analyses indicate that twin nucleation with $\Sigma3\{112\}$ ITB requires 0° misorientation angle of the growth directions. The $\{111\}\|\{0002\}$ textured film area (block 1-4) with smooth growth surfaces facilitates the formation of $\Sigma3\{112\}$ ITBs. Contrary, the non-

textured area with wavy-like layer structures increases the probability of Σ3{111} CTB formation.
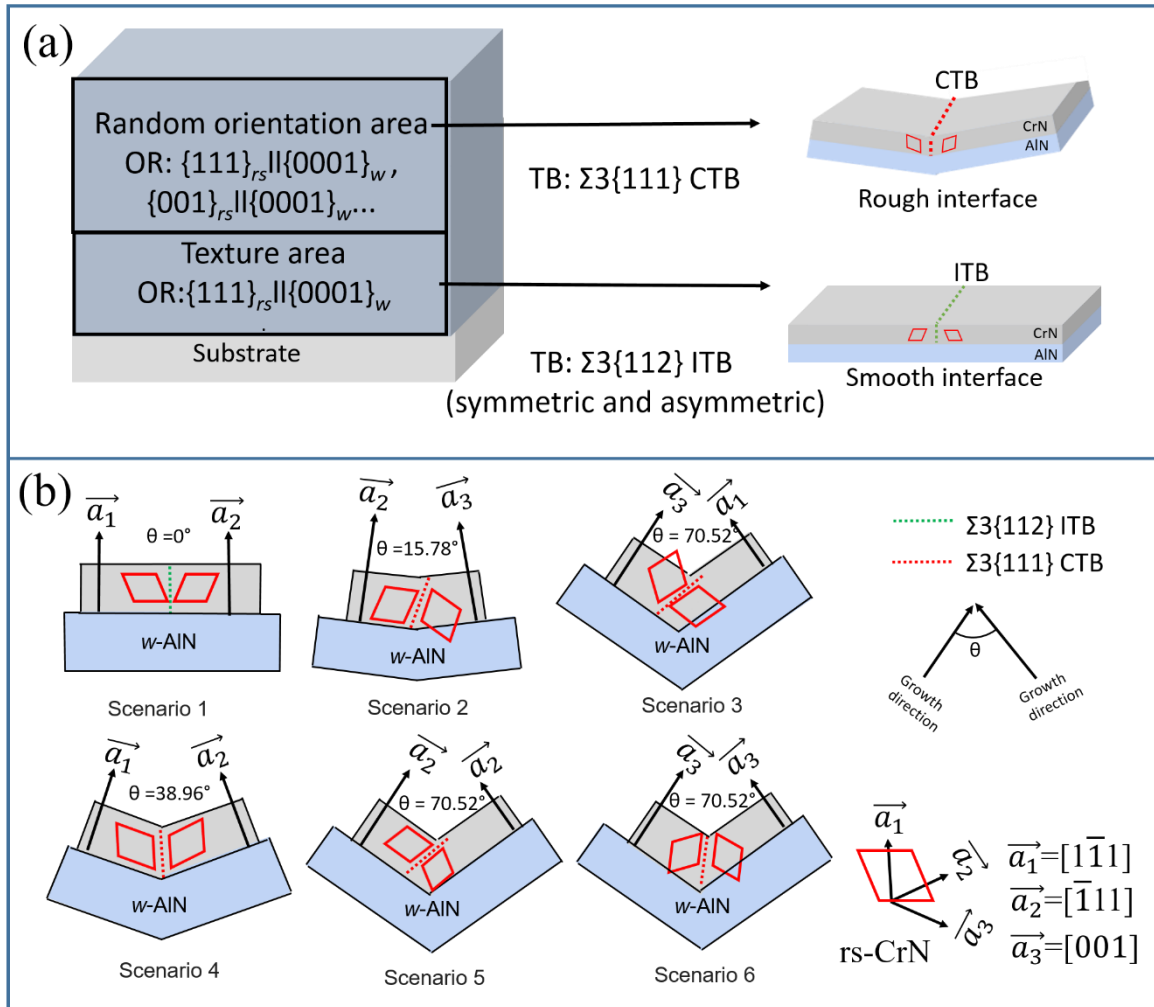

Fig. 11. (a) Schematic illustration of the possible interface orientations and TB structures in different film locations. (b) Schematic illustration of CrN TB formation on the *w*-AlN surface with different nucleation angles. The twin nucleation angle for Σ3{112} ITB mode in texture area is illustrated in scenario 1. Twin nucleation angles for Σ3{111} CTB mode in random orientation area are illustrated in scenario 2-6.
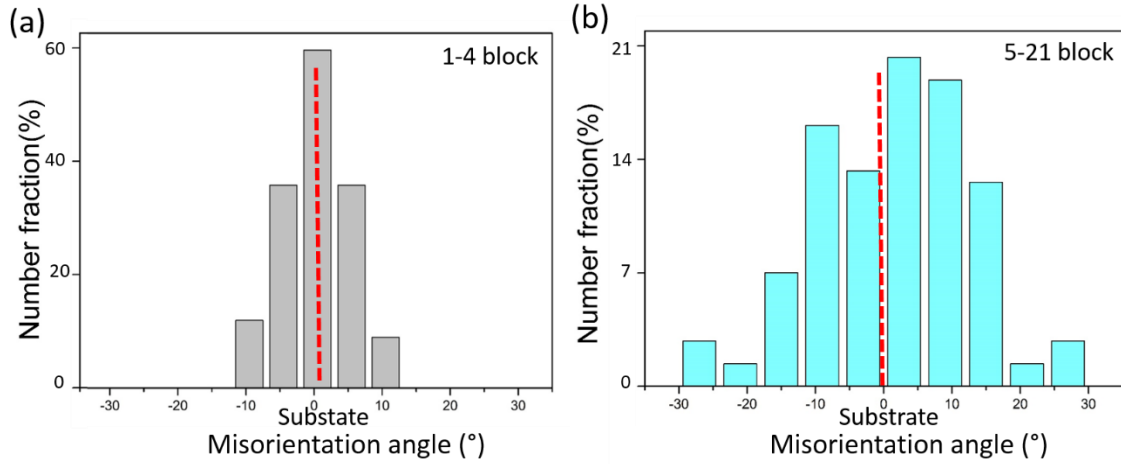
Fig.12. Histogram of misorientation angles of the growth direction of CrN grains in block 1-4 (a) and block 5-21 (b), relative to the [1$\bar{1}$02] direction of the Al$_2$O$_3$ substrate (0° reference).

5. Conclusions

The microstructure of a multilayer with alternating CrN and AlN layers was investigated using C$_S$-corrected TEM. From SAED patterns and HRTEM investigations, a high density of rock-salt twins with Σ3{112} ITBs were found in {111}||{0002} textured film areas (near the substrate region). The atomic-resolved images of *rs*-CrN{111}||*w*-AlN{0002} interfaces reveal that a single-atomic-layer terrace is closely associated with the formation of such growth-induced twin formations. The mirror-symmetric *w*-AlN/*rs*-CrN interfaces (for a twin on the single-atomic-layer terrace) hardly causes any change in the interface structure and energy variations. However, due to the interface structure and energy variations, growth-twins are more difficult to nucleate on the double atomic-layer terrace, which are also present.

In the non-textured film area (far away from the substrate area), rock-salt twins with Σ3{111} CTB are occasionally found. Due to the interface orientation variation, two twin nucleation modes with different misorientation angle of growth direction for Σ3{111} CTB were found. The results indicate that the hetero-phase interface-facilitating nucleation process plays a dominant role in rock-salt growth-twins, and provide new insights for their formation mechanisms in multilayers.

Acknowledgements

Reference

[1] I.J. Beyerlein, X. Zhang, A. Misra, Growth Twins and Deformation Twins in Metals, Annual Review of Materials Research 44(1) (2014) 329-363.
[2] L. Lu, X. Chen, X. Huang, K. Lu, Revealing the Maximum Strength in Nanotwinned Copper, Science 323(5914) (2009) 607-610.
[3] K. Lu, L. Lu, S. Suresh, Strengthening Materials by Engineering Coherent Internal Boundaries at the Nanoscale, Science 324(5925) (2009) 349-352.
[4] M. Dao, L. Lu, Y.F. Shen, S. Suresh, Strength, strain-rate sensitivity and ductility of copper with nanoscale twins, Acta Materialia 54(20) (2006) 5421-5432.
[5] L. Lu, Y. Shen, X. Chen, L. Qian, K. Lu, Ultrahigh Strength and High Electrical Conductivity in Copper, Science 304(5669) (2004) 422-426.
[6] J.A. Brown, N.M. Ghoniem, Structure and motion of junctions between coherent and incoherent twin boundaries in copper, Acta Materialia 57(15) (2009) 4454-4462.
[7] J. Wang, N. Li, O. Anderoglu, X. Zhang, A. Misra, J.Y. Huang, J.P. Hirth, Detwinning mechanisms for growth twins in face-centered cubic metals, Acta Materialia 58(6) (2010) 2262-2270.
[8] J. Wang, A. Misra, J.P. Hirth, Shear response of $\Sigma3\{112\}$ twin boundaries in face-centered-cubic metals, Physical Review B 83(6) (2011).
[9] D. Bufford, Y. Liu, J. Wang, H. Wang, X. Zhang, In situ nanoindentation study on plasticity and work hardening in aluminium with incoherent twin boundaries, Nature communications 5 (2014) 4864.
[10] Y. Tian, B. Xu, D. Yu, Y. Ma, Y. Wang, Y. Jiang, W. Hu, C. Tang, Y. Gao, K. Luo, Z. Zhao, L.M. Wang, B. Wen, J. He, Z. Liu, Ultrahard nanotwinned cubic boron nitride, Nature 493(7432) (2013) 385-8.
[11] Q. Huang, D. Yu, B. Xu, W. Hu, Y. Ma, Y. Wang, Z. Zhao, B. Wen, J. He, Z. Liu, Y. Tian, Nanotwinned diamond with unprecedented hardness and stability, Nature 510 (2014) 250.
[12] Z.J. Lin, L. Wang, J. Zhang, X.-Y. Guo, W. Yang, H.-K. Mao, Y. Zhao, Nanoscale twinning-induced elastic strengthening in silicon carbide nanowires, Scripta Materialia 63(10) (2010) 981-984.
[13] T. Fu, X. Peng, C. Huang, Y. Zhao, S. Weng, X. Chen, N. Hu, Effects of twin boundaries in vanadium nitride films subjected to tensile/compressive deformations, Applied Surface Science 426 (2017) 262-270.
[14] T. Fu, X. Peng, Y. Zhao, T. Li, Q. Li, Z. Wang, Molecular dynamics simulation of deformation twin in rocksalt vanadium nitride, Journal of Alloys and Compounds 675 (2016) 128-133.
[15] S.K. Yadav, X.Y. Liu, J. Wang, R. Ramprasad, A. Misra, R.G. Hoagland, First-principles density functional theory study of generalized stacking faults in TiN and MgO, Philosophical Magazine 94(5) (2013) 464-475.
[16] H. Yu, M. Bahadori, G.B. Thompson, C.R. Weinberger, Understanding dislocation slip in stoichiometric rocksalt transition metal carbides and nitrides, Journal of Materials Science 52(11) (2017) 6235-6248.
[17] Y. Zhang, Z.-R. Liu, D.-W. Yuan, Q. Shao, J.-H. Chen, C.-L. Wu, Z.-L. Zhang, Elastic Properties and Stacking Fault Energies of Borides, Carbides and Nitrides from First-Principles Calculations, Acta Metallurgica Sinica (English Letters) (2019).

[18] Q. Li, S. Xue, J. Wang, S. Shao, A.H. Kwong, A. Giwa, Z. Fan, Y. Liu, Z. Qi, J. Ding, H. Wang, J.R. Greer, H. Wang, X. Zhang, High-Strength Nanotwinned Al Alloys with 9R Phase, Advanced materials 30(11) (2018).

[19] S. Xue, Z. Fan, Y. Chen, J. Li, H. Wang, X. Zhang, The formation mechanisms of growth twins in polycrystalline Al with high stacking fault energy, Acta Materialia 101 (2015) 62-70.

[20] L. Velasco, A.M. Hodge, Growth twins in high stacking fault energy metals: Microstructure, texture and twinning, Materials Science and Engineering: A 687 (2017) 93-98.

[21] D. Bufford, Y. Liu, Y. Zhu, Z. Bi, Q.X. Jia, H. Wang, X. Zhang, Formation Mechanisms of High-density Growth Twins in Aluminum with High Stacking-Fault Energy, Materials Research Letters 1(1) (2013) 51-60.

[22] A. Madan, I.W. Kim, S.C. Cheng, P. Yashar, V.P. Dravid, S.A. Barnett, Stabilization of Cubic AlN in Epitaxial AlN/TiN Superlattices, Physical Review Letters 78(9) (1997) 1743-1746.

[23] I.W. Kim, Q. Li, L.D. Marks, S.A. Barnett, Critical thickness for transformation of epitaxially stabilized cubic AlN in superlattices, Applied Physics Letters 78(7) (2001) 892-894.

[24] D. Chen, X.L. Ma, Y.M. Wang, Thickness-dependent structural transformation in the AlN film, Acta Materialia 53(19) (2005) 5223-5227.

[25] J. Lin, J.J. Moore, B. Mishra, M. Pinkas, W.D. Sproul, Nano-structured CrN/AlN multilayer coatings synthesized by pulsed closed field unbalanced magnetron sputtering, Surface and Coatings Technology 204(6) (2009) 936-940.

[26] J. Lin, J.J. Moore, B. Mishra, M. Pinkas, X. Zhang, W.D. Sproul, CrN/AlN superlattice coatings synthesized by pulsed closed field unbalanced magnetron sputtering with different CrN layer thicknesses, Thin Solid Films 517(20) (2009) 5798-5804.

[27] J. Lin, N. Zhang, Z. Wu, W.D. Sproul, M. Kaufman, M. Lei, J.J. Moore, Thick CrN/AlN superlattice coatings deposited by the hybrid modulated pulsed power and pulsed dc magnetron sputtering, Surface and Coatings Technology 228(Supplement 1) (2013) S601-S606.

[28] Z. Chen, D. Holec, M. Bartosik, P.H. Mayrhofer, Z. Zhang, Crystallographic orientation dependent maximum layer thickness of cubic AlN in CrN/AlN multilayers, Acta Materialia 168 (2019) 190-202.

[29] Z. Zhang, Y. Long, S. Cazottes, R. Daniel, C. Mitterer, G. Dehm, The peculiarity of the metal-ceramic interface, Scientific Reports 5 (2015) 11460.

[30] Z. Zhang, X. Gu, D. Holec, M. Bartosik, P.H. Mayrhofer, H.P. Duan, Superlattice-induced oscillations of interplanar distances and strain effects in the CrN/AlN system, Physical Review B 95(15) (2017) 155305.

[31] G. Kresse, J. Furthmüller, Efficiency of ab-initio total energy calculations for metals and semiconductors using a plane-wave basis set, Computational Materials Science 6(1) (1996) 15-50.

[32] G. Kresse, J. Furthmüller, Efficient iterative schemes for ab initio total-energy calculations using a plane-wave basis set, Physical Review B 54(16) (1996) 11169-11186.

[33] G. Kresse, D. Joubert, From ultrasoft pseudopotentials to the projector augmented-wave method, Physical Review B 59(3) (1999) 1758-1775.

[34] J.P. Perdew, K. Burke, M. Ernzerhof, Generalized Gradient Approximation Made Simple, Physical Review Letters 77(18) (1996) 3865-3868.

[35] F. Spaepen, Interfaces and stresses in thin films, Acta Materialia 48(1) (2000) 31-42.

[36] D. Raoufi, A. Kiasatpour, H.R. Fallah, A.S.H. Rozatian, Surface characterization and microstructure of ITO thin films at different annealing temperatures, Applied Surface Science 253(23) (2007) 9085-9090.

[37] R.F. Londoño-Menjura, R. Ospina, D. Escobar, J.H. Quintero, J.J. Olaya, A. Mello, E. Restrepo-Parra, Influence of deposition temperature on WTiN coatings tribological performance, Applied Surface Science 427 (2018) 1096-1104.

[38] C.V. Thompson, Grain Growth in Thin Films, Annual Review of Materials Science 20(1) (1990) 245-268.

[39] D. Holec, P.H. Mayrhofer, Surface energies of AlN allotropes from first principles, Scr Mater 67(9) (2012) 760-762.

[40] V. Antonov, I. Iordanova, Density-functional study of the crystallographic structure of chromium nitride films, Journal of Physics: Conference Series 223 (2010) 012043.

[41] A. Karimi, G. Allidi, R. Sanjines, Relative orientation of the constituents on the degree of crystallographic coherence in AlN/TiN superlattices, Surface and Coatings Technology 201(7) (2006) 4062-4067.

[42] M. Wen, H. Huang, K. Zhang, Q. Meng, X. Li, L. Kong, C. Hu, W. Zheng, The AlN layer thickness dependent coherent epitaxial growth, stress and hardness in NbN/AlN nanostructured multilayer films, Surface and Coatings Technology 235(Supplement C) (2013) 367-375.

[43] K. Yalamanchili, F. Wang, H. Aboulfadl, J. Barrirero, L. Rogström, E. Jiménez-Pique, F. Mücklich, F. Tasnadi, M. Odén, N. Ghafoor, Growth and thermal stability of TiN/ZrAlN: Effect of internal interfaces, Acta Materialia 121(Supplement C) (2016) 396-406.

[44] D. Holec, P.H. Mayrhofer, Surface energies of AlN allotropes from first principles, Scripta Materialia 67(9) (2012) 760-762.

[45] J.P. Zhao, X. Wang, Z.Y. Chen, S.Q. Yang, T.S. Shi, X.H. Liu, Overall energy model for preferred growth of TiN films during filtered arc deposition, Journal of Physics D: Applied Physics 30(1) (1997) 5.

[46] S. Kibey, J.B. Liu, D.D. Johnson, H. Sehitoglu, Predicting twinning stress in fcc metals: Linking twin-energy pathways to twin nucleation, Acta Materialia 55(20) (2007) 6843-6851.

[47] K.Y. Yu, D. Bufford, Y. Chen, Y. Liu, H. Wang, X. Zhang, Basic criteria for formation of growth twins in high stacking fault energy metals, Applied Physics Letters 103(18) (2013) 181903.

[48] H. Bialas, K. Heneka, Epitaxy of fcc metals on dielectric substrates, Vacuum 45(1) (1994) 79-87.

[49] G. Dehm, M. Rühle, G. Ding, R. Raj, Growth and structure of copper thin films deposited on (0001) sapphire by molecular beam epitaxy, Philosophical Magazine B 71(6) (1995) 1111-1124.

[50] A. Hashibon, C. Elsässer, M. Rühle, Structure at abrupt copper–alumina interfaces: An ab initio study, Acta Materialia 53(20) (2005) 5323-5332.

[51] S. Ramanathan, B.M. Clemens, P.C. McIntyre, U. Dahmen, Microstructural study of epitaxial platinum and Permalloy/platinum films grown on (0001) sapphire, Philosophical Magazine A 81(8) (2001) 2073-2094.

[52] S. Schmidt, J. Lu, S.P. Keane, L.D. Bregante, D.O. Klenov, S. Stemmer, Microstructure and Dielectric Properties of Textured SrTiO3 Thin Films, Journal of the American Ceramic Society 88(4) (2005) 789-801.

[53] M. Vermeersch, F. Malengreau, R. Sporken, R. Caudano, The aluminium/sapphire interface formation at high temperature: an AES and LEED study, Surface Science 323(1) (1995) 175-187.

[54] D.L. Medlin, K.F. McCarty, R.Q. Hwang, S.E. Guthrie, M.I. Baskes, Orientation relationships in heteroepitaxial aluminum films on sapphire, Thin Solid Films 299(1) (1997) 110-114.

[55] G. Dehm, B.J. Inkson, T. Wagner, Growth and microstructural stability of epitaxial Al films on (0001) α-Al2O3 substrates, Acta Materialia 50(20) (2002) 5021-5032.

[56] S.W. Hieke, B. Breitbach, G. Dehm, C. Scheu, Microstructural evolution and solid state dewetting of epitaxial Al thin films on sapphire (α-Al 2 O 3), Acta Materialia 133 (2017) 356-366.

[57] J.P. Hirth, R.C. Pond, Steps, dislocations and disconnections as interface defects relating to structure and phase transformations, Acta Materialia 44(12) (1996) 4749-4763.

[58] X. Zhang, A. Misra, H. Wang, T.D. Shen, M. Nastasi, T.E. Mitchell, J.P. Hirth, R.G. Hoagland, J.D. Embury, Enhanced hardening in Cu/330 stainless steel multilayers by nanoscale twinning, Acta Materialia 52(4) (2004) 995-1002.

[59] K. Han, J.P. Hirth, J.D. Embury, Modeling the formation of twins and stacking faults in the ag-cu system, Acta Materialia 49(9) (2001) 1537-1540.

[60] I. Petrov, P.B. Barna, L. Hultman, J.E. Greene, Microstructural evolution during film growth, Journal of Vacuum Science & Technology A 21(5) (2003) S117-S128.

Supplementary Information

Growth-twins in CrN/AlN multilayers induced by hetero-phase interfaces

1. Crystallographic orientation evolution
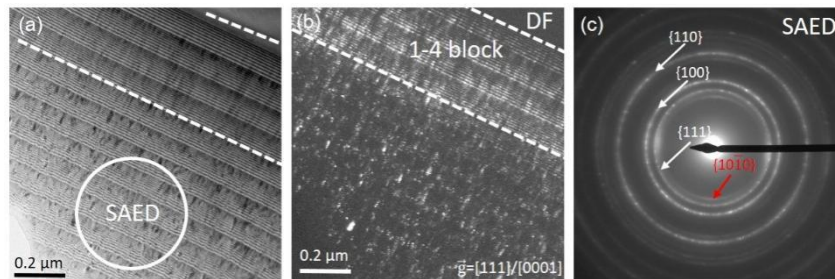
Fig. S1. **(a)** and **(b)** Cross-sectional TEM bright/dark-field images (dark-field images from the same area taken under the wurtzite/rock-salt $\vec{g}$ ={0001}||{111} reflections). **(c)** is the corresponding are selected area electron diffraction.

In order to investigate crystallographic orientation evolution in far from the substrate area, we carried out a comprehensive microscopy study on the microstructure of the film. The {111}/{0001} texture clearly appears in near the substrate area. However, the texture gradually disappears over the 4th block. Fig. S1 (c) shows the area selected area electron diffraction pattern from the area labeled in Fig.S1 (a), which exhibits a ring pattern. This suggests that grains grow

randomly over a large distance without any preferred orientation in far from the substrate area, forming a polycrystalline.
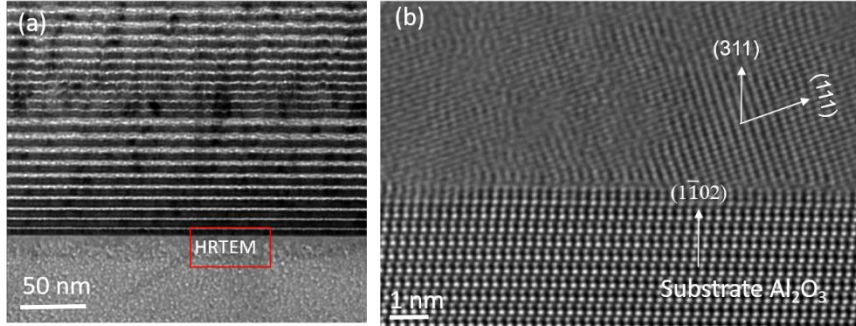
2. CrN/substrate interface

Fig. S2. (a) Cross-sectional TEM bright images in substrate area. **(b)** is the corresponding are selected area HRTEM image. The interface orientation relationship is $(311)/(1\bar{1}02)$.
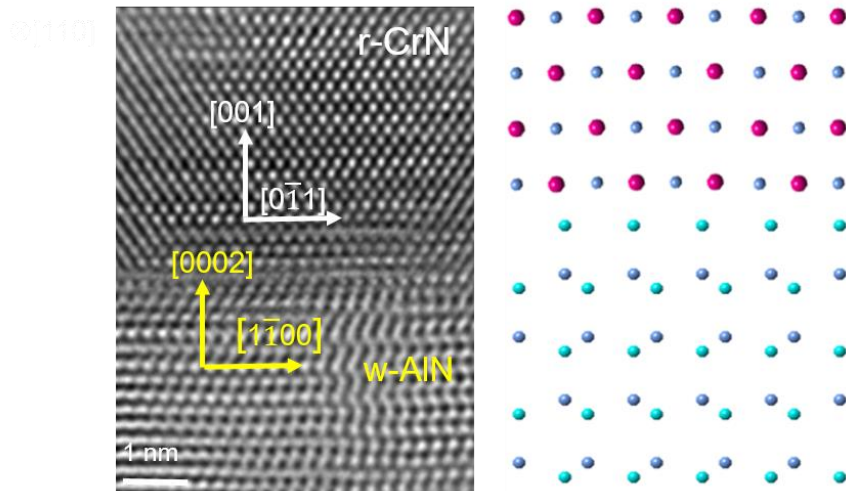
3. {001}/{0001} interface structure

Fig. S3. HRTEM and schematic image of $\{002\}[110]_{rs\text{-}CrN}||\{0002\}[1120]_{w\text{-}AlN}$ interface (taken in 10th block), which possesses a relatively high mismatch structure. The growth direction is from bottom to top.

4. Extended observations for Σ3{111} CTB formation mode
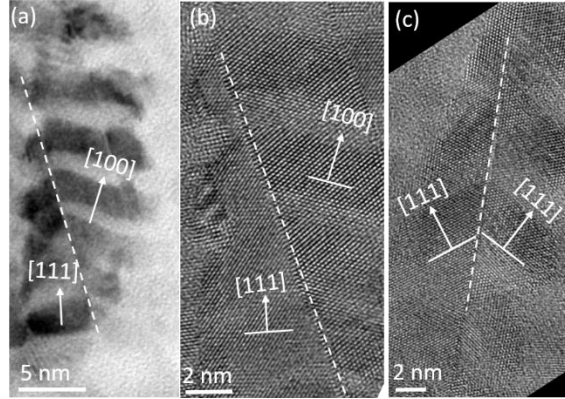
Fig. S4 (a-c). Additional example showing scenario 2 ($\Delta\theta$=15.78°) and scenario 4 ($\Delta\theta$=38.96°) growth modes for twins with Σ3{111} CTB.

In the non-textured area, Fig. S4(a) shows one cross-sectional TEM bright image taken in far away from the substrate area. Fig. S4 (b) is a corresponding HRTEM image taken from Fig. S4 (a). Fig. S4 (c) shows another HRTEM image of *rs*-CrN/*rs*-AlN columnar grains with CTB in the non-textured area. In Fig. S4 (b), crystallographic growth orientation for left grain is along the rock-salt <111> direction while the right grain is along the rock-salt <100> direction. In contrast, both columnar grains in Fig. S4 (c) have the same crystallographic growth orientation (both along the rock-salt <111> direction). In Fig. S4 (b) and (c), two columnar grains growth directions having 15.8° and 39.9° difference in misorientation, respectively. Hence, our extended HRTEM observations also confirm the presence of scenario 2 ($\Delta\theta$=15.78°) and scenario 4 ($\Delta\theta$=38.96°) growth modes for twins with Σ3{111} CTB.

Publication IV

Real-time atomic-resolution observation of coherent twin boundary migration in CrN

Zhuo Chen[1], Yonghui Zheng[1], Lukas Löfler[2], Matthias Bartosik[3], Huaping Sheng[1], Christoph Gammer[1], David Holec[2], Zaoli Zhang[1]*

[1] Erich Schmid Institute of Materials Science, Austrian Academy of Sciences, A-8700 Leoben, Austria

[2] Department of Materials Science, Montanuniversität Leoben, A-8700 Leoben, Austria

[3] Institute of Materials Science and Technology, TU Wien, A-1060 Vienna, Austria

* Corresponding author: zaoli.zhang@oeaw.ac.at

Abstract

Although coherent twin boundary (CTB) migration in *fcc* metals has been widely studied, little is known about the CTB migration behavior in the binary transition-metal nitrides system (e.g. rock-salt CrN). Using *in-situ* atomic-resolution electron microscopy, we report two different twin boundary defect (TD) nucleation and CTB migration modes at the CTB/ITB (incoherent twin boundary) and CTB/surface junctions. A new twin defect nucleation and CTB migration mode are observed from the CTB/surface junction. We show that such CTB migration is associated with a boundary structure alternating from an N-terminated to Cr-terminated, involving Cr and N atom respective motion, i.e., asynchronous CTB migration. We further reveal the dynamic and thermodynamic mechanism of such asynchronous migration through strain analysis and DFT simulations. Our findings uncover an atomic-scale dynamic process of defect nucleation and CTB migration in a binary system, which provides new insight into the atomic-scale deformation mechanism in complex materials.

1. Introduction

It is well known that most crystal structures do not possess simple geometric arrangements, which determines their more complex deformation mechanism. For complex material deformation, Kronberg proposed a synchronous slip and twinning deformation mechanism in 1957, whereby two shears operate in opposite directions on adjacent atomic planes [1]. This

mechanism has been shown to operate in the Laves phase and α-Alumina [2, 3]. However, due to the difficulty of characterization of complex materials, there has been no *in-situ* experimental evidence to support this deformation mechanism for many years.

Chromium nitride (CrN) is a transition metal nitride (TMN) with a complex structure, where metal and N atoms form an *fcc* sublattice. As a TMN, it exhibits high hardness, high-temperature stability, corrosion resistance, oxidation resistance, wear resistance, and has been widely used in industry, such as machine tools, medical implants, and aerospace engineering. However, the application of TMN ceramics is often restricted due to their poor ductility and toughness. To further improve the mechanical properties of TMNs, grain boundary engineering is an effective solution [4-6]. Among different grain boundaries, twin boundaries have received extensive attention. In *fcc* metals, Σ3{111} coherent twin boundaries (CTBs) are advantageous for their strength, ductility, electrical conductivity, plasticity, and thermal stability [7-11]. In particular, CTB defect motion and CTB migration play a crucial role in the deformation and softening mechanisms of materials containing nano-twins [12-14].

Although the CTB migration and twin boundary defect motion have been extensively studied in simple *fcc* metallic materials, these processes remain unclear in complex TMN materials. On the one hand, due to the difficulty of imaging the light element (nitrogen), there are no clear experimental results available on the genuine atomic structure of *rs*-TMNs CTB. On the other hand, TMNs have much high stacking fault energies (SFEs), reaching as high as ~1 J/m^2 [15-17]. From this, twinning in TMN is difficult, limiting the experimental observation of twin behavior in TMN. In this article, based on as-synthesized high-density growth twins [18], we report a new TD nucleation and CTB migration mode in the binary CrN. The observed CTB migration is associated with a boundary structure alternating from an N-terminated to Cr-terminated. More importantly, our *in-situ* experiments (as seen in the schematic drawing of Fig.S1, here, "Supplementary Figure xx" is abbreviated as 'Fig. Sxx' in context) and DFT simulation results confirm that CTB migration and TD gliding is an asynchronous process. Therefore, these results improve our understanding of the dynamic process of grain boundary migration and defect motion in complex materials.

2. Methods

2.1. Material fabrication

The thin film with a total thickness of ~2 μm, composed of alternating ~100 nm CrN and ~4 nm AlN layers (as seen in the Supplementary, Fig. S2) was synthesized by DC reactive

magnetron sputtering. We used polished Al_2O_3 (0001) substrates with an off-axis orientation of 0.2° towards $(10\bar{1}0)$ and a size of $10\times10\times0.5$ mm^3. The substrates were ultrasonically pre-cleaned in acetone and ethanol for 5 min each before mounting them in the AJA International Orion 5 deposition system. After evacuating the chamber down to a base pressure of ~ 5×10^{-4} Pa at room temperature, the substrates were thermally cleaned at 500 °C for 20 min followed by Ar-ion etching for 10 min at the same temperature in an Ar atmosphere at a pressure of 6 Pa by applying a constant bias voltage of -750 V. The film was grown at 500 °C by DC powering one 2" Cr and one 3" Al target (both 99.6 % purity) in an Ar/N_2 gas mixture (flow ratio of 5 sccm Ar/5 sccm N_2) at a total pressure of 0.4 Pa. The power densities used were ~12.3 (Cr target) and ~11.0 W/cm^2 (Al target), respectively. The nano-layer structure was realized using computer-controlled shutters mounted in front of the permanently running targets. Throughout the whole deposition process, a constant bias voltage of -50 V (floating potential was -20 V) was applied to the growing film and the substrate holder was rotated constantly with ~1 Hz to ensure dense and uniform film growth.

2.2. Material characterization

Cross-sectional TEM specimens were prepared using a standard TEM sample preparation approach, including cutting, grinding, and dimpling. Ar ion milling was carried out at a voltage of 4.0 kV with an angle of 6°, followed by a final low voltage ion-milling of 2.5 kV with an angle of 2°. Our experiments were performed in field-emission TEM equipped with an objective-lens aberration corrector (FEI Titan Themis 60-300 cubed with the operating voltage at 300 kV and JEOL 2100F with the operating voltage at 200kV). The aberration coefficients were set to be sufficiently small (-1 μm ~ +1μm), under which the HRTEM images taken were close to the Scherzer defocus condition. For recording *in-situ* HRTEM movies, a fast CMOS Ceta camera (FEI Titan Themis 60-300 cubed) and a CCD Orius camera (JEOL 2100F) were applied, where image sizes are 2048×2048 and 2048×1336, respectively. The exposure time was set to 100 ms. HRTEM image simulations were executed using the JEMS software. Moreover, a 300 kV field emission TEM (JEOL ARM300F) equipped with double C_S-correctors was used to obtain atomic-resolution HAADF images. The STEM−HAADF images were taken by an annular dark-field image detector with the inner semi-angle larger than 64 mrad. The nanoindentation was performed with an Hysitron Triboscope equipped with a spherical tip. The cross-sectional TEM specimens (after nanoindentation) were prepared using a Zeiss Auriga Laser FIB system, consisting of a focused ion beam column (Orsay Physics Ga+

ion FIB). The strain field in CrN twins was calculated based on the C_S-corrected high-resolution TEM images by the geometric phase analysis (GPA) method. According to the GPA algorithm, the displacement field can be obtained by selecting two non-collinear Bragg vectors in the power spectrum generated from a high-resolution TEM image. Strain maps (snapshot of movie S2) were calculated with respect to this reference lattice defined by $\overrightarrow{g_1}$ = [111] and $\overrightarrow{g_2}$ = [1$\bar{1}$1]. The directly measured <111>{11$\bar{2}$} shear strain is calculated from the change in the in-plane angle ($\alpha_{(111)/(11-1)}$), i.e. $\varepsilon = \frac{\Delta_\alpha}{70.5°}$ [19].

Following the approach described in Refs [20, 21], atom column positions were carefully measured by fitting a Gaussian function around each maximum of an intensity profile, and then the accurate center position for each maximum as found by fitting is assigned as the center of atom column position. Here, 25 HRTEM images taken from Movie S4 were used to determine the atomic positions.

In this study, an intensive electron beam irradiation means that a dose rate is $\sim 5 \times 10^4$ electrons/$\text{Å}^2 \cdot$s, while a normal beam illumination means that the dose rate is $\sim 1 \times 10^4$ electrons/$\text{Å}^2 \cdot$s,

2.3. DFT calculation

The calculations were performed using the Vienna Ab initio Simulation Package (VASP) [22] using the projector augmented wave method enabled pseudopotentials [23] with generalized gradient approximation [24] of the exchange and correlation effects. An automatically created k-point mesh with density of 50 and a cutoff energy of 500 eV were chosen for the calculations. The supercell used in the calculations was made up by a stack of 28 (111) CrN planes (alternating between Cr and N) with the initial twin boundary at the center. The calculations were done for anti-ferromagnetic order according to Ref.[25]. Following the different possible orders to move the twin a pair of Cr and N were stepwise displaced along the [112] direction to model the jumping of the atoms. At each of those steps, the energy of the system was calculated and then compared to the energy of the initial system.

3. Results

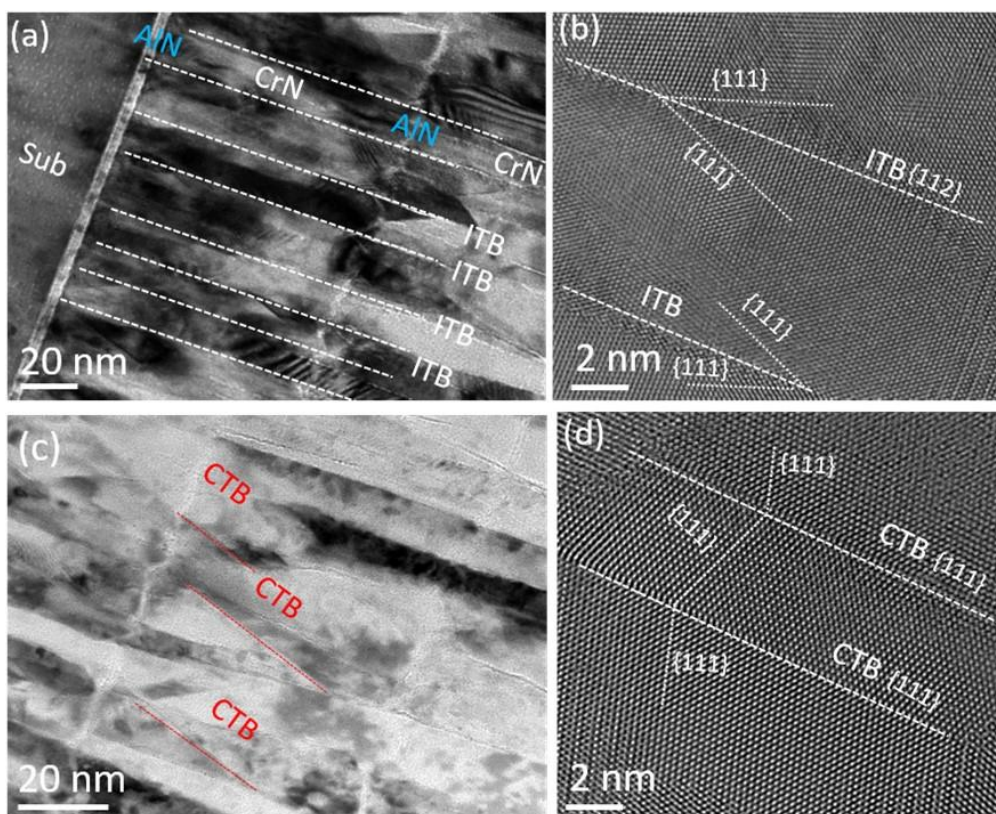## 3.1 Growth twins in CrN multilayers

Fig.1. **(a)** A bright-field image consisting of CrN columnar grains taken near the substrate. **(b)** A typical HRTEM image of CrN columnar grains with a Σ3 {1 1 2} incoherent twin boundary. **(c)** A bright-field image of CrN columnar grains away from the substrate about 100 nm. **(d)** A typical HRTEM image of Cr columnar grains with a Σ3 {1 1 1} coherent twin boundary.

Owings to high SFEs, twinning of TMNs is difficult [16, 26]. Thus, we applied the {111}/{0001} hetero-phase interface-facilitating twin nucleation and manufacturing high-density twins in rock-salt CrN (as seen in our previous research results [18]). As shown in Fig. 1a, the CrN layer thickness is 100 nm, and the AlN as the intermediate layer is 4 nm. Due to a well epitaxial stable relationship with the $[111]_{CrN}/[0001]_{AlN}$ (as seen in the Supplementary, Fig. S2), CrN columnar grains exhibit the [111] growth texture. Thus, most columnar grain boundaries have the Σ3 {1 1 2} incoherent twin boundary near the substrate area (as shown in Fig. 1a and 1b). However, as the thin film thickness increases, CrN grains grow with a large misorientation angle in the film area far away from the substrate (around 100 nm), and numerous Σ3 {111} coherent twin boundaries (CTBs) can be easily found, as shown in Fig.1c and 1d. The formation of CTB can be explained by the fact that occasionally certain adjacent

nuclei may happen to have the twinned orientation relationship [27], which requires rock-salt grains with specific and larger nucleation angle.

3.2 Observation of the CTB structure in CrN
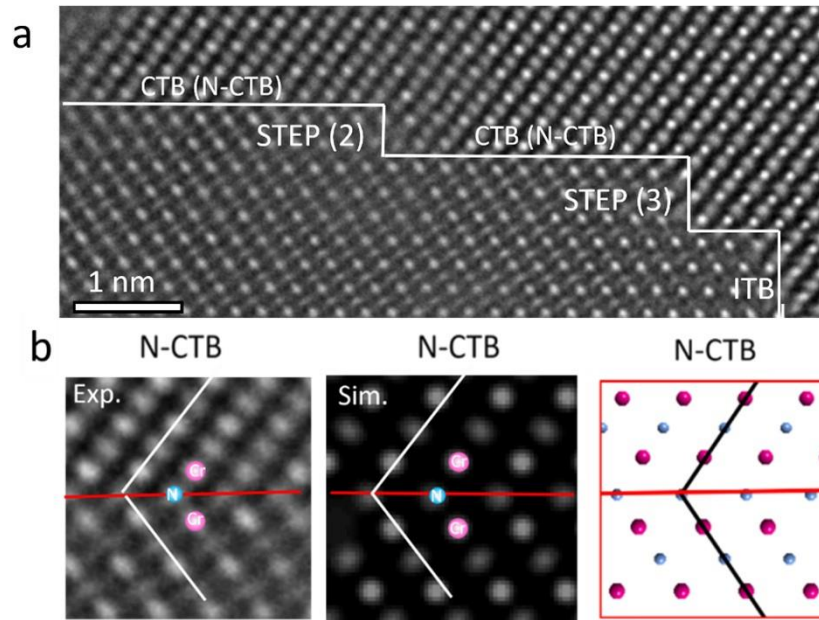
Fig.2. **(a)** HRTEM observation of an un-irradiated (normal illumination mode) $\Sigma3\{111\}$ CTB of *rs*-CrN, and a typical $\Sigma3\{112\}$ ITB is present on the right-hand side. In $\Sigma3\{111\}$ CTB, some stepped structures with a certain height can be observed, i.e., $2\times d_{\{111\}}$ height (STEP (2)) and $3\times d_{\{111\}}$ height (STEP (3)). **(b)** HRTEM experimental (enlarged image from Fig. 2a), simulation image and atomic model of N-terminated CTB. Image simulations were carried out under the following conditions: Cs = 0 and defocus = - 9.9 nm, close to the experimental conditions, with a specimen thickness of 3.1 nm.

The $\Sigma3\{111\}$ CTB in the rock-salt (*rs*) CrN is used as an example to show the TD nucleation and CTB migration. For *fcc* metals, the mirror-symmetrical plane for $\Sigma3\{111\}$ CTB is the metal atom $\{111\}$ plane. However, the binary rock-salt structure of TMN has a double *fcc* structure, i.e., transition metal and nitrogen atoms sit on two inter-penetrating *fcc* lattice. Thus, for the rock-salt TMN, two CTB structures may exist in a $\Sigma3\{111\}$ CTB, i.e., TM (TM=Transition Metal)-$\{111\}$ or N-$\{111\}$ as a mirror-symmetry plane of CTB. HRTEM observation of an unirradiated CTB (Figure 2a, illumination mode with a low beam current density) shows that the CTB is discontinuous, which includes some stepped structures with a certain height, i.e., $2\times d_{\{111\}}$ height and $3\times d_{\{111\}}$ height. Fig.2a was recorded from a very thin

area, where all atoms are resolved and exhibit either strong bright or weak bright contrast. Combined with the HRTEM image simulation, we can unambiguously assign the strong contrasts to Cr atom columns and the weak bright contrasts to N atom columns (as seen in Figure 2b). Thus, with individual Cr and N atoms clearly resolvable, $\Sigma 3\{111\}$ CTBs in Figure 2b only with an N-terminated were observed in an *rs*-CrN and no other variant structures of CTB are found.

3.3 CTB migration from CTB/ITB and CTB/surface junctions
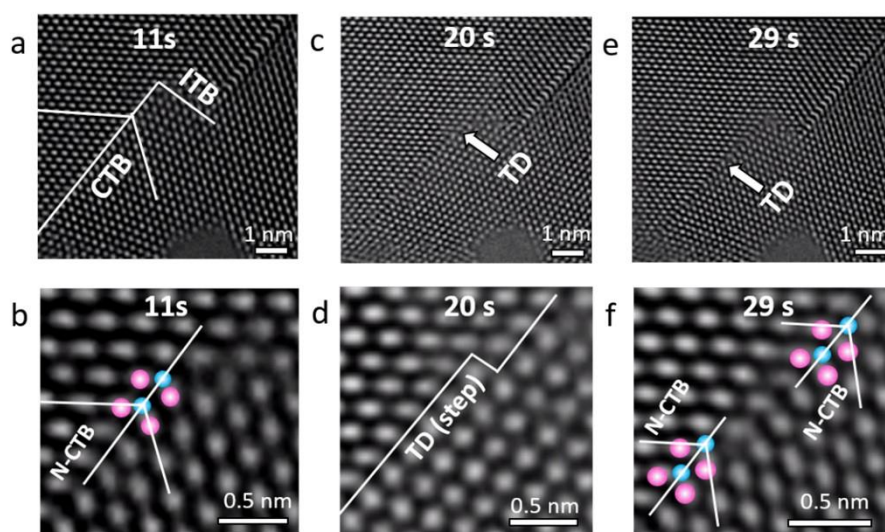
Fig. 3. **(a)-(f)** Series of HRTEM images (snapshots of Movie S1) of CTB migration from the CTB/ITB junction. (b), (d) and (f) are the enlarged images in the twin defect region at 11s, 20s, and 29s, respectively.

Twin boundary defect (TD) emission from the CTB/GB junction is a known mode for *fcc* metals [28]. However, such a mode has not yet been reported in nitride ceramics. Our first *in-situ* experiments demonstrate the emission of defects from the CTB/ITB (incoherent twin boundary) junction in CrN. The initial CTB is very smooth and exhibits no any steps, as shown in Fig.3a and 3b (at 11s, snapshots of Movie S1). After intensive electron beam irradiation for 20s, a step at the CTB was clearly emitted from the CTB/ITB junction (the step position was shown in Fig.3c and 3d). With further irradiation for 29s, the defect moves forwards, but the CTB hardly show any boundary structure alternating (as seen in Fig.3e and 3f), i.e., maintaining the N-terminated CTB (due to the sample thickness, the contrast of the N atom column here is too weak, as proved by HRTEM image simulation in Fig. S3). The TD emission from the CTB/ITB junction gives a twin boundary step, i.e., TD formation and with a height of $1 \times d_{\{111\}}$.

Hence, our experimental observation shows that TD nucleation and CTB migration can start from the CTB/ITB junction, where for such a migration mode, the boundary structure is unvaried.
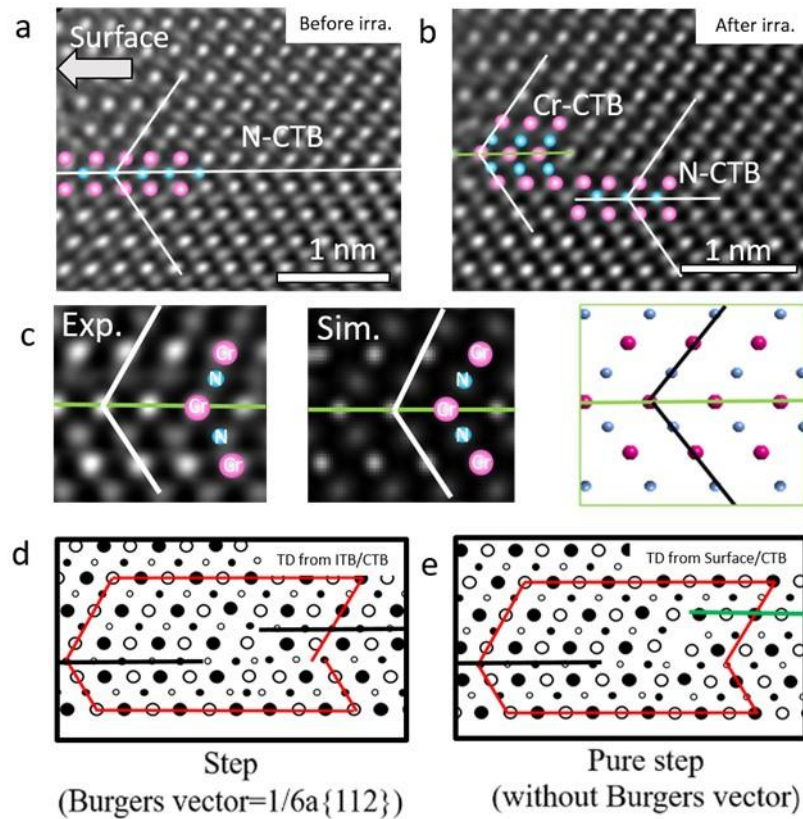

Fig. 4. **(a) and (b)** HRTEM images (before and after irradiation) showing the twin defect nucleation and CTB migration from the CTB/surface region. **(c)** HRTEM experimental (a clipping of Fig.4b), simulation image and atomic model of Cr-terminated CTB. Image simulations of (c) were carried out under the following conditions: Cs = 0 and defocus = - 9.9 nm, close to the experimental conditions, with a specimen thickness of 3.1 nm. **(d)** and **(e)** Dichromatic patterns show Burgers vector loop with TD from the CTB/ITB junction and CTB/surface junction, respectively. The black and green lines in Fig. 4 (d) and (e) indicate the CTB structures with the N-terminated and Cr-terminated, respectively.

However, a different twin boundary defect nucleation and CTB migration mode can be identified when emitted from the CTB/surface junction. Before intensive electron beam irradiation (Fig.4a), the initial $\Sigma 3\{111\}$ CTB is a smooth and defect-free grain boundary, and the structure shows a perfect N-terminated CTB. After intensive electron beam irradiation (Fig.4b), the CTB exhibits distinct feature and becomes imperfect at around the CTB/surface

junction. Interestingly, the CTB boundary structure exhibits alternating, i.e., part of the N-terminated CTB has transformed into the Cr-terminated CTB (as seen in Fig.4c).

In contrast to the above investigations (Fig. 3), here, our observation at the CTB/surface junction reveals a new type of twin boundary defect. In Fig. 3b, TD emission from the CTB/ITB junction shows a twin boundary step structure with the N-terminated/N-terminated and with a height of $1 \times d_{\{111\}}$. Thus, the TD structure has similarity to those in *fcc* metals, and the Burgers vector of such TD is 1/6a[112]. However, in Fig. 4b, the TD emission from the CTB/surface junction displays a twin boundary step structure with the N-terminated/Cr-terminated and a height of $1.5 \times d_{\{111\}}$. The dichromatic patterns in Fig.4d and Fig. 4e compare the two types of twin-boundary defect structure and display the structure difference (directly measured Burgers vector on the HRTEM micrographs is shown in Fig. S4). Interestingly, TD nucleation from the CTB/surface junction creates a simple step without the Burgers vector, i.e., a pure step [29]. To the author's knowledge, such a TD without the Burgers vector has never been reported in *fcc* metallic materials.

3.4 Reversible CTB migration
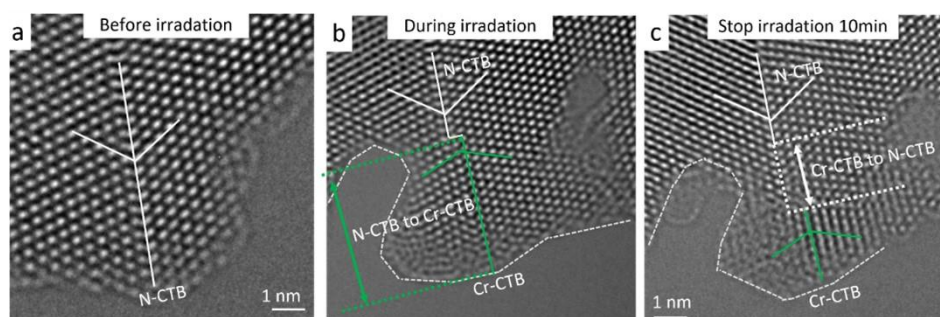
Fig. 5. **(a)** and **(b)** HRTEM images showing that the CTB structure varies from an N- terminated CTB to a Cr- terminated CTB. The white label shows the CTB with the N- terminated structure and green label shows the CTB with Cr- terminated structure. **(c)** HRTEM image displays the already created Cr-terminated CTB partially reverses to the N- terminated CTB after terminating irradiation for 10 min.

Under normal beam illumination, mostly observed CTB structures are with an N-terminated. This implies that the Cr- terminated CTB might not be stable (Actually, our DFT calculation confirms the energy difference for the two CTB structures). This is indeed proved by the following experiment. Fig. 5a and 5b show that the CTB structure changes from a fully

N-terminated CTB (white labels) to a part of Cr-terminated CTB (about 6 nm long, green labels) induced by intensive electron beam irradiation (enlarged images are seen in Fig. S5). When the electron beam is switched off, the Cr-terminated CTB partially (about 2.0 nm) transforms back to the N-terminated CTB (Fig. 5c). This is an energetically-driven process. When terminating the irradiation, the residual strain near the CTB/surface is likely to be released quickly, driving the CTB step to move in the opposite direction. A small residual stress/strain relaxation may trigger such an inverse process of the CTB migration. Therefore, compare with the Nr-terminated-CTB, experiment here proves that the CTB of Cr-terminated is unstable, and its CTB structure alternating requires a certain driving force.

3.5 Measurement of TD movement
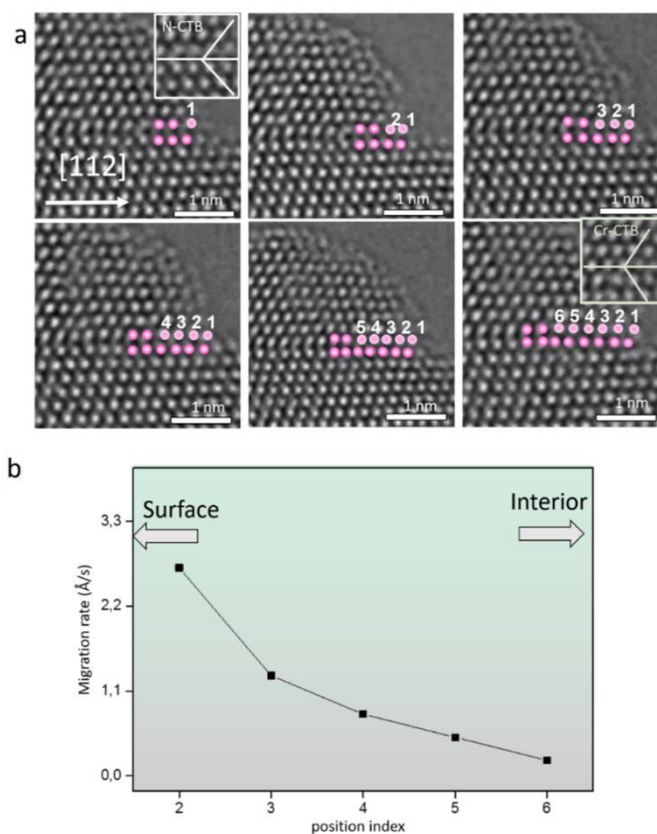
Fig. 6. **(a)** Series of HRTEM images show the CTB migration process from the CTB/surface junction (snapshots of Movie S2), where the labeled atoms represent the new migration position in the Cr-terminated CTB (from 1st to 6th atom). The inserted enlarged images show the CTB structure alternating from the N-terminated to the Cr-terminated CTB. **(b)** Measured migration rate of a single atom column according to Fig. 6a.

The TD motion events in the CTB captured by our *in-situ* atomic-resolution experiments allow us to measure the migration rate of individual atomic columns, further to gain insights into dynamic process of defect motion. A series of HRTEM images (Fig.6a) demonstrates the TD motion and CTB migration process at the CTB/surface junction (from the N-terminated to the Cr-terminated CTB). Every image in Fig.6a shows the change of one atomic column at CTB (from 1st to 6th), which confirms that the CTB migration is accomplished by TD motion. The moving rate of a single atomic column is measured and shown in Fig.6b, where the surface atom (the 1st) exhibits the highest migrating speed. However, as moving towards the interior from the surface, the migrating speed of the atomic column gradually decreases, and the migrating time finally reaches 4000 ± 100 ms. The difference of the migrating rate in 1st atomic column and 6th atomic column is attributed to the attenuation of surface strain. Detailed strain analysis is referred to the discussion section (Section 4.1.1).

3.6 Asynchronous CTB migration and TD movement
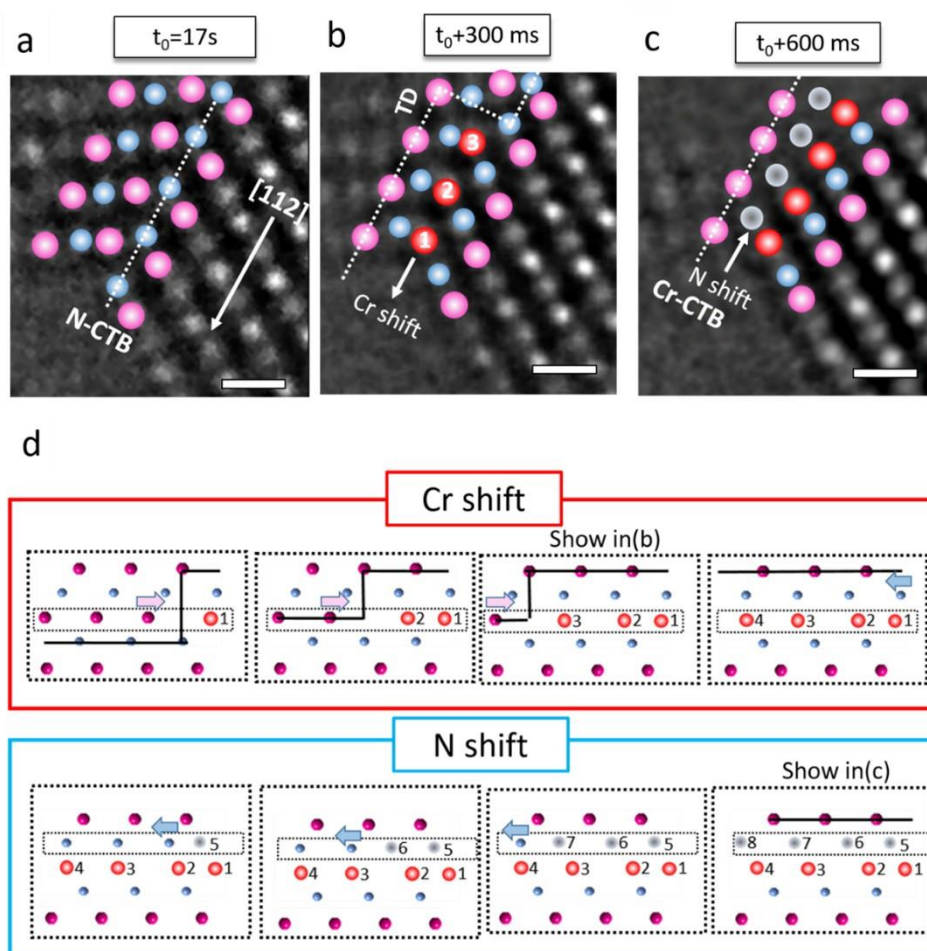
Fig. 7. **(a)-(c)** HRTEM images (snapshots of Movie S3) of the initial state, transitional state, and final stage of CTB migration from N-terminated to Cr-terminated, respectively. **(d)**

Schematic sequence of asynchronous CTB migration and the TD movement. The first stage is the migration of Cr atom from left to right (as labeled by the pink arrows and by 1st -4th Cr atoms), corresponding to the TD step moving to the left accordingly (the upper row in (d)). The second stage is the migration of N atom from right to left (as labeled by the blue arrows and by 5th-8th N atoms in the lower rows of Fig. 7d)).

The above result indicates that the CTB migration may involve a boundary structure alternating from an N-terminated to Cr-terminated. However, the Cr and N atom respective migration process remains unknown. Three possible modes of TD motion and CTB migration exist: (i) Cr atoms migrate firstly and then N, (ii) N atoms migrate firstly and then Cr, (iii) synchronous migration of Cr and N.

Here, we will reveal that the CTB migration process involves the asynchronous motion of Cr and N atoms (as seen in Movies S3). The initial CTB has the N-terminated boundary structure with individual Cr and N atoms resolvable (Fig. 7a, N-CTB). After a very short period (300 ms), a transient state appears with a boundary structure in between N-terminated and Cr-terminated CTB (Fig. 7b). The Cr atoms adjacent to the CTB have migrated (red atoms in Fig. 7b) by a vector of $1/6a[112]$ as confirmed by the corresponding simulation image (shown in Fig. S6). However, N atoms are still unaltered. This can be identified by comparing the atom contrast and checking the reference. In Fig. 7b, a twin boundary step structure with N-terminated/Cr-terminated and with a height of $1.5 \times d_{\{111\}}$ can also be found, which also confirms that the CTB migration is accomplished by TD motion.

After an additional 300 ms, a final state of the CTB migration with a Cr-terminated structure has been reached (Fig. 7c, Cr-CTB). Comparing Fig. 7a to Fig. 7c, it is found that the N atoms (grey atoms in Fig. 7c) have wholly migrated along the direction opposite to Cr atom motion and with a migration vector of $1/6a[\bar{1}\,\bar{1}\,\bar{2}]$. After the N atoms shift, a complete CTB migration from N-terminated to Cr-terminated has been achieved. The structure of the CTB has changed within a very short time, and the TD migration process is via an asynchronous atom migration mode in which the Cr atoms migration firstly followed by the N atoms. Fig.7d schematically illustrates asynchronous CTB migration and TD movement that occurred in Fig.7a-c. It involves two stages, the first is the migration of Cr atoms shift (as labeled by the pink arrows and by 1st -4th Cr atoms) in the upper row of Fig.7 (d), and one instantaneous state corresponds to Fig. 7b. The second is the migration of N atom from the right to left (as labeled by the blue arrows and by 5th-8th N atoms) in the lower rows of Fig.7(d), and one instantaneous state corresponds to Fig.7c.

141

Based on the above experimental observations, the dynamic process of CTB migration and TD motion is briefly summarized as follows: (i) the movement of Cr and N atoms is not synchronous, but with the Cr atoms migration firstly followed by the N atoms. (ii) during the CTB migration and TD movement, both Cr and N atoms shift via the shortest path and in the opposite migration direction. Here, by explicitly recording the atomic-resolution image of the transient state, the most critical finding is that the asynchronous motion mode of Cr and N atoms occurs during the TD motion and CTB migration.

3.7 TD nucleation at the surface
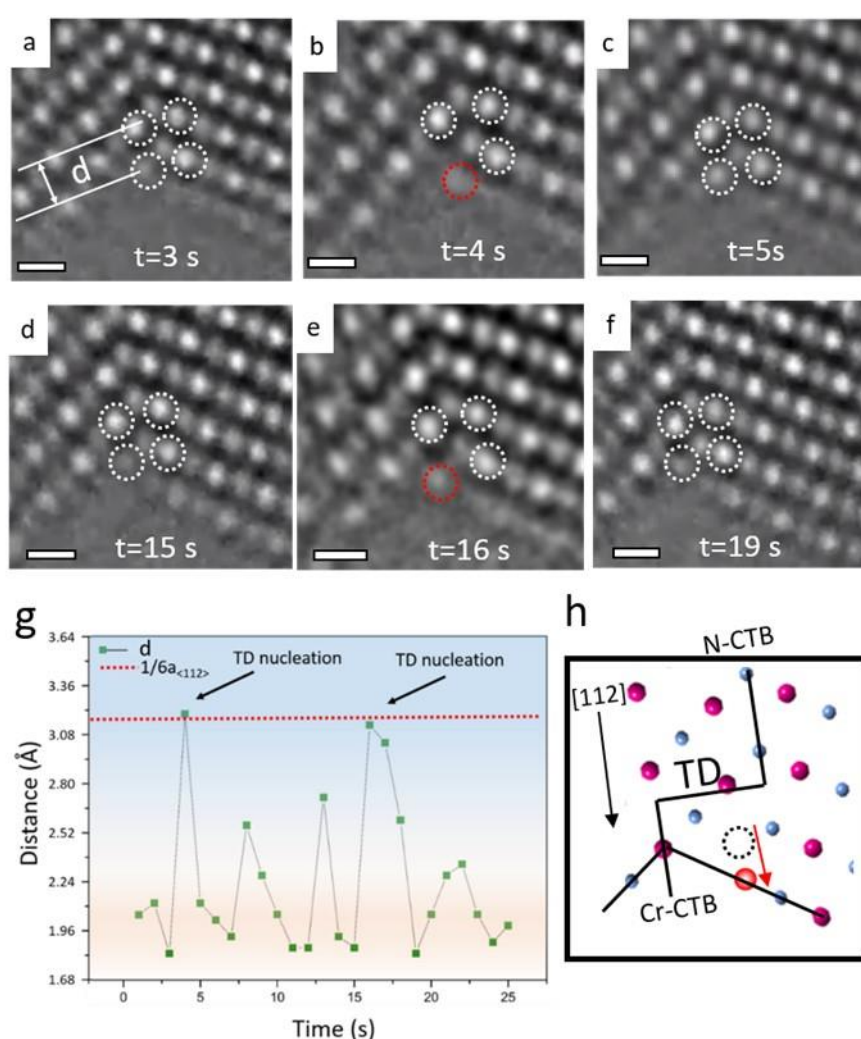
Fig. 8. **(a)-(f)** Series of HRTEM images (snapshots of Movie S4) illustrating the movement of atoms at the CTB/surface junction, the dotted circles represent the position of 4 Cr atoms, and the red ones correspond to two cases with a large deviation of Cr from their equilibrium positions. **(g)** The change of Cr-Cr atomic spacing ('*d*' in **a**) at the CTB/surface position in

Movie S4 with irradiation time. **(h)** A schematic model of the designated Cr atom jumping at the CTB/surface junction (the jumping direction is indicated by a red arrow). Scale bars: (a -f) 0.25 nm.

Our preceding observations confirm that TD formation and CTB migration in CrN can stem from the CTB/ITB junction. $\Sigma 3$ {1 1 2} incoherent twin boundaries (ITB) are dislocation walls composed of a series of high-density partial dislocations [30]. So, 1/6a [112] type partial dislocations may dissociate from the ITB and glide along the CTB. For TD nucleation from the surface, it may relate to its surface effects, e.g., surface reconstruction or relaxation. Theoretically, as the coordination number of atoms on the solid surface decreases, higher free energy at the surface/CTB junction results from the missing atom. Thus, under the electron beam, the surface atoms are more active and likely to deviate from their equilibrium positions.

Here (Movie S4, normal illumination mode), we analyze the TD nucleation process at the CTB/surface junction. Fig. 8a (Movie S4, t=3 s) presents a perfect N-terminated CTB at the thin edge of the sample. After 1s (t=4 s), one surface Cr atom (labeled by a red circle, Fig. 8b) jumps away from the normal lattice position at the CTB/surface junction. It is noted that the Cr atom jump is not arbitrary, but it is along the [112] direction (from the surface to vacuum) with a certain distance (see below). Prolonging the beam irradiation (t=5s), the surface Cr atom returns to the initial position, i.e., jumps back along the [$\overline{112}$] (Fig. 8c). In the total time of 25 s, we frequently observe the oscillation of the surface Cr atoms. The second significant jump of Cr atom occurred at t=15-19 s (Fig. 8d-f). Here, the variation of the Cr-Cr atomic spacing ("d") at the CTB/surface junction in consecutive 25s was evaluated, and plotted in Fig. 8g. Clearly, two significant Cr jumps were detected when t=4s, 16s, corresponding to a spacing of 3.31 Å and 3.26 Å, respectively. The striking change of Cr atom position represents the structural change of CTB at the surface, i.e., the active Cr atom actually moves close to the position that a Cr-terminated CTB stipulates, creating a TD (Fig.8h). Thus, under the stimulus of the electron beam, the TD could nucleate instantaneously at the CTB/surface junction.

4. Discussion

4.1 On the driving force of CTB migration and TD motion

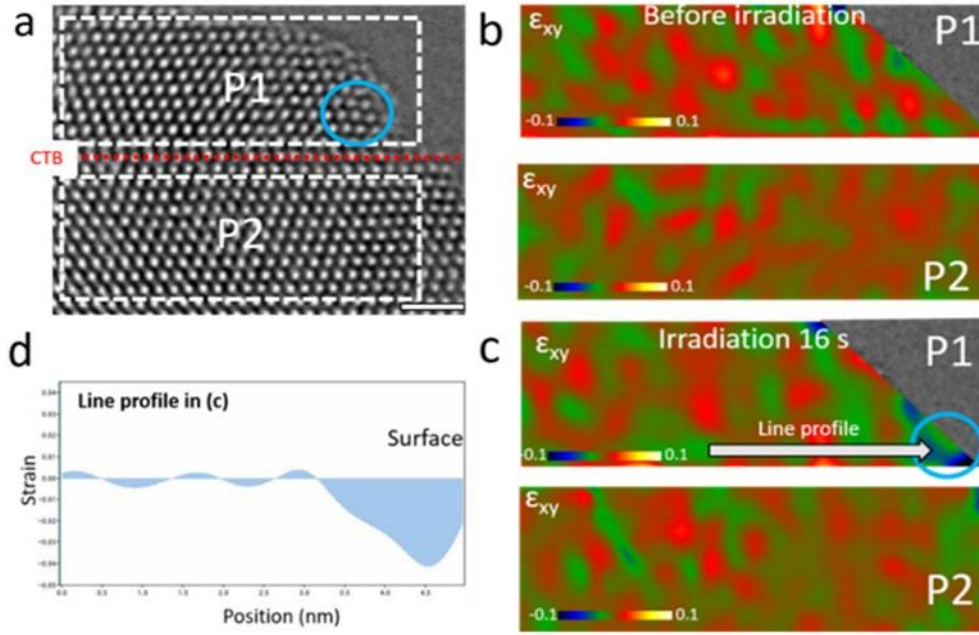### 4.1.1 Irradiation-induced strain as a driving force

143

Fig.9. **(a)** Snapshots of Movie S2 (t=16 s, 1 second before the CTB migration). White frames (labeled as p1 and p2 position) are used for GPA measurement. **(b) and (c)** GPA results of different irradiation time (before irradiation and t=16 s). **(d)** Line profile at the surface/CTB junction (along the line in (c)). Scale bars: (a) 1 nm.

Previous studies have reported the microstructure evolution driven by the irradiation-induced stress field, such as irradiation-driven dislocation motion [31, 32], propagation of cracks [31, 33, 34], and migration of grain boundaries [32, 35, 36]. Here, we observed that both CTB migration and TD motion could be initiated on the surface under intensive beam irradiation.

For the twin boundary, the interface energy of Cr-terminated CTB is higher than that of N-terminated CTB (referring to our DFT result below). Hence, there is no thermodynamic driving force for the spontaneous transformation of CTB. Sufficient strain/stress is required to initiate the TD motion in CrN. Through GPA, we confirm that high current density electron beam irradiation can effectively cause stress/strain concentration at the surface/CTB junction (Fig. 9a), which will be the main driving force for CTB migration and TD motion. The shear strain mapping (ε_{xy}) with different irradiation times are shown in Fig.9b and 9c. For the upper part of the CTB (p1 position), the surface region exists a maximum ~ 1% shear strain (ε_{xy}) before the intensive beam irradiation (Fig. 9b). It reaches ~ 4% shear strain after irradiation for t=16 s (Fig. 9c, just 1s before the TD motion and CTB migration). However, for the lower part of the CTB (p2 position), no significant strain changes are observed. The local strain variations

induced by irradiation is clearly visible from the line profile (Fig.9d). It displays a considerable strain concentration at the surface region, and the shear strain is rapidly attenuated towards the interior. Since the gradient strain/stress distribution, this also causes the migration speed of TD to gradually decrease as it moves from the surface to the interior (as seen Fig.6). Therefore, our GPA analysis confirmed that the irradiation-induced stress/strain field provides a driving force for CTB migration and TD movement.

Currently, the exact mechanism of lattice strain/stress concentration caused by electron beams is still unclear. It may be related to two factors. (i) Lattice deformation is caused by the vacancy effect [37-39]. When vacancies form, some of their chemical bonds are broken, causing distortion and deformation of the crystal lattice, ultimately leading to local strain concentration in thin regions. (ii) The thermal strain is caused by the local heating of the intensive electron beam [40].

As discussed, beam irradiation can be acted as a driving force for the CTB migration and TD motion. Throughout the observations, we further found that the CTB structure alternating can also be driven by the residual stress in the film (as seen in Supplementary Fig. S7), in addition to beam irradiation (i.e., Fig.7). For the un-irradiated CTB, we found that when the local position is subjected to high strain, the asynchronous migration of CTB can also be observed, as exemplified in supplementary Fig. S8. Thus, we confirmed that the driving force of CTB migration from the N-terminated CTB to the Cr-terminated CTB.

4.1.2 Strain driven asynchronous TD motion
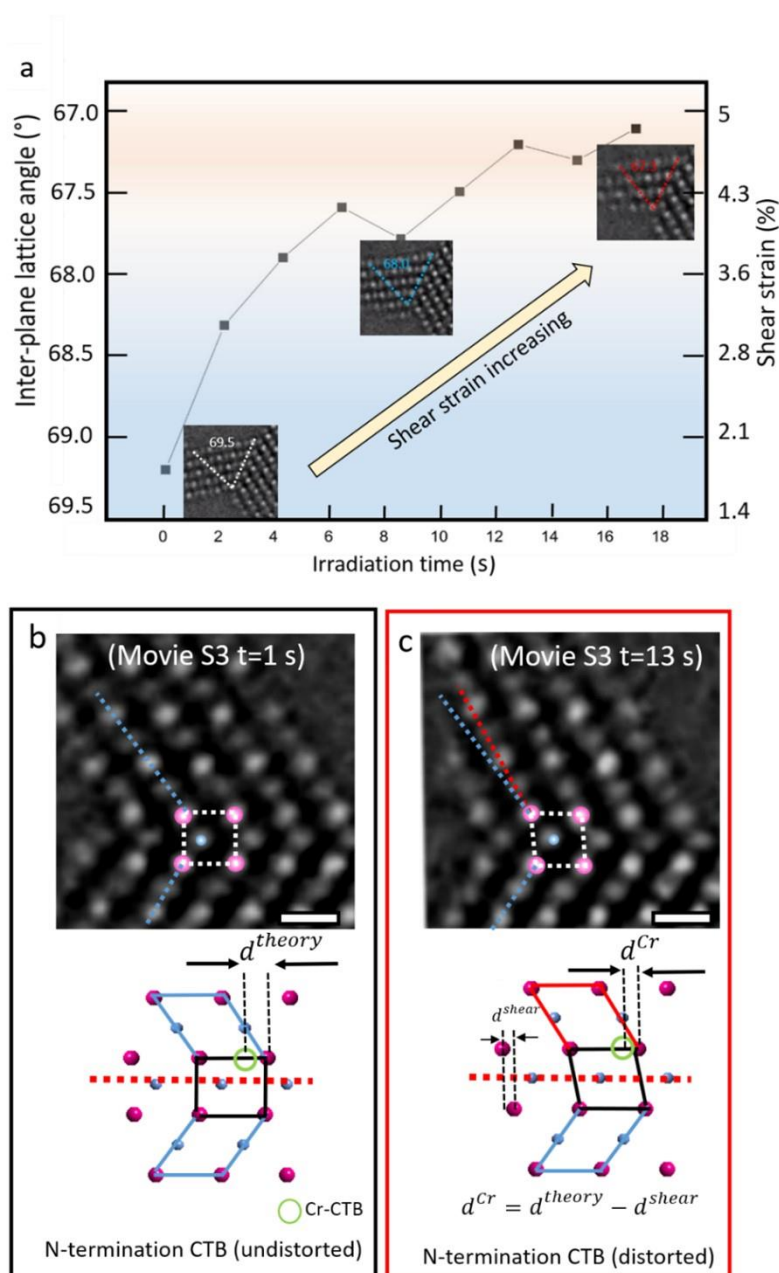
Fig. 10. **(a)** Measured lattice plane angle (or shear strain) change as a function of irradiation time just before the CTB migration (Movie S3, in consecutive 17 s). **(b)** HRTEM (snapshot of Movie S3 t=1s), and a schematic image of near-perfect N-terminated CTB. (**c**) HRTEM (snapshot of Movie S1, t=13 s), and schematic images of the distorted N-terminated CTB. Scale bars: (b,c) 0.25 nm.

The above discussion (section 4.1.1) clarifies that the strain/stress concentration generated by electron beam irradiation or the film growth is the driving force of CTB migration. Meanwhile, the strain/stress concentration also facilitates the migration of CTB in an

146

asynchronous mode. In Figs.7 (movie S3), we observe that TD motion and CTB migration process are asynchronous. As Fig. 10a showed, a 4.5% shear strain has been reached in the upper part of the CTB before initiating the migration of CTB. In fact, the presence of the shear strain facilitates the initial migration of Cr atoms, as demonstrated as follows. At t=1s (Movie S3), Fig. 10b shows a low lattice shear strain state since both are close to a theoretical value of 70.5° (the angle between $(11\bar{1})$ and $(1\bar{1}1)$ planes). After 13s of beam irradiation (Fig. 101c), the angle becomes α_1 =67.3° (also shown in Fig. S9). This translates to ~4.5% shear strain. By carefully comparing atomic-resolution images under different irradiation times, we found that the distorted CTB with N-terminated (caused by the shear strain) shortens the Cr atoms' migration distance. Before the CTB migration, the atomic structure of the N-terminated CTB is strongly distorted (by comparing the white square in Fig.10b and Fig.10c). Such a distortion effectively pushes Cr atoms (adjacent to the N-terminated CTB) close to the position of the Cr-terminated boundary (the green circle in schematic images of Fig.10b and Fig.10c), i.e., $d^{Cr} = d^{theory} - d^{shear}$. Therefore, the shifting distance of the Cr atom becomes smaller than the required one. In contrast, the N atom's shifting distance becomes larger than the required one (as analyzed in Fig. S10) i.e., $d^N = d^{theory} + d^{shear}$. Thus, the shear strain induced CTB structure distortion will facilitate asynchronous migration.

4.2 On the thermodynamic mechanism of CTB migration
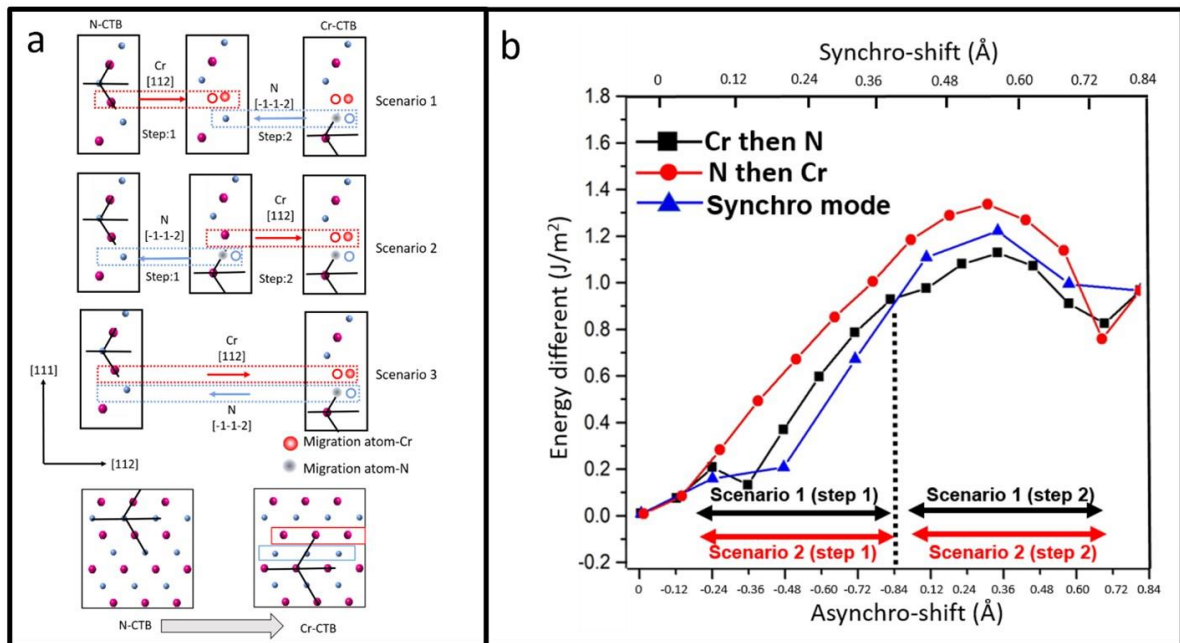
Fig. 11. **(a)** Schematic modes of different migration paths (Scenario 1,2,3, see text for details) from the N-terminated CTB (N-CTB) to the Cr-terminated CTB (Cr-CTB). The open circles denote the initial positions (before Cr and N atom migration). **(b)** DFT calculated energy barriers (relative to the energy of N-terminated CTB) as a function of migration displacement along the ⟨112⟩ direction. The black and red lines represent asynchronous modes, i.e., Scenario 1 and Scenario 2 in Fig 11(a). The blue line indicates a synchronous mode, i.e., Scenario 3 in Fig 11(a).

In order to rationalize the CTB structure altering from N-terminated to Cr-terminated, we apply DFT calculations and compare the energy barriers (the mode of N-terminated to Cr-terminated). Based on the experiment observation, three scenarios are considered for the migration paths, as shown in Fig.11a. Scenario 1 (experimentally observed migration path) is an asynchronous migration mode. The first migration is the Cr atom (with a migration vector of $1/6a[112]$), followed by N (with a migration vector of $1/6a[\overline{112}]$). Scenario 2 is a mode that the N atom migration first (with a migration vector of $1/6a[\overline{112}]$), and then moves the Cr (with a migration vector of $1/6a[112]$). Scenario 3 is a synchro migration mode of Cr and N atoms simultaneously with a migration vectors of $1/6a[112]$ and $1/6a[\overline{112}]$, respectively. The calculated energy differences of CTB for different scenarios are plotted in Fig.11b as a function of the migration displacements (from N-terminated to Cr-terminated CTB).

For all scenarios, the N-terminated CTB exhibits the lowest energy configuration, whereas the Cr-terminated CTB is a higher energy metastable separated from the N-terminated by an energy barrier. Compare with the other scenarios, scenario 1 exhibits the lowest energy barrier to migration, i.e., the "resistance" during the initial CTB migration process is much smaller in scenario 1 than in the other scenarios. Thus, this analysis corroborates our experimental observations on asynchronous migration from N-terminated to Cr-terminated (Figs. 7).

Furthermore, for the first half of the scenario 1 (Cr-before-N mode, black curve) in which Cr atoms migration along the [112] direction, the maximum energy is 0.97 J/m^2 (scenario-1, step 1), corresponding to the intermediate ball-on-ball configuration. However, for the first half of scenario 2 (N-before-Cr mode, red curve), the maximum energy of the first stage of N atoms migration is 1.24 J/m^2 (scenario-2, step 1). This indicates that the energy barrier for the first migration of Cr atoms is lower than that for the first migration of N atoms. This could also be proved by experimental observation. Figs. 12 shows an instantaneous TD nucleation event at the CTB/surface junction, where beam irradiation drives the lower energy-barrier Cr atoms to migrate firstly, i.e., TD nucleation, while the N atom is relatively stable.
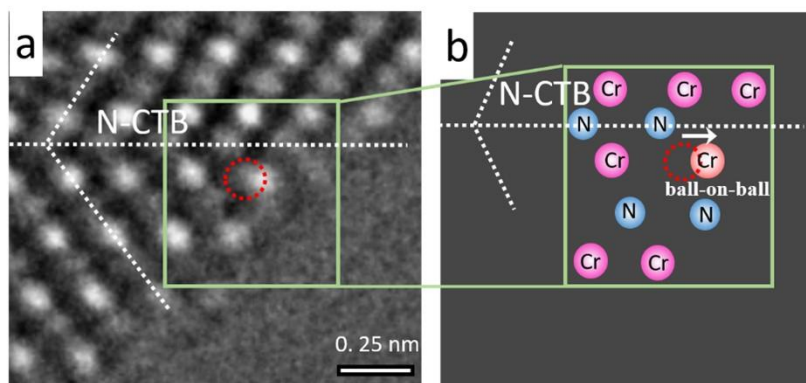
Fig. 12. **(a)** HRTEM (Movie snapshots) shows the instantaneous TD nucleation event at the CTB/surface junction. **(b)** Schematic atomic positions in (a). In this TD nucleation event, only one labeled Cr atom (the dotted circle represents the initial location of migrating Cr atom) showing the migration, where the adjacent N atom is relatively stable (the local atom positions are indicated by the rectangle).

In short, according to the DFT results, we infer that the CTB/surface migration mode has a different energy transformation mechanism relative to the CTB/ITB migration mode. Figs.13 schematically summarizes the CTB migration modes from the CTB/ITB and CTB/surface. For the CTB/ITB mode, CTB migration is not associated with a boundary structure alternating, which indicates that CTB have equal energy before and after migration. As for the CTB/surface mode, CTB migrates from the CTB/surface junction is an alternating structural process from N-terminated CTB to Cr-terminated CTB, which leads to the CTB have the higher energy after migration. However, according to our DFT results, the CTB with Cr-terminated structure is with a high-energy state (by comparing the initial point and ending point in the curves, which correspond to the N-terminated and Cr-terminated CTB, respectively), and metastable. Therefore, the Cr-terminated CTB is unstable, and its migration is easier than N-terminated, i.e., a smaller energy barrier needed for the Cr-CTB reversing to N-CTB (~ 0.17 J/m^2 obtained from the scenario 1 curve). This is exactly what we experimentally observed in Figs.5.

149
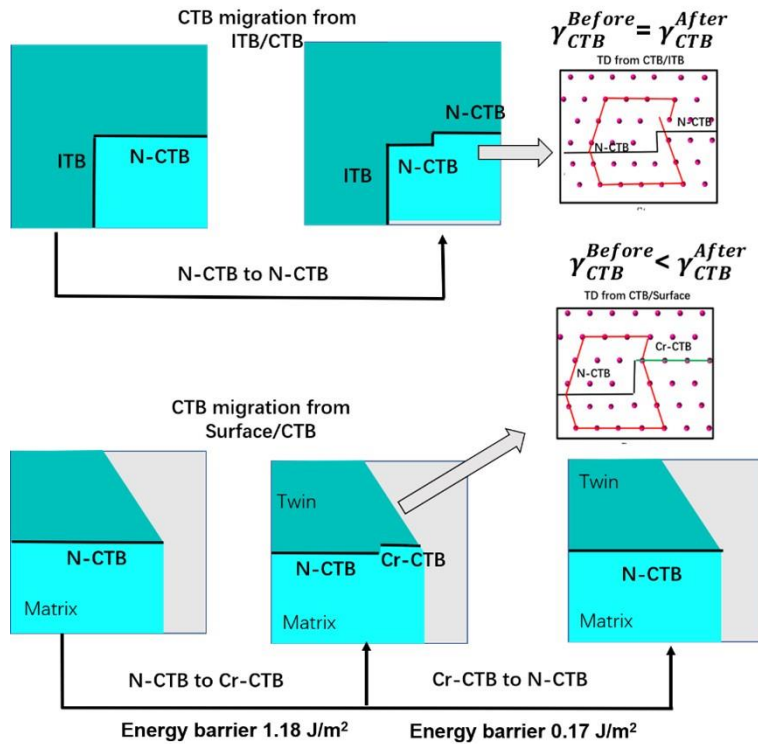
Fig.13. A summary of CTB migration modes from the CTB/ITB and CTB/surface junction

4.3 The effect of TMN twinning on mechanical properties

In *fcc* metals, a certain density of twins will soften the material [12-14]. Here, our multilayer has very high-density twins (as seen in Figs. S11), but the multilayer's hardness with twins is only 21 GPa (measured by nanoindentation). Such value is lower than that of multilayer CrN/AlN coatings with various bi-layer periods [41-45] and even lower than that of single-layer CrN coatings [41, 43, 46, 47]. This implies that twins barely harden the multilayer but limit the strength instead. We consider that the existence of many TBs may play a softening effect. To verify the CTB structure after loading/deformation, a TEM observation was carried out in the indented fill. Fig. 14a shows a top view after nanoindentation, where the position of FIB cutting is shown in a white frame (supplementary Figs. S12 shows the overall morphology of the indented cross-section coating). For indented coating, Fig. 14b shows an atomic-scale observation of CTB, which indicates the formation a completely Cr-terminated CTB. TEM observation here confirms that load/deformation can also drive the CTB migration from N-terminated CTB to the CTB completely terminated with Cr. Since the existence of CTB migration and TD motion behavior, it can dissipate the elastic strain energy and softening the material [12-14]. Meanwhile, previous molecular dynamics simulations (uniaxial tension/

150

compression deformation) showed that the mechanical properties with different types of CTB in *rs*-VN (metal-terminated and N-terminated) is dissimilar [48]. It indicates that metal-terminated CTB has lower critical stress than N-terminated CTB, and CTB migration behavior (accompanied by structural alternating) contributes to softening.

Furthermore, polycrystalline TMN coating has the intergranular fracture mode [49, 50]. The fragile grain boundary is also one of the important factors limiting its strength. In our CrN multilayer film, both Σ3{111}-CTB and Σ3{112}-ITB constitute main columnar grain boundaries. And Σ3{111}-CTB displays two different symmetrical plane structures, presenting different grain boundary strength and fracture toughness accordingly. An interesting property of GB is the work of separation W_{sep}, which is a measure of the energy required to cleave the GB into the free surfaces and is correlated to the fracture toughness. W_{sep} is given by the following formula:

$$W_{sep} = 2E_{surf} - E_{GB} \tag{1}$$

where E_{surf} is the corresponding surface energy for the facet (*hkl*) formed by cleaving the GB. E_{GB} is the corresponding grain boundary energy. Generally, rock-salt TMN {111} plane has much higher surface energy than {112} (as DFT results in Ref. [51] shown). For CrN ITB, although no calculation data are available, it can be considered that its energy is much larger than CTB. Thus, the work of separation for Σ3{111}-CTB will be larger than Σ3{112}-ITB, $W_{sep}^{ITB} < W_{sep}^{CTB}$. In *fcc* metals, CTB migration hardly involves boundary structural change and energy fluctuations, where CTB energy is also quite low. However, for CrN, our DFT result shows that the N-terminated CTB has much lower energy than Cr-terminated CTB (the energy difference is about 1 J/m^2). The work of separation for N-terminated will be larger than Cr-terminated CTB, i.e., $W_{sep}^{CTB-Cr} < W_{sep}^{CTB-N}$. Therefore, it is anticipated that CTB migration in CrN, involving the structural alternating from N-terminated to Cr-terminated boundary, will eventually cause a reduction of the CTB adhesion strength.
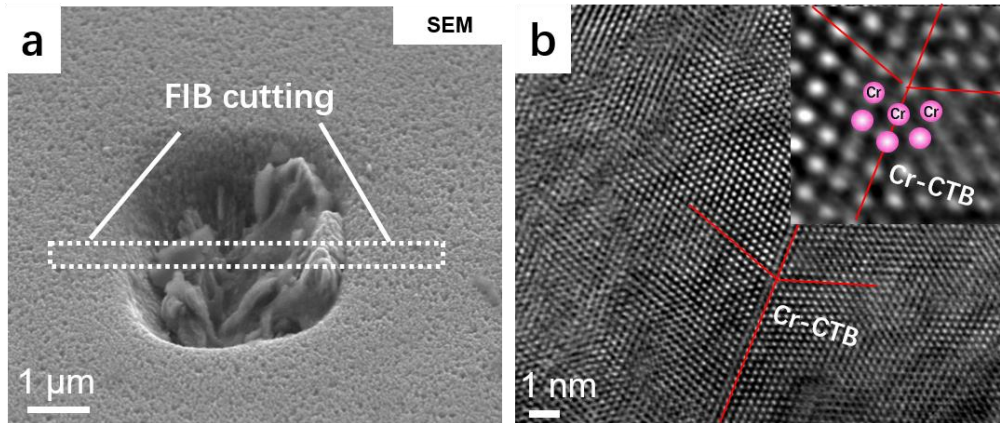
Fig.14 **(a)** SEM micrograph of top view of the indented thin film. **(b)** HRTEM observation of the CTB structure in the indented thin film.

5. Summary

We identified distinct CTB migration and TD nucleation mode using *in-situ* atomic-scale electron microscopy and fast recording system. The results obtained in the present paper can be summarized as follows:

(i) Twin boundary defect emission at the CTB/ITB junction has a 1/6a[112] Burgers vector. Moreover, the CTB migration from the CTB/ITB junction does not involve boundary structure alternating.

(ii) Twin boundary defect may also nucleate at the CTB/surface junction, but its structure hardly exhibits Burgers vector. The CTB migration involves boundary structure alternating from the N-terminated to Cr-terminated. Moreover, both TEM observations and DFT calculations confirm that the Cr-terminated CTB is with high energy and thus metastable.

(iii) CTB migration and TD motion from the surface are driven by the local stress, which originates from beam irradiation.

(iv) Under normal beam illumination, the CTB transformation from N-terminated to Cr-terminated can also be triggered by the internal stress or external load.

(v) *In-situ* HRTEM observation reveals that Cr and N atom respective motion is asynchronous. This is ascribed to the shear strain induced CTB structure distortion and the different migration energy barrier.

Through time-resolved HRTEM, we gain insight into the CTB migration and defect nucleation in a binary ceramic, which will improve our understanding of the deformation mechanism in complex materials

Acknowledgements

Reference

[1] M.L. Kronberg, Plastic deformation of single crystals of sapphire: Basal slip and twinning, Acta Metallurgica 5(9) (1957) 507-524.

[2] M.F. Chisholm, S. Kumar, P. Hazzledine, Dislocations in Complex Materials, Science 307(5710) (2005) 701-703.

[3] N. Shibata, M.F. Chisholm, A. Nakamura, S.J. Pennycook, T. Yamamoto, Y. Ikuhara, Nonstoichiometric Dislocation Cores in α-Alumina, Science 316(5821) (2007) 82-85.

[4] Z. Li, P. Munroe, Z.-t. Jiang, X. Zhao, J. Xu, Z.-f. Zhou, J.-q. Jiang, F. Fang, Z.-h. Xie, Designing superhard, self-toughening CrAlN coatings through grain boundary engineering, Acta Materialia 60(16) (2012) 5735-5744.

[5] R. Daniel, M. Meindlhumer, W. Baumegger, J. Zalesak, B. Sartory, M. Burghammer, C. Mitterer, J. Keckes, Grain boundary design of thin films: Using tilted brittle interfaces for multiple crack deflection toughening, Acta Materialia 122 (2017) 130-137.

[6] P.H. Mayrhofer, C. Mitterer, L. Hultman, H. Clemens, Microstructural design of hard coatings, Progress in Materials Science 51(8) (2006) 1032-1114.

[7] L. Lu, X. Chen, X. Huang, K. Lu, Revealing the Maximum Strength in Nanotwinned Copper, Science 323(5914) (2009) 607-610.

[8] K. Lu, L. Lu, S. Suresh, Strengthening Materials by Engineering Coherent Internal Boundaries at the Nanoscale, Science 324(5925) (2009) 349-352.

[9] M. Dao, L. Lu, Y.F. Shen, S. Suresh, Strength, strain-rate sensitivity and ductility of copper with nanoscale twins, Acta Materialia 54(20) (2006) 5421-5432.

[10] L. Lu, Y. Shen, X. Chen, L. Qian, K. Lu, Ultrahigh Strength and High Electrical Conductivity in Copper, Science 304(5669) (2004) 422-426.

[11] J.A. Brown, N.M. Ghoniem, Structure and motion of junctions between coherent and incoherent twin boundaries in copper, Acta Materialia 57(15) (2009) 4454-4462.

[12] Y.M. Wang, F. Sansoz, T. LaGrange, R.T. Ott, J. Marian, T.W. Barbee Jr, A.V. Hamza, Defective twin boundaries in nanotwinned metals, Nature Materials 12 (2013) 697.

[13] X. Ke, J. Ye, Z. Pan, J. Geng, M.F. Besser, D. Qu, A. Caro, J. Marian, R.T. Ott, Y.M. Wang, F. Sansoz, Ideal maximum strengths and defect-induced softening in nanocrystalline-nanotwinned metals, Nature Materials (2019).

[14] X. Li, Y. Wei, L. Lu, K. Lu, H. Gao, Dislocation nucleation governed softening and maximum strength in nano-twinned metals, Nature 464(7290) (2010) 877-880.

[15] S.K. Yadav, X.Y. Liu, J. Wang, R. Ramprasad, A. Misra, R.G. Hoagland, First-principles density functional theory study of generalized stacking faults in TiN and MgO, Philosophical Magazine 94(5) (2013) 464-475.

[16] H. Yu, M. Bahadori, G.B. Thompson, C.R. Weinberger, Understanding dislocation slip in stoichiometric rocksalt transition metal carbides and nitrides, Journal of Materials Science 52(11) (2017) 6235-6248.

[17] Y. Zhang, Z.-R. Liu, D.-W. Yuan, Q. Shao, J.-H. Chen, C.-L. Wu, Z.-L. Zhang, Elastic Properties and Stacking Fault Energies of Borides, Carbides and Nitrides from First-Principles Calculations, Acta Metallurgica Sinica (English Letters) (2019).

[18] Z. Chen, Q. Shao, M. Bartosik, P.H. Mayrhofer, H. Chen, Z. Zhang, Growth-twins in CrN/AlN multilayers induced by hetero-phase interfaces, Acta Materialia 185 (2020) 157-170.

[19] Wang L., Liu P., Guan P., Yang M., Sun J., Cheng Y., Hirata A., Zhang Z., Ma E., Chen M., Han X., In situ atomic-scale observation of continuous and reversible lattice deformation beyond the elastic limit, Nat. Commun. 4 (1) (2013) 2413.

[20] Z. Zhang, Y. Long, S. Cazottes, R. Daniel, C. Mitterer, G. Dehm, The peculiarity of the metal-ceramic interface, Scientific Reports 5 (2015) 11460.

[21] Z. Zhang, X. Gu, D. Holec, M. Bartosik, P.H. Mayrhofer, H.P. Duan, Superlattice-induced oscillations of interplanar distances and strain effects in the CrN/AlN system, Physical Review B 95(15) (2017) 155305.

[22] G. Kresse, D. Joubert, From ultrasoft pseudopotentials to the projector augmented-wave method, Physical Review B 59(3) (1999) 1758-1775.

[23] G. Kresse, J. Furthmüller, Efficient iterative schemes for ab initio total-energy calculations using a plane-wave basis set, Physical Review B 54(16) (1996) 11169-11186.

[24] J.P. Perdew, K. Burke, M. Ernzerhof, Generalized Gradient Approximation Made Simple, Physical Review Letters 77(18) (1996) 3865-3868.

[25] L.M. Corliss, N. Elliott, J.M. Hastings, Antiferromagnetic Structure of CrN, Physical Review 117(4) (1960) 929-935.

[26] S.K. Yadav, X.Y. Liu, J. Wang, R. Ramprasad, A. Misra, R.G. Hoagland, First-principles density functional theory study of generalized stacking faults in TiN and MgO, Philosophical Magazine 94(5) (2014) 464-475.

[27] S. Xue, Z. Fan, Y. Chen, J. Li, H. Wang, X. Zhang, The formation mechanisms of growth twins in polycrystalline Al with high stacking fault energy, Acta Materialia 101 (2015) 62-70.

[28] N. Lu, K. Du, L. Lu, H.Q. Ye, Transition of dislocation nucleation induced by local stress concentration in nanotwinned copper, Nature communications 6(1) (2015) 7648.

[29] J.P. Hirth, R.C. Pond, Steps, dislocations and disconnections as interface defects relating to structure and phase transformations, Acta Materialia 44(12) (1996) 4749-4763.

[30] J. Wang, N. Li, O. Anderoglu, X. Zhang, A. Misra, J.Y. Huang, J.P. Hirth, Detwinning mechanisms for growth twins in face-centered cubic metals, Acta Materialia 58(6) (2010) 2262-2270.

[31] T.H. Ly, J. Zhao, M.O. Cichocka, L.-J. Li, Y.H. Lee, Dynamical observations on the crack tip zone and stress corrosion of two-dimensional MoS2, Nature Communications 8(1) (2017) 14116.

[32] A. Azizi, X. Zou, P. Ercius, Z. Zhang, A.L. Elías, N. Perea-López, G. Stone, M. Terrones, B.I. Yakobson, N. Alem, Dislocation motion and grain boundary migration in two-dimensional tungsten disulphide, Nature Communications 5(1) (2014) 4867.

[33] L. Huang, F. Zheng, Q. Deng, Q.H. Thi, L.W. Wong, Y. Cai, N. Wang, C.-S. Lee, S.P. Lau, M. Chhowalla, J. Li, T.H. Ly, J. Zhao, In Situ Scanning Transmission Electron Microscopy Observations of Fracture at the Atomic Scale, Physical Review Letters 125(24) (2020) 246102.

[34] S. Wang, Z. Qin, G.S. Jung, F.J. Martin-Martinez, K. Zhang, M.J. Buehler, J.H. Warner, Atomically Sharp Crack Tips in Monolayer MoS2 and Their Enhanced Toughness by Vacancy Defects, ACS Nano 10(11) (2016) 9831-9839.

[35] L. Liu, J. Wang, S.K. Gong, S.X. Mao, High resolution transmission electron microscope observation of zero-strain deformation twinning mechanisms in Ag, Phys Rev Lett 106(17) (2011) 175504.

[36] S. Kurasch, J. Kotakoski, O. Lehtinen, V. Skákalová, J. Smet, C.E. Krill, A.V. Krasheninnikov, U. Kaiser, Atom-by-Atom Observation of Grain Boundary Migration in Graphene, Nano Letters 12(6) (2012) 3168-3173.

[37] A.V. Krasheninnikov, K. Nordlund, Ion and electron irradiation-induced effects in nanostructured materials, Journal of Applied Physics 107(7) (2010) 071301.

[38] R.F. Egerton, P. Li, M. Malac, Radiation damage in the TEM and SEM, Micron 35(6) (2004) 399-409.

[39] K. Zheng, C. Wang, Y.-Q. Cheng, Y. Yue, X. Han, Z. Zhang, Z. Shan, S.X. Mao, M. Ye, Y. Yin, E. Ma, Electron-beam-assisted superplastic shaping of nanoscale amorphous silica, Nature communications 1(1) (2010) 24.

[40] T. Yokota, M. Murayama, J.M. Howe, In situ Transmission-Electron-Microscopy Investigation of Melting in Submicron Al-Si Alloy Particles under Electron-Beam Irradiation, Physical Review Letters 91(26) (2003) 265504.

[41] M. Schlögl, J. Paulitsch, J. Keckes, P.H. Mayrhofer, Influence of AlN layers on mechanical properties and thermal stability of Cr-based nitride coatings, Thin Solid Films 531 (2013) 113-118.

[42] M. Schlögl, B. Mayer, J. Paulitsch, P.H. Mayrhofer, Influence of CrN and AlN layer thicknesses on structure and mechanical properties of CrN/AlN superlattices, Thin Solid Films 545(Supplement C) (2013) 375-379.

[43] G.S. Kim, S.Y. Lee, J.H. Hahn, S.Y. Lee, Synthesis of CrN/AlN superlattice coatings using closed-field unbalanced magnetron sputtering process, Surface and Coatings Technology 171(1) (2003) 91-95.

[44] J. Lin, J.J. Moore, B. Mishra, M. Pinkas, W.D. Sproul, Nano-structured CrN/AlN multilayer coatings synthesized by pulsed closed field unbalanced magnetron sputtering, Surface and Coatings Technology 204(6) (2009) 936-940.

[45] J. Lin, J.J. Moore, B. Mishra, M. Pinkas, X. Zhang, W.D. Sproul, CrN/AlN superlattice coatings synthesized by pulsed closed field unbalanced magnetron sputtering with different CrN layer thicknesses, Thin Solid Films 517(20) (2009) 5798-5804.

[46] B. Navinšek, P. Panjan, A. Cvelbar, Characterization of low temperature CrN and TiN (PVD) hard coatings, Surface and Coatings Technology 74-75 (1995) 155-161.

[47] S.-K. Tien, J.-G. Duh, Effect of heat treatment on mechanical properties and microstructure of CrN/AlN multilayer coatings, Thin Solid Films 494(1) (2006) 173-178.

[48] T. Fu, X. Peng, C. Huang, Y. Zhao, S. Weng, X. Chen, N. Hu, Effects of twin boundaries in vanadium nitride films subjected to tensile/compressive deformations, Applied Surface Science 426 (2017) 262-270.

[49] H.R. Azizpour A, Klimashin FF, Wojcik T, Poursaeidi E, Mayrhofer PH., Deformation and Cracking Mechanism in CrN/TiN Multilayer Coatings., Coatings 9 (2019) 363.

[50] N.J.M. Carvalho, J.T.M. De Hosson, Deformation mechanisms in TiN/(Ti,Al)N multilayers under depth-sensing indentation, Acta Materialia 54(7) (2006) 1857-1862.

[51] D. Holec, P.H. Mayrhofer, Surface energies of AlN allotropes from first principles, Scripta Materialia 67(9) (2012) 760-762.

Supplementary Materials
Real-time atomic-resolution observation of coherent twin boundary migration in CrN

Zhuo Chen[1], Yonghui Zheng[1], Lukas Löfler[2], Matthias Bartosik[3], Huaping Sheng[1], Christoph Gammer[1], David Holec[2], Zaoli Zhang[1#]

[1] Erich Schmid Institute of Materials Science, Austrian Academy of Sciences, A-8700 Leoben, Austria

[2] Department of Materials Science, Montanuniversität Leoben, A-8700 Leoben, Austria

[3] Institute of Materials Science and Technology, TU Wien, A-1060 Vienna, Austria

Corresponding author: zaoli.zhang@oeaw.ac.at

Captions for Movies (movie as seen in https://doi.org/10.1016/j.actamat.2021.116732**):**

Movie S1: Movie showing the TD emission and CTB migration from CTB/ITB junction. The video frequency is 20 fps. The movie is acquired using JEOL JEM 2100F with an image-side Cs-corrector. The electron dose rate was ~5×10^4 electrons/Å^2·s with the convergence beam

Movie S2: A movie showing TD nucleation and CTB migration in CrN caused by strong beam irradiation. The video frequency is 20fps. After 17 seconds, TD nucleation and CTB migration can be found. The movie is required by JEOL JEM 2100F with image-side Cs-corrected. The electron dose rate was ~5×10^4 electrons/Å^2·s with the convergence beam

Movie S3: Movie showing the time-evolution of the dynamic process of CTB migration that is undergoing an electron-beam-induced CTB migration from N-termination to Cr-termination. After 17 seconds, TD nucleation and CTB migration can be found. At ~18s, the CTB fully

migrate to the Cr-termination CTB. The video frequency is 20fps. The movie is acquired using FEI Titan Themis 80-300 with an image-side Cs-corrector. The electron dose rate was ~5×10^4 electrons/Å^2·s with the convergence beam

Movie S4: A movie showing the Cr atom jumps at the CTB/surface junction under strong beam irradiation. Within 25 seconds, two significant Cr jumps were detected (t=4 s and t=16 s). The video frequency is 20fps. The movie is acquired using FEI Titan Themis 80-300 with image-side Cs-corrector. The electron dose rate was ~1×10^4 electrons/Å^2·s with an electron beam expanding to near full fluorescent screen.

Supplementary Figures S1-S12:
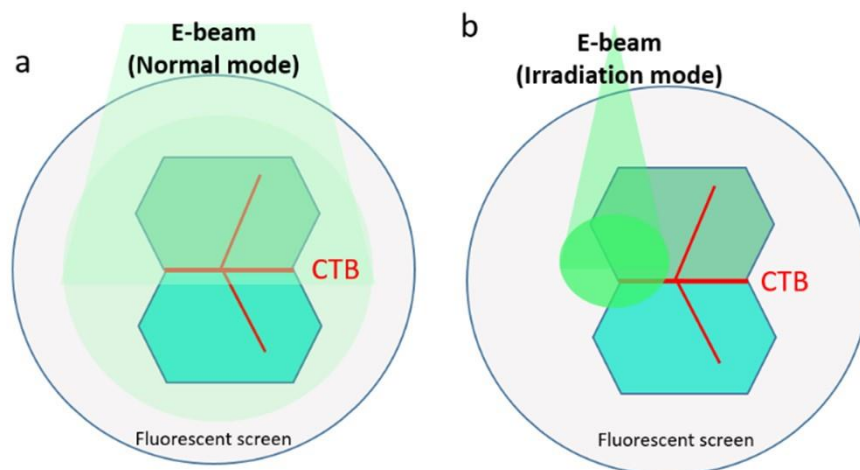
Supplementary Figure S1：a, A schematic view of the normal illumination mode. Under this image taken condition, the electron dose rate was ~1×10^4 electrons/Å^2·s with an electron beam expanding to near full fluorescent screen. **b,** A schematic view of electron beam illumination mode during the *in-situ* experiments. Under this mode, the electron dose rate was ~5×10^4 electrons/Å^2·s with the convergence beam (near 1/8 fluorescent screen).
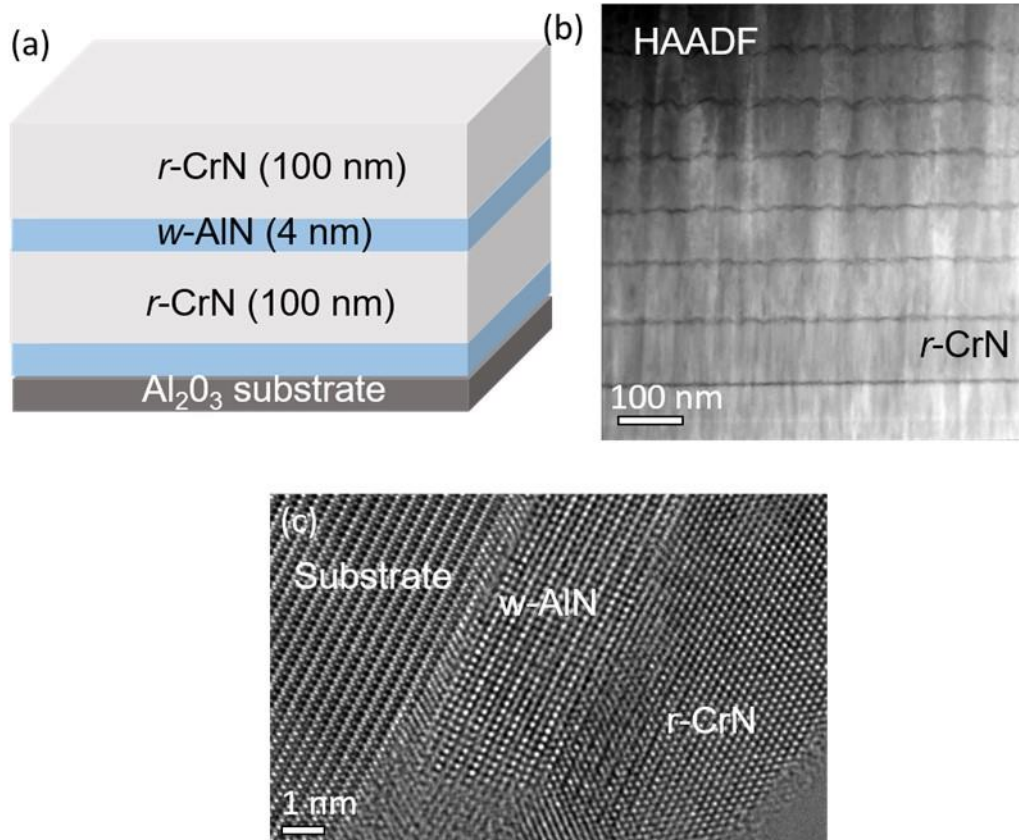
Supplementary Figure S2: **a,** A schematic view of CrN multilayer structure on the Al_2O_3 (0006) substrate. **b,** A low magnification HAADF image of CrN thin film with bright contrast of CrN layer and dark contrast of the AlN layer. **c,** A typical HRTEM image from the substrate-film interface area, where the AlN exhibits a wurtzite-type structure.
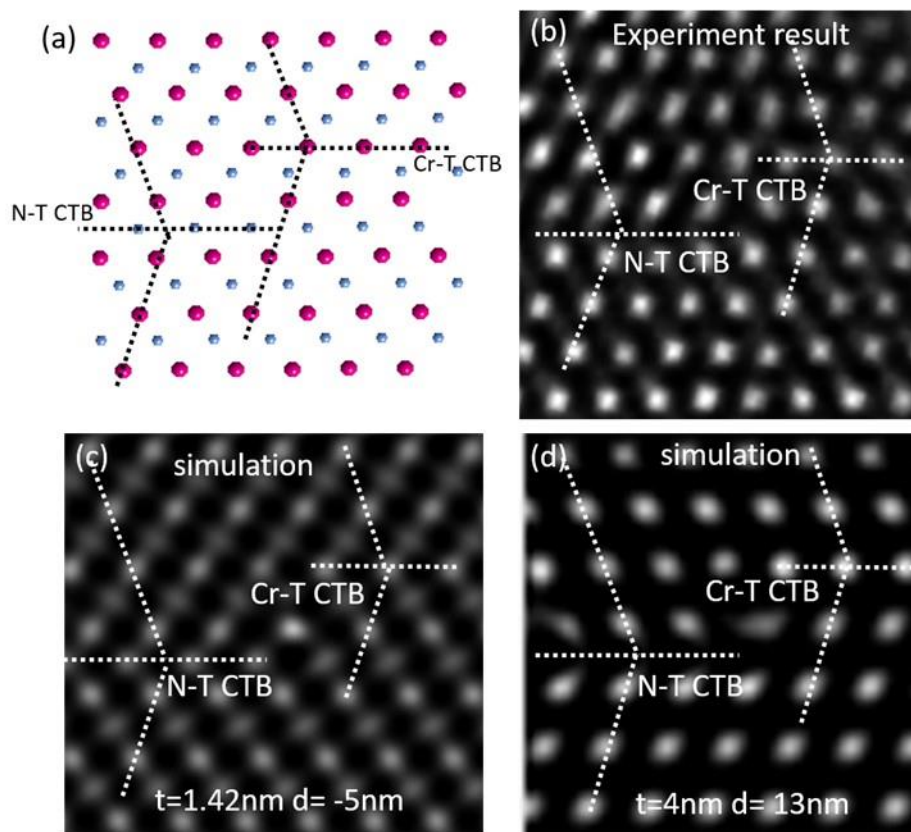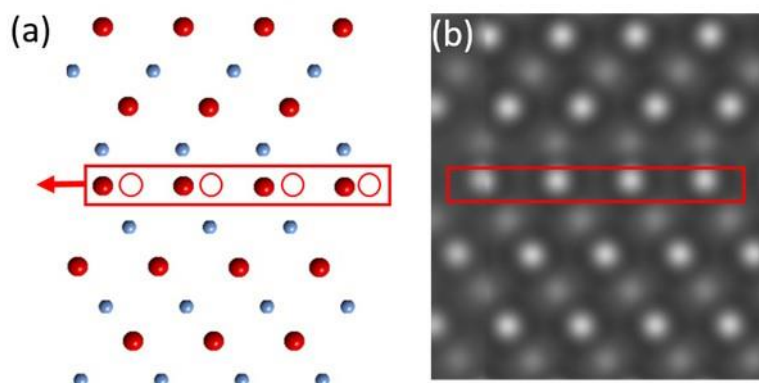
Supplementary Figure S3: a, Schematic structural model of CTB step in CrN, where the upper position of the terrace is N-termination CTB and lower position is Cr-termination CTB. **b,** a snapshot of HRTEM Movie S2. **c, d,** HRTEM image simulation results at different sample thickness. Simulation conditions: TEM: 2100F, Cs=0.0, Cc=1.2mm, acceleration voltage=200kv. In Fig. S3c, the sample thickness is thin enough. Thus, in CrN $\Sigma 3\{111\}$ CTB the contrast of N atoms can be observed. However, as the sample thickness increasing, the N contrast will gradually become weaker until it totally disappears. When the sample thickness is about 4 nm, there only show the Cr atom contrast (as seen in Fig. S3d). Thus, combining image simulation with experimental observation, we can distinguish whether the CTB is the N-termination or the Cr-termination.
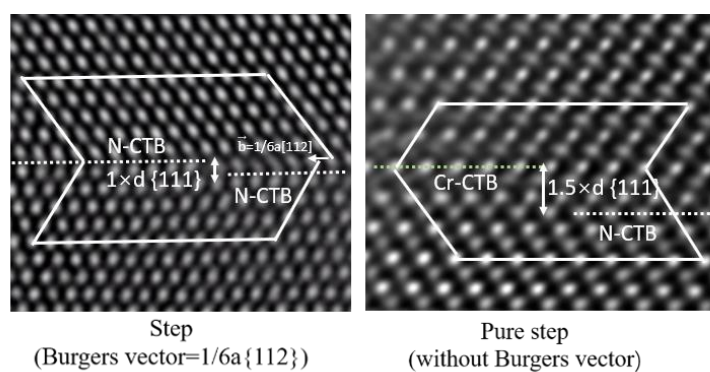
Supplementary Figure S4: Directly measured Burgers vector on the HRTEM micrographs of Fig.3c and Fig.4b. TD emission from the CTB/ITB junction shows a twin boundary step structure with N-terminated/N-terminated and with a height of $1\times d_{\{111\}}$ (Fig.3c). The Burgers vector of such TD is 1/6a[112]. However, TD emission from the CTB/surface junction displays a twin boundary step structure with N-terminated/Cr-terminated and with a height of $1.5\times d_{\{111\}}$ (Fig.4b).
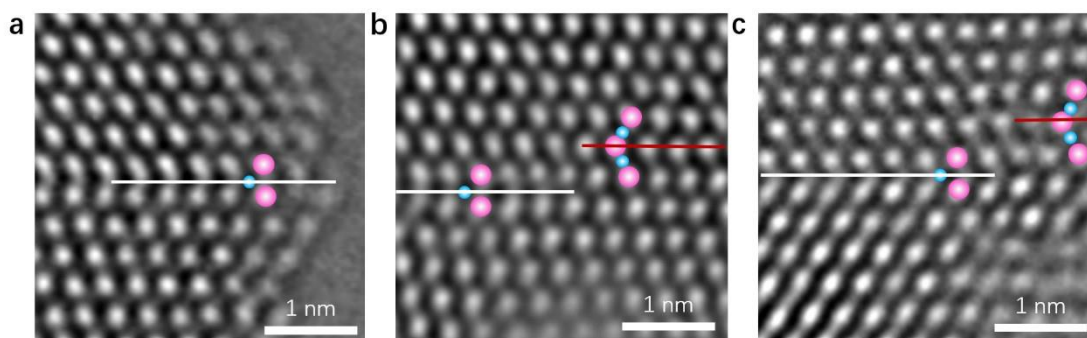
Supplementary Figure S5: The enlarged HRTEM image in Figs. 5. **a,** show that the CTB has a fully N- terminated CTB structure. **b,** show that the CTB structure varies from an N- terminated CTB to a Cr- terminated CTB. **c,** displays the already created Cr- terminated CTB partially reverse to N- terminated CTB after terminating irradiation for 10 min.


Supplementary Figure S6: a, Schematic structural model of the transitional stage (ball on ball) from N-termination CTB to Cr-termination CTB. **b,** HRTEM image simulation result using the model in **a**. Simulation conditions: TEM: FEI Titan Themis 80-300, Cs=0, acceleration voltage=300kV, defocus=- 9.4 nm and thickness = 1.7 nm.
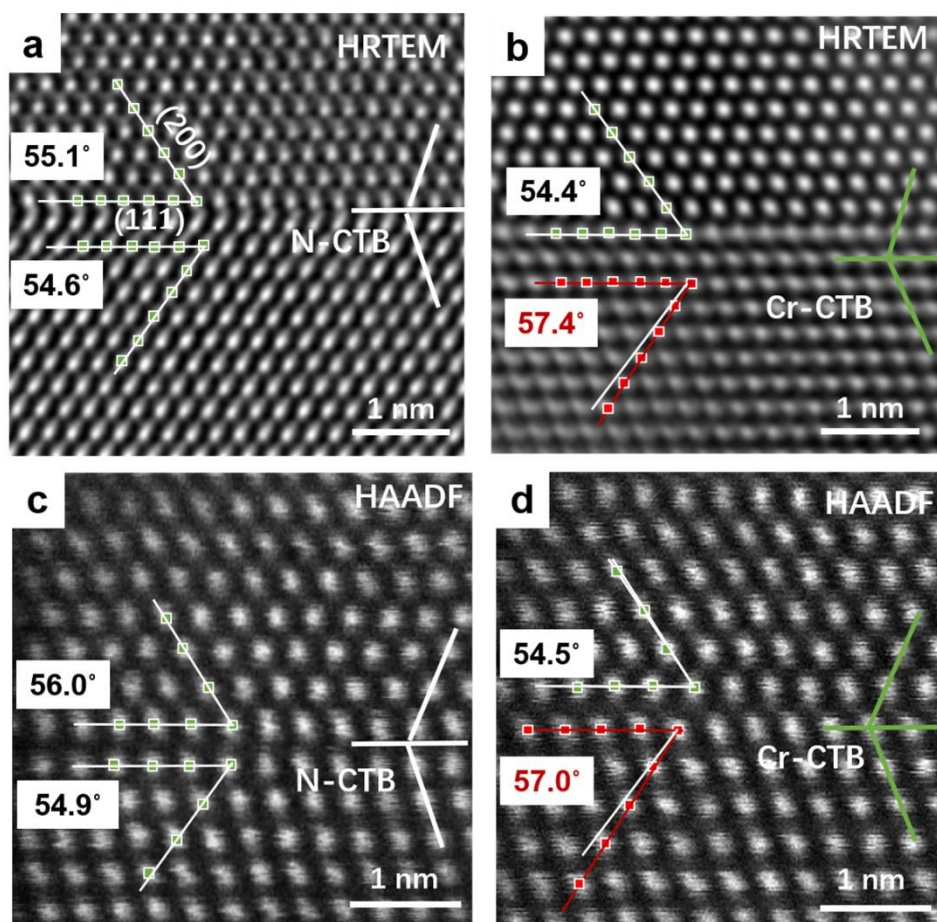
Supplementary Figure S7: (a) and **(b),** HRTEM images of un-irradiated (normal illumination mode) N-terminated CTB and Cr-terminated CTB, respectively. **(c)** and **(d),** HAADF images of un-irradiated (normal illumination mode) N-terminated and Cr-terminated CTB, respectively. In a-d, the lattice angle is determined by $[11\bar{1}]/[100]$ direction

Throughout the observations, we found that the CTB structure alternating can also be driven by the internal stress, in addition to beam irradiation (i.e., Fig.7). Nitride coatings manufactured by reactive magnetron sputter generally exhibit very high intrinsic residual stress [127, 128]. This stress may drive the alternation of CTB structure. Figs. S7 show HRTEM and HAADF images from un-irradiated N-terminated and Cr-terminated CTB (under a normal illumination mode). For the N-terminated CTB (Fig.S7 a and c), the measured lattice plane angles (the angle between $(11\bar{1})$ and (200) planes) in the CTB region are 54.6˚—56.0˚, corresponding to a shear strain of 0.2% —2.3%. However, for the Cr-terminated CTB, the measured lattice plane angles in the lower part of Fig. S7b and d are 57.0˚ and 57.4˚, respectively. This indicates that a certain

strain/stress, i.e., 4.2% and 4.9% shear strain, drive CTB migration and structure alternating (from N-CTB to Cr-CTB). Thus, we infer that the formation of the Cr-terminated CTB can effectively accommodate stress concentrations.
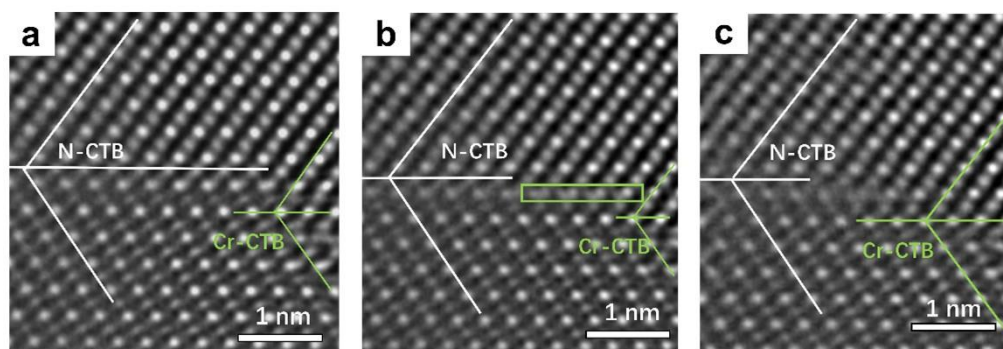

Supplementary Figure S8: Three continuous snapshots HRTEM images demonstrating the asynchronous CTB migration process from N-terminated to Cr- terminated under a normal illumination mode (~10000 electrons/$\text{Å}^2\cdot$s).

Under a normal illumination mode (no intense electron beam irradiation), we found that when the local location is subjected to high strain conditions, the asynchronous CTB migration process can also be observed. Figs S8 shows three consecutive snapshots (exposure time with 1s) under a normal illumination mode, where indicate the alternation of the CTB structure from N-terminated CTB to Cr- terminated CTB. In Fig. S8a (initial state), we observe a twin boundary step structure with N-terminated/Cr-terminated. By measuring the lattice plane angle of the upper part, we know that the shear strain reaches up to 4.5%. This means that the strain in Fig. S8a is already very close to the critical stress state for migration (see our GPA result in Figs 9), which means any external stimulus may stimulate its migration. After about 1s, part of the Cr {111} plane (as indicated in green frame) migrates. However, the position of the N atom has not changed in Fig. S8b, indicating that Fig. S8b is a transitional state of its CTB migration from N-terminated to Cr- terminated. Finally, Fig. S8c (final stage) shows that the CTB structure has been fully transformed to a Cr- terminated CTB. Therefore, three continuous states (Fig. S8) indicate that the motion of Cr and N atoms also is not synchronous, i.e., Cr atoms migration firstly followed by the N atoms, consistent with our observation results under intense electron beam irradiation in Figs 7 of manuscript.
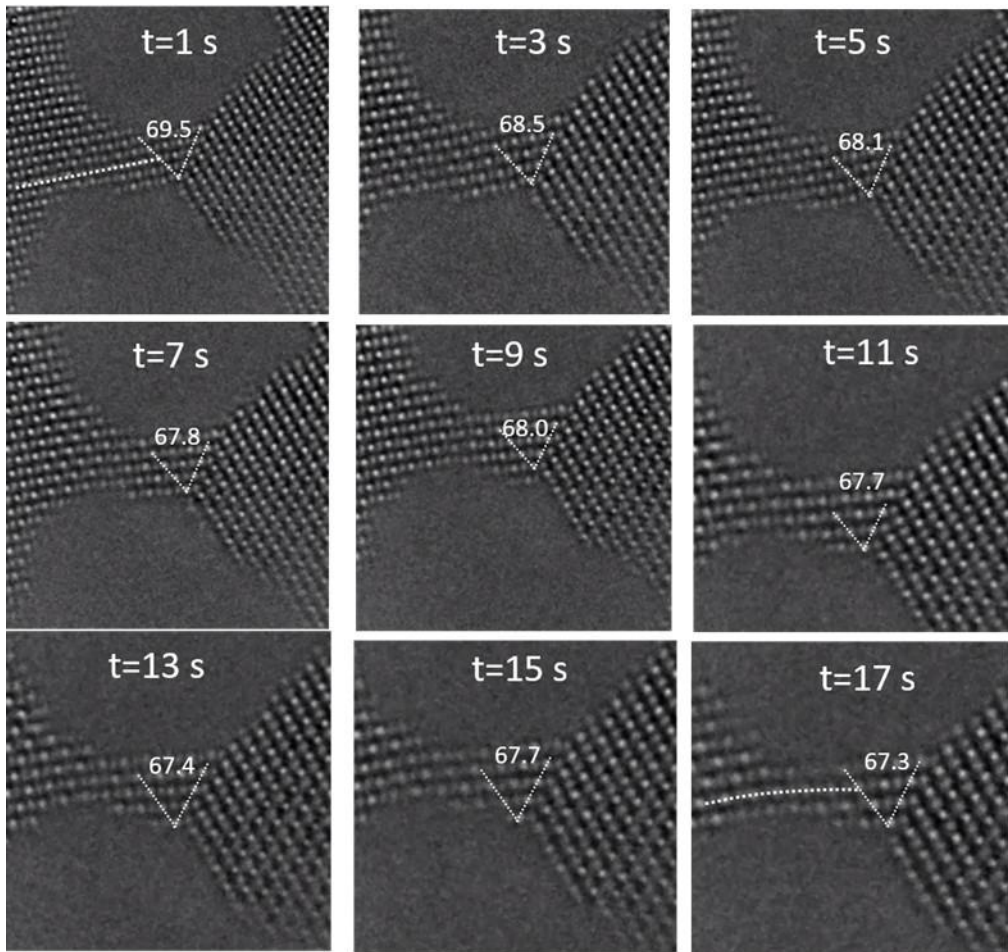
Supplementary Figure S9: Selected movie frames from movie S3 (1-17s). The time of the image capture (in seconds) is given at the top. Here we measured the inter-plane lattice angles $((11\bar{1})/(1\bar{1}1))$ at different times (1-17s, with an interval of 2 seconds) in the same location. The inter-plane lattice angle decreases continuously from 69.5° to be 67.3°.
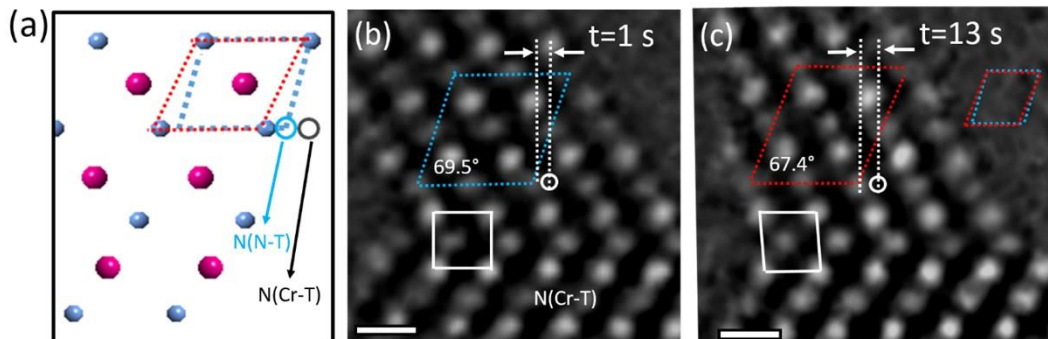
Supplementary Figure S10: a, The schematic image of distorted N-termination CTB (induced by shear strain/stress). The blue circle is the position of perfect N-termination CTB (without shear strain/stress). The black circle corresponds to the position of the final structure of CTB migration (Cr-termination CTB). **b, c,** Snapshots of Movie S3 at t=1 s and t=13s, respectively. In **c**, the shear strain in the upper part is larger than that in **b** becuase the α angle changes from 69.5° to 67.4°. Scale bars: **(b)** and **(c)** 0.25 nm. Under the shear strain/stress, Cr atoms at the CTB will be closer to the Cr-termination position and the shift distance will be shorter than the required distance. Under the same shear strain/stress, N atoms will be away from the Cr-termination position, and the shift distance will be longer than the theoretical distance (as seen in Fig. S10a). This can also be confirmed by our experiment observation (as seen Supplementary in Fig. S10b and c).
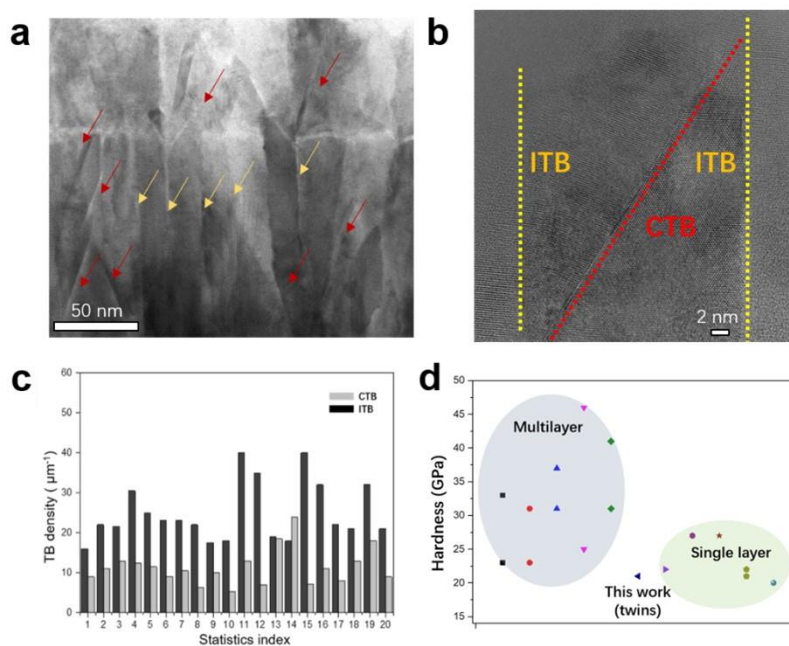
Supplementary Figure S11: a, bright-field images of CrN columnar grains away from the substrate about 300-400 nm, where the red and yellow labels indicate CTBs and ITBs, respectively. **b,** HRTEM observation the columnar grain boundaries (with CTB and ITB). **c,** the statistics of CTB and ITB density (number of CTB per unit length). Here, a total of 20 STEM BF images (statistics index 1-20) were used for TBs density statistics. (d) A summary of hardness values plotted with multilayer AlN/CrN and single layer CrN.
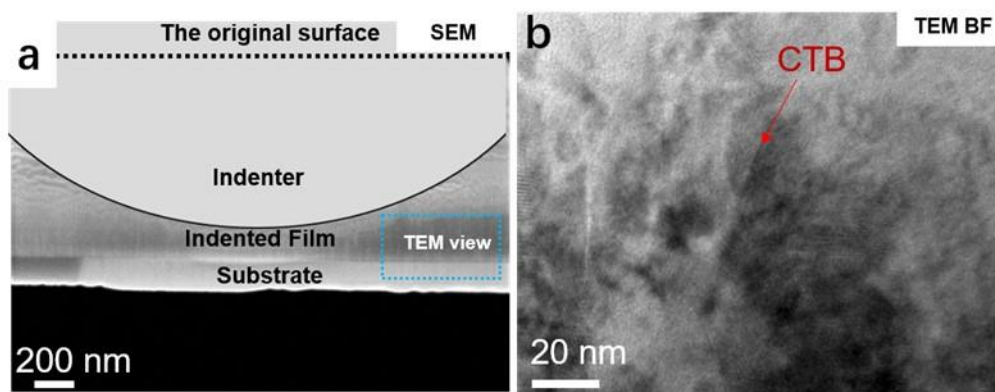
Supplementary Figure S12 a, SEM micrograph of cross-sectional view of the indented thin film. The dotted line shows the original sample surface (film thickness ~2 μm). The blue frame is the TEM observation position. **c,** TEM-BF cross-sectional view of the indented thin film.

The nanoindentation was performed with a Hysitron Triboscope equipped with a spherical tip. The cross-sectional TEM specimens were prepared using a Zeiss Auriga Laser FIB system, consisting of a focused ion beam column (Orsay Physics Ga+ ion FIB). A SEM image (Fig. S12a) illustrates the overall morphology of the indented cross-section. Fig. S12c shows a TEM BF image in the indented film (the TEM view position as seen the blue frame in Fig. S12b), where a CTB can be found.

Reference

[1] I. Petrov, P.B. Barna, L. Hultman, J.E. Greene, Microstructural evolution during film growth, Journal of Vacuum Science & Technology A 21(5) (2003) S117-S128.

[2] H.K. Tönshoff, H. Seegers, Influence of residual stress gradients on the adhesion strength of sputtered hard coatings, Thin Solid Films 377-378 (2000) 340-345.